

12-1-2010

Using High-Powered, Frequency-Narrowed Lasers For Rb/¹²⁹Xe and Cs/¹²⁹Xe Spin-Exchange Optical Pumping To Achieve Improved Production of Highly Spin-Polarized Xenon For Use In Magnetic Resonance Applications

Nicholas Whiting

Southern Illinois University Carbondale, whiting_nick@hotmail.com

Follow this and additional works at: <http://opensiuc.lib.siu.edu/dissertations>

Recommended Citation

Whiting, Nicholas, "Using High-Powered, Frequency-Narrowed Lasers For Rb/¹²⁹Xe and Cs/¹²⁹Xe Spin-Exchange Optical Pumping To Achieve Improved Production of Highly Spin-Polarized Xenon For Use In Magnetic Resonance Applications" (2010). *Dissertations*. Paper 172.

This Open Access Dissertation is brought to you for free and open access by the Theses and Dissertations at OpenSIUC. It has been accepted for inclusion in Dissertations by an authorized administrator of OpenSIUC. For more information, please contact opensiuc@lib.siu.edu.

USING HIGH-POWERED, FREQUENCY-NARROWED LASERS FOR Rb/¹²⁹XE
AND Cs/¹²⁹XE SPIN-EXCHANGE OPTICAL PUMPING TO ACHIEVE
IMPROVED PRODUCTION OF HIGHLY SPIN-POLARIZED XENON FOR USE
IN MAGNETIC RESONANCE APPLICATIONS

by

Nicholas Whiting

B.S., Southern Illinois University, 2005

A Dissertation

Submitted in Partial Fulfillment of the Requirements for the
Degree of Doctor of Philosophy

Department of Chemistry and Biochemistry

in the Graduate School

Southern Illinois University Carbondale

December 2010

DISSERTATION APPROVAL

USING HIGH-POWERED, FREQUENCY-NARROWED LASERS FOR RB/¹²⁹XE
AND CS/¹²⁹XE SPIN-EXCHANGE OPTICAL PUMPING TO ACHIEVE
IMPROVED PRODUCTION OF HIGHLY SPIN-POLARIZED XENON FOR USE
IN MAGNETIC RESONANCE APPLICATIONS

By

Nicholas Whiting

A Dissertation Submitted in Partial

Fulfillment of the Requirements

for the Degree of

Doctor of Philosophy

in the field of Physical Chemistry

Approved by:

Dr. Boyd M. Goodson Chair

Dr. Qinfeng Ge

Dr. Gabriela Perez-Alvarado

Dr. Kara Huff-Hartz

Dr. Mark Byrd

Graduate School
Southern Illinois University Carbondale
July 15, 2010

AN ABSTRACT OF THE DISSERTATION OF

Nicholas Whiting, for the Doctor of Philosophy degree in Physical Chemistry, presented on July 15, 2010, at Southern Illinois University Carbondale.

TITLE: USING HIGH-POWERED, FREQUENCY-NARROWED LASERS FOR RB/¹²⁹XE AND CS/¹²⁹XE SPIN-EXCHANGE OPTICAL PUMPING TO ACHIEVE IMPROVED PRODUCTION OF HIGHLY SPIN-POLARIZED XENON FOR USE IN MAGNETIC RESONANCE APPLICATIONS

MAJOR PROFESSOR: Dr. Boyd M. Goodson

Nuclear magnetic resonance (NMR) spectroscopy has been extensively used to investigate numerous systems of interest, ranging from collections of molecules to living organisms. However, NMR suffers from one key drawback: an inherent lack of detection sensitivity, as compared to other common forms of spectroscopy. This is due to the minute nuclear magnetic moments and low nuclear spin polarization levels at thermal equilibrium ($\sim 10^{-5}$ to 10^{-6}), and thus necessitates the use of relatively large sample volumes. One way to overcome this low detection sensitivity is to introduce a species with highly non-equilibrium nuclear spin polarization, such as 'hyperpolarized' xenon-129. Hyperpolarized xenon can either be used as its own chemical sensor (due to its exquisitely sensitive chemical shift range), or the non-equilibrium polarization may be transferred from xenon to another molecule of interest (such as a protein or inclusion complex).

Hyperpolarized xenon is produced through a process known as spin-exchange optical pumping (SEOP), where the angular momentum from resonant, circularly-polarized light is transferred to the electronic spins of an alkali-metal, and is subsequently transferred to the xenon nuclei through gas-phase collisions. While SEOP has been extensively characterized throughout the years, new experimental techniques and emerging technologies have considerably advanced the field in recent years, and may enable a new understanding of the underlying physics of the system.

The first five chapters in this dissertation review background information and the principal motivations for this work. Chapter one reviews the basics of NMR, from the various components of the nuclear spin Hamiltonian and different spin-relaxation pathways to the reasons behind the low polarization of nuclear spins at thermal equilibrium and a few alternative methods to ‘boost’ the NMR signal. Chapter two discusses the fundamental aspects of SEOP, including the electronic spin polarization of the alkali-metal, polarization transfer to the xenon nuclei, and different avenues for the spin polarization to be depleted. The third chapter covers the practical considerations of SEOP from the viewpoint of an experimentalist; namely, the experimental differences when using a variety of alkali metals and noble gases, as well as different SEOP apparatuses and experimental parameters. Chapter four details a variety of different light sources that may be used for SEOP; specifically, the use of laser diode arrays (LDAs) are reviewed, including LDAs that have been frequency-narrowed for more

efficient light absorption by the alkali metal. The fifth background chapter covers a variety of magnetic resonance applications of hyperpolarized xenon, including molecular biosensors, specific and non-specific binding with proteins, materials studies, and *in vivo* applications. The sixth chapter is used as an overview of the dissertation research, which is presented in chapters seven through eleven.

Chapter seven details the arrangement of the particular SEOP apparatus used in this research, as well as the experimental protocol for producing hyperpolarized xenon. The eighth chapter accounts the implementation and characterization of the first frequency-narrowed LDA used in this research, as well as an equal comparison to a traditional broadband LDA. Chapter nine introduces the use of *in situ* low-field NMR polarimetry, which was used to distinguish an anomalous dependence of the optimal OP cell temperature on the in-cell xenon density; the low-field set-up is also used to examine the build-up of nuclear spin polarization in the OP cell as it occurs. The tenth chapter covers the use of high power, frequency-narrowed light sources that are spectrally tunable independent of laser power; this allows for the study of changes to the optimal spectral offset as a function of in-cell xenon density, OP cell temperature, and laser power. Xenon polarization build-up curves are also studied to determine if the spectral offset of the laser affects the nuclear spin polarization dynamics within the OP cell. Finally, chapter eleven accounts the use of high power, broadband LDAs to perform SEOP in which cesium is used as the alkali metal;

these results demonstrate (for the first time) that the xenon polarization generated by cesium optical pumping can surpass that of rubidium OP under conditions of high laser flux and elevated in-cell xenon densities.

ACKNOWLEDGMENTS

I have encountered a great number of helpful people during my time at SIUC, many of whom have assisted in my experimental research and contributed to my overall understanding of science. Before I leave SIUC to embark on a postdoctoral research fellowship, I would like to express my sincere gratitude to the following individuals.

First and foremost, I am deeply grateful for the years of guidance and support that I have received from my advisor, Dr. Boyd Goodson. I honestly feel that I may very well have not made it as far as I have if not for the scientific motivation and relentless quest for answers that he instills on his students. Boyd (i.e., ‘the boss’) has served as an excellent scientific role model, and I wish him nothing but the best of fortunes in the future.

Working under Boyd has also provided ample opportunities to meet other scientists of high regard, and to forge long-lasting collaborations, some of which have enabled the research presented here. Of particular note, I would also like to thank Dr. Michael Barlow (University of Nottingham, UK) for the contribution of lasers, optical equipment, and experimental knowledge, all of which have greatly aided my research.

My gratitude also extends to the other members of my graduate committee: Drs. Qinfeng Ge, Gabriela Perez-Alvarado, Kara Huff-Hartz, and Mark Byrd for their assistance through the process of completing my PhD requirements.

Next, I would like to thank my lab mates over the years. In particular, my good friend Peter Nikolaou, who took me under his wing during my early days in the lab; indeed, it is quite remarkable to be able to work with someone who is also such a good friend outside of the lab. Along with Peter, I would like to especially thank Neil Eschmann, who assisted with many of the optical pumping experiments, and is also a good friend (good luck in California). In addition to Peter and Neil, I would like to express my appreciation to all of the other lab mates that I've had throughout the years; both the 'old' group: Xiaoxia, Indrajit, Kassie, Caitlin, Brooke, Brad, Sheeja, and Jennifer; the 'new' group: Ping, Laura Walkup, Laura Buck, and Brogan; the undergraduates and summer REU students who have contributed to the lab: Kyle P., Shavonne, M., Ashley S., Briena B., Alisha L., Katelyn E., Kaili R., and Allie H.; and also to a number of various people throughout the Chemistry Department: thank you. While the allotted space only allows the brief mentioning of your names, you have all left an indelible impression on me (for the good).

Furthermore, I would like to thank my family for their support over the last several years; I am especially appreciative for the love, support, and understanding provided by my wife, Keithsha, who has essentially put her life on hold for the last few years so that I could complete my PhD research.

Finally, I am thankful to the National Science Foundation, who has provided me with a two-year International Research Fellowship to the University of Nottingham (UK), thus providing me with additional motivation for completing this dissertation.

TABLE OF CONTENTS

	<u>PAGE</u>
ABSTRACT	i
ACKNOWLEDGMENTS	v
LIST OF TABLES	xiv
LIST OF FIGURES	xv
CHAPTERS	
CHAPTER 1 – Basics of Nuclear Magnetic Resonance	1
1.1 Introduction	1
1.2 Basic Description of NMR	3
1.3 Relevant Components of the Nuclear Spin Hamiltonian	6
1.3.1 <i>Static Field</i>	6
1.3.2 <i>Transverse Field</i>	7
1.3.3 <i>Chemical Shift</i>	7
1.3.4 <i>Dipolar Couplings</i>	9
1.3.5 <i>Scalar Couplings</i>	10
1.3.6 <i>Quadrupolar Couplings</i>	11
1.4 Nuclear Spin Relaxation Mechanisms	12
1.4.1 <i>Longitudinal Relaxation</i>	13
1.4.2 <i>Transverse Relaxation</i>	15
1.5 Improvements to Nuclear Spin Polarization	16

CHAPTER 2 – Fundamental Aspects of Spin-Exchange Optical Pumping	20
2.1 Introduction	20
2.2 Optical Polarization of Alkali-Metal Electrons	21
2.3 Nuclear Polarization of Noble Gas Atoms via Spin-Exchange	24
2.4 Spin-Relaxation Mechanisms	28
CHAPTER 3 – Practical Considerations of SEOP	32
3.1 Introduction	32
3.2 Choice of Alkali-Metal	33
3.2.1 <i>Rubidium</i>	34
3.2.2 <i>Cesium</i>	35
3.2.3 <i>'Hybrid' Alkali-Metal SEOP</i>	36
3.3 Choice of Noble Gas	38
3.3.1 <i>Helium-3</i>	38
3.3.2 <i>Xenon-129</i>	39
3.3.3 <i>Krypton-83 & Xenon-131</i>	41
3.4 Additional Considerations	43
3.4.1 <i>SEOP Apparatus Designs</i>	43
3.4.2 <i>Optical Pumping Cell Conditions</i>	45
3.4.3 <i>Buffer Gas Choices</i>	47
3.4.4 <i>Xenon Density Effects</i>	49

3.4.5 Cell Temperature/Laser Power/Spectral Offset	51
CHAPTER 4 – Laser Technology for Optical Pumping.....	53
4.1 Introduction.....	53
4.2 Broadband Laser Diode Arrays	53
4.3 Fixed-Frequency VHG-LDAs	55
4.4 Tunable VHG-LDAs	59
4.4.1 VHG-TEC Tuning.....	59
4.4.2 Mechanical Tuning.....	60
4.4.3 ‘On-Chip’ VHG-LDAs	62
4.5 Emerging Laser Technology for Cs/ ¹²⁹ Xe SEOP	64
CHAPTER 5 – Magnetic Resonance Applications of Hyperpolarized Xenon	67
5.1 Introduction.....	67
5.2 Properties of Xenon	67
5.2.1 General Physical Properties	67
5.2.2 NMR Properties	69
5.3 Polarization Transfer Methods.....	71
5.3.1 Low-Field Thermal Mixing.....	72
5.3.2 SPINOE	73
5.4 Xenon Binding in Hydrophobic Cavities of Proteins.....	75

5.5 Xenon as a Molecular Biosensor	78
5.6 Diffusion in Porous Media/Surface Studies.....	81
5.7 Low-Field and Remote Detection Techniques	82
5.8 Void-Space and Tissue Imaging.....	84
CHAPTER 6 – Research Outline.....	87
6.1 Introduction.....	87
6.2 Goals and Initiatives of this Dissertation Research.....	87
6.3 Primary Research of this Dissertation.....	88
6.4 Significance of this Dissertation Research.....	89
CHAPTER 7 – SEOP Apparatus Description and Basic Experimental Parameters	92
7.1 Introduction.....	92
7.2 SEOP Apparatus & Experimental Procession	92
7.3 Calculation of Xenon Polarization.....	99
CHAPTER 8 – Implementation of Frequency-Narrowed VHG-LDAs for Rb/ ¹²⁹ Xe SEOP.....	102
8.1 Introduction.....	102
8.2 Characterization of Laser Output.....	103
8.3 Comparison of VHG-LDA with Previous Broadband LDA.....	106

8.4 Monitoring P_{Rb} <i>In Situ</i>	107
8.5 Dual-Bar VHG-LDA Characteristics	112
8.6 Xenon Density Anomaly	115
8.7 Conclusions	117

CHAPTER 9 – Interdependence of In-Cell Xenon Density and

Temperature for Rb/ ^{129}Xe SEOP	119
9.1 Introduction	119
9.2 <i>In Situ</i> P_{Xe} Measurement via Low-Field NMR Polarimetry	120
9.3 Dependence of Optimal Cell Temperature on Xe Density	125
9.4 Dependence of T_{OPT} on Buffer Gas Composition/Density	127
9.5 Xenon Nuclear Spin Polarization Dynamics	128
9.6 Ultrahigh P_{Xe} Values at High Xenon Densities	136
9.7 Conclusions	139

CHAPTER 10 – Variable Excitation Wavelength Studies of

Rb/ ^{129}Xe SEOP	141
10.1 Introduction	141
10.2 ‘On-Chip’ VHG-LDAs	143
10.3 Improved Low-Field Detection Capabilities	146
10.4 P_{Xe} Dependencies on T_{cell} , $[\text{Xe}]_{\text{cell}}$, Spectral Offset, & Laser Flux....	
.....	148

10.4.1 Dependence of P_{Xe} on Laser Flux and T_{cell}	148
10.4.2 Dependence of P_{Xe} on Laser Flux and Spectral Offset.....	150
10.4.3 Dependence of P_{Xe} on Laser Flux at Different T_{cell} 's and Spectral Offsets	151
10.4.4 Dependence of P_{Xe} on T_{cell} and Spectral Offset	153
10.4.5 Dependence of P_{Xe} on $[Xe]_{cell}$ and Spectral Offset	156
10.5 P_{Xe} Comparison of Narrowed Versus Broadband LDAs at Increased Laser Flux	158
10.6 P_{Xe} Dynamics as a Function of T_{cell} , $[Xe]_{cell}$, & Spectral Offset ..	159
10.6.1 Higher Power, 'On-Chip' VHGLDAs	160
10.6.2 P_{Xe} Build-Up Dynamics as a Function of Spectral Offset and $[Xe]_{cell}$	163
10.6.3 P_{Xe} Build-Up Rates and Steady-State Values as a Function of T_{cell} at Different $[Xe]_{cell}$, Spectral Offsets	168
10.7 Conclusions	170
10.8 Summary and Outlook on Rb/ ^{129}Xe SEOP	172
CHAPTER 11 – Preliminary Studies of Cs/ ^{129}Xe SEOP	177
11.1 Introduction	177
11.2 Experimental Considerations	179
11.3 Improving Laser Technology for Cesium Optical Pumping	180

11.4 P_{Xe} Dynamics Studies at the Cs D_1 , D_2 , & Rb D_1 Absorption Lines.....	183
11.5 Optical Pumping at the Cs D_1 vs D_2 Wavelengths.....	188
11.6 Comparison of Steady-State HP ^{129}Xe Production via Rb/ ^{129}Xe versus Cs/ ^{129}Xe SEOP	192
11.7 Summary and Outlook on Cs/ ^{129}Xe SEOP	197
REFERENCES	201
CURRICULUM VITA	219

LIST OF TABLES

<u>TABLE</u>	<u>PAGE</u>
Table 5.1 Physical and NMR Properties of ^{129}Xe & ^{131}Xe	69

LIST OF FIGURES

<u>FIGURE</u>	<u>PAGE</u>
Figure 1.1 Cartoon comparison of hyperpolarized and thermally polarized nuclear spins.....	17
Figure 2.1 Cartoon showing alkali-metal electron spin polarization and subsequent spin-exchange with noble gas nuclei.....	22
Figure 2.2 Cartoon of spin-exchange and spin-destruction pathways.....	29
Figure 3.1 Photograph of OP cell under conditions of Rb energy pooling, resulting in emission of 421 nm light.....	48
Figure 4.1 Spectral comparison of a frequency-narrowed vs broadband LDA; diagram of primary components of a typical VHG-LDA.....	56
Figure 4.2 Example spectral output from an 'unlocked' VHG-LDA.....	58
Figure 4.3 Diagram of TEC-tuned VHG-LDA; corresponding laser output....	60
Figure 4.4 Spectral output of mechanically-tuned VHG-LDA; photograph of prototype module.....	61
Figure 4.5 Diagram of 'on-chip' integrated VHG-LDA.....	62
Figure 4.6 Photograph of a 3-diode 'on-chip' VHG-LDA prototype.....	63
Figure 4.7 Spectral outputs of 'on-chip' VHG-LDA compared to that of a typical broadband LDA.....	64
Figure 4.8 Spectral outputs from Cs D ₁ & D ₂ broadband LDAs.....	65
Figure 5.1 Phase diagram for physical properties of xenon.....	68
Figure 5.2 Chemical shift range of xenon in various chemicals of interest.....	71

Figure 5.3 Example SPINOE spectrum of HP ^{129}Xe in cryptophane-A.....	74
Figure 5.4 HP ^{129}Xe signal decay upon dissolution in zinc myoglobin.....	77
Figure 5.5 NMR spectrum of HP ^{129}Xe dissolved in cryptophane-A	79
Figure 7.1 SEOP apparatus design.....	93
Figure 7.2 Photograph of optics arrangement.....	96
Figure 7.3 Photograph of cryogenic condenser coil for HP ^{129}Xe collection ...	98
Figure 7.4 Comparison of hyperpolarized vs thermally polarized ^{129}Xe NMR signals at high field	101
Figure 8.1 Spectral output comparison of Comet vs standard LDA.....	104
Figure 8.2 Spectral tuning range of Comet laser.....	105
Figure 8.3 P_{Xe} as a function of T_{cell} for the standard LDA and Comet laser (driven to two different laser powers and spectral offsets)..	107
Figure 8.4 Transmitted laser spectra upon magnetic field cycling; cartoon demonstrating changes to laser absorption upon B_0 cycling.....	108
Figure 8.5 P_{Xe} , $\langle P_{\text{Rb}}(z) \rangle$, and percent transmittance of laser light as a function of laser power/ spectral offset.....	111
Figure 8.6 Spectral output comparison of Comet, Integra, & standard LDA..	113
Figure 8.7 Spectral tunability of Integra laser	114
Figure 8.8 P_{Xe} vs xenon density at various laser powers using the Integra..	116
Figure 9.1 Photograph of OP cell with low-field detection coil.....	122
Figure 9.2 Example low-field HP ^{129}Xe NMR spectra at 37.5 kHz.....	123

Figure 9.3 Comparison of high-field NMR signals both with and without retro-reflecting mirror installed post-cell.....	124
Figure 9.4 Low-field HP ^{129}Xe signal as a function of cell temperature for a variety of xenon densities.....	125
Figure 9.5 Low-field HP ^{129}Xe signals normalized by xenon density as a function of OP cell temperature.....	127
Figure 9.6 Low-field HP ^{129}Xe signal as a function of cell temperature for a variety of overall cell pressures (and Xe/N ₂ pressure ratios).....	128
Figure 9.7 P_{Xe} build-up curves at a variety of xenon densities	130
Figure 9.8 P_{Xe} build-up curves at a variety of cell temperatures.....	131
Figure 9.9 Estimate of the OP ‘efficiency’ as a function of xenon density	132
Figure 9.10 Time constant of P_{Xe} build-up curves plotted as a function of estimated Rb number density	134
Figure 9.11 Plot of γ' versus P_a^{-1}	135
Figure 9.12 Measurement of ultrahigh of P_{Xe} at high xenon densities.....	137
Figure 10.1 Spectral tunability of ‘on-chip’ VHG-LDA as functions of diode temperature and driving current	145
Figure 10.2 Photograph of OP cell with new ‘bucking’ coil	146
Figure 10.3 Noise comparison of traditional low-field detection coil & ‘bucking’ coil; HP ^{129}Xe signal detected at low field with ‘bucking’ coil.....	147
Figure 10.4 Low-field HP ^{129}Xe signal as a function of laser power for different cell temperatures.....	149

Figure 10.5 Low-field HP ^{129}Xe signal as a function of spectral offset for different laser powers and xenon densities	151
Figure 10.6 Low-field HP ^{129}Xe signal as a function of laser power for three different spectral offsets and two different cell temperatures.....	152
Figure 10.7 Low-field HP ^{129}Xe signal as a function of laser power for three different spectral offsets for $[\text{Xe}]_{\text{cell}} = 2000$ torr Xe at 75°C	153
Figure 10.8 Low-field HP ^{129}Xe signal and laser percent transmittance as a function of laser spectral offset at various cell temperatures ...	155
Figure 10.9 Laser percent transmittance as a function of spectral offset for two xenon densities	156
Figure 10.10 Low-field HP ^{129}Xe signal and laser percent transmittance as a function of laser spectral offset for two xenon densities	157
Figure 10.11 Low-field HP ^{129}Xe signal comparison of frequency-narrowed versus broadband LDAs at high laser powers.....	158
Figure 10.12 Photograph of laser modules; photograph of high-power 'on-chip' VHGLDA fiber-coupled to single-axis polarizer	161
Figure 10.13 Laser power vs driving current for high-power 'on-chip' VHGLDA; excitation wavelengths used in SEOP experiments..	162
Figure 10.14 P_{Xe} build-up curves at different excitation wavelengths.....	163
Figure 10.15 P_{Xe} build-up curve time constants vs estimated Rb density	165
Figure 10.16 γ' versus P_a^{-1} for a variety of excitation wavelengths	166
Figure 10.17 γ' vs xenon density for a variety of excitation wavelengths.....	167

Figure 10.18 Steady-state ^{129}Xe signal & P_{Xe} build-up curve time constants as a function of cell temperature for different spectral offsets	169
Figure 11.1 Spectral outputs for Cs D ₁ , D ₂ , & Rb D ₁ broadband lasers; power versus driving current for two Cs D-line broadband lasers.....	181
Figure 11.2 Photograph of Cs D-line broadband laser fiber-coupled to single-axis polarizer	182
Figure 11.3 Selected P_{Xe} build-up curves at the Cs D ₁ , D ₂ , & Rb D ₁ lines....	183
Figure 11.4 P_{Xe} build-up curve time constants as a function of alkali metal density for SEOP runs at the Cs D ₁ , D ₂ , & Rb D ₁ wavelengths...	184
Figure 11.5 γ' versus xenon density and P_a^{-1} for SEOP runs at the Cs D ₁ , D ₂ , & Rb D ₁ wavelengths	186
Figure 11.6 P_{Xe} build-up curve time constant as a function of xenon density for SEOP runs at the Cs D ₁ , D ₂ , & Rb D ₁ wavelengths	187
Figure 11.7 Diagram of D ₁ versus D ₂ optical pumping	190
Figure 11.8. Comparison of high field ^{129}Xe NMR signals attained via Cs D ₁ and D ₂ SEOP.....	191
Figure 11.9 Low-field HP ^{129}Xe signal as a function of xenon density for SEOP runs at the Cs D ₁ , D ₂ , a& Rb D ₁ wavelengths.....	193
Figure 11.10 P_{Xe} comparison of Cs/ ^{129}Xe vs Rb/ ^{129}Xe SEOP, measured at high field for a variety of xenon densities	194
Figure 11.11 P_{Xe} & estimated P_{AM} for a variety of xenon densities	196

CHAPTER 1

BASICS OF NUCLEAR MAGNETIC RESONANCE

1.1 INTRODUCTION

Nuclear magnetic resonance (NMR)¹ has long been used by the scientific community to study the interactions of nuclear spins with magnetic fields for numerous (and diverse) systems of interest. The phenomenon of NMR occurs when nuclei in a static magnetic field interact with a second oscillating magnetic field (induced by a pulse of radiofrequency—or, ‘rf’) whose frequency is resonant to the energy-level difference of the nuclei of interest. The discovery of NMR is widely attributed to the simultaneous, independent works of Purcell, Torrey, and Pound (who detected weak rf signals from paraffin wax) and Bloch, Hansen, and Packard (who studied rf signals from water) in the winter of 1945.¹

Since its discovery, the field of magnetic resonance has greatly expanded, running the gamut from Earth’s field² ($\sim 50 \mu\text{T}$) to over 20 T, and employing very simple pulse sequences as well as quite complicated ones that can transfer polarization amongst nuclei. NMR has also used various detection techniques (e.g., Faraday induction, superconducting quantum interference devices—‘SQUIDS’, and optical atomic magnetometry)³ to study a variety of diverse systems (e.g., body tissue and fluids, proteins, explosives, surfaces, plants, porous media, petroleum, and too many more to list).

Presently, a multitude of NMR spectroscopic techniques exist for numerous types of experiments. NMR can be used by organic chemists⁴ to elucidate structures of small molecules through simple one-dimensional (1-D) experiments (mostly through observation of ¹H & ¹³C NMR spectra). Physical chemists often probe chemical structure, function, and dynamics with 1-D as well as multidimensional NMR experiments⁵, while biochemists (and biophysicists) may use multidimensional NMR to examine proteins⁶ and nucleic acids. Molecular dynamics and chemical kinetics⁷ may be studied in a time-resolved manner using NMR. The progression of chemical (and photochemical)⁸ reactions may also be examined via NMR, as the products will be chemically—and spectroscopically—distinguishable from the reactants. For added resolution or chemical-discernability, isotopically-labeled nuclei may be utilized. The molecular structures of solids (e.g., crystals, powders, metal-hydrides, polymers, etc.) can be determined via solid-state NMR (SSNMR), where the solid is tightly packed into a rotor and can be spun at high speeds (tens of kHz—to decrease spectral linewidths) and at variable angles with respect to the applied magnetic field. Furthermore, by using magnetic-field gradients to encode space onto frequency, magnetic resonance imaging (MRI)⁹ is able to obtain high-resolution images of soft tissue in humans and animals without the damages of ionizing radiation, making it the most widely known magnetic resonance technique.

1.2 BASIC DESCRIPTION OF NMR

NMR is used to study certain nuclear isotopes that possess a quantum mechanical property known as ‘spin’.¹⁰ This spin provides the nucleus with an intrinsic angular momentum that can be thought of (in layman’s terms) as a simple, physical rotation; however, the true quantum mechanical origin of spin is much more abstract and difficult to understand.¹ Luckily, detailed knowledge of the fundamental origin of spin is unnecessary for understanding NMR (and is therefore beyond the scope of this work). Consider a nucleus with a spin quantum number (I) equal to $\frac{1}{2}$ (such as a ^1H nucleus); an applied magnetic field (B_0) splits the degeneracy of the two main energy levels for the spin—levels that can be referred to by the value of the magnetic quantum number (m_I) of $+1/2$ (for the lower energy state) and $-1/2$ (higher energy state). Due to this magnetic field-induced energy splitting (i.e., the so-called ‘Zeeman effect’), the energy difference between these two m_I states can be denoted as¹¹:

$$\Delta E = -\hbar\gamma B_0, \quad (1.1)$$

where \hbar is Planck’s constant divided by 2π and γ is the gyromagnetic ratio. These two states can be thought of as aligning with (‘ α ’, or ‘spin-up’) or against (‘ β ’, or ‘spin-down’) the applied magnetic field. Because these alignments are imperfect (due to quantum uncertainty), a portion of the spin vector lies in the xy plane (perpendicular to B_0), causing the spin vector to precess about the z -axis at a frequency of $\omega_0 = -\gamma B_0$ (i.e., the Larmor frequency).

Because of the Zeeman energy splitting for an ensemble of spins, there is a difference in population between the two spin states that follows a Boltzmann-type distribution¹²:

$$N_{\beta} / N_{\alpha} = \exp(-\Delta E/kT) , \quad (1.2)$$

where N_{β} and N_{α} are the populations of spins in the $m_l = -1/2$ and $+1/2$ spin states, respectively, T is the temperature in Kelvin, and k is Boltzmann's constant (note that conditions where $N_{\alpha} > N_{\beta}$ assume positive gyromagnetic ratios). The sum of the bulk nuclear spin magnetization (M_0) will be aligned along the z -axis, and the nuclear spin polarization (P) can be defined as the difference in spin populations¹³:

$$P = (N_{\beta} - N_{\alpha}) / (N_{\beta} + N_{\alpha}) , \quad (1.3)$$

At thermal equilibrium, the values for P are quite low even in strong (~ 10 T) magnetic fields (on the order of $\sim 10^{-5}$ to 10^{-6}), as $\Delta E \ll kT$. Here (because $\tanh(x) \rightarrow x$ for small values of x), the nuclear spin polarization at thermal equilibrium can be approximated by¹¹:

$$P_{\text{eq}} \approx \gamma \hbar B_0 / 2kT , \quad (1.4)$$

While individual spins can be thought to precess around B_0 (i.e., the z -axis), the phases of an ensemble of spins will be random. Thus, all xy components of the bulk nuclear spin magnetization (M) will cancel (leaving the net magnetization along z , proportional to P).

If an rf pulse (with photon energy $E = \hbar\omega_0$) is directed at the nuclear spins (aligned in B_0), some of this resonant energy will be absorbed, causing a change in spin-states (e.g., 'flipping' $\alpha \rightarrow \beta$). Provided that the oscillating rf field (B_1) is

perpendicular to B_0 , the bulk nuclear spin magnetization (M_0) will 'tip' into the xy -plane, precessing around the direction of B_1 for its duration. If B_1 ceases, some amount of M_0 has a projection into the laboratory x - y plane, and then the bulk M_0 will precess about B_0 — inducing an oscillating current in a detection coil that is perpendicular to B_0 . This oscillating current (with frequency $\omega \sim \omega_0$) is what generates the observed NMR signal.

The oscillating NMR signal (as 'picked-up' by the detection coil) decays with time (due to relaxation processes; see *below*); this process results in a free-induction decay (FID) signal. The experiment may be repeated and the generated signals summed, so as to increase the final signal-to-noise ratio (SNR). This (summed) signal may then be Fourier-transformed (FT), thereby converting the time parameter into a frequency parameter, and generating a usable NMR spectrum.

Modern NMR spectrometers use quite large, cryogenically-cooled (liquid He & N₂) superconducting magnets, with fields ranging from a few T to more than 20 T. Lower-field NMR spectroscopy that uses permanent or electro-magnets is less prevalent nowadays, but can have certain applications (such as detecting hyperpolarized species¹⁴), and has been enjoying a resurgence likely due to the interest in portable NMR. The high magnetic fields of current NMR technology result in typical Larmor frequencies in the MHz regime; as such, most of the spectrometer-related hardware (frequency sources, amplifiers, etc.) are similar to those used in conventional radio broadcasts. The sample of interest is usually lowered into a 'probe' (placed inside the magnet); this probe contains the

pulse/detect coil, and also allows for temperature control and sample rotation. Because of the differences in γ for different nuclear species, spectrometers will often have multiple channels, each of which requires ‘tuning’ to achieve optimal pulse/detect sensitivity for the specific sample. The FT NMR spectra are then recorded on a computer and analyzed using a variety of NMR processing software.

1.3 RELEVANT COMPONENTS OF THE NUCLEAR SPIN HAMILTONIAN

The fundamental concepts of NMR are most efficiently explained in the context of a quantum mechanical approach. As such, the energy of the nuclear spin system can be represented by an operator known as the Hamiltonian. This operator is comprised of many contributions, both external and internal to the spin system, with varying magnitudes. A detailed quantum mechanical rationalization to these contributions lies beyond the scope of this work; instead, the following sub-sections describe the various contributions to the nuclear spin Hamiltonian in a more general fashion.

1.3.1 Static Field

The static field (B_0) generated by the superconducting magnet dominates the nuclear spin Hamiltonian, with its magnitude typically in the MHz regime¹:

$$\hat{H}_j^{\text{static}} = -\gamma_j B_0 \hat{I}_{jz}, \quad (1.5)$$

This contribution is typically referred to as the Zeeman interaction, with the term $(-\gamma_j B_0)$ denoting the Larmor frequency of the spin (I_j).¹ Of course, the magnetic

field is experienced for all sample types, regardless of physical state or degree of order (long-range/short-range).

1.3.2 Transverse Field

The second external contribution comes from the rf field (B_1) generated along (say) the x -axis of the laboratory frame by the pulse/detect coil. While pulsing rf, this contribution can be approximated as¹:

$$\hat{H}_j^{\text{RF}}(t) \approx -1/2 \gamma_j B_1 \{ \cos(\omega_{\text{ref}} t + \phi_p) \hat{I}_{jx} + \sin(\omega_{\text{ref}} t + \phi_p) \hat{I}_{jy} \}, \quad (1.6)$$

where ω_{ref} is the spectrometer reference frequency, $1/2 \gamma_j B_1$ is the nutation frequency (a measure of how strongly the rf field influences resonant spins I_j), and ϕ_p is the pulse phase. The contribution is zero when the rf is not being pulsed. B_1 can be divided into a resonant component (that rotates in the same sense as the spin precession) and a non-resonant component (rotates opposite to Larmor frequency); in most cases, the non-resonant component can be neglected due to its (nearly) non-existent influence on the spins.¹ Together, the static field and applied radiofrequency make up the external contributions to the spin Hamiltonian.

1.3.3 Chemical Shift

Aside from the external contributions mentioned above, the nuclei in the sample of interest experience both magnetic and electric fields that originate from within. These contributions make up the internal portion of the spin Hamiltonian.¹ For instance, the chemical shift contribution arises due to the fact

that each nucleus has a different local magnetic environment, and therefore possesses a slightly different resonance frequency. The static field induces ring currents in the electron clouds of the molecule; these ring currents generate a induced magnetic fields that are much smaller than the static field ($\sim 10^{-4} B_0$), but are still able to bring about appreciable shifts to each nuclei's precession frequency (due to the induced fields' proximity to the nuclei).¹ This induced field is directly proportional to B_0 ; as such, the magnitude (Hz to kHz) of the consequent shift in NMR frequency is often reported in parts-per-million (ppm); moreover, because all substances have such fields inducing varying amounts of frequency shift, such chemical shifts are usually reported in comparison to a reference standard (e.g., tetramethylsilane, or 'TMS' for ^1H and ^{13}C shifts). This allows for direct comparisons of chemical shifts across different sample types when using different magnetic field strengths.

In its simplest case, the chemical shift contribution for a substance in an isotropic liquid (upon motional averaging) can be approximated as¹:

$$\hat{H}_j^{\text{CS}} = -\gamma_j B_0 \delta_j^{\text{iso}} \hat{I}_{jz} , \quad (1.7)$$

where δ_j^{iso} is the average of the chemical shift over all possible orientations of the molecule. While simple for isotropic solutions, the chemical shift for anisotropic liquids and solids can be more complex, as motional averaging will be incomplete (or non-existent) and the orientation of the molecule with respect to B_0 matters. For example, NMR spectra of polycrystalline solids often contain peaks with inhomogeneous broadening—a result of chemical shift anisotropy (CSA)¹⁵, where a continuous distribution of overlapping, unresolvable peaks

merge into a single 'chair-shaped' or 'tent-shaped peak (depending on the local molecular symmetry).

There are a number of factors that determine the extent of chemical shift in a sample of interest. The main contribution that determines the range of shifts for a given isotope is from low-lying excited electronic states; as heavier atoms tend to have a greater density of states than lighter atoms, the heavier atoms will have wider chemical shift ranges (i.e., ~10 ppm range for ^1H , compared to a ~200 ppm range for ^{13}C).¹ Another contribution comes from neighboring groups; proximity to electronegative atoms pulls the electron density away from the nuclei of interest, thus changing the local magnetic field that it 'senses'. As such, neighboring species can still affect the chemical shift despite a lack of chemical bonds (an effect sometimes referred to as a 'physical shift'). Changes to the molecular dynamics can also influence chemical shift; chemical exchange or rapid rotation about a single bond may merge two otherwise distinguishable peaks.¹⁶ Indeed, information derived from NMR chemical shifts must be interpreted with great care.¹

1.3.4 Dipolar Couplings

Because nuclear spins behave like miniature bar magnets, they each generate a magnetic field through space. When another nucleus (along with its own magnetic field) comes in close proximity to the first one, they are able to interact with each other's fields. This is referred to as dipolar coupling—an effect that occurs through space, without the involvement of electron clouds or electron

spins. This interaction may be intermolecular or intramolecular, and can be represented as¹:

$$\hat{H}_j^{\text{DD}} = b_{jk} \{3(\hat{I}_j \cdot \mathbf{e}_{jk})(\hat{I}_k \cdot \mathbf{e}_{jk}) - \hat{I}_j \cdot \hat{I}_k\}, \quad (1.8)$$

where \mathbf{e}_{jk} is a unit vector that is parallel to the line running through the centers of the two nuclei (\hat{I}_j, \hat{I}_k), and b_{jk} is the dipole coupling constant¹:

$$b_{jk} = -(\mu_0/4\pi)(\gamma_j\gamma_k\hbar/r_{jk}^3), \quad (1.9)$$

where r_{jk} is the distance between the nuclei and μ_0 is a constant ($4\pi \times 10^{-7} \text{ H m}^{-1}$).

Thus, the magnitude of the dipolar interaction scales as the inverse cube of the internuclear distance. Spectroscopic measurement of these dipolar interactions provides information about the distances between nuclei, as well as the geometrical form of the molecule being studied.¹ Dipolar couplings are generally present in the NMR spectra of solids and anisotropic liquids, while the effect is largely averaged to zero in isotropic liquids due to motional averaging.

1.3.5 Scalar Couplings

While dipolar couplings are present ‘through space’, a second kind of nuclear-nuclear coupling exists that uses bonding electrons to assist in the coupling interaction. Scalar (or, ‘J’) coupling survives the motional averaging of isotropic liquids, and provides spectral proof of chemical bonds (through small but measurable splittings in NMR peaks). This intramolecular coupling is only present if two nuclei are linked by a small number of chemical bonds, and can help elucidate a molecule’s connectivity through these bonds. The J-coupling interaction can be represented as¹:

$$\hat{H}_{jk}^J = 2\pi \hat{I}_j \cdot J_{jk} \cdot \hat{I}_k , \quad (1.10)$$

where J_{jk} represents the J-coupling tensor (a 3 x 3 matrix), which is averaged to a single scalar value for isotropic liquids. For solids and anisotropic liquids, a small J-anisotropy exists, but is typically dwarfed by the dipolar interaction¹ (and can be difficult to measure separately). J-coupling can also provide information about secondary structures of proteins by providing a measure of the torsional angle of peptide links.¹⁷

1.3.6 Quadrupolar Couplings

The previously described internal contributions to the nuclear spin Hamiltonian solely are comprised of magnetic interactions. However, there is one type of internal contribution, quadrupolar couplings, that is an electronic interaction. For spins greater than $I = 1/2$, nuclei are non-spherical (prolate or oblate), giving rise to the nuclear quadrupolar moment that can strongly interact with local electric field gradients (EFGs) that are produced by surrounding electron clouds. This interaction is mostly intramolecular, and can be denoted as¹:

$$\hat{H}_j^Q \approx \omega_j^Q (3\hat{I}_{jz}^2 - \hat{I}_j \cdot \hat{I}_j) , \quad (1.11)$$

where ω_j^Q is the quadrupolar frequency, the value of which depends on the physical state of the sample. In isotropic liquids, ω_j^Q averages to zero, while in solids and anisotropic liquids¹:

$$\omega_j^Q(\Theta) = V_{zz}^j(\Theta) \cdot \{3eQ_i / 4\hat{I}_j(2\hat{I}_j - 1)\} , \quad (1.12)$$

where Q_i is the electric quadrupole moment of the nucleus, e is the proton charge, and V_{zz}^j is the electric field gradient at the nucleus, dependent on the orientation (Θ) of the molecule with respect to B_0 .¹

While the quadrupolar interaction does not appear to affect the position of peaks in the NMR spectra of isotropic liquids, it can strongly influence the *relaxation* of nuclear spins (with $I > 1/2$) in the randomly oriented liquids. This phenomenon is due to the additional energy levels brought about by $I > 1/2$ nuclei; while spin $1/2$ nuclei have only two spin energy levels ($2n + 1$), increasing the spin quantum number increases the number of energy levels (and possible spin-orientations) in the spin-system. Additionally, the magnitude of the quadrupolar moment affects the relaxation, as fluctuations to the electrostatic interaction energies results in transitions between nuclear spin states.

1.4 NUCLEAR SPIN RELAXATION MECHANISMS

At thermal equilibrium, the nuclear spin-state populations adopt a Boltzmann distribution, with the lower energy level containing a slightly larger spin population. Upon irradiation with rf, the overall spin magnetization (M_0) is tipped into, and precesses around, the x-y plane. However, once the rf field is turned off, M_0 will slowly relax back to its equilibrium position along the z-axis. This process is referred to as spin relaxation, and can be divided into two categories: spin-lattice (i.e., longitudinal) relaxation and spin-spin (i.e., transverse) relaxation. Such relaxation is typically incurred by small fluctuations in the interactions between the spins and their environment¹⁸, such as nuclear-

nuclear & electron-nuclear dipolar interactions, along with quadrupolar interactions (and many more). Measuring these different types of relaxation can provide information regarding molecular dynamics over a wide range of time scales (as different relaxation mechanisms have different mathematical dependencies over varying time scales). Relaxation measurements also help to establish experimental parameters (as well as the feasibility of a planned experiment).

1.4.1 Longitudinal Relaxation

Upon rf excitation, the α - β population difference will be altered. After B_1 is turned off, this fraction (M_z) of M_0 will gradually return to its equilibrium state by 'relaxing', or releasing the extra energy to its surrounding environment (or, 'lattice'). The time period governing the return of M_z to thermal equilibrium (i.e., along the z-axis)¹¹ is given by¹:

$$M_z(t) = M_z(0)(1 - \exp(-t/T_1)) , \quad (1.13)$$

where T_1 is the spin-lattice relaxation time constant. T_1 values can range from microseconds to days, but are usually on the order of seconds—depending on a number of criteria. The most notable criterion is the choice of nuclei; for instance, $I=1/2$ nuclei with small gyromagnetic ratios tend to have longer T_1 's due to weaker dipolar interactions, whereas $I>1/2$ nuclei tend to experience shorter T_1 's because of quadrupolar interactions with the fluctuating electric fields.¹

There are three common NMR methods for measuring T_1 . The first method, 'saturation recovery', uses a train of 90° pulses to saturate the equilibrium

polarization (i.e., effectively equaling the populations of the spin states in an incoherent manner). Then, the magnetization is allowed to grow in for a specified amount of time (τ) before being detected; the experiment is repeated, each time changing τ . The full recovery behavior is plotted as a function of Eq. 1.13, and the T_1 value is extracted. The second T_1 measurement method is referred to as 'inversion recovery'; in this experiment, a long, fixed delay allows thermal equilibrium to be restored, followed by a 180° pulse (inverting α & β populations). After a variable delay (thus allowing M_0 to 'grow' from $-z$ towards $+z$), a 90° pulse measures the magnetization (positive or negative) along the z -axis at that point in time. The experiment is repeated, and the relaxation/recovery profile is fitted to a similar equation:

$$M_z(t) = M_z(0)(1 - 2\exp(-t/T_1)), \quad (1.14)$$

This method has twice the dynamic range as the saturation recovery experiment, and allows for greater precision in T_1 measurements. However, it suffers from the long initial delay period, which (upon repetition) can make measurements of samples with long T_1 's cumbersome. Finally, the '*nfids*' method of T_1 calibration can only be used in species with non-equilibrium polarizations (such as hyperpolarized ^{129}Xe); this method uses a (delay- α -acquire)_n sequence (with a small tipping angle α). The weak α -pulses sample the (initially-hyperpolarized) magnetization as it returns to thermal equilibrium; in this work, the *nfids* method is used for determining the ^{129}Xe T_1 in the gas-phase as well as when dissolved in solution.

1.4.2 Transverse Relaxation

The amount of transverse relaxation experienced by spins can be divided into homogenous and inhomogenous dephasing. In the first case, once the magnetization has been tipped into the x - y plane (by an rf pulse), the spins that comprise the magnetization vector (M_{xy}) will slowly lose coherence and begin to dephase until they are distributed about the x - y plane (yielding no net x - y magnetization). This randomization occurs even in perfectly homogenous magnetic fields, and the time constant (T_2) of this dephasing can be found from¹:

$$M_{xy}(t) = M_{xy}(0)(\exp(-t/T_2)) , \quad (1.15)$$

During T_2 relaxation, the population of spin-states remains the same, but the relative phases during Larmor precession will 'relax' or dephase due to spin-spin interactions. This occurs across the sample without prejudice, and is hence referred to as homogenous broadening; relaxation from T_2 is almost always less than or equal to that of T_1 .¹

The second type of transverse relaxation is due to magnetic field inhomogeneity. Because B_0 is never perfectly homogenous, the spins will experience varying magnetic fields throughout the sample. This results in a broad range of resonance frequencies, and a rapid loss in NMR signal. In virtually all experiments, this T_2^* relaxation plays a larger role than true T_2 relaxation. This inhomogenous dephasing is given by¹¹:

$$T_2^* = (\pi\Delta\nu_{1/2})^{-1} , \quad (1.16)$$

where $\Delta\nu_{1/2}$ denotes the full-width at half-maximum (FWHM) for a Lorentzian lineshape (i.e., the Fourier transformation of the NMR signal). Indeed, it is this

T_2^* dephasing that results in the exponential decay of the detected FID signal from 'whence' NMR peaks are derived. T_2 and T_2^* relaxations can be differentiated by using a 'spin-echo' pulse sequence¹, where the reversible dephasing due to the inhomogeneous B_0 is refocused and detected (whereas dephasing due to T_2 processes cannot be refocused). T_2 values are typically more important than T_2^* values, as the former reflects fundamental aspects of the system, while the latter just reflects the limitations of the magnet (or the user).

1.5 IMPROVEMENTS TO NUCLEAR SPIN POLARIZATION

In some ways, NMR experiments are inherently difficult, as the actual attainable signal is incredibly weak and the Larmor frequencies must be measured with parts-per-billion accuracy. The weak NMR signal can be attributed to the very small nuclear magnetic moments which, for the most part, cancel each other out (Fig. 1.1 *top*)¹⁹—leading to thermal polarizations of only $\sim 10^{-5}$ to 10^{-6} . This result necessitates relatively large sample volumes (compared to other forms of spectroscopy); indeed, it takes at least 10^{17} nuclear spins to actually obtain a usable NMR signal.¹ From Eq. 1.4, (seemingly) the only ways to increase the equilibrium nuclear spin polarization involve increasing B_0 and/or decreasing the sample temperature. In fact, both of these measures have been utilized, despite their inherent drawbacks: magnet cost and size do not scale linearly with magnetic field strength (and are rapidly reaching their technical

limits), and many samples (especially biological ones) do not ‘appreciate’ significantly lowered temperatures (i.e., <4 K).

However, there are ways to increase the nuclear spin polarization in a non-equilibrium fashion. These ‘hyperpolarized’ techniques provide dramatic improvements in P for short time durations in a non-renewable fashion (i.e., once P has been ‘used up’, the spins revert back to thermal equilibrium—requiring ‘fresh’ polarized product to be further introduced if the experiment is to be continued). Many of these hyperpolarization techniques involve spin-polarizing electrons, which can then transfer angular momentum to nuclei through electron-nuclear hyperfine interactions. In turn, this process generates highly non-Boltzmann distributions of nuclear spins (e.g., $N_\alpha \gg N_\beta$), leading to NMR signal enhancements of three to five orders of magnitude (Fig. 1.1 *bottom*).¹⁹

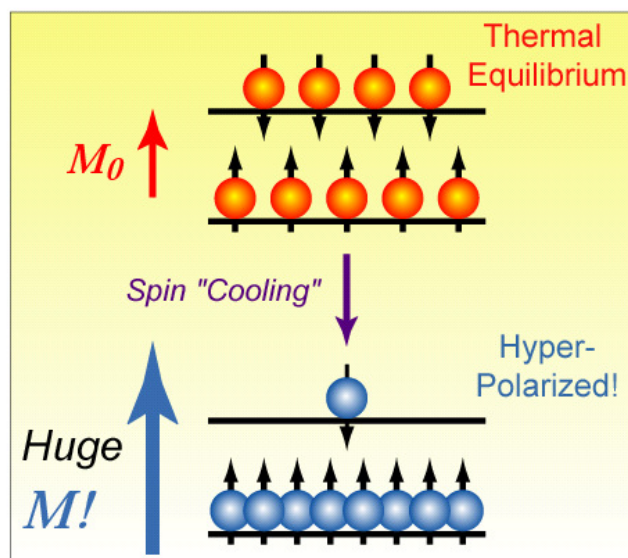


Fig. 1.1. Spin-up vs spin-down populations at thermal equilibrium (*orange*) and after hyperpolarization (*blue*), resulting in a much larger magnetization vector (M) and increased NMR signals.¹¹¹

One such hyperpolarization process is ‘dynamic nuclear polarization’ (DNP)^{20,21}, which can be achieved via microwave irradiation of the sample’s electrons (near their Larmor frequency); this electron spin polarization can then be transferred to nuclei of interest (^1H , ^{13}C , etc.) for increased sensitivity in MR studies. As is often the case in modern DNP experiments, one species is hyperpolarized via DNP in one apparatus, then ‘shuttled’ to (and infused throughout) the sample of interest (in a nearby NMR magnet). The necessity of two devices arises from the technical challenge of generating high-power microwaves at the Larmor frequency of electrons in a high-field magnet (although this issue can be side-stepped with access to a gyrotron²²). DNP devices are commercially available (albeit expensive), or can be built in the lab (with the right expertise); DNP can also come about in chemically-induced (CIDNP)²³ and photo-chemically induced (photo-CIDNP) fashions^{24,25} (where electron spin populations are driven out of equilibrium by chemical reactions or photoexcitation, respectively).

Another type of hyperpolarization technique takes advantage of the unique molecular symmetry and spin statistics of H_2 , which is present in two nuclear-spin isomers (*ortho* $\uparrow\uparrow$ and *para* $\uparrow\downarrow$). The *ortho*-hydrogen isomer dominates at room temperature (75:25); however, when flowing H_2 through a catalyst (e.g., $\text{FeO}(\text{OH})$) at low temperatures ($\leq 77\text{ K}$), it becomes energetically favorable for the H_2 to convert predominately to the *para* state.²⁶ This favoritism arises from the fact that the overall wavefunction is required to be antisymmetric (protons are fermions), and since the rotational ground state is symmetric, the nuclear spin

wavefunction must be anti-symmetric. *Para*-H₂ itself is NMR inactive (the spins cancel each other out, giving no net signal), but when undergoing a chemical reaction with another species to form an asymmetric product (say, a hydrogenation reaction across an asymmetric double bond), the hydrogen atoms find themselves in magnetically inequivalent sites. The *para*-H₂ selectively populates the spin-states of the product, and results in a differentiation of the resulting NMR spectra based on this asymmetric addition (as opposed to typical thermal population differences that are dependent on ΔE)—thus greatly intensifying the NMR signals of *para*-H₂ products.²⁷ *Para*-H₂ has been used to increase MR detection sensitivity in hydrogenation reactions,²⁶ microreactors²⁸, animal imaging²⁹, and a slew of additional NMR/MRI applications.^{27,30}

The remainder of this work will consist of an in-depth review of spin-exchange optical pumping of noble gases (i.e., ¹²⁹Xe), from both fundamental and practical viewpoints. Briefly, spin-exchange optical pumping is used to generate large nuclear spin polarizations in noble gases (up to ~70%; compared to ~0.003% at thermal equilibrium)¹⁹, leading to massive NMR signal enhancements of ~5 orders of magnitude. This increase in detection sensitivity has been used to improve existing MR experiments, as well as allow for novel MR experiments and approaches that would not otherwise be possible (not to mention a host of experiments in fundamental physics beyond the scope of this dissertation).

CHAPTER 2

FUNDAMENTAL ASPECTS OF SPIN-EXCHANGE OPTICAL PUMPING

2.1 INTRODUCTION

The use of optical methods to enhance the polarization of nuclear spins to levels unattainable by other means finds its roots in the 1950's, when Kastler³¹⁻³⁴ first demonstrated the ability to drive electronic spin populations out of thermal equilibrium using light. Kastler also considered the possibility of transferring this non-equilibrium spin polarization from electrons to nuclei³³; indeed, this prediction was soon realized in heavy metal vapors³⁵⁻³⁷ and noble gases³⁸⁻⁴⁰, and later, in condensed phases⁴¹⁻⁴⁶ (such as anthracene, via photo-CIDNP).

Generally, the optical pumping (OP) of noble gases can be attained via two approaches: *metastability-exchange OP (MEOP)* and *spin-exchange OP (SEOP)*—via an alkali-metal vapor). During MEOP^{39,47,48}, the noble gas is 'directly' polarized by creating metastable atoms (e.g. $^3\text{He}^*$) via a radiofrequency discharge, followed by optical pumping of the electron spins of the metastable atoms. The buildup of nuclear spin polarization ensues during subsequent metastability-exchange collisions with the remaining ground-state atoms. MEOP has been used to generate very high nuclear spin polarizations (>50-80%) in low-density ^3He (and has also been demonstrated⁴⁹ with ^{21}Ne); however, it is not practical for heavier noble gas isotopes (i.e., ^{83}Kr , ^{129}Xe , ^{131}Xe).

In the second approach (SEOP)⁴⁹, the high electron spin polarization of an optically-pumped alkali-metal vapor is transferred to noble gas nuclei via gas-

phase collisions. Alkali-metal atoms are ideal because of their simple electron spin-states ($S = 1/2$) and strong absorption cross-sections. Following the work of Kastler³¹⁻³⁴, Bouchiat, Carver, and Varnum³⁸ discovered that the ^3He nuclei present in alkali metal pumping cells became slowly polarized as a result of spin-exchanging collisions with the electronically spin-polarized alkali metal atoms. Hyperpolarized xenon nuclei were generated using the same approach (by Grover⁴⁰), but with a much higher spin-exchange rate (i.e., faster 'pump-up' time). Since this early work, the field of SEOP has been further progressed and studied in considerable detail through the pioneering work by Happer, Cates, Walker, and many others.⁵⁰⁻⁵⁶

2.2 OPTICAL POLARIZATION OF ALKALI-METAL ELECTRON SPINS

In the first step of SEOP, angular momentum is transferred from resonant, circularly polarized (CP) photons to the electron spins of an alkali metal vapor (i.e. Na, K, Rb, Cs—for simplicity, Sections 2.2 & 2.3 will focus on Rb/ ^{129}Xe SEOP). For instance (see Fig 2.1(a)), when CP light (e.g., with $\sigma+$ polarization) is applied at the Rb D_1 transition (794.76 nm) in the presence of a weak magnetic field (B_0 , and neglecting electron-nuclear hyperfine splitting for simplicity), the population of the electronic spins is selectively driven from $m_j = -1/2$ in the ground state ($5^2S_{1/2}$) to $m_j = +1/2$ in the excited state ($5^2P_{1/2}$), as dictated by the conservation of angular momentum. The magnetic field is applied parallel (or anti-parallel) to the direction of light propagation (i.e., along the z-axis), and defines the quantization axis for the light-matter interaction; the

Rb metal (pre-loaded, for example, in an inert-atmosphere glove-box) is typically vaporized and kept to a chosen number density by using a forced-air oven.

Collisions between the Rb atoms and other gas-phase species (i.e., xenon & buffer gases) will effectively equalize the populations of the excited-state m_j sublevels, and therefore, equalize the repopulation rates of the ground m_j sublevels. The depletion of the ground $m_j=-1/2$ sublevel and simultaneous accumulation of spin population in the ground $m_j=+1/2$ sublevel will quickly reach steady state, resulting in an electronically spin-polarized alkali metal vapor.

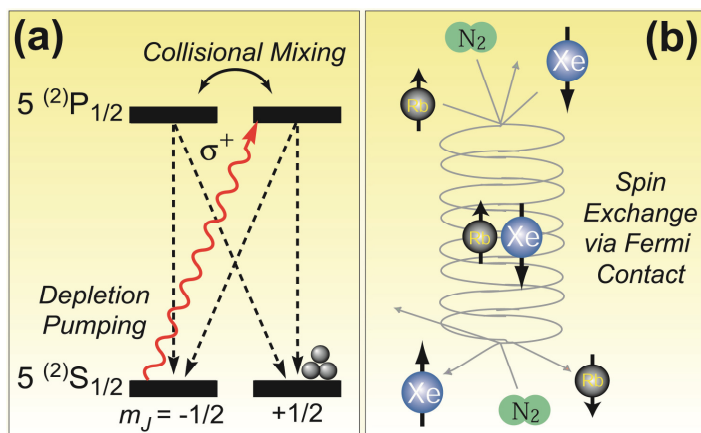


Fig. 2.1 SEOP. **(a)** Optical polarization of Rb electron spins. **(b)** Transfer to Xe nuclei via spin exchange. N_2 is shown as the third body facilitating formation / breakup of the vdW complex (adapted from Ref.⁵⁴).

The steady-state Rb electronic spin polarization (P_{Rb}) can be described by the standard definition for spin-1/2 particles (i.e., restating Eq. 1.3):

$$P = \frac{N_+ - N_-}{N_+ + N_-}, \quad (2.1)$$

(where N_+ and N_- refer to the number of Rb atoms in the $m_J = +1/2$ and $-1/2$ states, respectively). P_{Rb} will be a function of position in the cylindrical OP cell, as determined by⁵⁷:

$$P_{\text{Rb}}(z, r) = \frac{\gamma_{\text{OP}}(z, r)}{\gamma_{\text{OP}}(z, r) + \Gamma_{\text{SD}}}, \quad (2.2)$$

where (z, r) specifies the ‘depth’ into the cell (z) and the radial distance (r) from the cell’s central axis (assuming a colimated, cylindrically symmetrical laser beam). The optical pumping rate at a given position within the OP cell ($\gamma_{\text{OP}}(z, r)$) is as follows⁵⁸:

$$\gamma_{\text{OP}}(z, r) = \int \Phi(z, r, \nu) \cdot \sigma_0(\nu) d\nu, \quad (2.3)$$

where $\Phi(z, r, \nu)$ is the light flux per unit frequency (ν) at position (z, r) —indicating the importance of resonant laser power (and the advantages of high power, frequency-narrowed light sources⁵⁹) in the overall performance of SEOP—and $\sigma_0(\nu)$ is the frequency-dependent Rb D₁ absorption cross-section. In Eq. 2.2, the Rb electron spin destruction (SD) rate (Γ_{SD}) at any distance from the cell walls is given by:

$$\Gamma_{\text{SD}} = \sum_i k_{\text{SD}}^i \cdot [M_i], \quad (2.4)$$

where k_{SD}^i is the SD rate per collision with a given gas species (i) and $[M_i]$ is the number density of that gas species; indeed, collisions with heavy species (particularly xenon) are generally expected to dominate the Rb SD rate at high partial pressures, thus lowering the highest achievable P_{Rb} (and thus lowering the resulting P_{Xe}); P_{Rb} usually equilibrates with the photon flux in a matter of milliseconds.

Once the Rb vapor achieves an electron spin polarization (in one of the m_j sublevels) that approaches unity, the vapor should become more optically transparent, as the electron spin population in the light-absorbing state becomes increasingly depleted.⁵⁰ Because of this, most OP cells are designed to be many optical depths thick, as the highly polarized Rb vapor in the front of the cell allows light to pass directly through without attenuation. Monitoring of the laser transmission through the cell can provide a simple, qualitative check on the level of rubidium polarization during SEOP (and will be discussed in Sec. 8.4).⁵⁹

2.3 NUCLEAR SPIN POLARIZATION OF NOBLE GAS ATOMS VIA SPIN-EXCHANGE

The presence of noble gases in the OP cell (i.e., ^3He , ^{21}Ne , ^{83}Kr , ^{129}Xe , ^{131}Xe) results in gas-phase collisions between the electronically spin-polarized Rb vapor and the noble gas (in this case, ^{129}Xe). During such a collision, the optically-induced spin polarization can be transferred from a polarized Rb electron spin (S) to an unpolarized Xe nuclear spin (or other noble gas, so long as $I \neq 0$); this spin-exchange is mediated by Fermi-contact hyperfine interactions⁶⁰:

$$\alpha \vec{S} \cdot \vec{I} = \frac{\alpha}{2} [S^+ I^- + S^- I^+] + \alpha S_z I_z, \quad (2.5)$$

where the bracketed ('flip-flop') term gives rise to the spin exchange, and the coupling constant (α) is proportional to the probability of finding the unpaired Rb electron at the ^{129}Xe nucleus.

Although the Rb density is generally several orders of magnitude lower than that of the xenon, and the chance of a mutual spin flip during a given encounter is low⁵⁴, ¹²⁹Xe nuclear spin polarization can accumulate over time due to the long-lasting ¹²⁹Xe T_1 (the in-cell spin-lattice relaxation time is typically on the order of minutes to tens of minutes). P_{Xe} will build-up as a function of time (t) according to the following relation⁵⁸:

$$P_{Xe} = P_{Rb}(z, r) \cdot \left(\frac{\gamma_{SE}}{\gamma_{SE} + \Gamma_{Xe}} \right) \cdot \{1 - \exp[-(\gamma_{SE} + \Gamma_{Xe})t]\}, \quad (2.6)$$

where γ_{SE} gives the Rb-Xe spin-exchange (SE) rate and Γ_{Xe} is the effective ¹²⁹Xe nuclear spin relaxation rate (or, $1/T_1^{Xe}$) during optical pumping. During SEOP, the primary contributors to Γ_{Xe} will generally be wall collisions, while diffusion through local field gradients and gas-phase collisions with other species (like xenon) typically provide much weaker contributions.^{61,62} In the limits of $t \rightarrow \infty$ and $\gamma_{SE} \gg \Gamma_{Xe}$, then P_{Xe} will approach P_{Rb} .

The Rb-Xe spin-exchange is mediated by two-body collisions and three-body complex formations (see Fig. 2.1(b)—typically consisting of Rb-Xe-N₂; under conditions of high $[Xe]_{cell}$, the more abundant complex may be Rb-Xe-Xe⁵³). The degree to which the two-body versus three-body (van der Waals molecules—‘vdW’) processes contribute to spin-exchange is subject to experimental conditions; it is traditionally thought that van der Waals molecules would only form under low xenon density ($[Xe]_{cell}$) conditions⁵³ (less than a few hundred torr Xe—higher $[Xe]_{cell}$ values increase the vdW breakup rate due to collisions), and binary collisions would dominate spin-exchange under higher

$[\text{Xe}]_{\text{cell}}$. Thinking about the problem semi-classically, the electron-nuclear hyperfine interaction between Rb and ^{129}Xe will partially transfer ‘some’ of the spin polarization from the Rb electrons to the ^{129}Xe nuclei during such collisions. Multiple collisions increase P_{Xe} levels to several tens of percent (~ 5 orders of magnitude greater than thermally polarized ^{129}Xe).⁵⁴

The efficiency of the Rb-Xe polarization transfer can therefore be determined by the SE rate^{53,57,63}:

$$\gamma_{SE} = [\text{Rb}]_{\text{cell}} \cdot \left\{ \frac{\gamma_{\text{RbXe}}}{[\text{Xe}]_{\text{cell}}} \left(\frac{1}{1+br} \right) + \langle \sigma v \rangle \right\}, \quad (2.7)$$

where $[\text{Rb}]_{\text{cell}}$ is the in-cell Rb number density (dependent on T_{cell} —typically $\sim 10^{11}$ - $10^{14}/\text{cm}^3$)⁵⁴, γ_{RbXe} is the 3-body SE rate, $\langle \sigma v \rangle$ is the velocity-averaged 2-body SE cross-section (in cm^3/s), and for Xe/ N_2 gas mixtures, it can be shown that:

$$br = 0.275 \cdot \left(\frac{\text{N}_2 \text{ pressure}}{\text{Xe pressure}} \right), \quad (2.8)$$

N_2 is added to quench unwanted Rb fluorescence⁶⁴ and to collision-broaden the Rb absorption line⁵⁴; helium is also often used for collision-broadening. The factor 0.275 (or, ‘ b ’) is calculated from the quotient of the characteristic pressures of Xe and N_2 at which the molecular breakup rate (τ^{-1}) equals the spin-rotation frequency ($\gamma N/\hbar$) in the limit where only one of the gases is responsible for the formation and breakup of the vdW molecules.^{53,57,63} The proficiency of spin-exchange under a particular set of experimental conditions can be monitored via the time constant of the P_{Xe} buildup curves (Γ)⁵³ (monitored *in situ*):

$$\Gamma = [\text{Rb}]_{\text{cell}} \cdot \left\{ \frac{\gamma_{\text{RbXe}}}{[\text{Xe}]_{\text{cell}}} \left(\frac{1}{1+br} \right) + \langle \sigma v \rangle \right\} + \Gamma_{\text{Xe}} = ([\text{Rb}]_{\text{cell}} \cdot \gamma') + \Gamma_{\text{Xe}} , \quad (2.9)$$

where γ' contains the spin-exchange contributions from both binary collisions and van der Waals complex formations. γ' can be figured from the slope of a plot of Γ vs $[\text{Rb}]_{\text{cell}}$ (i.e., P_{Xe} buildup curve time constants as a function of T_{cell}), where Γ_{Xe} is the y-intercept; alternatively, it should be possible to calculate γ' from the following⁵³:

$$\gamma' = \left\{ \frac{\gamma_{\text{RbXe}}}{2.48 \times 10^{19} \text{ cm}^{-3}} \left(\frac{1}{P_a} \right) + \langle \sigma v \rangle \right\} , \quad (2.10)$$

where $2.48 \times 10^{19} \text{ cm}^{-3}$ is the number density of 760 torr Xe gas at 296 K, and $1/P_a$ is a dimensionless quantity that is primarily the xenon pressure in fractions of an atmosphere, with a correction for the presence of nitrogen as a buffer gas⁵³:

$$\left(\frac{1}{P_a} \right) = \left\{ \frac{760 \text{ torr}}{[\text{Xe}]_{\text{cell}}} \right\} \cdot \left(\frac{1}{1+br} \right) , \quad (2.11)$$

The plot of γ' versus P_a^{-1} should result in a straight line, with a slope equal to the 3-body SE rate γ_{RbXe} (divided by 2.48×10^{19} ; using Eq. 2.10) and y-intercept equal to σv (the binary SE cross-section).

The \square term γ_{SE} is dependent on T_{cell} in the following way: increases to T_{cell} bring about higher $[\text{Rb}]_{\text{cell}}$, thus raising γ_{SE} ; however, increased $[\text{Rb}]_{\text{cell}}$ makes the OP cell more optically opaque, and Rb vapor in the rear of the cell may not be properly illuminated.^{65,66} Such 'dark' Rb is unpolarized (but still capable of spin-exchange with ^{129}Xe), and thus will decrease the volume averaged, or 'global',

P_{Rb} ; indeed, optimizing the cell temperature is a balancing act, as increases to T_{cell} will maximize the buildup rate of P_{Xe} to a point, after which losses to global P_{Rb} will tend to drive down the overall ^{129}Xe polarization. In any case, P_{Xe} will accumulate over time, eventually reaching steady-state⁵⁸:

$$P_{\text{Xe}}(t = \infty) = \frac{\gamma_{\text{SE}}}{\gamma_{\text{SE}} + \Gamma_{\text{Xe}}} \cdot \langle P_{\text{Rb}}(z, r) \rangle, \quad (2.12)$$

Thus, P_{Xe} is limited by the volume-averaged rubidium electron spin polarization $\langle P_{\text{Rb}}(z, r) \rangle$, along with the magnitudes of γ_{SE} and Γ_{Xe} .

2.4 KEY SPIN-RELAXATION MECHANISMS

The angular momentum endowed by the circularly polarized photons can be lost through a number of avenues, both from the electronically polarized Rb (via Γ_{SD}) and the spin-polarized ^{129}Xe nuclei (via Γ_{Xe}). The primary contribution to P_{Rb} loss is through collisions with xenon atoms; indeed, P_{Xe} is typically expected to significantly decrease upon increased $[\text{Xe}]_{\text{cell}}$ due to the subsequent drop in P_{Rb} levels. Due to this interplay, increases in $[\text{Xe}]_{\text{cell}}$ are directly compensated for by corresponding losses in P_{Xe} , resulting in a (at best) fixed NMR signal-to-concentration ratio (SCR)⁶³ at increased xenon densities, complicating experimental efforts to produce sizeable amounts of highly polarized xenon.

Aside from ‘spin-destroying’ collisions with xenon, there are a number of non-spin-conserving interactions that work to depolarize optically pumped rubidium (Fig 2.2). For instance, collisions with buffer gases (N_2 , He) will ‘relax’ the Rb to varying degrees, depending on the buffer gas density and SD rate contribution per gas species (Eq. 2.4). Values for k_{SD} have been estimated as the

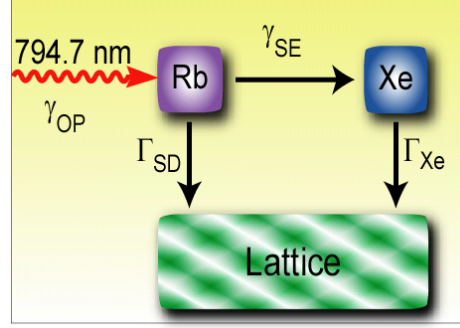


Fig. 2.2 Schematic of spin-polarization (γ_{OP}), exchange (γ_{SE}), and destruction (Γ_{SD} , Γ_{Xe}) mechanisms.¹⁴

following: $2 \times 10^{-18} \text{ cm}^3 \text{ s}^{-1}$ for He, $9 \times 10^{-18} \text{ cm}^3 \text{ s}^{-1}$ for N_2 , and $5.2 \times 10^{-15} \text{ cm}^3 \text{ s}^{-1}$ for Xe ⁶³; indeed, the three orders of magnitude increase in the spin destruction rate from xenon dwarfs the contributions from the other gases (which are typically omitted when considering P_{Rb} losses). Other factors that promote P_{Rb} depolarization include contact with the inner surface of the OP cell walls⁶⁷, Rb-Rb collisions⁶⁸ (which have been shown to be magnetic-field dependent⁶⁹), and the absorption of resonant, randomly polarized photons (a process which can be effectively quenched through the addition of sufficient amounts of N_2).⁶⁴

Once the spin-polarization has been transferred to the xenon nuclei, it can still be lost through a collection of pathways. In-cell ^{129}Xe T_1 's can range from tens of seconds to tens of minutes, depending on experimental conditions. The major contributions to P_{Xe} relaxation can be summarized in the equation below⁷⁰:

$$\Gamma_{\text{Xe}} = \Gamma_t + \Gamma_p + \Gamma_g + \Gamma_w \quad (2.13)$$

where Γ_t and Γ_p are the relaxation rate contributions due to transient and persistent Xe-Xe dimers, while Γ_g and Γ_w describe the P_{Xe} loss rate due to

polarized ^{129}Xe atoms traversing through gradients in the applied magnetic field and losses due to wall collisions, respectively.

Transient Xe-Xe dimers are formed via binary collisions, where the collision frequency depends on $[\text{Xe}]_{\text{cell}}$, while persistent dimers form through three-body interactions and exist in a stable form until broken apart by colliding with another atom⁶²; together, these interactions represent the intrinsic P_{Xe} in-cell relaxation mechanisms. Transient Xe-Xe dimers only contribute minimally to the ^{129}Xe T_1 under most experimental conditions⁷⁰ (although Γ_t increases with $[\text{Xe}]_{\text{cell}}$, the overall contribution is typically a small fraction of what is expected from wall relaxations⁶²). Persistent Xe-Xe dimers have a greater effect on ^{129}Xe T_1 , and are dependent on the OP gas composition and density (both $[\text{Xe}]_{\text{cell}}$ and buffer gases) and the magnetic field strength (and is also slightly dependent on T_{cell}).⁷⁰ The average lifetime of persistent dimers can be a factor of 40 greater than that of transient dimers (~115 vs ~2.85 picoseconds),⁶² leading to increased relaxation through spin rotation interactions. Dimers formed between Xe and other types of atoms are not as detrimental to P_{Xe} levels because the binding energies are weaker.⁷⁰

The primary extrinsic contributions to P_{Xe} relaxation are through collisions with the inner wall surfaces of the OP cell; most glassware contains paramagnetic impurities that will depolarize xenon upon contact^{71,72} (due to the unpaired, randomly polarized electrons in the paramagnetic species—many research groups try to circumvent this obstacle by using siliconizing surfactants⁵⁸ to coat the inner walls of the OP cell). Wall collisions have long been thought to

dominate Γ_{Xe} ; however, recent work from the B. Saam group (U. of Utah) has indicated that persistent Xe-Xe dimers may be the major culprit for P_{Xe} losses at low xenon densities.^{62,70} In addition to wall relaxation, ^{129}Xe can depolarize by traversing through a magnetic field gradient; however, this will typically have negligible effects on P_{Xe} for $[\text{Xe}]_{\text{cell}}$ values greater than ~ 0.1 amagat (particularly in the homogenous magnetic fields typically used in optical pumping).^{61,62,70} Additionally, xenon can also become depolarized via spin-exchange with an unpolarized (or randomly polarized) Rb electron⁶⁵ (such as 'dark' Rb vapor that is not sufficiently illuminated by a light source)—although technically, this contributes to γ_{SE} (and reduces P_{Rb} , while not affecting Γ_{Xe}).

CHAPTER 3

PRACTICAL CONSIDERATIONS OF SEOP

3.1 INTRODUCTION

The physical processes underlying SEOP are surprisingly complex and interdependent; despite decades of research into the optical, atomic, and molecular physics of these processes, they have yet to be sufficiently explored within regimes most relevant for MR applications. The equations presented in Chapter 2 do a good job of describing the overall SEOP process; however, if these equations completely described *all* aspects of SEOP, not only would it be possible to predict exactly what experimental conditions would be optimal for a given experiment, it should also be possible to quantitatively predict the result. Oftentimes, there is a disconnect between what is theoretically expected and what is experimentally achievable; this problem can be due to operating under non-optimal conditions, unforeseen experimental variables, or a poor understanding of the ‘true’ physics behind the system being studied. Therefore, the remainder of this chapter will outline many of the practical considerations of SEOP from the viewpoint of an experimentalist; these include choices of alkali metals, noble gases, and a variety of other pertinent (if often overlooked) experimental parameters.

3.2 CHOICE OF ALKALI METAL

The use of an alkali-metal vapor is the most obvious choice for the initial step of SEOP, as the Group 1 metals possess one unpaired electron in their valence shell; in turn, these single unpaired electrons can be easily spin-polarized upon absorption of circularly-polarized photons. Additionally, the absorption lines of the alkali metals are strong, and reside in areas of the electromagnetic spectrum that coincide with wavelengths that can be easily reached by present-day high-power laser technology. The alkali metals also have low melting points, which allows for optical pumping under moderate temperatures (because vaporization of the metal is required), and prevents high-temperature degradation to the surfactant coating on the inner walls of the optical pumping cell.^{54,71}

With regard to periodic trends, upon descending the periodic table (from lithium to francium), the metals increase in core size and reactivity (e.g., with water), but decrease in melting temperature and energy required for light absorption (i.e., higher absorption wavelengths). While optical pumping is possible with any of the alkali metals, the main focus on this work will be on rubidium and cesium. Lithium is not commonly used in any mainstream SEOP practices (but has been optically pumped to create an 'electromagnetically induced transparency'⁷³ that may be used to slow light⁷⁴ in dilute media). While sodium and potassium have both been used extensively in ³He SEOP, they are not as efficient for polarizing ¹²⁹Xe, as they suffer from decreased binary SE cross-sections⁵² compared to the heavier alkali metals. The use of francium for

SEOP has not been reported (to the author's knowledge), likely due to its extreme scarcity in nature.

3.2.1 Rubidium

Rubidium has long served as the 'workhorse' alkali metal for the SEOP community⁵⁴—particularly for heavier noble gases—due to a variety of experimental advantages. Rubidium benefits from its large spin-exchange cross-section⁷⁵ with ^{129}Xe , which increases the likelihood of a spin-conserving collision with the noble gas. Optical pumping can take place at relatively moderate operational temperatures⁷⁶ due to the high vapor pressure of Rb metal ($\sim 3.9 \times 10^{-7}$ torr at 25 °C; melting temperature ~ 39 °C)⁷⁷; this property lowers the risk of chemical breakdown of the OP cell's surfactant coating. Moreover, the Rb D₁ transition ($5^{(2)}\text{S}_{1/2} \rightarrow 5^{(2)}\text{P}_{1/2}$) occurs at 794.76 nm, a wavelength that has long been available to (low-power) dye lasers, titanium sapphire lasers, and gallium aluminum arsenide lasers⁷⁸; more recently, advances in solid-state laser technology has spurred the use of high-powered laser diode arrays (LDAs)⁶⁵ for Rb/ ^{129}Xe SEOP. The Rb D₂ ($5^{(2)}\text{S}_{1/2} \rightarrow 5^{(2)}\text{P}_{3/2}$) absorption line (780.03 nm) is not typically used for SEOP (as it can only be polarized to a level of 50%—see Section 11.5), but can be probed to monitor $[\text{Rb}]_{\text{cell}}$ (by measuring the degree of Faraday rotation imparted on a probe beam directed perpendicularly through the OP cell)⁷⁹ as well as P_{Rb} (via optical ESR).

High-quality (99.95+%) rubidium metal is typically pre-loaded into the OP cell in an inert-atmosphere glovebox (or via distillation) prior to being attached to

the SEOP apparatus. The amount of alkali metal loaded varies between set-ups; for experiments included in this work ('stop-flow' SEOP), amounts on the order of ~0.2 grams are typically used. For continuous-flow set-ups, between 2-5 grams⁸⁰ can be used (and some large-scale set-ups can be loaded with tens of grams⁸¹). This bulk Rb is usually a natural-abundance isotopic mixture of ~72% ⁸⁵Rb ($I=5/2$) and ~28% ⁸⁷Rb ($I=3/2$)⁵³; the fact that there are two (stable) Rb isotopes has minimal bearing on the physics of optical pumping relevant to this dissertation.

3.2.2 Cesium

While rubidium is the most commonly used alkali-metal choice for SEOP, there are many possible advantages to using *cesium*: for example, the Cs-¹²⁹Xe spin-exchange cross-section has been estimated⁷⁸ to be ~1.9-fold greater than that of Rb-¹²⁹Xe, yet the Cs-¹²⁹Xe collisional spin-destruction cross-section⁸² may be up to 2-fold smaller.⁸³ These potential benefits can be combined with more minor positives, including having a lower melting temperature (~28.5 °C, giving a higher vapor pressure of $\sim 1.45 \times 10^{-6}$ at 25 °C)⁷⁷, thus allowing even milder in-cell conditions.⁸⁴ Due simply to the lower energy of the Cs D-lines relative to those of Rb, more photons per Watt of light can be emitted by light sources for Cs optical pumping.⁸⁴ The greater energy spacing between the Cs D₁ ($6^{(2)}S_{1/2} \rightarrow 6^{(2)}P_{1/2}$) and D₂ ($6^{(2)}S_{1/2} \rightarrow 6^{(2)}P_{3/2}$) absorption lines (894.3 & 852.1 nm, respectively) could possibly serve as an intriguing benefit as well, as it has been speculated that P_{Rb} might be disadvantageously affected by simultaneous

pumping of the 'red' wing of its D_2 line).^{85,86} These factors would seem to point to an 'easy' improvement in hyperpolarized ^{129}Xe generation using Cs instead of Rb by raising the steady-state noble-gas polarization 'ceiling', as well as decreasing the time required to achieve peak polarization (as well as possible benefits to increased in-cell ^{129}Xe T_1 's; see Chapter 11).

However, to date, virtually no (net) benefits for Cs usage in SEOP have yet been realized (at least until the present work). One likely reason is that there has not been a prevalence of light sources available at the Cs D-line wavelengths that are equivalent to what now exists for Rb (i.e., high power, frequency-narrowed, spectrally tunable LDAs). This technological limitation has likely stifled what can be achieved with SEOP using cesium, and has worked to prevent the 'parameter space' for Cs/ ^{129}Xe SEOP from being properly 'mapped out' to find the optimal conditions for achieving the highest P_{Xe} values. The ongoing developments⁸⁷ regarding new high-powered light sources that are capable of hitting the Cs D-lines will thus play a key role in advancing the field of Cs/ ^{129}Xe SEOP (which will be summarized in Chapter 11).

3.2.3 'Hybrid' Alkali-Metal SEOP

Another possible method involves the simultaneous use of two alkali metals for SEOP. This approach has already been used in ^3He optical pumping, using both rubidium and potassium as the alkali metals.⁸⁵ The logic behind this idea is as follows: Rb excels at absorbing (spin-polarized) photons, but does not transfer this angular momentum to ^3He with high efficiency (~2% efficiency, or ~50 photons required to produce one polarized ^3He). Potassium has a high SE

efficiency with ^3He (~25% efficiency), but does not absorb photons as well as Rb^{88} (and the light sources aren't as well developed); however, the SE efficiency of Rb to K (electron to electron) is highly efficient. This situation reflects one of the few instances where adding a third (seemingly unnecessary) step in the middle can actually increase the efficiency of a system; in cases of K/Rb hybrid SEOP where the ratio of potassium to rubidium is very high, the majority of the spin-exchange with ^3He comes from efficient SE with potassium, with less 'lossy' SE with rubidium^{85,68}. This method has been used to produce small quantities of ^3He with spin-polarizations reaching upwards of ~75%.⁸⁵

Along similar lines to the K/Rb hybrid approach to ^3He SEOP⁸⁵, it may be possible to achieve even higher P_{Xe} values/quantities through a Rb/Cs hybrid method. If superior laser excitation may be achieved with Rb and better spin-exchange with Cs, then a Rb/Cs approach (where Rb polarizes the Cs before spin-exchange with Xe) may be the best overall option. The SE efficiency of Rb- ^{129}Xe has been estimated at ~4%, while the SE efficiency of Cs- ^{129}Xe has not yet been reported (to the author's knowledge); if it is significantly greater than 4%, then this hybrid approach may be a way to circumvent the currently sub-par laser technology for Cs optical pumping (assuming that Rb-Cs SE is highly efficient). Future planned experiments will establish the feasibility of a Rb/Cs hybrid SEOP apparatus and determine the benefits of using one laser (say, tuned to Rb D_1) versus two lasers (respectively tuned to a Rb & Cs absorption line), as well as the most effective amounts/ratios of the two alkali metals.

3.3 CHOICE OF NOBLE GAS

Although all of the NMR-active noble gases have the ability to achieve nuclear spin polarization enhancements via SEOP, they each have advantages and disadvantages regarding the degree of this polarization, the lifetimes of the polarized spins, and their relevance for certain types of applications. For instance, neon-21 ($I=3/2$) is capable of hyperpolarization, but suffers from a low natural isotopic abundance (0.27%)⁸⁰, small SE cross-sections⁵⁴, and a general lack of useful MR applications. The most commonly used noble gases for MR sensitivity enhancement are the ($I=1/2$) isotopes ^3He and ^{129}Xe ; less attention is typically given to quadrupolar species ($I>1/2$), most notably ^{83}Kr and ^{131}Xe , due to their shorter relaxation times. The following subsections will provide a quick overview of these four relevant HP gases, with emphasis on SEOP considerations and basic applications (more detailed SEOP considerations and MR applications for HP ^{129}Xe are reviewed in Chapters 2 & 5, respectively).

3.3.1 Helium-3

Of the noble gas isotopes with nuclear spin $I>0$, ^3He and ^{129}Xe have received the most attention for applications^{19,89-91} in part because they are spin $I=1/2$ isotopes—making it much easier to preserve and use their polarization while yielding simpler NMR spectra. Moreover, ^3He has a relatively high magnetic moment⁵⁵, very long HP lifetimes (on the order of days)⁹², and has been regularly polarized to levels of 70-80%+. ⁹³ ^3He SEOP occurs almost entirely through binary collisions (often with potassium or rubidium), with very

small (near-negligible) contributions from 3-body interactions.⁵⁴ However, due to the very slow spin-exchange rate (despite quite long ^3He in-cell T_1 's), the 'pump-up' time of HP ^3He can take many hours.⁹⁴

The most prevalent MR application of hyperpolarized ^3He is lung imaging; traditional lung MRIs are sorely lacking due to the low concentration of ^1H spins in lung-space. Aside from increased resolution, HP ^3He lung MRIs⁸⁹ can provide information about lung ventilation (from spin-density mapping), alveolar size distributions (via ^3He diffusion mapping), and oxygenation levels (via ^3He relaxation rates).⁸⁰ Hyperpolarized ^3He lung imaging has been extensively used in the study of emphysema⁸⁹, asthma⁹⁵, and chronic obstructive pulmonary disease (COPD).⁹⁶ In addition to lung imaging, HP ^3He has also been used as spin-polarized targets for probing nuclear structure and fundamental symmetries.^{97,98}

^3He suffers from a very low natural abundance ($\sim 0.00013\%$), and is instead primarily produced as a by-product of tritium depletion in nuclear reactors.⁹⁹ As such, the amount of ^3He available to scientists is subject to the whim of national governments, and the market price of ^3He can fluctuate greatly (at the time of the writing of this thesis, ^3He prices have sky-rocketed due to governmental rationing). Indeed, the long-range sustainability of HP ^3He for MR applications appears cloudy at best, as many groups that require large amounts of ^3He for non-MR applications have already begun to change research directions.

3.3.2 Xenon-129

While ^3He and ^{129}Xe are the only spin-1/2 HP gases that are regularly used in SEOP, their similarities end there. ^{129}Xe has a relatively high natural abundance (~26%; xenon gas is available for extraction from the atmosphere), shorter (but still useful) HP lifetimes (minutes to tens of minutes), and can also be polarized to a high extent if great effort is applied (~70%+).⁸¹ The 'pump-up time for ^{129}Xe is merely a matter of minutes, and ^{129}Xe does not suffer from the quadrupolar relaxation that its 'isotopic cousin' (^{131}Xe) does. The high spin-exchange rates afforded by Rb/ ^{129}Xe & Cs/ ^{129}Xe SEOP allow the P_{Xe} to build quickly, but increased spin-destruction rates decrease the lifetimes of the polarized spins. While ^3He is primarily spin-polarized through binary collisions alone, ^{129}Xe can be polarized through both binary and three-body interactions.⁵³ Isotopically enriched ^{129}Xe can be used in cases where ultra-high sensitivity is required; for most situations, though, natural abundance ^{129}Xe is adequate for MR applications. Also, xenon can be efficiently collected (following OP) and removed from its corresponding buffer gases by freezing in liquid nitrogen⁶⁴ (unlike ^3He).

HP ^{129}Xe lung MRIs are lacking in detection sensitivity when compared to HP ^3He ; however, the chemical shift of ^{129}Xe provides information about the local magnetic environment of the xenon atoms that is not afforded by HP ^3He imaging.⁸⁰ The exquisitely sensitive chemical shift of ^{129}Xe is due to its large, easily polarizable electron cloud.¹⁹ Moreover, ^{129}Xe has a predilection for dissolving in fluids and interacting with molecular cavities and surfaces, and

possesses MR parameters (i.e., chemical shift) that are sensitive to the local magnetic environment.¹⁹ Additional HP ¹²⁹Xe applications will be reviewed in detail in Chapter 5.

3.3.3 Krypton-83 & Xenon-131

Two noble gas isotopes with $I > 1/2$, ⁸³Kr ($I=9/2$) and ¹³¹Xe ($I=3/2$), have received some attention recently¹⁰⁰, but their polarization by SEOP⁸⁰ and subsequent use in NMR/MRI experiments¹⁰¹ are challenged by their nuclear quadrupolar moments (which contribute to short spin-relaxation times). Over recent years, T. Meersmann (and group—formerly at CSU) have pioneered the use of HP ⁸³Kr for NMR/MRI applications, showing that the relatively mild strength of the ⁸³Kr quadrupolar moment ($Q=0.28 \times 10^{-28} \text{ m}^2$)¹⁰² can allow for surprisingly high nuclear spin polarization from SEOP—along with relaxation times in samples that are long enough to allow useful MR experiments.¹⁰¹ Despite this progress, to date ⁸³Kr has not been hyperpolarized to anything close to the extent of ¹²⁹Xe or ³He; it suffers from less efficient SEOP due to a smaller Rb-⁸³Kr spin-exchange cross-section¹⁰⁰ and higher relaxation rates¹⁰³ from quadrupolar interactions with cell walls. Furthermore, the low natural abundance of ⁸³Kr (~11.5%) decreases detection sensitivity, and may necessitate use of isotopically enriched ⁸³Kr for some applications¹⁰² (an expensive option).

The quadrupolar response of HP ⁸³Kr can be highly sensitive to the nature and geometry of the local environment (by sensing the local electric field gradient) in a manner complementary to the chemical shift⁸⁰; in other words, HP

^{83}Kr can be used to sense different (yet complementary) kinds of magnetic information than what can be explored with HP ^3He & ^{129}Xe . Also, Kr has a smaller diameter than ^{129}Xe (~ 3.9 vs. ~ 4.4 Å) and has somewhat different absorption characteristics and chemical shift dependencies.¹⁰⁰ Moreover, its lower magnetic moment makes it less sensitive to paramagnetic relaxation (from O_2 or surface impurities), and its quadrupolar relaxation is highly sensitive to surface hydrophobicity¹⁰⁴—all properties that make HP ^{83}Kr an exciting tool for a variety of magnetic resonance applications.

If greater understanding of ^{83}Kr SEOP (along with improvements in methodology) can translate into major increases in P_{Kr} , the outlook for HP ^{83}Kr NMR/MRI experiments (such as surface studies and lung imaging) will dramatically improve. Additionally, such improvements for ^{83}Kr may warrant a re-visitation of HP ^{131}Xe (natural abundance $\sim 21\%$)⁸⁰, despite its much stronger quadrupolar influence. While the absolute value of the quadrupolar moment of ^{83}Kr is about twice that of ^{131}Xe ($Q = -0.12 \times 10^{-28} \text{ m}^2$), the interactions are greater for ^{131}Xe due to its smaller nuclear spin value, larger and more polarizable electron cloud, and correspondingly larger Sternheimer antishielding factor¹⁰²—this leads to even quicker ^{131}Xe T_1 's on the order of seconds, and limits the potential applications of HP ^{131}Xe .

Provided that sufficient progress can be made to both increasing P_{Xe} levels for ^{131}Xe and extending the lifetime of the polarized spins, then the quadrupolar characteristics of ^{131}Xe could be exploited for porous media/surface studies and lung imaging. One potential future application could be to use HP ^{129}Xe & ^{131}Xe

(produced simultaneously in a single batch) to perform human lung imaging, with the two polarized species providing different types of MR information (sensitivity enhancement-based contrast, chemical shift, and quadrupolar relaxation) in a single breath.

3.4 ADDITIONAL CONSIDERATIONS

When performing SEOP of a given noble gas isotope, a number of experimental conditions must be considered. Aside from the type of alkali metal, noble gas, and laser source (Chapter 4), there are numerous interdependent experimental parameters that must be both individually and collectively optimized to achieve peak P_{Xe} production. The following sections detail several of these parameters and experimental ‘choices’; this list is not intended to be all-encompassing, but rather to highlight many of the pertinent, if often overlooked, aspects of SEOP (unless stated otherwise, these sections primarily consider Rb/ ^{129}Xe SEOP—although much of the information can be directly applied to alternative SEOP configurations).

3.4.1 SEOP Apparatus Designs

There are several types of SEOP apparatuses used for generating hyperpolarized xenon; these setups can be divided into four categories. The first category is commonly referred to as ‘batch-mode’ OP^{19,54,105-107}; using this method, an OP cell is loaded with Xe, Rb, and buffer gases, then closed (via a stopcocked valve—or simply sealed in the glass cell) and placed in a weak

magnetic field. This field (~ 30 gauss) is often produced by a set of Helmholtz coils, or can be provided by the fringe field of a high-field NMR magnet. The cell is then heated with a forced-air oven and irradiated with circularly-polarized laser light at the proper wavelength. Following OP, (usually ~ 5 -30 minutes), the cell is cooled (so that the Rb may condense) and the Xe is removed by expansion into an evacuated container. The main limitation of this method is the small amount of xenon that can be polarized at a given time, due to typical losses to P_{Xe} upon increased $[Xe]_{cell}$.

To combat the limitation of only being able to produce small amounts of HP ^{129}Xe under conditions that would allow high P_{Xe} values, a 'continuous-flow' setup was developed⁵⁷ to produce much greater quantities of highly polarized ^{129}Xe . Typically, a premixed gas, comprised of $\sim 1\%$ Xe, $\sim 1\%$ N_2 , and $\sim 98\%$ ^4He , continuously flows from the premixed bottle through a heated chamber (where the gas mixture becomes pre-saturated with Rb vapor), and into the OP cell. The mixture is then optically pumped with a high-power LDA; the gas pressure (5-10 atm) and cell temperature (~ 150 °C) are usually kept high to increase pressure broadening, $[\text{Rb}]_{cell}$, and γ_{SE} (and $[\text{Xe}]_{cell}$ is kept low to maximize γ_{SE} from 3-body interactions, and further minimize Γ_{Xe}). More recently, continuous-flow setups have increased in laser power (210 W LDA system; P_{Xe} values up to $\sim 65\%$)⁶⁵, as well as size and complexity (~ 2 m OP cell; P_{Xe} values up to $\sim 70\%$).⁸¹ A third approach to SEOP extends the concept of the continuous-flow system by recirculating the pumping mixture back into the OP cell; this resulted in a ~ 3.5 -fold enhancement in P_{Xe} (up to $\sim 69\%$ with 80 W laser light)

A hybrid SEOP apparatus was introduced⁵⁸ that combines many of the features of the batch-mode and continuous-flow designs; the work presented in this thesis was obtained using this 'stopped-flow'¹⁰⁸ technique (the particulars of this SEOP apparatus will be discussed in detail in Chapter 7). Using this method, large amounts of HP ^{129}Xe are generated with systematic repetition of batch-mode SEOP at relatively high $[\text{Xe}]_{\text{cell}}$ values. A 75 cc cylindrical OP cell (pre-loaded with Rb) is filled sequentially with xenon and nitrogen to an arbitrary amount/ratio. Once optical pumping is complete, the xenon may be collected by simple expansion into an evacuated container. The xenon may also be separated from the buffer gases by cryo-collection, a method where the xenon freezes in a condenser that is immersed in liquid nitrogen (while gaseous N_2 is pumped off). Cryo-collection¹⁰⁹ must take place in a strong magnetic field (> 500 gauss) to prevent HP ^{129}Xe relaxation due to dipolar interactions with neighboring ^{131}Xe (which will then also quickly relax). The OP cell and transfer lines may then be evacuated and reloaded with fresh xenon and nitrogen, and the OP cycle is repeated until the desired amount of HP ^{129}Xe has been accumulated (limited by the ~ 3 hour ^{129}Xe T_1 at 77 K and $B_0 > 500$ G). The hyperpolarized xenon is then quickly sublimated and expanded into a sample of choice for increased-sensitivity MR studies.

3.4.2 Optical Pumping Cell Conditions

In order to minimize P_{Xe} losses due to wall collisions, the internal surfaces of the OP cell and apparatus (any surface visited by the HP gas) should be as free

of paramagnetic impurities as possible. In fact, most OP cell preparations (prior to the loading of an alkali metal) include coating the inner surfaces of the cell & condenser with a siliconizing surfactant, such as Surfasil (Pierce) or octadecyltrichlorosilane (OTS).^{19,58} This coating prevents polarized xenon atoms from coming into contact with paramagnetic centers in the glassware. Some research groups (especially those interested in ^3He SEOP) have even taken the extra precaution of fabricating OP cells from special glasses that have fewer paramagnetic impurities.⁹²

Air contamination of the cell, condenser, and transfer lines must also be minimized to prevent the exposure of the HP gas to paramagnetic oxygen (which will shorten the relaxation time). Furthermore, rubidium will degrade when exposed to oxygen or water vapor; over time, contamination of the OP cell can lead to the formation of rubidium oxides and supoxides, which can not only coat the cell walls (reducing transparency) but can also change the Rb phase diagram (e.g., forming contaminated rubidium that is liquid at room temperature, with suppressed vaporization—necessitating increased T_{cell}).

In addition to surfactant-coating the inner cell walls, there are several steps typically taken to preserve the purity of the SEOP set-up. The entire apparatus is often evacuated using a diffusion pump or turbo-molecular pump, with vacuum levels often reaching on the order of 10^{-6} torr. Also, the high-purity xenon and buffer gases pass through O_2 filters (or, 'getters') before entering the OP cell. Loading of Rb is performed in an inert-atmosphere glovebox, with very low concentrations of oxygen and water vapor. When not in use, OP cells are often

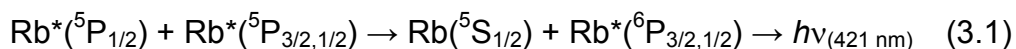
stored under a few atmospheres of internal pressure (xenon & nitrogen) to prevent atmospheric gases from leaking in through the sealed stopcocks. It has been the experience of the author that high purity Rb is paramount to success in SEOP.

3.4.3 Buffer Gas Choices

SEOP is typically performed in the presence of buffer gases (i.e., N_2 , 4He), which significantly increase the optical pumping efficiency due to pressure broadening of the Rb absorption line (and is especially useful when using broadband LDAs). As mentioned previously, the electronically excited Rb can relax via the spontaneous emission of a randomly polarized, omnidirectional photon that can be re-absorbed by other Rb atoms (thus depolarizing them).⁶⁴ To combat this radiation trapping, nitrogen gas is often added to the optical pumping mixture; the high density of states in the ro-vibrational manifold of N_2 makes it quite efficient for de-exciting Rb non-radiatively during Rb- N_2 collisions, thereby quenching the undesirable fluorescence.⁵⁴ Nitrogen densities of ~ 0.1 to ~ 0.3 amagat typically suppresses all radiative emissions by excited Rb. The vast majority of the Rb/ ^{129}Xe SEOP community uses this small amount of nitrogen to prevent radiation trapping; the remainder of the OP cell is typically filled with 4He , as it still promotes collisional broadening of the Rb absorption profile, while contributing less to the overall spin-destruction rates.⁵⁴ Other buffer gases that could be used include hydrogen, deuterium, and argon.^{108,110} Unless stated

otherwise, the work that is presented in the results sections of this thesis were obtained with a binary mixture of xenon and nitrogen gases only.

Indeed, optical pumping in the absence of N_2 has been shown to produce lower P_{Xe} values and results in not only emission at ~ 794 and ~ 780 nm, but also a violet emission by the Rb vapor at ~ 421 nm; this is due to an ‘energy pooling’ effect.⁶⁴ Under conditions of little to no nitrogen, two excited Rb atoms on a collisional trajectory can pool their energies, resulting in one Rb becoming more excited, and the other relaxing to ground state. Eventually, the highly excited Rb will release a photon at 421 nm to relax to the ground state (Fig 3.1). This emission results primarily from the following process:



Like the D_1 and D_2 -emitted light, the violet light actively depolarizes the Rb vapor, thus lowering the achievable P_{Xe} level. In addition to the 421 nm line, there are several other emission lines caused by Rb relaxation from a variety of

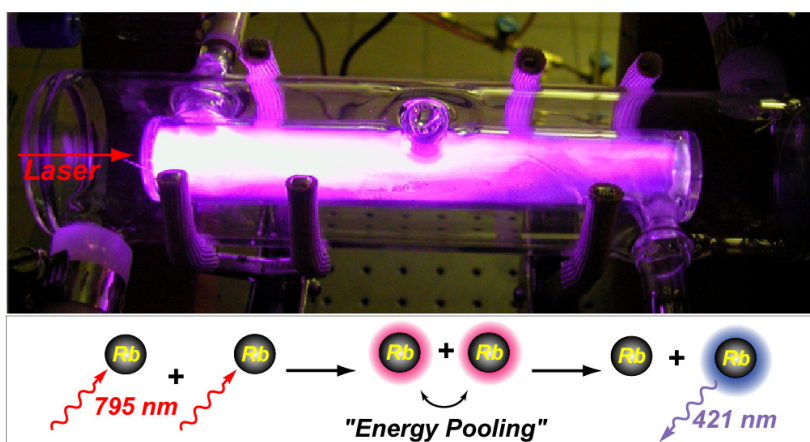


Fig. 3.1 Emission of 421 nm light resultant from Rb^* - Rb^* energy pooling mechanism, caused by $Rb/^{129}Xe$ SEOP in the absence of nitrogen as a buffer gas.^{64,111}

excited states (even upwards of 11D).¹¹¹ Furthermore, the author has noted⁵⁹ a seemingly irreversible degradation of the OP cell after running under conditions of low $[N_2]_{\text{cell}}$, possibly due to damages to the surfactant coating of the OP cell.

Recent work by Happer and co-workers¹¹² demonstrates the relevance of cell heating and energy transport in OP cells. Using *in situ* Raman scattering measurements on N_2 under typical but mild SEOP conditions (~ 15 W of broadband LDA irradiation, $T_{\text{cell}} \sim 100$ °C), ro-vibrational temperatures upwards of nearly 900 °C were observed. This excess thermal energy could potentially affect the nature of energy transport within the cell on both the macroscopic and molecular levels, especially under conditions of increased resonant laser flux (using narrowed light sources), higher T_{cell} , and different OP gas density/compositions. Indeed, the amounts and types of buffer gases can play a (possibly significant) role in the transport of dissipated laser energy across the OP cell.

3.4.4 Xenon Density Effects

Maximal P_{Xe} values are normally achieved by running under very low $[Xe]_{\text{cell}}$ (on the order of ~ 10 torr Xe or less) in order to minimize P_{Rb} losses due to Rb-Xe collisions.⁶³ Also, increased total cell pressures (and $[Xe]_{\text{cell}}$) results in losses to the contribution of three-body spin-exchange interactions to γ_{SE} ⁵³; this results in an overall reduced Rb-Xe spin-exchange rate, to the limit of the purely binary SE term. Because of these effects, increases in $[Xe]_{\text{cell}}$ are typically expected to be (more than) compensated for by corresponding losses to P_{Xe} , resulting in a

steady-state 'signal-to-concentration' ratio (SCR)⁶³ at increased xenon densities. This problem makes the production of large quantities of highly polarized ¹²⁹Xe experimentally challenging. Currently, the only way around this problem is to use complex, expensive continuous-flow systems that polarize a small amount of xenon at an instant (~0.1-60 torr Xe) and accumulate the hyperpolarized gas over time.^{57,113}

In addition to lowered P_{Xe} values, SEOP at high $[Xe]_{cell}$ can become a bit more experimentally challenging for another reason: while collision-broadening of the Rb D-lines is well-known⁵⁴, the Rb absorption lines can also be shifted, as well as undergo asymmetric lineshape changes, due to the presence of other gas species (especially xenon).¹¹⁴ These changes take place in a gas-specific, pressure-dependent, and temperature-dependent manner, depending on the amount and type of gases in the OP mixture. The effects from xenon are particularly strong, as increased $[Xe]_{cell}$ promotes a 'red'-shift and asymmetric broadening on the 'red'-side of the Rb D₁ (as well as the Rb D₂).¹¹⁴ These effects are important for optimizing the spectral offset of the SEOP light source, as narrow-band lasers may completely miss the actual Rb absorption depending on the OP gas mixture; also, the optimal spectral offset for achieving high P_{Xe} values may be dramatically shifted from what would be expected. Similar studies measuring the effects of OP gas mixtures on the Cs D₁ & D₂ absorption lines have also been researched.⁸⁶

3.4.5 Cell Temperature / Laser Power / Spectral Offset

Increases to the OP cell temperature raises $[\text{Rb}]_{\text{cell}}$ ¹¹⁵, which in turn increases γ_{SE} and improves P_{Xe} . However, if $[\text{Rb}]_{\text{cell}}$ climbs too high, the OP cell will become optically dense, and laser light will not be able to penetrate throughout the cell, preventing sufficient illumination of the entire cell volume.⁶⁵ While the illuminated Rb atoms will be polarized to near unity⁵⁴, P_{Rb} will drop to zero in the 'dark' regions of the cell. Hence, even if γ_{SE} is high, 'global' P_{Rb} will suffer, reducing the highest attainable P_{Xe} values⁶⁶ (as hot, dark Rb still spin-exchanges with xenon, just not in a 'constructive' manner). Additionally, increased T_{cell} can be detrimental to organic cell coatings^{71,72}, increasing the HP ^{129}Xe relaxation rate due to wall collisions.

Increases to $[\text{Rb}]_{\text{cell}}$ necessitate the use of higher-powered lasers⁶⁵, thus allowing the light to penetrate further into the OP cell at high cell temperatures. The high resonant flux from narrow-band lasers may possibly promote the use of lower cell temperatures, as a large fraction of the light may be absorbed in the front portion of 'optically thick' OP cells (and there is less 'off-resonant' light passing through that can be absorbed further into the cell), leaving the rear of the cell relatively 'dark'. Also, high resonant laser flux may add additional heat to the OP pumping mixture, so that it may actually be beneficial to lower the T_{cell} to compensate for the added energy.¹¹⁶

The combination of high OP cell temperatures and high laser fluxes may cause thermal gradients and instabilities where the undissipated heat from the laser absorption compounds $[\text{Rb}]_{\text{cell}}$ (and thus further light absorption) in a self-

reinforcing way (i.e., the 'Rb run-away effect').⁶⁵ Indeed, simulations⁶⁶ have shown that, at increased cell temperatures, not only is 'dark' Rb a problem, but that mass energy flow in a longitudinal fashion increases the residency time of the xenon with the OP cell's walls (increasing Γ_{Xe}), as well as prolonging contact with the non-illuminated, unpolarized Rb vapor. Additionally, the effects of extremely high N_2 temperatures (as N_2 possesses a much higher thermal conductivity than Xe)¹¹² have yet to be explored under conditions of high resonant laser flux and high $[N_2]_{cell}$ (& low $[He]_{cell}$).

In theory, the highest rubidium electron spin polarizations *should be* achieved when the laser is tuned to the center of the Rb D_1 absorbance line (i.e., 794.76 nm), using the highest laser power available.^{57,58} However, in practice, there are many considerations when determining the optimal laser offset (many of which are interdependent). For instance, the density/composition of the OP gas mixture may shift (and asymmetrically broaden) the Rb absorption lines.¹¹⁴ Also, through the course of this work, it seems especially important to optimize T_{cell} , laser flux, and spectral offset, so as to allow a good fraction (~30-50%) of the laser light to transmit through the cell (without being absorbed), especially when using narrowed light sources (so as to minimize 'dark' Rb).¹¹⁶ This state can be readily achieved by lowering T_{cell} and pumping slightly (~0.1 nm) off-resonance.⁵⁹ Indeed, perhaps to compensate for their own spectral narrowness, it may prove advantageous to optically pump just a bit off-resonance when using frequency-narrowed light sources, thus allowing the light to penetrate further into the OP cell, and minimize areas of unpolarized Rb.

CHAPTER 4

LASER TECHNOLOGY FOR OPTICAL PUMPING

4.1 INTRODUCTION

From the beginnings of SEOP to the present, there have been great advances in the technology of light sources used to optically pump alkali metals (especially Rb). Early studies used discharge lamps⁵⁰ and simple optics (including water baths that act as IR filters¹¹⁷) to spin-polarize the Rb electrons. Eventually, these methods gave way to the emerging laser technology of the day, such as titanium sapphire and dye lasers.^{54,118} These light sources benefited from incredibly narrow spectral outputs (on the order of 0.1 nm FWHM—full width at half maximum—or less) and clean lineshapes. However, especially in their infancy, they suffered from extremely low powers (from fractions of a watt to a few watts)¹¹⁸; they are also quite expensive¹¹⁹, have a large laboratory ‘footprint’¹²⁰, and require an experienced and skilled operator.

4.2 BROADBAND LASER DIODE ARRAYS

Recent advances to solid-state laser diode arrays (LDAs) have revolutionized the field of optical pumping.⁵⁴ LDAs can emit laser light at high powers (tens, even hundreds of watts)⁶⁵, are relatively cheap, rugged, long-lasting, take up very little space, have easily attainable power and cooling requirements, and are quite simple to use. Briefly, diode lasers¹²¹⁻¹²⁴ are based on semiconductors; as such, they operate by injecting electrons and electron

holes from opposite ends of a p - n junction (e^- from n -doped; holes from p -doped) upon an electrical bias. Recombination of the electrons and holes (in the 'active region') releases a spontaneous emission of light; this light bounces back and forth through an optical cavity. As these photons pass by other energized electrons, they promote a stimulated emission, where an extra photon is produced with the same phase, polarization, frequency, and traveling in the same direction as the original (non-consumed) photon. A cascading effect (or, amplification) takes place upon repeated passes, resulting in the medium lasing. This (fastly-dispersing) emitted light is then collimated and launched into an optical fiber; LDAs are modular, as arrays of laser diodes may be stacked vertically to achieve output powers in the kilowatt regime.¹²⁵

Despite the numerous benefits of optical pumping with LDAs, they suffer from one important drawback: broad, uneven lineshapes.⁵⁹ These broad spectral outputs (usually 2-3 nm FWHM) dwarf the relatively narrow atomic absorption lines (generally, ~ 0.1 nm or less during SEOP conditions). Because of this discrepancy, much of the laser output is wasted, as it is too far off-resonance to be significantly absorbed (see Fig. 4.1). This loss in absorption efficiency can necessitate high incident laser powers (up to hundreds of watts), presenting thermal-management problems.⁶⁵ While this low absorption efficiency can be partially mitigated by increased pressure-broadening of the Rb D_1 line⁵⁴, this practice can bring on its own experimental complications—namely, losses to the SE rate due to decreased 3-body interactions⁵³ (not to mention increased difficulty in separating the HP ^{129}Xe from the buffer gases—due to limitations in

the cell design—and increased risk of explosions). Also, LDAs traditionally have a poor spatial beam quality (or, ‘spot’) and are only available in certain wavelengths¹²⁶ (with a limited range of tunability).

To combat these problems, two methods have been developed to constrict the LDA output bandwidth: external cavity narrowing^{120,127,128}, and more recently—volume holographic grating (VHG) narrowing¹²⁹. External cavity narrowing^{120,127,128} employs planar dispersive gratings to provide feedback to the individual LDA elements; however the optical alignment is critical to maintain feedback to all the elements to ensure acceptable spectral quality and energy efficiency (typically ~40-66%^{127,128}). Whether the gratings can withstand sufficiently high intensities is questionable¹²⁷, as the low efficiency of external cavity laser diode arrays (ECLDAs) produces a large amount of heat in the gratings upon increased laser power.¹²⁷ ECLDAs also require a sizable work area, as the frequency-narrowing components (lenses, gratings, mirrors, etc.) are external to the LDAs, and must be expertly placed and aligned to provide optimal feedback to the individual laser elements.

4.3 FIXED-FREQUENCY VHG-LDAS

While ECLDAs have worked to increase the efficiency of SEOP with resonant, frequency-narrowed laser light ranging from a few to tens of watts¹²⁰, they still suffer from low efficiency and require a particular skill set to effectively operate. Alternatively, volume holographic gratings (VHGs—also known as volume Bragg gratings (VBGs)) can spectrally narrow LDAs with efficiencies

exceeding 90%.¹³⁰ VHG are bulk slabs of photosensitive glass¹³¹ which contain Bragg planes of varying indexes of refraction; the VHG retro-reflects a narrow band of the laser emission into the LDA elements, forcing them to lase at this injected wavelength (Fig. 4.1b).⁵⁹ Thus, the VHG works as a frequency-selective feedback element (FSFE), as each individual laser element effectively has its own optical feedback.¹¹⁶

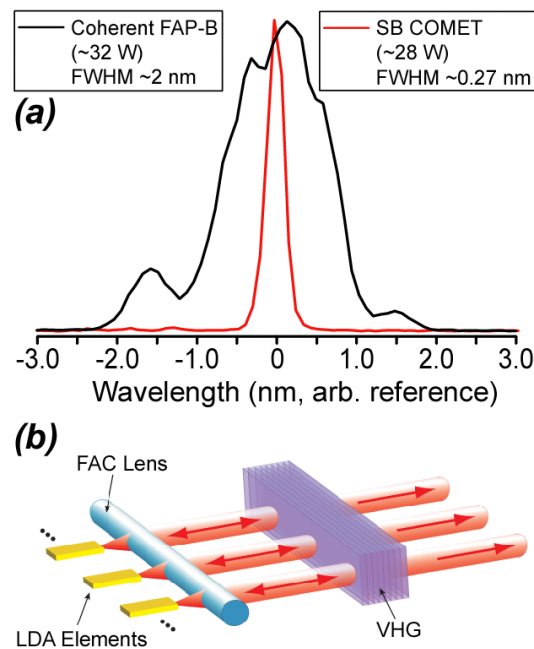


Fig. 4.1. (a) Comparative output of a ~32 W broadband LDA (~2 nm FWHM—*black*) versus ~28 W of VHG-narrowed light (~0.27 nm FWHM—*red*). Vertical scale normalized to equal heights. Note that the output quality of the broadband LDA is unusually good—the lineshape of most broadband LDAs is usually much worse. (b) Primary components of the VHG-narrowed (fixed-frequency) ‘Comet’ LDA, consisting of a (multi-source) laser bar, collimating optics (FAC—fast axis collimator), and the VHG grating—all of which reside in the LDA’s compact housing.^{59,111}

The VHG structures are recorded (by holographic techniques) in the photosensitive alumino-sodia-silicate glass, doped with silver, and then sensitized with cerium. After annealing (500-600 °C), the hardened glass is thermally, physically, and chemically stable, and has a high optical damage threshold.¹³² Furthermore, as VHG-LDAs are self-contained, they take up little space, are fairly inexpensive, and require almost no more expertise to operate than what is needed with a standard broadband LDA. VHG-LDAs can often be ‘driven’ with simple, inexpensive power supply units, and cooled with thermoelectric coolers (TECs) or water chiller plates. The laser output is often directed into an optical fiber (of arbitrary length), which is then coupled into an optics box that contains a collimator, beam splitter, and quarter-wave plate (to induce circular polarization), before irradiating the cell.

The efficient output-narrowing achieved from VHG-LDAs has many benefits for SEOP; typical linewidths vary from ~0.2-0.5 nm⁵⁹ (Fig. 4.1a), while output powers can easily reach 150+ watts.¹³³ This ability to narrow the spectral output by an order of magnitude without sacrificing overall laser flux has already directly translated to increased P_{Xe} values (~3-fold watt-for-watt increase in P_{Xe} —as discussed in Section 8.3).⁵⁹ Aside from increased P_{Xe} values, high-power, frequency-narrowed light sources also allow for more detailed fundamental studies of optical pumping; of particular interest is monitoring how changes to the excitation wavelength (i.e., the laser’s spectral offset) affect P_{Rb}/P_{Xe} under various conditions¹¹⁶ (these experiments are simply not possible using broadband LDAs).

Spectrally tuning conventional LDAs is achieved by varying the LDA temperature ($\sim 0.3 \text{ nm}/^\circ\text{C}$)⁵⁹; however, the nature of the VHG feedback makes tuning VHG-LDAs more difficult. Indeed, changing the output wavelength of VHG-LDAs is a non-trivial function of the separate temperatures of the LDA *and* the VHG (which itself is primarily determined by the laser power).⁵⁹ By changing the VHG temperature (temperatures of $\sim 15\text{-}40 \text{ }^\circ\text{C}$ are operationally safe for the laser diode, while the actual VHG can withstand much a wider temperature range¹³⁴), a slight change in the element spacing within the VHG occurs, thus altering the laser's spectral profile. Generally speaking, increases to the laser power or diode temperature induce a 'red'-shift (to higher wavelengths), and vice-versa; changes to the laser power typically have a much greater effect than diode temperature changes (as the laser power directly heats the VHG). This makes direct comparisons of SEOP at different excitation wavelengths difficult

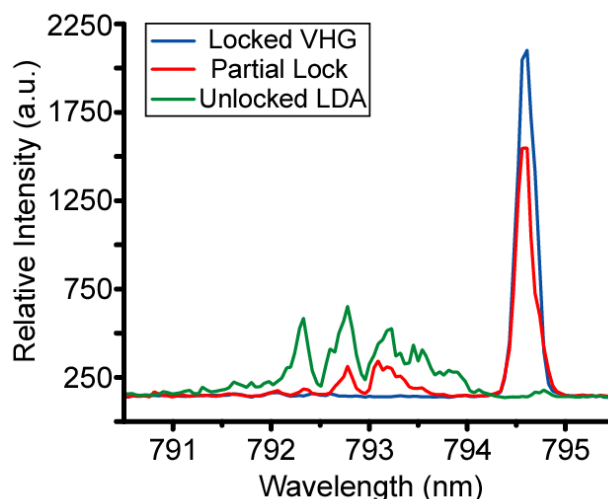


Fig. 4.2. Output of tunable VHG laser, showing spectral output under conditions of un-locked (green), partial lock (red), and optimal (blue) VHG alignment (by physically moving the grating). Note total lack of any parasitic “bleeding” at the locked laser wavelength.¹³⁴

due to the necessary changes in laser flux. Additionally, it is critical to remain in a particular range of laser powers and temperatures; journeys outside of this range are met with a loss of laser 'lock' (resulting in broader, uneven lineshapes and spurious output some distance away from the 'locked' output—Fig. 4.2).¹⁰⁰

4.4 TUNABLE VHGLDAS

Due to the increased interest in SEOP studies involving changes to the spectral offset, next-generation VHGLDAs have been developed that are able to spectrally tune over a wide range of wavelengths (1.5+ nm), with minimal changes to the output power. This allows for the direct, 'apples-to-apples' comparison of $P_{\text{Rb}}/P_{\text{Xe}}$ values at different excitation wavelengths¹¹⁶, a feat not possible with the first generation, fixed-frequency VHGLDAs.

4.4.1 VHGLDAs Tuning

Thus far, there have been a few methods of achieving this increased spectral tunability: the first technique employs a separate thermoelectric cooler to independently heat and cool the VHGLDAs separate from the laser diode (Fig. 4.3a). Thus, the laser is spectrally tuned by changing the temperature of the VHGLDAs itself, with minimal changes to the output from the laser diode. Unfortunately, preliminary studies¹³⁴ of this method posed many limitations (Fig. 4.3b), primarily consisting of a small tuning range (~0.2 nm) despite drastic changes of VHGLDAs temperature ($\Delta T_{\text{VHGLDAs}} \sim 125 \text{ }^\circ\text{C}$) (possibly due to poor anchoring to the TEC).¹³⁴ Additionally, the output power from the laser was significantly below

specifications, and spurious ‘unlocked’ output bled through, likely due to a (small, but significant) misalignment of the VHG.

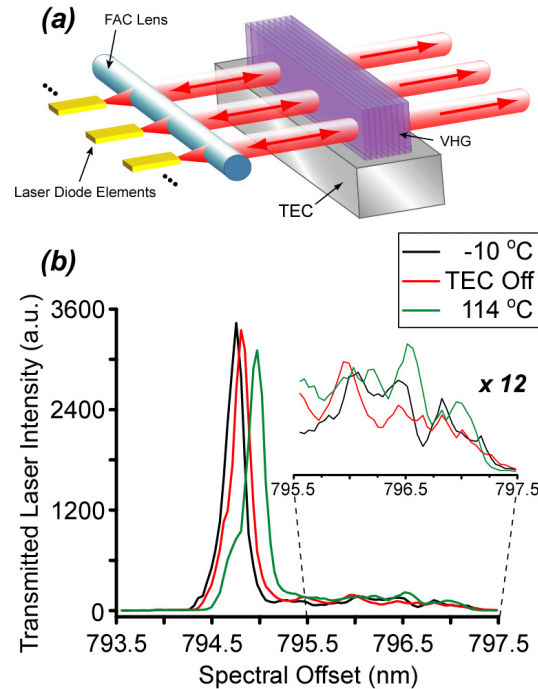


Fig. 4.3. (a) Tunable VHG-LDA. Similar to 4.1b, with additional TEC mounted to control temperature of VHG. **(b)** Spectral output of TEC-tunable VHG-LDA; minimal tuning range despite large ΔT_{VHG} . Noticeable loss in power with increased red-shift and ‘unlocked’ output at higher wavelengths under all conditions.¹³⁴

4.4.2 Mechanical Tuning

Another approach to changing the laser’s spectral offset involves physically moving a ‘chirped’ VHG relative to the light emission source.¹³⁵ The VHG is made so that the spacing between the gratings changes (say, from closer to farther apart) as a function of distance across the VHG (in the vertical direction); moving the grating up and down changes the wavelength of light emitted from

the laser. For instance, by pulling the VHG up, the spectral output red-shifts, while pushing down on the VHG blue-shifts the laser emission. Additionally, the output *linewidth* can be varied by rotating the VHG perpendicular to the central axis of the light beam.

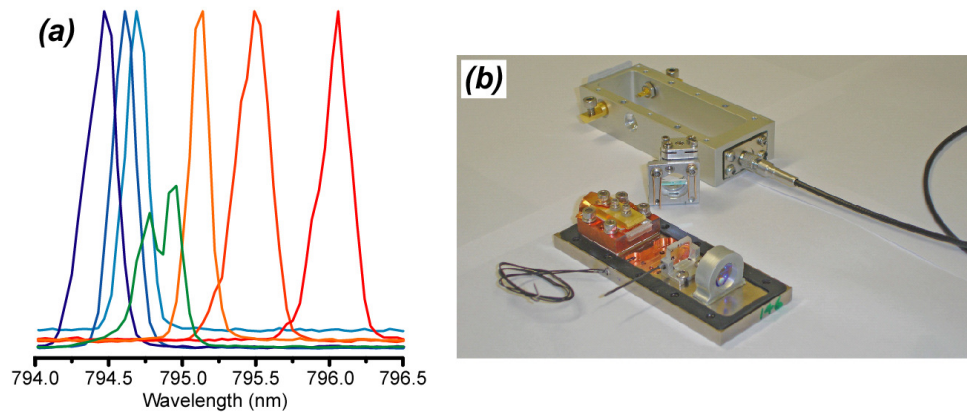


Fig. 4.4. (a) Normalized spectral output from mechanically tunable 'chirped' VHG-LDA at $T_{\text{cell}}=90$ °C (green line shows Rb absorbance). **(b)** Photo of tunable VHG-LDA prior to assembly; Flexure mount holding the 'chirped' VHG is shown in the center.¹³⁵

Figure 4.4a demonstrates the increased tunability of this mechanical approach¹³⁵; despite the increased tunability ($\Delta\lambda \sim 2+$ nm), changing wavelengths in this fashion can prove cumbersome. Early versions of this design (Fig. 4.4b) required ramping down the laser, removing the top, physically adjusting the VHG with a small lever, replacing the top, and turning the laser back to full power. Even then, it was a 'best guess' as to the extent of physically moving the VHG to achieve the desired wavelength (if a particular wavelength was sought, then the process may need to be repeated several times). Future generations of this design may attach the VHG to a translational stage, thus allowing for mechanical

tuning from outside of the module box, and significantly simplifying the tuning process.

4.4.3 'On-Chip' VHG-LDAs

To date, the optimal method for tunable VHG-LDAs (combining tunability range and ease of operation) has been through 'on-chip' integrated Bragg grating LDAs.¹³⁴ These devices are fabricated in a similar way to conventional laser diodes, with the Bragg grating defined by optical lithography into a photoresist and etched in the cladding; afterwards, the cladding is regrown on top of the grating to produce the top electrical contact¹³⁴ (Fig. 4.5).

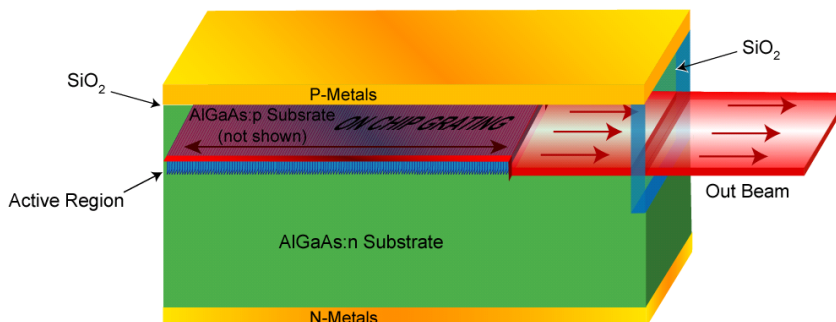


Fig. 4.5. Schematic of 'on-chip' integrated VHG-LDA. Bragg grating etched into lasing medium, instead of as a separate optic (i.e., Fig 4.4b). Laser tuning achieved by simply varying the laser diode temperature.¹¹⁶

An additional benefit of 'on-chip' VHG-LDAs is the ability to vastly increase total laser flux without dramatic increases in size. As the Bragg gratings are etched into the laser diodes themselves, several diodes can be placed inside a single module and launched into a single optical fiber (Fig 4.6). This is opposed to the previously-described lasers, where each diode requires its own complete

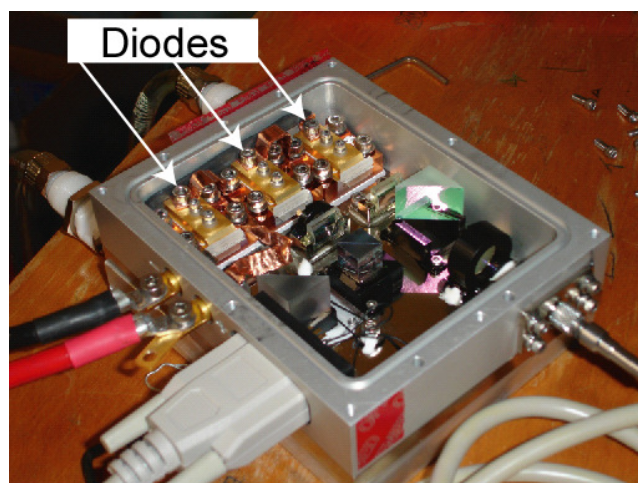


Fig. 4.6. Photograph of prototype 'on-chip' VHG-LDA module, with three laser diodes launching into a single optical fiber.¹³⁴

module and the fiber-coupling must be spliced among the modules. This new design also increases the ability to control the linear polarization of the light from each diode, thereby allowing circular polarization of the light with a simple collimating lens and $\lambda/4$ retarder plate and obviating the need for a secondary, skew beam.¹³⁴

Because of this ability to efficiently scale-up, an 'on-chip' VHG-LDA comprised of three diodes can have output powers exceeding 80 W, while a six-diode module may exceed 150 W¹³⁶ (and ~200 W, 8 module systems are now available). Tuning the spectral output is simply achieved by varying the temperature of the module (thus tuning the spacing of the built-in grating)¹³⁴; alternatively, changing laser power will also vary the spectral output (by 'ramping-up' the LDA, the emission wavelength increases). Most modules are capable of tuning over a wide range (> 1.5 nm; Fig. 4.7), allowing SEOP studies on either side of the Rb absorbance line over a wide range of laser fluxes.¹³⁴ This flexibility

in spectral offsets facilitates in-depth studies regarding changes to the Rb D₁ absorption line upon increases to the in-cell xenon density.

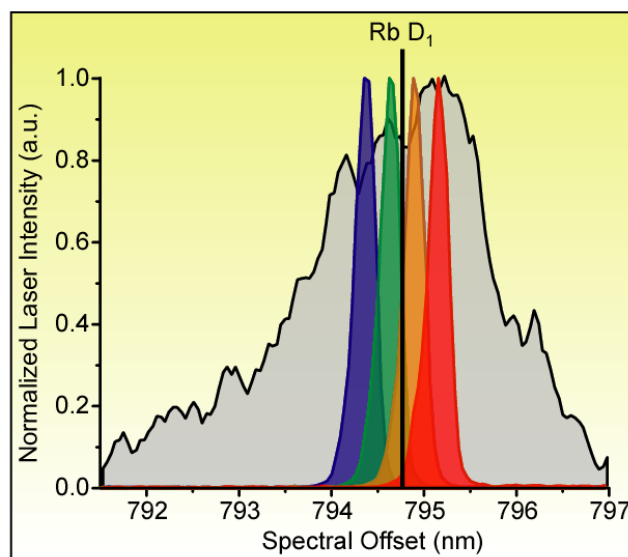


Fig. 4.7. Spectral outputs from a broadband LDA (grey) and a next-generation, frequency-narrowed 'on-chip' VHG-LDA tuned to different wavelengths (color). Ability to spectrally tune via changes to diode temperature independent of output flux allows excitation wavelength-dependent SEOP studies.¹³⁶

4.5 EMERGING LASER TECHNOLOGY FOR Cs/¹²⁹Xe SEOP

Despite the many potential benefits of Cs/¹²⁹Xe SEOP, there have been relatively few advances in this field, as compared to Rb/¹²⁹Xe SEOP. This is primarily due to insufficient advances in available light sources at the Cs excitation wavelengths. Laser diode arrays are only manufactured at particular wavelengths, and despite some measure of tunability, the Cs D₁ line (894.3 nm) lies too far away from the most commonly used LDA wavelengths. There have been some early studies that were able to optically pump Cs using indium-

gallium-arsenide LDAs, but those lasers suffered from very low power (~ 0.3 W resonant output) and resulted in low P_{Xe} values ($\sim 2.5\%$).⁸⁴ Also, B. Driehuys achieved P_{Xe} values of $\sim 6\%$ using a 7.2 W, frequency-narrowed (~ 0.15 nm FWHM) laser tuned to the Cs D₁ line; however, this was only approximately half the xenon polarization attained from Rb/¹²⁹Xe SEOP using a broadband laser.¹³⁷

Recently, studies of SEOP at the Cs D₁ and D₂ absorption lines via high-power (~ 50 W) broadband laser diode arrays (Fig 4.8) have shown that, indeed, cesium may be more efficient for producing hyperpolarized ¹²⁹Xe than rubidium⁸⁷ (see Chapter 11). The long-term goal for advancing SEOP using Cs will be to

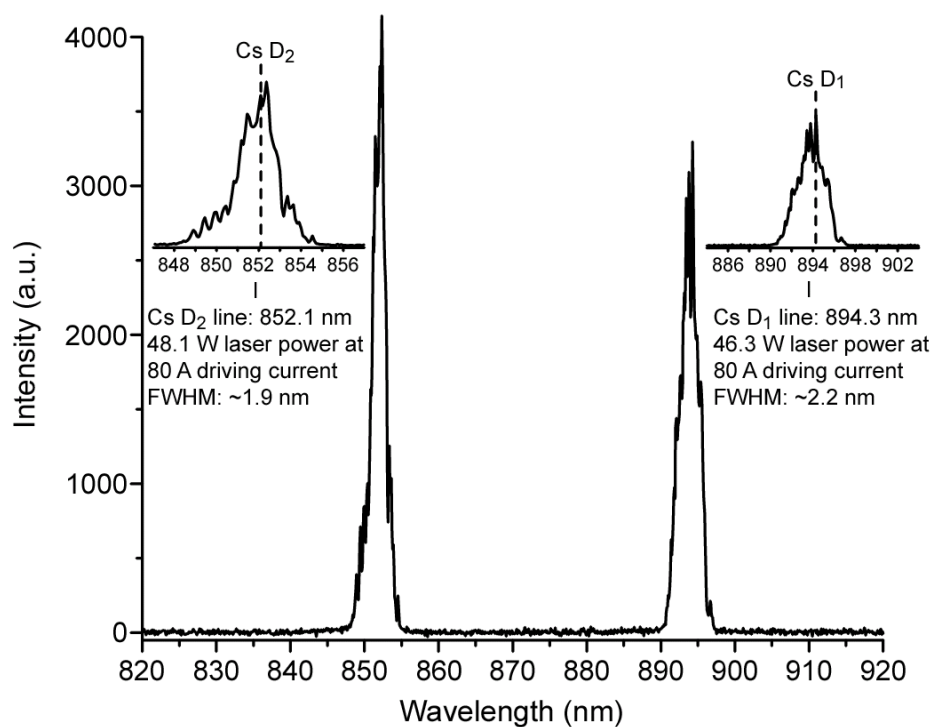


Fig. 4.8. Plots of two new broadband lasers that can selectively excite the D₁ (*right inset*) and D₂ (*left inset*) absorption lines of cesium.⁸⁷

develop high-power, frequency-narrowed, tunable light sources (on the scale of what is currently available for optically pumping Rb), and use them to further 'map out' the experimental parameter space of Cs/¹²⁹Xe SEOP, with the hope of being able to generate large quantities of highly polarized ¹²⁹Xe that will compete with/surpass the levels already attained via Rb optical pumping.

CHAPTER 5

MAGNETIC RESONANCE APPLICATIONS OF HYPERPOLARIZED XENON

5.1 INTRODUCTION

The inherent lack of detection sensitivity in most traditional magnetic resonance experiments limits the usefulness and applicability of this otherwise powerful scientific tool.¹⁹ However, the enhancements in signal intensity afforded by hyperpolarized species can improve existing NMR/MRI applications as well as allow for novel MR approaches to otherwise unworkable problems. Over the years, HP ^{129}Xe has been extensively used to increase the MR detection sensitivity for numerous studies involving diverse systems of molecules, organisms, and materials.¹⁹ The remainder of this chapter will highlight a few of the various applications of HP ^{129}Xe in the field of magnetic resonance.

5.2 PROPERTIES OF XENON

5.2.1 General physical properties

The various physical states of xenon exist under conditions (temperatures and pressures) that can be readily achieved in the laboratory¹⁹; under atmospheric conditions, xenon exists in the gas-phase at room temperature (Fig. 5.1). At just below ambient pressure, the triple-point of xenon exists at ~160 K; Xe can also be easily solidified by freezing in liquid nitrogen (~77 K). This allows for the efficient collection of Xe after optical pumping and provides a way to

remove the buffer gases in the OP mixture (as well as to 'de-gas' aqueous samples that contain Xe dissolved in solution). Liquid xenon (which can be used as a hydrophobic solvent)¹⁹ can be collected at fairly moderate pressures (1-10 atm) through condensation at around 170-200 K; supercritical xenon is also attainable under relatively mild conditions (~58 atm and near ambient temperatures).¹³⁸

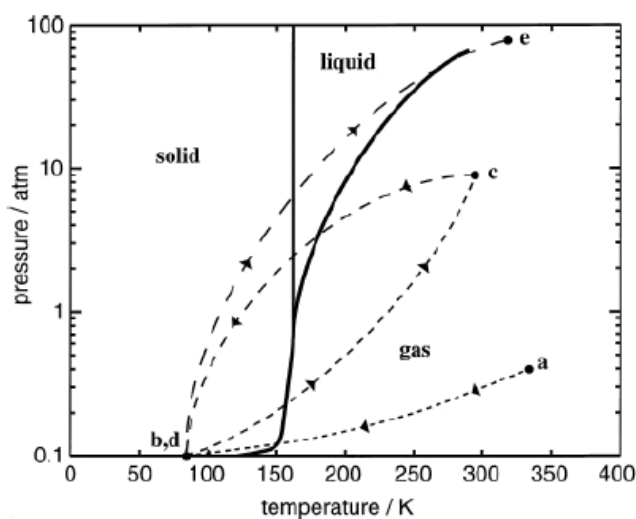


Fig. 5.1. Phase diagram for physical properties of xenon (disregard pathway lines (dotted and dashed)). Figure courtesy of Ref ¹⁹.

The hydrophobic nature and strong van der Waals interactions provide xenon with good solubility qualities in hydrophobic surroundings (i.e., membranes, lipids, fatty tissues, etc.).^{139,140} The lipophilic properties of xenon allow it to engage in specific and nonspecific interactions with proteins, material surfaces, and inclusion complexes.^{19,139,141} This lipophilicity also contributes to xenon's propensity for effecting anesthesia; indeed, xenon NMR may be a good way to study the mechanism of general anesthesia (which is currently poorly

understood).^{140,142} The lack of toxicity allows high concentrations of xenon to be used for *in vivo* imaging and spectroscopy; however, the fractional concentration of xenon should remain below 35% to circumvent unwanted anesthetic effects.¹⁴²

5.2.2 NMR Properties

Xenon atoms are highly polarizable (due to their large electron clouds), with an atomic radius of $\sim 2 \text{ \AA}$ and van der Waals volume of $\sim 42 \text{ \AA}^3$. Two NMR-active xenon isotopes (^{129}Xe & ^{131}Xe) have sufficient natural abundance to undertake gas-phase, solution, and solid-state NMR studies (as summarized in Table 5.1).

Table 5.1. Physical and NMR properties of ^{129}Xe & ^{131}Xe .¹

Isotope	Natural Abundance (%)	Spin (<i>I</i>)	$\gamma_{\text{Xe}} / \gamma_{\text{H}}$
^{129}Xe	26.4	1/2	-0.2781
^{131}Xe	21.2	3/2	0.0824

^{129}Xe is the more commonly used isotope in NMR studies due to its long T_1 ; in the gas phase (after collection from the OP cell), the T_1 of the HP ^{129}Xe can typically last for 90+ minutes, depending on the integrity of the storage container (at low $[\text{Xe}]_{\text{cell}}$ and high B_0 , HP ^{129}Xe T_1 's have been measured in excess of 90 hours).⁷⁰ When stored in the condensed phase, T_1 values of ^{129}Xe range from ~ 3 hours (at 77 K) up to ≥ 100 hrs (at 4.2 K)^{143,144} when kept in high magnetic fields (≥ 500 Gauss). The presence of the external field prevents (or at least, slows down) coupling with the quadrupolar ^{131}Xe in the lattice. While generation of HP

^{131}Xe is possible, the very short T_1 values (~ 0.1 s due to quadrupolar relaxation) limit its general applicability in NMR studies. Indeed the (typically) two orders of magnitude increase in T_1^{Xe} (as compared to ^{131}Xe) makes ^{129}Xe the isotope of choice for most MR-application studies. In theory, the T_1 of xenon in a homogeneous B_0 should only be comprised of relaxation due to spin-rotation during Xe-Xe collisions¹⁴⁵:

$$T_1^{\text{Xe}} \approx 56 \text{ hrs}/\rho, \quad (5.1)$$

where ρ is the xenon density in amagats. However, in practice, the hyperpolarized T_1^{Xe} is also greatly limited by collisions with the inner wall surfaces of its container.^{71,72}

^{129}Xe -based NMR (as opposed to ^1H & ^{13}C) benefits from zero background signal (in most samples), making the interpretation of spectra very straightforward. ^{129}Xe also benefits from an exquisitely sensitive chemical shift range ($>7,500$ ppm) due to its large, easily polarizable electron cloud. Strong electron deshielding effects make xenon a very effective chemical ‘sensor’; indeed, a chemical shift range of over 200 ppm can be found from simply dissolving xenon in a solution (Fig. 5.2).¹⁹

Because of its impressive chemical shift sensitivity, long T_1 's, and ability to be hyperpolarized, ^{129}Xe has been extensively used in the magnetic resonance community for a variety of applications. However, due to its nonrenewable nature, whichever rf pulse sequence used for the particular HP NMR experiment must occur faster than the timescale of T_1^{Xe} . Also, to prevent complete depletion

of the polarization enhancement in only an instant, small tipping angle pulses must also be used. By applying each pulse of tipping angle ' α ', the remaining z-

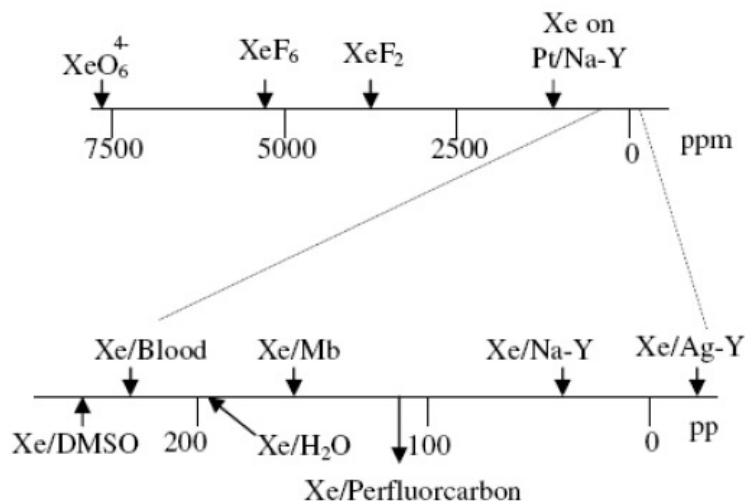


Fig. 5.2. Chemical shift for xenon in various environments. Figure courtesy of Ref.¹⁹

component of the magnetization is reduced by a factor of $\cos(\alpha)$.¹⁹ The only way to replenish the HP signal enhancement (for signal averaging or multiple separate experiments run in series) is to introduce freshly polarized gas between pulses (via continuous flow set-ups).^{146,147} This non-renewable polarization can be used to one's advantage, as the HP signal can be efficiently and completely destroyed at will, and the threat of any 'HP background' signal is minimal (due to dilution and short T_1^{Xe} 's in solution). These two factors may lead to a more straightforward interpretation of HP ¹²⁹Xe MR spectroscopy & imaging.¹⁹

5.3 POLARIZATION TRANSFER METHODS

The increased spin polarization from HP ^{129}Xe allows for its use as an MR probe for a variety of diverse systems of interest. However, for the most part, the information that is obtained for the underlying molecular structure and dynamics is indirect, and must be inferred from the chemical shift and/or relaxation characteristics of xenon atoms in close contact with the species of interest. A more direct method, where the overall NMR signal of the species of interest itself is increased, would be preferred. Thus, a substantial amount of research has been spent developing novel spin-systems that are able to transfer the high polarization of the ^{129}Xe nuclei to other nuclei of interest (i.e., ^1H & ^{13}C).

5.3.1 Low-Field Thermal Mixing

The earliest (and simplest) method of transferring polarization from ^{129}Xe to other species of interest is through a process known as low-field thermal mixing. Using this method, HP ^{129}Xe and the species of interest (first demonstrated in ^{131}Xe ; now typically a ^{13}C -labeled molecule is used)^{148,149} are combined and allowed to mix so that the HP ^{129}Xe throughout the sample is very homogeneous. The sample is then rapidly frozen; an applied magnetic field (or, 'mixing field') is swept so that the Zeeman energies of the two spin species are matched by their dipolar couplings.¹⁹ At this point, the nuclear spins equilibrate in polarization (or, reach an 'average' P).

While useful, the efficiency of the polarization transfer is low, with typical enhancements of ^{13}C signal "only" around ~200-fold.¹⁴⁸ Other limitations include

the difficulty of using xenon “ice” (or frozen solutions)¹⁹, the types of molecules that can be polarized (typically limited to molecules that contain few alternative NMR-active nuclei) and the homogeneity of the species of interest (i.e., how ‘evenly’ the HP ¹²⁹Xe mixes with the target molecules). Recent studies have addressed the latter two limitations¹⁵⁰, where HP ¹²⁹Xe and ¹³C-labeled acetic acid were mixed together in the gas phase before freezing, thus increasing the homogeneity of the sample and leading to a factor of ~10 enhancement in ¹³C signal.

5.3.2 SPINOE

In the 1950’s, Albert Overhauser hypothesized the (through-space) transfer of spin polarization between electrons and nuclei¹⁵¹; this is the basic concept of one type of DNP. In a coupled spin-system, when one of the spin species is disturbed (by continuous irradiation with a weak rf field), the polarization of the other species deviates from equilibrium.¹⁵² The (nuclear-nuclear) NMR equivalent of this process is referred to as the Nuclear Overhauser Effect (or, NOE). For experiments using HP ¹²⁹Xe as one of the species in the coupled spin-system, the effect was given the moniker of SPINOE, or spin polarization induced-NOE, and was used to show an enhancement (~2x) of ¹H signal in partially deuterated benzene (also, by inverting the polarization of the HP ¹²⁹Xe, the ¹H signal inverted as well).¹⁵²

The experimental freedoms of SPINOE are greater than those attained via low-field thermal mixing; for one, SPINOE works with xenon dissolved in isotropic

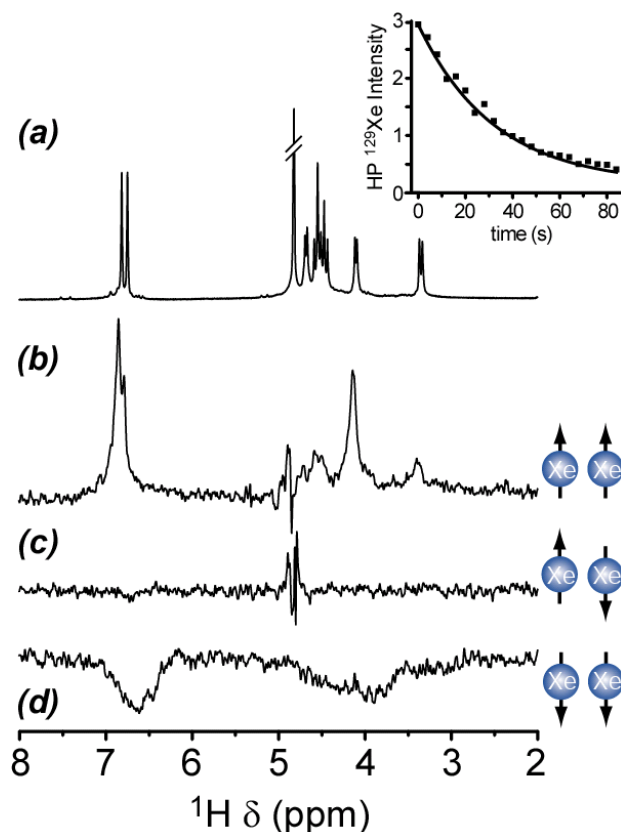


Fig. 5.3. Example SPINOE spectra of HP ^{129}Xe in water-soluble cryptophane-A hexaacid. **(a)** High resolution ^1H spectra (at thermal equilibrium) of cryptophane-A. *Inset:* Magnetization decay of the HP ^{129}Xe in the water-soluble cryptophane-A hexaacid solution. **(b)** ^1H SPINOE spectra with HP ^{129}Xe “positively-polarized”. **(c)** Difference SPINOE, with efficient ^1H equilibrium signal suppression. **(d)** ^1H SPINOE spectra with HP ^{129}Xe “negatively-polarized”. Decreased resolution likely due to decreased sample homogeneity from “shaking” the HP ^{129}Xe into solution.¹⁵⁴

liquids. There is no need to freeze the xenon and sample together (indeed, a continuous-flow OP apparatus can be quite beneficial by delivering freshly polarized ^{129}Xe to the liquid sample), and samples of interest can be selectively deuterated to further enhance a specific $\text{HP } ^{129}\text{Xe} \rightarrow ^1\text{H}$ polarization transfer. One novel twist is to use *liquid* xenon as the solvent in the SPINOE sample (thus increasing the xenon density and $^{129}\text{Xe} \rightarrow ^1\text{H}$ cross-relaxation rate).¹⁹ The use of

certain rf pulse sequences allows for greater flexibility, as the equilibrium NMR signal can be depleted (known as a 'difference SPINOE')¹⁹, allowing for the observation of small, specific SPINOE effects (Fig. 5.3). This particular benefit can be quite useful; to date, however, the obtained enhancements (particularly of ¹³C) using SPINOE have been quite small, and are not currently up to the level of LF thermal mixing.¹⁵³ Future SPINOE work in the Goodson laboratory will concentrate on inclusion complexes (i.e., cryptophanes) and proteins (such as myoglobin)¹⁵⁴; Fig. 5.3 demonstrates a set of SPINOE experiments of xenon in a water-soluble cryptophane-A hexaacid, which includes: a high resolution ¹H NMR spectra, SPINOE ¹H spectra of 'positively' polarized xenon, a difference SPINOE where all ¹H signal is suppressed, and a SPINOE ¹H spectra using 'negatively' polarized xenon (produced by inverting the magnetic field used during optical pumping).

5.4 XENON BINDING IN HYDROPHOBIC CAVITIES OF PROTEINS

The sensitive chemical shift range, relatively small size, and propensity for hydrophobic environments make ¹²⁹Xe an intriguing option for biomolecular NMR studies. In particular, changes to the chemical shift may provide details concerning changes to the chemical composition and structure of proteins.¹⁵⁵ This information is made available through both specific (xenon binding to hydrophobic cavities) and nonspecific (xenon interacting with surface residues on proteins) interactions. While the specific interactions are weak (due to low xenon association constants; $\leq 200 \text{ M}^{-1}$), the nonspecific interactions are even

weaker (but continue to arise in systems that feature denatured protein or free amino acids in solution).¹⁵⁶ Thus, the presence of a hydrophobic 'pocket' may be deduced from comparing the NMR spectra of a protein in its natively-folded state versus in a denatured form. However, due to its typically fast exchange ($\sim\mu\text{s}$) between the protein and solution environments, only one ^{129}Xe NMR peak appears in the spectrum.

While many biomolecules contain hydrophobic pockets of relevant size ($43\text{-}165 \text{ \AA}^3$)¹⁵⁶, the most widely studied protein for ^{129}Xe binding thus far has been myoglobin (Mb).¹⁵⁷⁻¹⁶⁰ Myoglobin is a ~ 17 kDa α -helical globular protein that consists of 153 amino acid residues and a heme group; the primary function of the protein is to store oxygen for muscle tissues.^{161,162} Xenon-Mb interactions have been studied in detail using both NMR and X-ray crystallography^{139,157}; indeed, it appears that there are four specific xenon binding sites in sperm-whale myoglobin (SWMb), with varying degrees of xenon affinity.¹³⁹ These binding sites are inaccessible to the solvent (as they are 'hidden' in the protein's hydrophobic core); their functions have not yet been determined, but the protein may have to undergo concerted conformational changes in order to bind the xenon.¹⁹

As myoglobin is a cheap, rugged, and readily available protein that willingly binds to xenon and has been highly characterized throughout the years, it is a logical choice for HP ^{129}Xe NMR studies. However, the iron-containing, paramagnetic heme compound in the center of the protein is a strong depolarizing force for hyperpolarized nuclei (contributing the ^{129}Xe T_1 's on the order of ~ 0.1 seconds). While there have been a number of different approaches

to circumvent this obstacle, the one used in the Goodson laboratory has been to chemically substitute the paramagnetic heme for a diamagnetic zinc protoporphyrin IX compound, thus making 'zinc myoglobin' (ZnMb).

Preliminary work on this system (primarily by Xiaoxia Li)¹⁶³ studied both specific and nonspecific xenon-ZnMb interactions, with the future goal of studying the system in an anisotropic, liquid crystalline environment. From this earlier work, it was shown that HP ^{129}Xe can be successfully delivered to ZnMb, and a sufficiently long HP ^{129}Xe T_1 (~60 sec) can be obtained so as to allow for future novel experiments (Fig 5.4). Additional findings include changes to the ^{129}Xe chemical shift (and linewidth) upon variation of the temperature, ZnMb

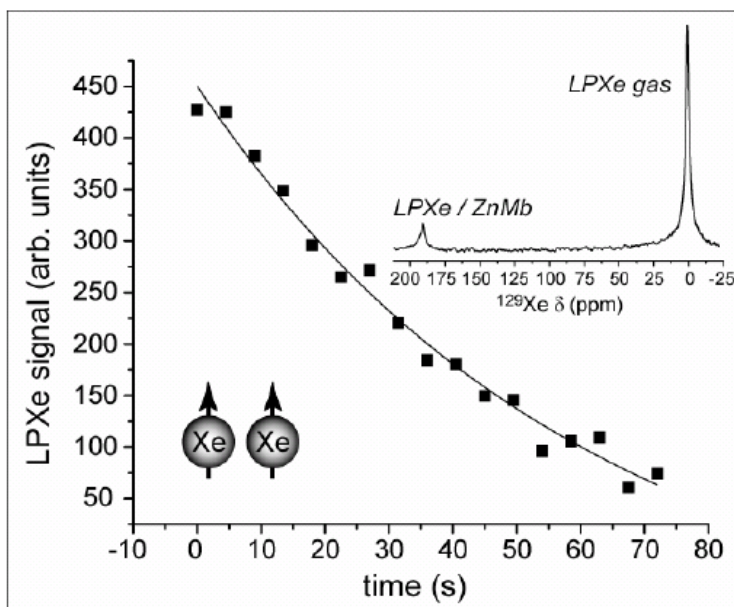


Fig. 5.4. ^{129}Xe NMR signal decaying after addition of ~1.6 atm of HP ^{129}Xe into 2 mM ZnMb (at 9.4 T), corresponding to a ^{129}Xe T_1 of ~60 sec (small tipping angle pulses ($\alpha \sim 19^\circ$) used). *Inset:* HP ^{129}Xe NMR spectra from first collected point on curve. Relatively low SNR is mostly due to line broadening and non-optimal infusion into sample (via shaking). Strength of gas peak due to increased [Xe] in gas phase (~10x) compared to xenon in solution (gas peak appears because part of detector coil is above the liquid/gas interface); figure courtesy of X. Li.¹⁹⁹

concentration, and xenon concentration that are consistent with specific and nonspecific ^{129}Xe -ZnMb interactions (additionally, changes to several of the ^1H resonances occur with varying the xenon density). The collected data supports the idea of at least two strong xenon-binding sites (as well as multiple non-specific binding sites) in the protein.¹⁶³

5.5 XENON AS A MOLECULAR BIOSENSOR

When studying binding in hydrophobic protein cavities, ^{129}Xe is commonly referred to as being 'unfunctionalized'; indeed, as the ^{129}Xe chemical shift responds to different chemical 'stimulations' simultaneously, it is difficult to differentiate exactly which event causes which chemical shift effect.¹⁵⁶ Hence, there has been substantial work¹⁶⁴⁻¹⁶⁶ to functionalize xenon as a molecular biosensor, typically using supramolecular cage compounds that bind xenon with high affinity ($>1000 \text{ M}^{-1}$).¹⁵⁶

Cryptophanes^{167,168} are a class of roughly spherical, cage-like molecules that are comprised of rigid, bowl-shaped aromatic structures connected by flexible aliphatic linker chains. While cryptophanes in general can be used as an inclusion complex for a variety of small organic guests, 'cryptophane-A' in particular is well suited for xenon-binding, due to the size of the hydrophobic cavity and strong binding affinity ($>3000 \text{ M}^{-1}$ in 1,1,2,2-tetrachloroethane; dependent on solvent).¹⁶⁹ Furthermore, the trapped xenon does not have to overcome significant steric constraints to move into, and out of, the cage; this results in a xenon residence time of milliseconds instead of hours.^{19,169}

Cryptophane-A can also undergo conformational changes that influence the size and binding capacity of the hydrophobic pocket, thus altering the dynamics of how xenon is bound and released.^{19,170} Figure 5.5 demonstrates the chemical shift range of HP ^{129}Xe in cryptophane-A, as three resonances appear: free ^{129}Xe in solution, ^{129}Xe bound to a cryptophane-A host, and ^{129}Xe gas (above the sample, but within the detection region of the NMR coil).¹⁵⁴

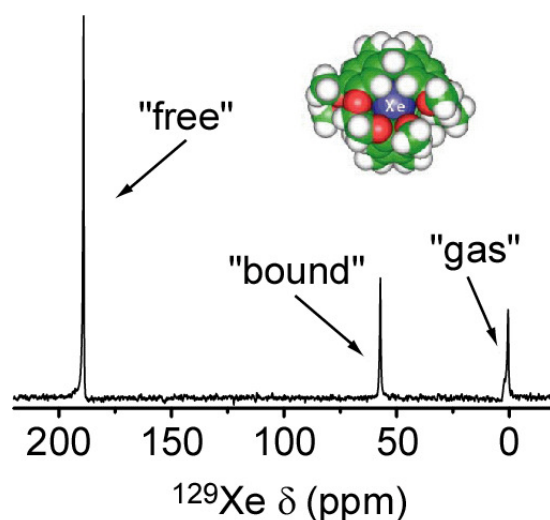


Fig. 5.5. NMR spectra of HP ^{129}Xe dissolved in cryptophane-A. Sensitive ^{129}Xe chemical shift allows resolution of free xenon dissolved in solution, xenon bound in the cryptophane cage, and gaseous xenon above the aqueous sample.¹⁵⁴

For a truly functionalized biosensor, the cryptophane cage should be augmented with a linker chain; at the end of the linker is a ligand that specifically binds to a target (such as a particular protein).¹⁷¹ The sensitive chemical shift of ^{129}Xe allows for easy discrimination of xenon in different chemical environments; indeed, the ^{129}Xe chemical shift is able to differentiate between free ^{129}Xe in solution and ^{129}Xe bound to a functionalized cryptophane cage that is bound

(versus not bound) to its target. This biosensor has already been shown to work in a model system using a biotin-functionalized cryptophane biosensor (with HP ^{129}Xe inside the cage) binding to the protein avidin.¹⁷² This effect can be further expanded by placing several different chemical sensing ligands onto the cryptophane cages, thus allowing for the simultaneous detection of various chemical moieties; the slightest modification to the biosensor is projected through the exquisite chemical shift of the HP ^{129}Xe .¹⁵⁶

To further increase the usefulness of HP ^{129}Xe biosensors, additional methods have been enacted to further allow the differentiation of the biosensor in its bound versus unbound states (relative to its target). One of these methods is known as hyperpolarized chemical exchange saturation transfer, or 'HYPER-CEST'.³ Using this method, the binding of the xenon biosensor to its target is detected indirectly. Using the sensitivity of the ^{129}Xe chemical shift, the resonance frequency of HP ^{129}Xe inside a biosensor that is bound to its target is specifically saturated, thus depleting the hyperpolarized signal; as the 'old' xenon moves out of the cage, 'fresh' HP ^{129}Xe moves in, and is subsequently depleted as well. The NMR detection frequency is set to that of ^{129}Xe free in solution; as *this* signal becomes attenuated, the prevalence of biosensors that are bound to their targets can be monitored. If one knows what the HP ^{129}Xe T_1 is in that specific solution, the concentrations of xenon and biosensor, as well as the residence time of the xenon in the cage, it is possible to back-calculate the concentration of the target species. In the future, the HYPER-CEST method may

produce an enhanced method of detecting particular biomolecules *in vivo* using HP ^{129}Xe -functionalized biosensors.

5.6 DIFFUSION IN POROUS MEDIA/SURFACE STUDIES

The physical properties of porous materials can depend on overall porosity, as well as the size distribution and connectivity of the pores. This makes the nondestructive characterization of porous species experimentally challenging, especially when the system is optically opaque. ^{129}Xe is an inert gas, and is able to provide contrast for material inhomogeneity and morphology in a nondestructive manner.¹⁹ The main drawbacks of ^{129}Xe imaging via thermally polarized xenon (low density & low nuclear spin polarization) are mitigated by using hyperpolarized ^{129}Xe ; the high spin polarization is able to overcome the small number of nuclear spins that penetrate into the porous material.¹⁷³

The increased detection sensitivity of HP ^{129}Xe allows for a variety of materials studies, such as gas diffusion and flow through porous media and the imaging of macroscopic void spaces in materials. Many of these studies are aided in the use of a continuous flow SEOP apparatus, so that a constant stream of freshly-polarized ^{129}Xe is introduced into the system. Indeed, a continuous flow of HP ^{129}Xe has allowed for chemical shift imaging (CSI) of zeolites; this CSI serves as an extra source of contrast imaging, in addition to nuclear spin density and T_2^* contrasts.¹⁷⁴ Polarization-weighted images can be used to ‘visualize’ the transport of HP gases through porous media, allowing for the study of flow profiles and diffusion coefficients.¹⁷⁵ HP ^{129}Xe has even been used in MR studies

to probe multiwall carbon nanotubes; xenon is able to penetrate to the interior of the nanotube, and the chemical exchange of xenon in and out of the tubes has been shown to be temperature dependent.¹⁷⁶

Applications of HP ^{129}Xe MR imaging and spectroscopy of material surfaces include changes to the chemical shift and lineshape of HP ^{129}Xe frozen in thin films ($\sim 1\ \mu\text{m}$ thick) on the surfaces of sample containers with different geometries (i.e., spherical, cylindrical, etc.). The container geometry affects the ^{129}Xe due to the bulk diamagnetic susceptibility of solid xenon, while the chemical shift appears to be temperature-dependent.¹⁷³ This line of work was later taken a step further, by transferring the high nuclear spin polarization of HP ^{129}Xe to the ^1H and ^{13}C spins on the surface of high surface area solids through a dipole-dipole cross-relaxation between surface spins and HP ^{129}Xe atoms adsorbed to the surface.¹⁷⁷ Polarization transfer between HP ^{129}Xe and surface nuclei can also be mediated by SPINOE, resulting in 'surface-enhanced' NMR spectroscopy of surfaces.¹⁴⁶ Preliminary studies of the dipole-dipole interaction between HP ^{129}Xe and solid, lyophilized proteins has shown changes to the ^{129}Xe chemical shift and lineshape depending on the type of protein and temperature.¹⁷⁸

5.7 LOW FIELD & REMOTE DETECTION TECHNIQUES

The low nuclear spin polarization of thermally-polarized NMR samples necessitates the use of strong magnetic fields in order to detect the resulting weak signals. However, high field magnets come with a number of logistical

drawbacks; among them are the high prices to manufacture, house, upkeep, and fill with cryogenics on a regular basis, time and additional resources required for cryogen fillings, and the inherent physical dangers of strong magnetic fields. Additionally, high-field magnets are highly immobile and impractical for field use.

The added detection sensitivity of hyperpolarized noble gases has helped to facilitate magnetic resonance studies at lower magnetic fields¹⁷⁹, as the non-equilibrium spin polarization is not dependent on the strength of the applied magnetic field. Indeed, if high-resolution MR spectroscopy and imaging can be accomplished at a fraction of the magnetic fields currently used today (such that superconducting magnets are no longer necessary), the price and portability of MR systems will become much more favorable and will likely result in a dramatic increase in general applicability.³ HP ^{129}Xe has already been shown as a viable means to study systems at low magnetic fields, including ^{129}Xe detected with an atomic magnetometer.¹⁸⁰ Of course, the ultimate goal would be to use the Earth's magnetic field as a source of B_0 . The obvious benefits of an Earth's field MR system include price (B_0 is free), availability (everywhere), high levels of homogeneity, and lower precession frequency (less energy to needed perturb spins).¹⁸¹

Conventional MR methods dictate that the encoding (or, rf pulse) and detection steps must take place in the same rf coil. The optimization of the system as a whole is a compromise, where neither step is truly optimal. Using remote detection (RD), the two steps are spatially separated and optimized individually.¹⁸² RD NMR is specifically well-suited for flow studies, where the

whole sample is encoded using a large coil, then the flowing species is physically concentrated and detected using a smaller coil, thus optimizing the filling factor (or, volume of sample versus volume of detection coil) and increasing detection sensitivity. Remote detection of HP ^{129}Xe flow studies in porous media^{183,184}, microfluidics^{185,186}, aerogels¹⁸⁷, and variously shaped phantoms¹⁸² have been quite useful in advancing this emerging technology.

The combination of remote detection of nuclear spins and low B_0 spectroscopy will hopefully lead the field of magnetic resonance in a new direction, away from superconducting magnets. This potential paradigm shift may be mediated by the use of HP ^{129}Xe as a flow species that has a high nuclear spin polarization, relatively long relaxation times, and can differentiate its environment through changes to its chemical shift. Useful time-of-flight (TOF) information can also be gained from these remote-detection experiments.¹⁸³

5.8 VOID-SPACE & TISSUE IMAGING

HP ^{129}Xe has great potential to increase sensitivity and contrast for many *in vivo* magnetic resonance studies. Of particular interest are the advantages in void-space imaging (such as lungs); traditional MRI methods have difficulty imaging the lungs, due to the very low concentration of ^1H present in the gas phase. The increased nuclear spin polarization of HP ^{129}Xe compensates for the lower spin-density in the gaseous phase. HP ^{129}Xe lung MRIs have been used to study air passageways (and blockages) in lung branching¹⁹, as well as lung surface areas¹⁸⁸ and the exchange of xenon between void space and lung

tissue.¹⁸⁹ Inhalation of HP ^{129}Xe can vastly increase contrast in lung imaging, helping in the study of emphysema, asthma, chronic obstructive pulmonary disease, and lung cancer.¹⁹

Human lung MRI experiments work in the following way: immediately following inhalation of a 'breathing mixture' (typically ~70% hyperpolarized xenon and ~30% oxygen)¹⁸⁸, the patient holds their breath during the signal acquisition. Alternatively, if a continuous flow of breathing mixture is being supplied, the spectrometer can be gated to synchronize the acquisition to the breathing cycle.¹⁹ Inhalation of HP ^{129}Xe has also allowed imaging of the oral cavity¹⁹⁰, nasal cavity¹⁹¹, and paranasal sinuses.¹⁹²

In addition to void-space imaging, HP ^{129}Xe dissolved in blood and tissues¹⁹³ may potentially serve as an important source of contrast for *in vivo* MR studies. Valuable information can be attained from localized ^{129}Xe NMR spectroscopy, chemical shift imaging, chemical-exchange spectroscopy, and blood perfusion studies in the human body.¹⁹ Indeed, xenon dissolved in blood provides two resonance peaks, one each for xenon in red blood cells and in plasma.¹⁹⁴ For blood studies, the HP ^{129}Xe can be pre-dissolved in a saline solution, then injected into the blood sample; the HP ^{129}Xe T_1 is roughly 5 seconds when dissolved in blood.¹⁹⁴ The chemical shift of HP ^{129}Xe has been found to be sensitive to blood oxygenation levels, and may potentially be used in the identification of tumors by their large variations in local oxygenation levels.¹⁹

During the course of void-space lung imaging, additional resonance frequencies were found, and later assigned to xenon dissolved in lung tissue.¹⁹⁵

Recent studies have measured the gas-exchange rate of xenon between the alveolar and capillary red blood cells; this gas exchange across the thin tissue barrier is the fundamental function of the lung¹⁸⁹, and its characterization can lead to a greater understanding of the various diseases of the lungs. The solubility of xenon in tissue can vary by over an order of magnitude from aqueous to lipid-rich environments—this is a potential source of novel contrast, as ¹H concentrations vary little throughout the body.¹⁹ Brain imaging via HP ¹²⁹Xe has also been pursued; some benefits include increased contrast, oxygenation-level sensing, and blood-perfusion and solubility studies.^{142,196}

CHAPTER 6

RESEARCH OUTLINE

6.1 INTRODUCTION

This chapter will provide an overview of my dissertation research that is presented in Chapters 7-11 in this work. More specifically, this chapter will attempt to set up the evolution of the presented research, and how these studies relate to the long-term goals of the Goodson laboratory.

6.2 GOALS AND INITIATIVES OF THIS DISSERTATION RESEARCH

The principal goals of the Goodson laboratory have been to ‘amplify’ the NMR signatures of weak interactions between molecules of interest (such as cryptophane and zinc myoglobin) and corresponding ligands (primarily ^{129}Xe) aligned in liquid-crystalline media. The objective is to combine the optical enhancement of xenon nuclear spin polarization and the restoration of ‘host-ligand’ dipolar couplings (using liquid crystals) to allow a portion of the high magnetization of the hyperpolarized xenon to be transferred to the molecule of interest (thus ‘amplifying’ its NMR signature). My initial goal in this research plan was to provide an adequate amount of highly polarized xenon to ensure the feasibility of the NMR experiments of interest and to assist in the MR application studies (primarily of xenon binding to zinc myoglobin); during the course of this work, a significant portion of the research branched into a study of the

fundamental aspects of spin-exchange optical pumping using frequency-narrowed light sources under a variety of experimental parameters.

6.3 PRIMARY RESEARCH OF THIS DISSERTATION

One can divide the optical pumping community (or more specifically, the research initiatives of the various OP groups) into three main branches: those who study SEOP towards the goal of understanding the fundamental physics of the system, those who study SEOP to try to find ways to improve it through the development of new approaches and technologies, and those who use SEOP only to produce hyperpolarized noble gases for a variety of magnetic resonance applications. My research time in the Goodson laboratory has covered all three facets of optical pumping: studies of fundamental SEOP parameters, optimizing the SEOP apparatus to achieve very high xenon nuclear spin polarizations at high xenon densities (using frequency-narrowed laser sources and *in situ* polarimetry), and then using that high level of magnetization for MR application studies (i.e., characterization of xenon in bicelles¹⁹⁷, proteins¹⁹⁸, and inclusion complexes; polarization transfer techniques such as SPINOE¹⁵⁴, etc.).

My time in the Goodson laboratory began with assisting in the final stages of constructing the SEOP apparatus, as well as developing the experimental protocol used for P_{Xe} production (Chapter 7). The introduction of frequency-narrowed light sources is discussed in Chapter 8, along with the observation of an unexpected dependence of P_{Xe} on the in-cell xenon density. Chapter 9 details an anomalous interdependence between the optimal cell temperature for

achieving peak P_{Xe} values and the in-cell xenon density (found using *in situ* low-field NMR polarimetry); studies of P_{Xe} buildup curves indicate that this temperature dependence is not due to changes to the HP ^{129}Xe relaxation rate, but rather should be attributed to some other aspect of the optical pumping process (such as alkali-metal polarization or spin-exchange rate). Chapter 10 details our use of high-power VHG-LDAs that are spectrally tunable (independent of laser power); this new laser technology allows the observation of changes to the Rb D_1 lineshape and spectral offset under conditions of high in-cell xenon density. P_{Xe} dynamics studies also show unexplained changes to the Rb- ^{129}Xe spin-exchange efficiency as a function of excitation wavelength. Finally, Chapter 11 introduces our preliminary results using cesium (instead of rubidium) as the alkali-metal for SEOP; Cs OP demonstrates (at both high and low magnetic fields) the capacity to surpass Rb OP, especially under conditions of high $[\text{Xe}]_{\text{cell}}$.

6.4 SIGNIFICANCE OF THIS DISSERTATION RESEARCH

Although the field of SEOP has been widely studied throughout the years⁵⁴, the results presented in this dissertation highlight the use of high power VHG-LDAs, a laser technology that has not been commonly used for SEOP until very recently.¹²⁹ As such, the work presented here represents one of the few comprehensive studies of SEOP using VHG-LDAs and high $[\text{Xe}]_{\text{cell}}$'s, and serves as a platform to further build on. Many of the results detail unexpected dependencies of the xenon density on a collection of experimental parameters,

such as T_{cell} , laser flux, spectral offset, etc., which are not commonly found in the literature. Also, the preliminary studies of Cs/ ^{129}Xe SEOP represent the only time that the predicted superiority of Cs over Rb has actually been demonstrated in an even comparison at elevated laser fluxes and high $[\text{Xe}]_{\text{cell}}$.

The resulting work in this dissertation is immediately relevant to the goals of the Goodson laboratory by demonstrating the ability to produce high quantities of highly spin-polarized xenon using batch-mode SEOP. This has allowed NMR studies that characterize the dissolution of xenon in a variety of molecules of interest^{197,199}; it has also facilitated our attempts at polarization transfer techniques, such as SPINOE.¹⁵⁴ Indeed, the results presented in this dissertation have even sparked an acute interest in developing a batch-mode SEOP apparatus that would be used for human lung imaging (amongst other applications); unlike the presently used continuous-flow polarizers, this apparatus would polarize single batches of high-density xenon to a sufficient extent ($\geq 20\%$) to enable lung imaging. This modular technique would be simpler and much cheaper than current flow-through polarizers, and may provide academics with a viable alternative to expensive continuous-flow set-ups, without having to make their own SEOP apparatus from scratch.

Having improved xenon nuclear spin polarization methodologies should benefit the development of xenon-functionalized molecular biosensors¹⁷², low- (or, possibly Earth's-) field MR spectroscopy and imaging¹⁷⁹, remote detection of polarized spins¹⁸², *in-vivo* void-space and tissue imaging¹⁸⁸, and a number of other MR applications that will benefit from larger quantities of highly spin-

polarized xenon.¹⁹ Indeed, large amounts of HP ^{129}Xe can improve existing NMR/MRI applications, as well as enable new studies that may not be otherwise possible.

CHAPTER 7

SEOP APPARATUS DESCRIPTION AND BASIC EXPERIMENTAL PARAMETERS

7.1 INTRODUCTION

The purpose of this chapter is to detail the particulars of the specific SEOP apparatus used for the experiments described in this dissertation. As noted in Chapter 3, there are many different types of SEOP apparatuses, and for each type, numerous variations are possible. This chapter will describe the SEOP apparatus as it was initially constructed; any additional instrumentations or techniques (i.e., low-field NMR polarimeter, various laser sources, retro-reflection, etc.) will be discussed in the flow of the text during subsequent chapters. Also addressed in this chapter are a ‘run-through’ of a typical SEOP experiment and the method used to determine the polarization level of the optically-pumped xenon.

7.2 SEOP APPARATUS & EXPERIMENTAL PROCESSION

The optical pumping apparatus used for the experiments that are detailed in this dissertation includes aspects of different literature designs^{57,58,81,106,200}; the apparatus⁶⁴ (Fig 7.1) is modular and relatively inexpensive, and can be operated in either batch¹⁰⁵ or “stopped-flow”^{58,106} modes.

The SEOP apparatus is centered around a (Rosen-designed⁵⁸) Pyrex optical pumping cell; this 'cell within a cell' construction consists of a ~75 cc inner cell (which contains the gas mixture) surrounded by an outer jacketing cell (through which hot air is blown, allowing it to function as the oven). The inner cell has two valves (an 'inlet' for gas loading and an 'outlet' for evacuation) that are controlled by Teflon stopcocks with viton o-rings (alternatively, glass stopcocks can also be used). Initially, the OP cell is cleaned through an overnight submersion in a base bath (saturated KOH solution), followed by distilled water

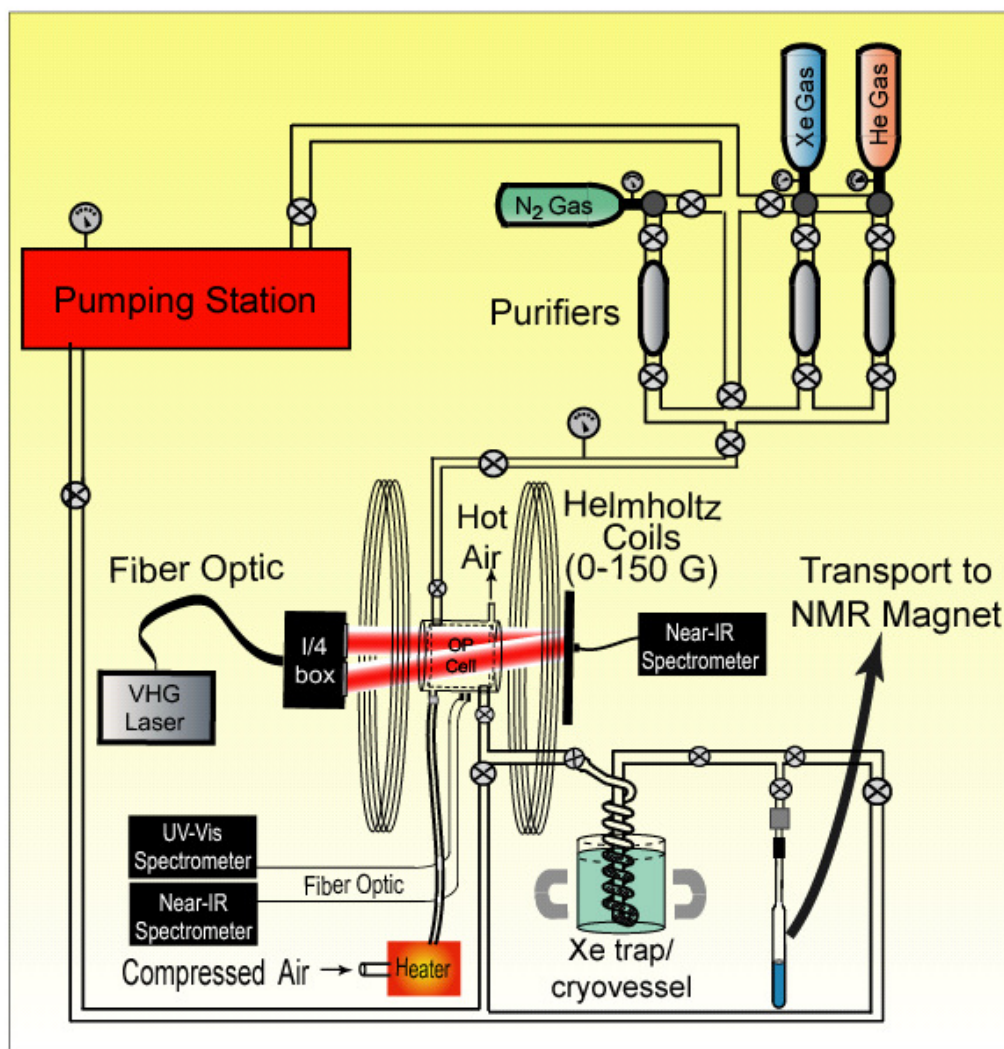


Fig. 7.1. SEOP apparatus schematic.⁶⁴

and methanol rinses, ~30-45 minutes of sonication in a methanol bath, and a final methanol rinse.

After allowing to dry, the inside surfaces of the inner cell are coated with a ~1:5 solution of Surfacil (Pierce) and hexanes; typically, 2 or 3 coating cycles (wash with pure hexanes—coat with Surfacil/hexane solution—wash again) are completed. After a final methanol rinse, the cell is allowed to dry overnight. This cleaning procedure is only done after reacting away the 'old' alkali metal (in *tert*-butanol, with a small amount of added methanol) and before loading with fresh alkali metal.

After evacuating the cell, the alkali metal is loaded in an inert-atmosphere (N_2) glovebox using a pipetting method, where the alkali metal is liquefied (through heating) and a small amount (~0.2 g) is pipetted into the OP cell (and then quickly re-solidifies). Alkali-metal loadings are only performed as needed; a 'good' loading may last for over six months (depending on the rate of introduction of impurities to the system, typically through loading the gas mixture into the cell). The OP cell is then placed in its holders and attached to the vacuum/gas handling manifold, and then evacuated ($\sim 8 \times 10^{-6}$ torr) with a diffusion pump. The alkali metal is distributed via cycles of heating, cooling, and evacuation (as dissolved gases, mostly nitrogen, will slowly outgas from the alkali metal). The alkali metal is eventually coated as a thin film throughout the inner cell (through differential heating of the front and back of the cell); a mostly complete and homogenous coverage is preferred (while keeping the optical windows free of alkali metal). Finally, the cell is aligned to the laser beam (which itself is aligned

to the central axis of the Helmholtz coil pair). The majority of the experiments used a circular polarizer (CP) box (Coherent) with two beams; the cell is aligned to the 'on-axis' beam.

The OP cell resides inside of a Helmholtz coil (HC) pair (22" inner diameter; Walker Magnetics), with a typical applied magnetic field of ~32 gauss. High purity xenon (natural abundance) and nitrogen are loaded through a (home-made) stainless steel gas handling manifold; the gases pass through oxygen scrubbers (LabClear) prior to entering the cell. The xenon/nitrogen ratio can be easily varied (the 'lower-density' gas is loaded first, with the 'higher-density' gas backloaded on top of the existing gas); most typical loadings total ~2000 torr of overall gas pressure inside the OP cell. Nominally, the ratio is 300 torr Xe and 1700 torr N₂; the nitrogen is added to quench Rb fluorescence⁶⁴ and pressure-broaden the alkali metal absorption line.⁵⁰ Helium can be used as a second buffer gas (many groups use only a small amount of N₂ and mostly He)⁵⁷; however, we have experienced great difficulties in using helium as a buffer gas. This problem is most likely due to contamination from poor quality He cylinders; with the exception of a few specific runs, most of the results presented in the subsequent chapters used binary Xe/N₂ gas loading mixtures.

A number of laser sources were used during the course of this work, and will be explained in greater detail throughout the following chapters. Briefly, a laser diode array, which is controlled by a power supply unit (where changing the driving amperage changes the laser output) and cooled by either a thermoelectric cooling plate (which can be controlled electronically) or a water-

chiller plate (controlled by changing the temperature of a recirculating water chiller) is used for SEOP. The laser fiber-couples (typically through a 1 m fiber; ranged from 30 cm to ~2 m) into a circular polarizer optics box (Fig 7.2), which typically consists of a collimator, prism, and quarter-wave optics.

The laser output is generally a mixture of two different light polarizations (whose propagation planes are perpendicular to each other); the prism separates the two polarizations into two separate beams (one 'straight', one 'skew'). While often in equal ratios, it was found that by gently manipulating the fiber optic (by stretching and/or bending), the ratio could be improved to as much as 85/15 (in favor of the 'straight' beam). The skew beam is angled by $\sim 10^\circ$ off-axis, and is both more difficult to align and may not be as efficient at optical pumping (due to its off-axis incidence on the cell). Once separated, each beam passes through its own quarter-wave plate (thus circularly-polarizing the light) and is directed at the OP cell (positioned ~ 30 inches away).

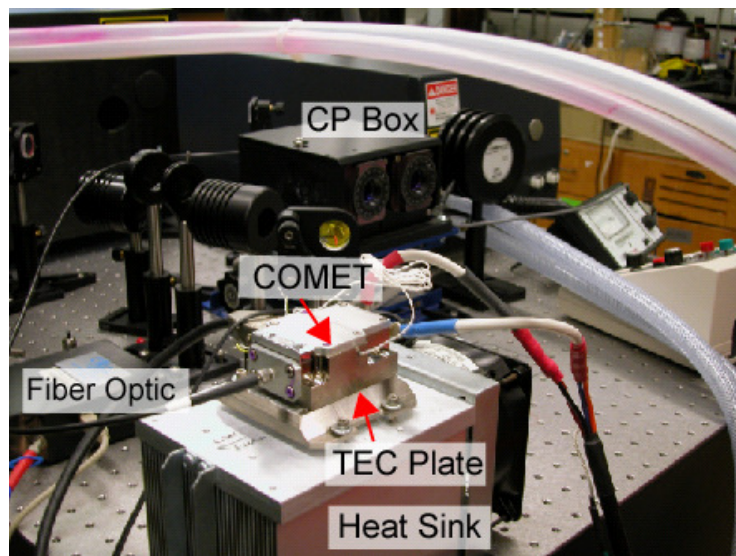


Fig. 7.2. Laser arrangement. VHG-LDA (Comet) sits atop TEC plate and heat sink, and fiber-couples into CP box.¹¹¹

Once the laser has been turned on to its operational settings, the spectral profile can be monitored by a small IR spectrometer (Ocean Optics HR2000+) that is fiber-coupled to a small pinhole drilled in the backstop directly behind the OP cell. The laser output can be measured by optical power meters; typically, the output from the CP box is measured (one beam at a time) to determine if the laser is performing as it should. Alternatively, the output from the bare fiber can also be measured (as laser power losses due to the optical fiber and CP box total ~15%). Beam alignment can be monitored with an IR-viewing scope or IR-active card (only at low laser powers); it is imperative to wear proper eye safety goggles at all times and keep objects out of the beam path.

Compressed air is forced through a small, home-made furnace (heating wire wrap inside of a thick glass cylinder, controlled by changing the output on a Variac), then into the outer jacket of the OP cell; this serves to vaporize the alkali metal. The cell exhaust temperature is measured with a digital thermometer; alternatively, a small thermocouple can be placed on the outer glass surface of the inner cell (the difference between these two methods is ~14 °C for our arrangement). The temperature of the cell is mostly controlled by changing the output of the Variac; however, large amounts of laser power can also have a strong effect on the cell temperature. Once the cell has reached its operational temperature (~60-120 °C), optical pumping is allowed to progress for ~5-20 minutes. Following this time period, the Variac is turned off and the cell is allowed to cool (~5 min); alternatively, some additional protocol for cooling the cell more quickly can also be implemented (to combat *in-cell* HP $^{129}\text{Xe } T_1$).

Once the cell has cooled (to ~ 30 °C), the contents are collected by one of two methods. In the first method, the contents are simply expanded into a pre-evacuated volume, and further expanded into a stopcocked NMR tube (also pre-evacuated and coated with Surfamil). Alternatively, the contents can be pumped through a glass spiral condenser coil (Fig 7.3) that is submerged in liquid N_2 , allowing the xenon to be captured and the buffer gas to be pumped away. The high polarization of the frozen xenon is maintained^{143,200} by a pair of ~ 1 T, 4"x4"x1" rare-earth magnets (Indigo Instruments) that produce a magnetic field of ≥ 1500 G throughout the storage region. Virtually all ($\pm 5\%$) of the xenon is captured by the condenser; similarly, the strong field¹⁴³, combined with the avoidance of "warm solid xenon" (^{129}Xe T_1 is ≤ 10 s near the triple point)²⁰⁰, minimizes polarization losses during freezing/sublimation to about 20-25%. For

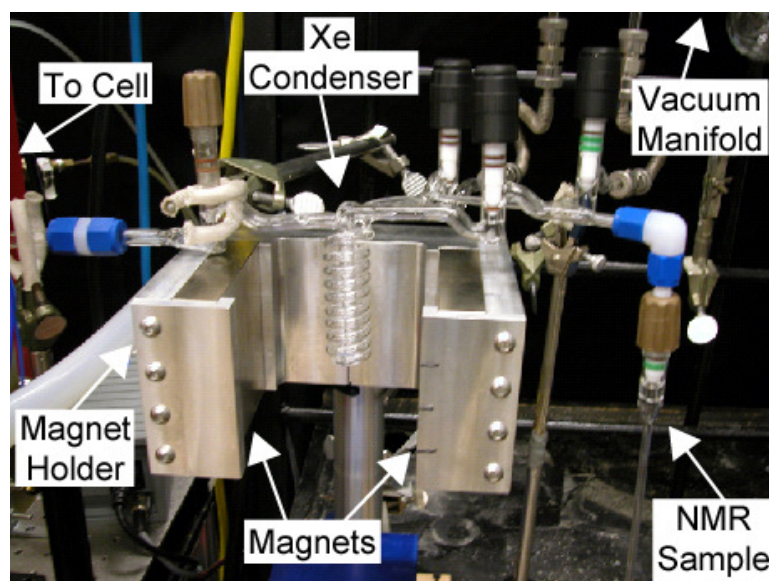


Fig. 7.3. Condenser coil for xenon freeze-out; coil sits between two large permanent magnets held in an aluminum holder. Magnetic field in storage region >1500 G.⁶⁴

use in 'stop-flow' mode, the liquid nitrogen dewar is incrementally raised up the length of the condenser coil as additional SEOP runs (and additional HP ^{129}Xe collections) are performed; in practice, we have cumulatively frozen a total of three batches before transferring to an NMR sample. The solid xenon is quickly sublimated by rapid immersion in warm water; the gaseous xenon can then be expanded into a stopcocked NMR tube and transferred to the high-field magnet. The efficient design allows for the cost-effective use of isotopically enriched ^{129}Xe , and multiple OP cycles can be used to prepare larger HP ^{129}Xe quantities.⁵⁸

7.3 CALCULATION OF XENON POLARIZATION

In order to determine if the SEOP run can be deemed successful (i.e., sufficient P_{Xe} is collected to allow for a particular MR application to be attempted), the absolute ^{129}Xe nuclear spin polarization must first be determined. High-field ^{129}Xe NMR spectra were recorded at 9.4 T (110.6 MHz) using a Varian Inova spectrometer. Hyperpolarized ^{129}Xe spectra were obtained with a single 1 μs *rf* pulse ($\alpha \approx 6.7^\circ$); corresponding thermally polarized ^{129}Xe signals were obtained from the same sample following careful addition of sufficient O_2 gas to reduce the ^{129}Xe T_1 (to a few seconds) to permit efficient signal averaging ($\alpha = 90^\circ$; typical recycle delay = 20 s). The number of scans required for a thermal acquisition varied with xenon density (higher xenon density \rightarrow fewer scans needed); under nominal conditions (300 torr Xe loaded into OP cell), about 2000 scans are acquired (requiring ~ 11.5 hours of spectrometer time).

The resulting ^{129}Xe NMR spectra were analyzed using Mestre-C, a common NMR processing software. The NMR peaks were integrated (with the integration area chosen manually); a total of five separate integrations per peak were averaged together to achieve the final peak integral value (standard deviation of each set of five measurements was used as the error). The P_{Xe} signal enhancement is calculated using the following equation:

$$P_{\text{Xe}}(\text{enhancement}) = \left\{ \frac{I_{\text{HP}}}{I_{\text{TH}}} \cdot \left(\frac{\sin \alpha_{\text{TH}}}{\sin \alpha_{\text{HP}}} \right) \cdot \left(\frac{N_{\text{TH}}}{N_{\text{HP}}} \right) \right\}, \quad (7.1)$$

where I_{HP} and I_{TH} are the integrals of the hyperpolarized and thermal NMR peaks, respectively, α is the tipping angle of the rf detection pulses, and N is the number of scans (N_{HP} is typically 1); it is generally assumed that all other experimental parameters (e.g., gain) are kept constant between the HP and thermal experiments.

Once the P_{Xe} enhancement level is calculated (generally between a few thousand and tens of thousands), the absolute xenon nuclear spin polarization can be determined by multiplying the nuclear spin polarization at thermal equilibrium (i.e., Eq. 1.4) with the determined P_{Xe} enhancement (Eq. 7.1); under our conditions, this turns out to be $\sim 9.02 \times 10^{-6}$ multiplied by the P_{Xe} enhancement value. P_{Xe} values generally ranged from a few percent to several tens of percent. Figure 7.4 demonstrates a typical comparison of a HP ^{129}Xe peak (single scan; small tipping angle pulse) with a thermal ^{129}Xe experiment (2000 scans averaged; 90° pulses), corresponding to a P_{Xe} enhancement of $\sim 19,000$.

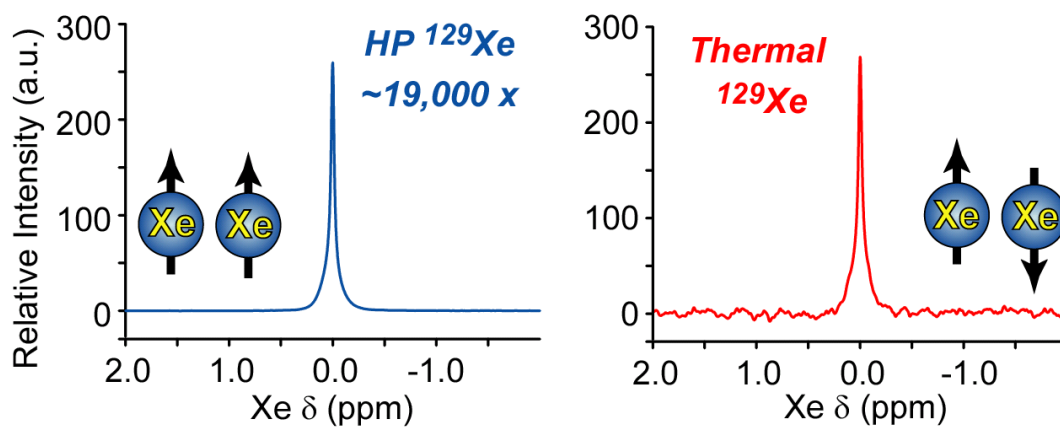


Fig. 7.4. Normalized NMR signal at 9.4 T (110.6 MHz) from ~ 600 torr HP xenon (*left*, 1 scan; $\alpha=6.7^\circ$) & corresponding thermal data (*right*, 2000 scans averaged; $\alpha=90^\circ$), taken after careful O_2 addition.¹¹¹

CHAPTER 8

IMPLEMENTATION OF FREQUENCY-NARROWED VHGLDAS FOR RB/¹²⁹XE SEOP

8.1 INTRODUCTION

Spin-exchange optical pumping has been shown capable of generating high nuclear spin polarizations in noble gases⁵⁴ for a variety of NMR/MRI^{19,91} and fundamental physics⁹⁷ applications. While a number of different light sources^{19,54,57,58,65,81,91,97,106,107,118,201} have been used to prepare hyperpolarized ¹²⁹Xe (along with other noble gases) via SEOP, laser-diode arrays have become increasingly popular due to their high photon flux, low costs, and operational simplicity. However, one key drawback of conventional LDAs is the poor quality of the emitted light—particularly the breadth of their spectral output (~2-3 nm) compared to the relatively narrow atomic absorption lines. The resulting low absorption efficiency may necessitate high incident laser powers (up to hundreds of Watts), thus presenting thermal-management problems. Additionally, while this low absorption efficiency can be partially mitigated by collision-broadening of the alkali spectral line^{57,114}, this practice brings on its own complications. To combat these problems, two methods have been developed to further constrict the LDA wavelength range: external cavity narrowing^{120,127,128}, and more recently—volume holographic grating (VHG) narrowing.¹²⁹

The remainder of this chapter reports our preliminary investigations of the use of VHG-narrowed LDAs to prepare HP ¹²⁹Xe. It begins with implementing

and characterizing the output from the first VHG-LDA in our lab, while comparing it to the previous broadband LDA used for SEOP. The narrowed laser emission also allowed for *in situ* monitoring of the P_{Rb} levels during SEOP through changes to the transmitted laser intensity upon cycling the applied magnetic field. The chapter ends with the addition of a second, higher power VHG-LDA that was used to demonstrate an unexpected dependence of P_{Xe} on $[Xe]_{cell}$.

8.2 CHARACTERIZATION OF LASER OUTPUT^{14,59,111}

The first VHG-LDA used in the Goodson Lab will be referred to as the ‘Comet’; the Comet is a single-bar (SB) laser module that was an engineering prototype from Spectra-Physics/Newport. The Comet was mounted to the same TEC/heat sink that was occupied by our original (‘standard’) broadband laser (a 40 W Coherent FAP-B), was driven with the same 65 amp diode and thermoelectric cooling drivers (Newport), and fiber coupled into the same CP optics box. In order to focus the 19 frequency-locked laser elements into a single-core 200 μm silica-clad optical fiber, the Comet employs additional slow-axis collimation (SAC) and achromatic lenses after the VHG (1.5 mm thick).¹³¹

The Comet’s spectral profile is narrowed by nearly an order of magnitude (Fig. 8.1) compared to that of the standard LDA, while providing nearly the same incident laser power (the Comet yields a lower watt-to-amp ratio than the standard LDA, but can be driven to higher currents). This increase in resonant laser power dramatically increases the efficiency of the light absorption, as less laser flux is wasted due to being too far off-resonance to be absorbed. In

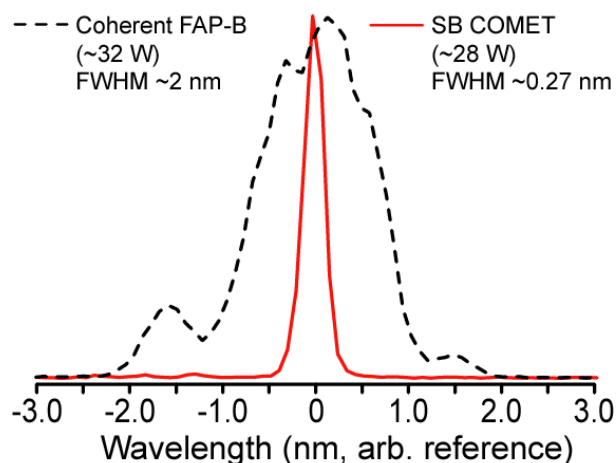


Fig. 8.1. Normalized spectral output of a standard fiber-coupled LDA (black, dashed) and (single-bar) VHG-narrowed Comet (red, solid).⁵⁹

addition to the increased line-narrowing, the Comet also benefits from a ‘clean’ spectral profile (Fig. 8.1).

The 1 m optical fibers used with both the Comet and the standard LDA maintain much of their original linear polarizations; this ‘memory’ of the LDAs’ polarizations affects the power ratio of the two side-by-side circularly-polarized beams emitted from the CP box—causing the ratio of the beam intensities to be sensitive to the strain on the fiber. For the standard LDA and the Comet, the nominal beam intensity ratios (straight vs. angled) emitted from the CP box were ~72:28 and ~80:20, respectively.

While spectral tuning of conventional LDAs may be achieved by varying the LDA temperature ($\sim 0.3 \text{ nm}/^\circ\text{C}$), tuning VHG-narrowed LDAs is a non-trivial function of LDA and VHG temperatures (as discussed in Sec. 4.3). For example, increased driving current for the Comet (Fig. 8.2) provides greater laser flux in addition to red-shifting of the centroid towards the Rb D_1 center ($\sim 0.02 \text{ nm}/\text{amp}$,

with operational range of ~ 0.3 nm); the spectral linewidth also broadens with increased driving current. Increases to the LDA temperature (at constant driving current) also result in red-shifting and line-broadening (*not shown*).

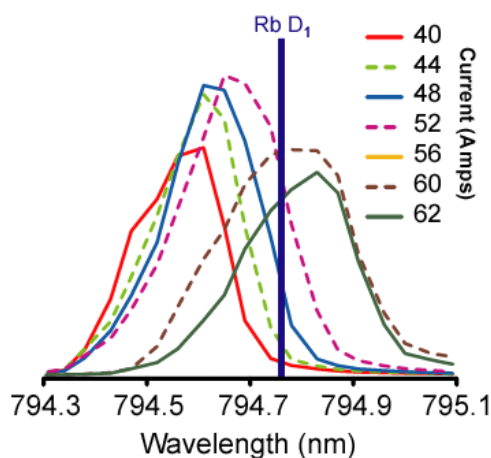


Fig. 8.2. Spectral output of the Comet as a function of laser diode driving current, showing the lineshape broadening and red-shifting ($\Delta\lambda \sim 0.3$ nm) of the centroid as the laser power increases. FWHM examples: at 40 A: ~ 0.24 nm; 52 A: ~ 0.27 nm; 62 A: ~ 0.33 nm. Rb D_1 at 794.76 nm (air referenced) is included for comparison.⁵⁹

When using the Comet for SEOP, the maximum P_{Xe} values are achieved with a driving current of 52 A—corresponding to an incident power, FWHM, and Rb D_1 offset of ~ 27 W, ~ 0.27 nm, and $\sim (-)0.1$ nm, respectively. The amount of pressure-broadening (Rb D_1 ~ 0.1 nm FWHM)¹¹⁴ present under these conditions appears sufficient for effective absorption of the frequency-narrowed light, as the laser profile is absorbed quasi-homogeneously by the Rb vapor despite the slight blue-shift of optimal laser conditions. This is opposed to conventional broadband LDAs, where the Rb absorption line is typically ‘hole-burned’ into the broad, uneven spectral profile—even under conditions of high pressure broadening and high Rb vapor densities. The optimal driving current for the Comet also provides

the highest peak intensity (watts versus spectral linewidth; Fig 8.2); however, it does not give the highest integrated power or the highest intensity at the Rb D₁. Indeed, higher driving currents yield increased laser flux, as well as red-shifting of the centroid toward the D₁ center—but result in reduced P_{Xe} values when closer to the true Rb D₁ resonance (it is generally expected that the highest P_{Xe} values are achieved when the laser is tuned exactly on resonance).

8.3 COMPARISON OF VHGLDA WITH PREVIOUS BROADBAND LDA^{59,64,111}

Upon switching from the standard LDA to the Comet, we observed a nearly three-fold (watt-for-watt) improvement in P_{Xe} (Fig. 8.3). The dependences of P_{Xe} on T_{cell} are similar for the two lasers (with and without VHG-narrowing), and the Comet peaked at a temperature ~10 °C lower than that of the standard LDA. The relatively mild optimal cell temperature, combined with the unexpected D₁ offset preference and the modest fraction of laser light absorbed during optimal conditions (less than half of incident light absorbed for optimal OP) are consistent with the OP being laser-power-limited—despite the high resonant laser power. Nevertheless, increasing the Comet's driving current to provide greater incident laser flux and improved D₁ resonance yielded markedly decreased P_{Xe} values across the entire temperature range (Fig. 8.3).

This seems to indicate that uniform cell illumination may be more important than total laser power for SEOP (at least under these conditions). In later experiments using the Comet, further OP optimization (i.e., improved cell preparation/laser alignment) provided routine P_{Xe} values of ~15-17% and ~21-

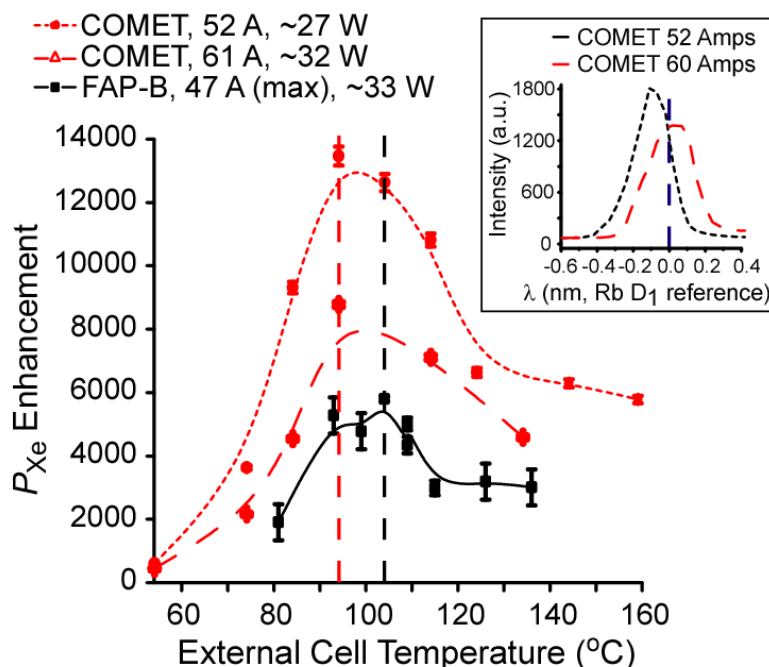


Fig. 8.3. P_{Xe} values obtained with Comet (52 A, ~27 W: dotted red circles; 61 A, ~32 W: dashed red triangles) and a standard LDA (47 A, ~33 W: solid black squares, from Ref.⁶⁴) as a function of T_{cell} (inner-cell surface temperature; $[Xe]_{cell}=300$ torr). T_{OPT} appears to be slightly lower for the Comet (vertical lines). The data's asymmetry about T_{OPT} is an artifact resulting from higher- T_{cell} OP runs transiting through more-optimal T_{cell} 's during cell cool-down. *Inset:* Comet's spectral output profiles at 52 A (black dotted) & 60 A (red dashed), indicating that the improved P_{Xe} observed in the main figure occurs when the laser is tuned slightly from the Rb D_1 line.⁵⁹

24% (with and without cryo-collection; $[Xe]_{cell}=300$ torr), consistent with ~75% of P_{Xe} surviving the cryo-collection and transfer processes⁶⁴.

8.4 MONITORING P_{Rb} IN SITU^{59,111}

The narrow, clean lineshape of the Comet allows small changes in the amount of laser light transmitted through the cell to be recorded when the external magnetic field (B_0) is cycled (Fig. 8.4a)—thereby potentially providing an *in situ* measurement of P_{Rb} . This effect is due to 'bleaching' of the Rb D_1 line from efficient depletion pumping of the ground-state magnetic sublevels; this

phenomenon has been previously measured using high-resolution lasers¹⁰⁶, but would be extremely difficult to monitor with conventional broadband LDAs (and, to our knowledge, has not been reported previously).

This observed effect arises from the following (Fig. 8.4*b*): the first step of the OP process—whereby the Rb electrons become spin-polarized—leaves a smaller concentration of Rb atoms in the laser-absorbing m_j state (neglecting Rb

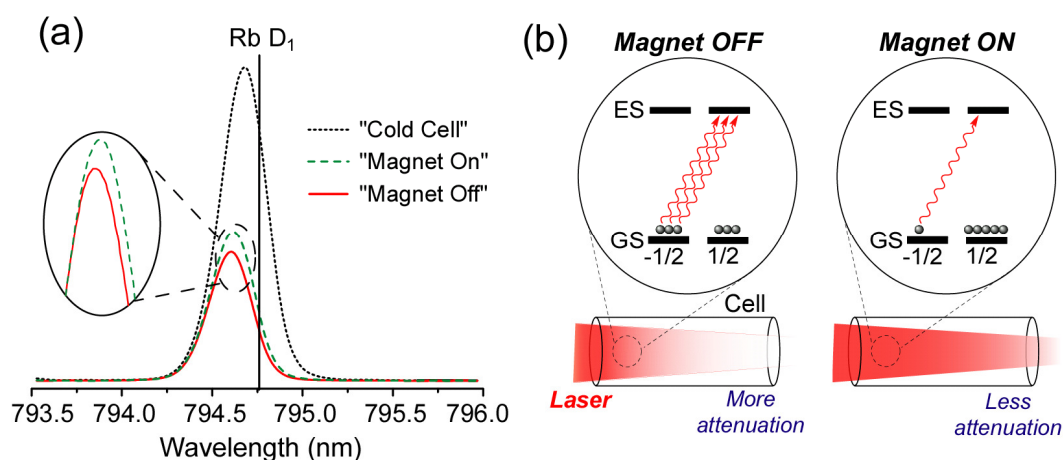


Fig. 8.4. (a) Near-IR spectra of Comet's output (mathematically smoothed for clarity) transmitted through the cell near optimal OP conditions (compared with that obtained with a cold cell; black dotted line), showing the effect of magnetic field cycling (with B_0 off: red solid line; with B_0 on: green dashed line). The integrated differences in the transmitted spectra generated with such field cycling were used to provide the estimates of $\langle P_{\text{Rb}} \rangle$.⁵⁹ (b) Schematic demonstrating 'bleaching' effect of transmitted laser beam at Rb D_1 line when external field (B_0) is cycled.¹¹¹

nuclear spin sublevels). In turn, this population reduction allows slightly more laser light to be transmitted through the cell (as there are less Rb atoms in the 'light absorbing' state) and allows P_{Rb} to be estimated from the difference in the transmitted laser spectra (compared to when B_0 is turned off). In the absence of B_0 , the m_j splitting is much smaller, leading to inefficient depletion pumping (and

more Rb atoms in the 'light-absorbing' state, thus the transmitted laser beam becomes more attenuated).

The spectral profile of the laser light transmitted through the cell was observed using a near-IR spectrometer via a pinhole (drilled into the optical backstop) behind the OP cell. Changes in these spectral profiles that are caused by cycling B_0 can be integrated to estimate the average Rb polarization along the central axis of the OP cell (or, $\langle P_{\text{Rb}} \rangle$) using a simplistic model. While previous works²⁰²⁻²⁰⁴ have studied the measurement of P_{Rb} via optical transmission methods, the experimental conditions for the work presented here are sufficiently different so as to warrant an alternate approach (and corresponding set of assumptions). Here we assume the following: a near absence of any significant population of electronically excited Rb*; $\approx 100\%$ circularly-polarized light; a constant total Rb number density across the OP cell (N_{T}); and that $P_{\text{Rb}} \approx 0$ when B_0 is turned off.⁵⁴

Adapted from Beer's Law;

$$A = -\ln T = -\ln\left(\frac{I_{\text{hot}}}{I_{\text{cold}}}\right), \quad (8.1)$$

where A is the absorbance, T is the transmittance, and I_{hot} & I_{cold} are the integrated intensities of the transmitted laser spectra obtained when a (relevant OP gas mixture-loaded) cell is respectively 'hot' and 'cold' (i.e., with and without Rb vapor present). Because only Rb atoms in one of the two ground-state magnetic sublevels can act as absorbers (say $m_J = +1/2$ with σ^- light), A is denoted by:

$$A = \sigma(\lambda)l\langle N^+ \rangle, \quad (8.2)$$

where $\sigma(\lambda)$ is the (wavelength-dependent) absorption cross-section for the Rb vapor, l is the path length of the cell, and $\langle N^+ \rangle$ is the number density of Rb atoms in the $m_j = +1/2$ spin state (averaged along the z-axis of the cell). Next,

$$\langle P_{Rb} \rangle = \frac{\langle N^+ \rangle - \langle N^- \rangle}{N_T}, \quad (8.3)$$

where $N_T = \langle N^+ \rangle + \langle N^- \rangle$. Since $\langle P_{Rb} \rangle \approx 0$ when $B_0 = 0$, $\langle N^+ \rangle$ under these conditions is given by: $\langle N^+ \rangle \approx 0.5 * N_T$. The terms $\sigma(\lambda)$ and l cancel when A is divided by A_0 (the absorbance when $B_0 = 0$) to give $(A/A_0) = 2\langle N^+ \rangle/N_T$. Eq. 8.3 can be rearranged and combined with the relationship for (A/A_0) to give:

$$|\langle P_{Rb} \rangle| = \frac{A}{A_0} - 1, \quad (8.4)$$

where the absolute value is required because the differential absorbance will be insensitive to the light helicity.

P_{Rb} at each position within the cell will quickly reach steady state (in a matter of milliseconds) with the resonant laser flux; because the illumination decreases not only along z (the long axis of the cell) but radially outward from this central axis as well, P_{Rb} will generally be a function of both z and r (or, $P_{Rb}(z,r)$). Because the transmitted light is sampled through a pinhole directly behind the cell, the values of P_{Rb} determined via this method are actually z -averaged measurements of P_{Rb} for $r \approx 0$; thus, this $\langle P_{Rb} \rangle$ value is expected to overestimate the 'global' P_{Rb} average (as P_{Rb} is expected to be highest along the cell's z -axis, falling off towards the cell's walls), especially under conditions of

highly non-uniform illumination (or, high absorbance conditions). Separately, this method would underestimate P_{Rb} if a (sufficiently strong) residual B_0 persisted when the HC pair was turned off.

Using this simplistic model, we were able to estimate $\langle P_{\text{Rb}} \rangle$ values during SEOP runs that varied the driving current (thus, spectral offset and laser power) of the Comet. Despite some run-to-run variability, these results (Fig. 8.5) may

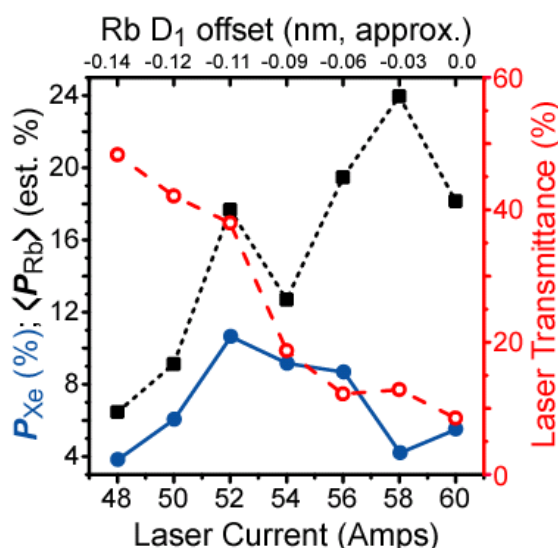


Fig. 8.5 P_{Xe} (blue circles), $\langle P_{\text{Rb}}(z) \rangle$ (black squares; estimated via changes in laser transmission during B_0 cycling) as functions of Comet driver current (& Rb D_1 offset), plotted against the laser transmittance at the cell's center (red open circles); the lines are to guide the eye.⁵⁹ Approximate D_1 offset values are at the top; $[\text{Xe}]_{\text{cell}} = 300$ torr, $T_{\text{cell}} = 100$ °C (the Rb D_1 linewidth and shifting should be ~ 0.1 nm and $\sim (+)0.04$ nm, respectively due to gas density/composition).¹¹⁴

help explain the observed dependence of P_{Xe} on the Rb D_1 offset. When the Comet is tuned far from D_1 (e.g., with an LDA current of ~ 48 -50 A), P_{Xe} tracks $\langle P_{\text{Rb}} \rangle$ and both are relatively low (while the laser transmittance is high). However, when the laser approaches resonance to the Rb D_1 (~ 58 -60 A), $\langle P_{\text{Rb}} \rangle$ along the cell's center axis is high, but global P_{Xe} is relatively low; here the low laser

transmittance at the cell's center directly implies even poorer illumination within a significant portion of the cell's rear and outer regions. Indeed, P_{Xe} is greatest with an intermediate D_1 offset where both $\langle P_{Rb} \rangle$ and the transmittance are still relatively high—consistent with optimal P_{Xe} requiring a balance between efficient laser absorption *and* global cell illumination sufficient to minimize xenon depolarization from 'dark' Rb in those regions.

8.5 DUAL-BAR VHGLDA CHARACTERISTICS ^{14,59}

To further study the effects of incident laser power and spectral offset on P_{Xe} , a second VHGNarrowed LDA was introduced. The 'Integra' is a dual-bar, turn-key laser system that was loaned to the Goodson lab from Spectra-Physics/Newport. The Integra combines two VHGLDA modules (each one similar to the Comet), but with simplified optical arrangements: Instead of using fast-axis and slow-axis collimating lenses (FAC & SAC, respectively; used to collimate the quickly diverging beam that is inherent to diode lasers), individual optical fibers (400 μm) are brought within ~ 600 μm of each laser element (giving 19 fibers per module). This close proximity ensures that each diverging fast-axis beam is launched into its fiber, but requires that each module's VHGL (placed between the LDA elements and the fibers) has to be thin (500 μm)—this results in somewhat reduced spectral narrowing and lineshape quality (Fig. 8.6). Obtaining the optimal spectral output from the Integra required overdriving the current ($\sim 104.6\%$), giving nearly twice the power of the Comet—albeit with nearly twice the spectral width. Also, due to the Integra's design, the best 'beam ratio'

achieved (regarding the CP box) was ~55:45, as fiber manipulation had minimal impact on polarization preservation.

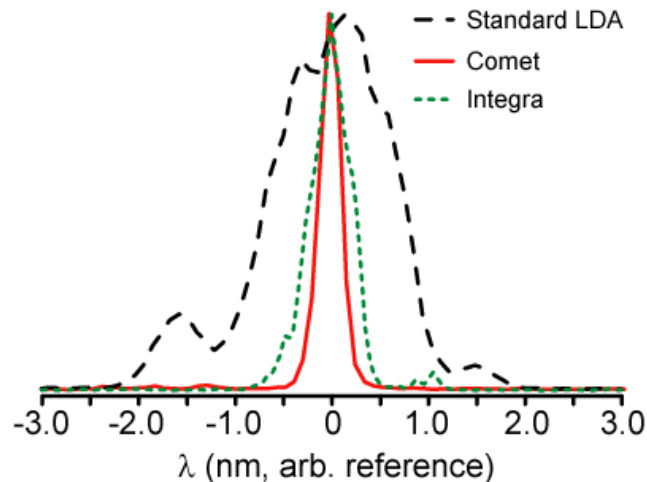


Fig. 8.6 Normalized output of a standard fiber-coupled LDA (*black, dashed*), Comet (*red, solid*), and Integra (*green, dotted*). Conditions: Standard LDA & Comet—same as Fig. 8.1. Integra: ~55 W (at 96 A), $\Delta\lambda_{FWHM}=0.49$ nm.⁵⁹

The output for the Integra red-shifts with increased current (similar to the Comet), but at a reduced rate (~0.006 nm/amp, as a consequence of its design differences). At 94 A (i.e., 47 A/diode, 100% current, 51.6 W at cell) the centroid is ~(-)0.18 nm from the Rb D₁ ('blue' side) with a diode temperature of 25 °C, and ~0.09 nm from D₁ at 35 °C (these are the nominal Integra laser conditions for OP results presented here). Generally the Integra's linewidth varies between ~0.4-0.6 nm FWHM. The Integra also suffered from some amount of spurious, 'unlocked' output at lower driving currents; Figure 8.7 demonstrates the (quite low) tunability of the Integra.

The very similar Rb D₁ offsets for the Comet and Integra under nominal conditions (~0.11 and ~0.09 nm, respectively) enabled their performance for SEOP to be compared. To allow a more direct comparison, the optical fiber for the Comet was carefully strained until the beam ratio exiting the CP box was reduced to that of the Integra. The HP ¹²⁹Xe NMR spectra obtained at 9.4 T indicated P_{Xe} enhancement factors of ~8,800 (P_{Xe} ~7.8%) and ~16,000 (P_{Xe} ~14.3%) for the Comet and Integra, respectively. Although the Comet has a narrower spectral output, this advantage translated into only a small W-for-W P_{Xe} benefit; thus at least under the given conditions, the Integra's output was sufficiently narrow to allow its higher total power to be exploited for improved HP ¹²⁹Xe production.

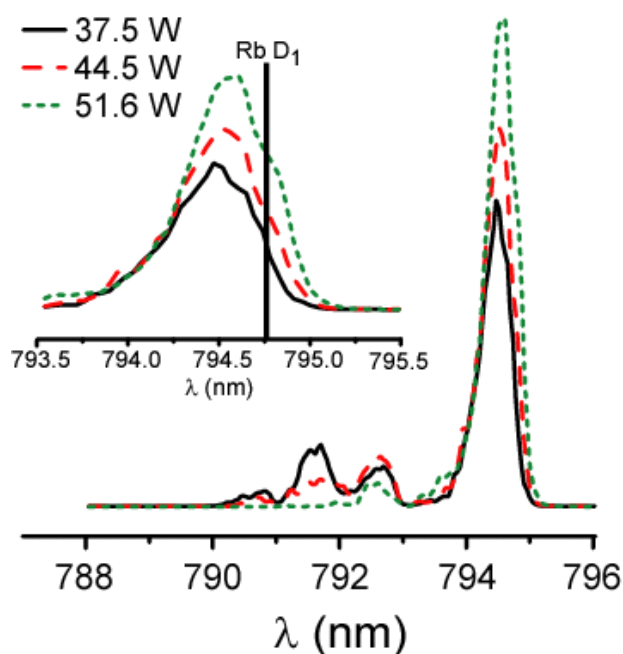


Fig. 8.7 Integra's spectral output as a function of driving current (37.5 W: *black*; 44.5 W: *red*; 51.6 W: *green*). Lineshape improves (and slightly red-shifts) with increased driving current. *Inset*: Close-up of Integra's laser output near the Rb D₁ line. Reduced lineshape quality, with the presence of additional features away from the main line, indicates incomplete VHG locking at low driving currents. Such features were not minimized until the Integra was over-driven at ~104.6% current (96 A, 54.5 W at cell; *not shown*).¹⁴

8.6 XENON DENSITY ANOMALY^{14,59}

P_{Xe} is generally expected^{58,63,66,106} to decrease smoothly and dramatically upon increased $[Xe]_{cell}$, as the xenon polarization becomes ‘capped’ by corresponding reductions in P_{Rb} levels (due to the strong contribution to the Rb spin-destruction rate from increased Rb/Xe collisions).^{53,54} Thus, the majority of SEOP setups typically employ relatively low running Xe partial pressures (~1-70 torr) in order to achieve high (>10%) P_{Xe} values; this potentially limits many applications that simultaneously require both high Xe densities/amounts *and* high P_{Xe} values.

The minimal change in spectral profile upon increasing the driving current of the Integra was exploited to examine the dependence of P_{Xe} on laser flux (without changing the spectral offset) at different Xe partial pressures. While the

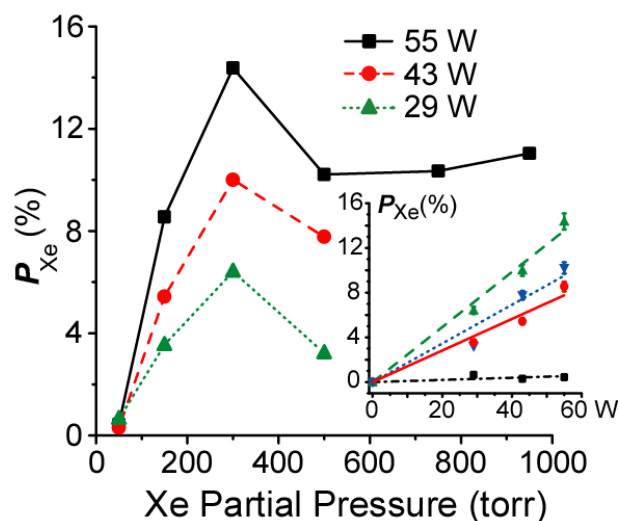


Fig. 8.8 P_{Xe} vs. $[Xe]_{cell}$ (variable Xe partial pressure; constant total cell pressure of 2000 torr, backfilled with N_2) at various Integra laser powers (55 W: *black squares*; 43 W: *red circles*; 29 W: *green triangles*). *Inset*: Same data, but with P_{Xe} plotted as a function of laser power for different Xe loadings; data points are fitted to lines (forced through zero). 50 torr: *black squares*; 150 torr: *red circles*; 300 torr: *green triangles*; 500 torr: *blue inverted triangles*.⁵⁹

experiment was (originally) geared to examining the dependence of P_{Xe} on laser flux, a more interesting dependence of P_{Xe} on $[Xe]_{cell}$ was observed. Initially, we expected to see the relationship described above: high P_{Xe} at low $[Xe]_{cell}$, dropping precipitously upon increased $[Xe]_{cell}$. Instead, we have reproducibly observed a quite different trend (Fig. 8.8), wherein P_{Xe} initially rises with increasing $[Xe]_{cell}$, peaks (at ~ 300 torr Xe), and then falls off but remains uncharacteristically high ($>10\%$)—even at ~ 1000 torr Xe—to give among the highest P_{Xe} values at such high $[Xe]_{cell}$ (as reported at the time).

A similar qualitative trend was also observed in an initial study using the Comet¹¹¹, and the effect does not appear to be an artifact of cell contamination or variances in the Xe collection efficiency (following OP). Additionally, laser energy-dependent mechanisms (such as those involving highly elevated internal temperatures of the N_2 buffer gas)¹¹² may affect the OP process, but do not appear to cause the observed dependence of $[Xe]_{cell}$ on P_{Xe} given that similar trend lines are observed at various incident laser powers. Indeed, the data shows the potential utility of additional laser flux, as P_{Xe} rises almost linearly with power (except at low $[Xe]_{cell}$ —Fig. 8.8 *inset*). While this dependence of P_{Xe} on $[Xe]_{cell}$ is contrary to what is typically expected, it can be utilized to provide large quantities of highly polarized ^{129}Xe using batch-mode SEOP; these large amounts of highly spin-polarized ^{129}Xe can be used for a variety of MR applications, including material surface studies and human lung imaging.

Separately, we observed (using the spectrally-narrowed output from the Comet) that it was also possible to utilize the violet emission ($6P \rightarrow 5S$) from Rb^* -

Rb* energy-pooling processes⁶⁴ as a sensitive *in situ* indicator of laser detuning from the Rb D₁ line (when observing the cell under conditions that are non-optimal for SEOP—i.e., low [N₂]_{cell} conditions). Somewhat surprisingly, the wavelengths and relative intensities of the Rb lines were more sensitive than expected¹¹⁴ to buffer gas composition—observations that will be further pursued and reported in greater detail elsewhere.

8.7 CONCLUSIONS

The work presented thus far has demonstrated the utility of high power, frequency-narrowed laser sources for fundamental SEOP studies, as well as for producing highly spin-polarized noble gases for NMR/MRI applications. A ~3-fold (watt-for-watt) increase in P_{Xe} was observed upon switching to the Comet from a conventional broadband LDA. Changes to the transmitted laser spectra upon B_0 cycling provided an *in situ* estimate of the rubidium electron spin polarization, which seemed to increase as the Comet was tuned closer to resonance. However, a slight (blue-shifted) spectral offset was shown to benefit P_{Xe} values; despite the fact that ‘on-resonance’ optical pumping provided higher laser power (and P_{Rb} estimates), lower P_{Xe} values were observed. This finding, along with the large amounts of light that transmit through the cell (>50%; due to low T_{OPT}) under ideal conditions demonstrates the necessity of optimal cell illumination for high-quality SEOP. These signs also seem to point to the need for even higher powered frequency-narrowed light sources. While the origins of the anomalous dependence of P_{Xe} on $[Xe]_{cell}$ are not immediately evident, the results can be

exploited for numerous MR applications that require large amounts of highly polarized ^{129}Xe .

CHAPTER 9

INTERDEPENDENCE OF IN-CELL XENON DENSITY AND TEMPERATURE

FOR Rb/¹²⁹Xe SEOP

9.1 INTRODUCTION

Assuming a Rb/¹²⁹Xe SEOP system, the highest ¹²⁹Xe nuclear spin polarization values that are achievable typically require very low in-cell xenon partial pressures during SEOP, as $[Xe]_{\text{cell}}$ is the primary limiter of rubidium electron spin polarization levels due to increased Rb-Xe collisions/spin-destruction mechanisms^{58,63,81} (see Eq. 2.7). Also, it is generally expected that, at high xenon densities (i.e., $[Xe]_{\text{cell}}$ more than a few hundred torr)⁵³, the three-body spin-exchange pathway becomes progressively less influential, and most Rb/¹²⁹Xe spin-exchange results from binary collisions only (which are less efficient at transferring spin polarization due to their transient nature).

Because of this interplay, increases in $[Xe]_{\text{cell}}$ are directly compensated for by corresponding losses in P_{Xe} , resulting in a flat (or worse) dependence of the NMR signal-to-concentration ratio (SCR)⁶³ on increasing $[Xe]_{\text{cell}}$. This makes the production of sizeable amounts of highly spin-polarized ¹²⁹Xe experimentally challenging, as well as limiting the scope of potential applications—many of which require high ¹²⁹Xe NMR signal (which is the product of $[Xe]_{\text{cell}} \cdot P_{Xe}$). Most current processes employ complex, expensive set-ups that polarize a small amount of gas at an instant (usually $\ll 60$ torr Xe for high P_{Xe} levels) and slowly accumulate the hyperpolarized gas over time.^{57,113}

In Chapter 8, an unexpected interdependence of P_{Xe} and $[Xe]_{cell}$ was reported, where P_{Xe} values are initially low (<1% at 50 torr Xe), rise with increasing $[Xe]_{cell}$, peak (~15% at 300 torr Xe), and then fall off but remains uncharacteristically high at elevated $[Xe]_{cell}$ (>10% at 1000 torr Xe); this anomalous trend is quite different from what is conventionally expected: high P_{Xe} at low $[Xe]_{cell}$, precipitously falling upon increased $[Xe]_{cell}$. To further study this unexplained phenomenon, low-field NMR detection capabilities were installed to enable the monitoring of P_{Xe} values (and build-up dynamics) *in situ*. The remainder of this chapter details low-field ^{129}Xe NMR studies of P_{Xe} as a function of $[Xe]_{cell}$, buffer gas density/composition, and T_{cell} ; both 'steady-state' P_{Xe} levels and build-up curves (P_{Xe} as a function of time) were evaluated. Attempts were made to extract fundamental SEOP parameters (such as the binary spin-exchange cross section and three-body spin-exchange rate) from these P_{Xe} build-up curves. Finally, upon further optimization of the SEOP apparatus and experimental parameters, ultra-high P_{Xe} enhancements were recorded for high $[Xe]_{cell}$'s, including >57,000 at 50 torr Xe and >11,000 at 2000 torr Xe, while using only ~29 W of frequency-narrowed laser light (provided by the Comet). These ^{129}Xe nuclear spin polarization levels are the highest ever reported at such high xenon densities (to our knowledge), and may pave the way for efficient, cost-effective HP ^{129}Xe human lung imaging from single-batch SEOP.

9.2 *IN SITU* P_{Xe} MEASUREMENT VIA LOW-FIELD NMR POLARIMETRY^{14,205}

The P_{Xe} results presented thus far in this dissertation have been measured exclusively at high field (9.4 T); because of this limitation, each data point requires its own separate OP run (gas loading, temperature equilibration, ‘pump-up’ time, cool-down time, collection, transfer to stopcocked NMR tube, then to NMR magnet). As such, each data point requires approximately 45 minutes to an hour to complete, resulting in only 6-10 OP runs in a day (and large amounts of xenon and buffer gases consumed). This detection method also suffers from the inability to monitor changes to P_{Xe} levels as they occur in real time during optical pumping (such as the P_{Xe} vs T_{cell} asymmetry in Fig. 8.3), potentially leading to inconclusive or skewed data.

In order to facilitate more efficient OP parameter optimization, and to better study P_{Xe} build-up and decay dynamics *in situ*, a low-field (LF) NMR polarimeter, centered around a low-frequency NMR spectrometer (Magritek-‘Aurora’), was recently added to the SEOP apparatus (detection range: ~0-100 kHz). The spectrometer is connected to a home-made pulse/detect saddle coil (constructed from PTFE; hand-wound with copper wire; positioned around the OP cell—Fig. 9.1) that is optimized for ^{129}Xe NMR detection at only 37.5 kHz ($B_0 \sim 32$ G). Custom PTFE cell mounts with Garolite posts reduce magnetic field inhomogeneity across the OP cell (the previous cell holders were metal and cast a magnetic field gradient across the cell that prevented the detection of the LF NMR signal). Furthermore, the large permanent magnets used for P_{Xe} cryo-

collection (Fig. 7.3) must also be removed for LF NMR detection, as they cast an even larger magnetic field gradient.

The addition of the LF polarimeter allows a multitude of data points to be taken for each OP gas loading, meaning that a variety of experimental parameters (i.e., laser flux, spectral offset, T_{cell} , 'pump-up' times, etc.) can be 'mapped out' quickly and efficiently for each gas loading. This not only eases the optimization of various parameters, but allows for experiments that are simply not possible without *in situ* detection (such as P_{Xe} build-up and decay dynamics).

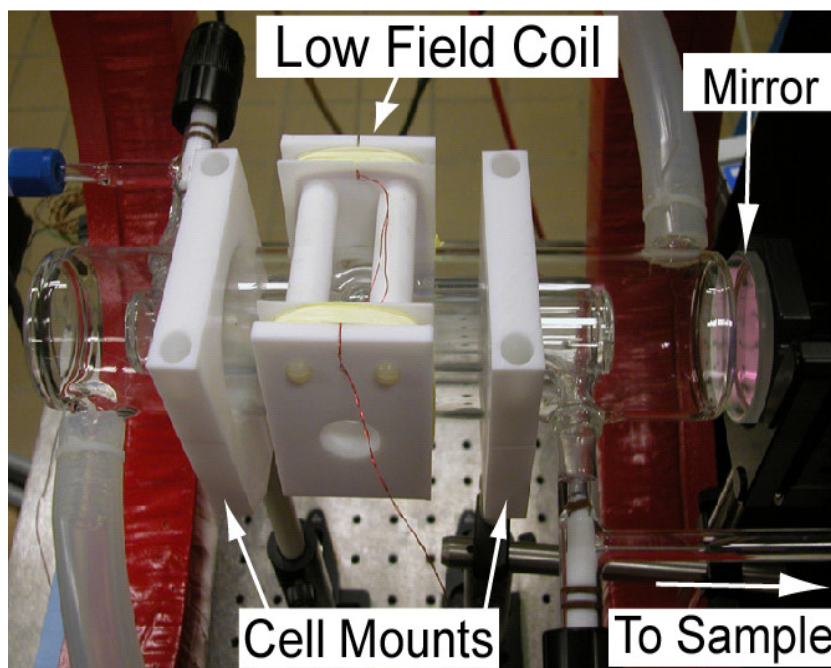


Fig. 9.1 OP cell in Teflon mounts, with home-made LF pulse/detect saddle coil sitting on top. 2" mirror residing behind the cell retro-reflects light back through, thus helping to eliminate regions of 'dark' Rb within the OP cell.¹⁴

The general procedure for low-field detection is quite similar to a 'saturation recovery' NMR pulse sequence, and proceeds as follows: A series of 'crusher'

pulses are applied to ‘reset’ P_{Xe} throughout the cell (~300 pulses; 0.1 ms recycle delay). Then, P_{Xe} is allowed to accumulate for a set amount of time (nominally 5 minutes), and detected with a single pulse (1.25 ms; $\alpha \sim 52^\circ$) for the active volume (~25% of the cell). The LF spectra are simple to interpret (Fig 9.2), with a single ^{129}Xe gas peak at 37.5 kHz (typical noise level ~10-25 counts, mostly from HC power supply unit; all LF studies done in the absence of any rf/af shielding). This particular resonance frequency was chosen so that it resides in a frequency range that is not heavily populated with rf/af noise sources (aside from the HC power supply, which cannot be turned off during LF detection—or SEOP experiments in general), as well as corresponding to a highly characterized B_0 regime for SEOP.

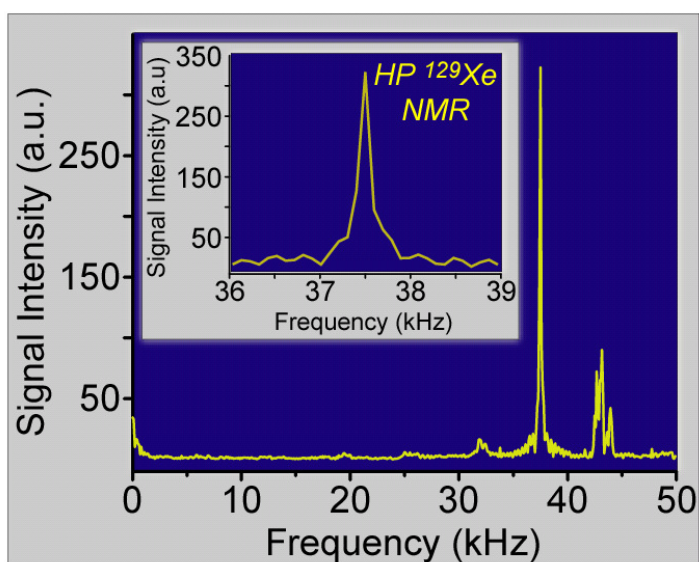


Fig. 9.2 Example LF ^{129}Xe NMR spectra, showing a single peak at 37.5 kHz ($B_0 \sim 32$ G). The somewhat noisy baseline is dwarfed by the massive HP ^{129}Xe NMR peak.¹⁴

The SEOP set-up was also supplemented with a 2-inch mirror, installed post-cell (Fig. 9.1) to retro-reflect laser light back into the OP cell (thus minimizing areas for ‘dark’, unpolarized Rb). Although the circular polarization of the laser light changes upon reflection off the mirror, because the reflected light beam traverses backwards through the applied magnetic field, the ‘helicity’ with respect to the quantization axis remains the same—and thus imparts the same angular momentum to the Rb. As such, the added mirror instantly provided a ~29% ‘free’ increase in P_{Xe} under nominal conditions (as measured at high field—Fig 9.3). The benefits of the added mirror become less significant at higher OP cell temperatures; as the Rb vapor becomes increasingly optically thick, it will absorb more of the laser light (leaving less light that can actually make it to the mirror).

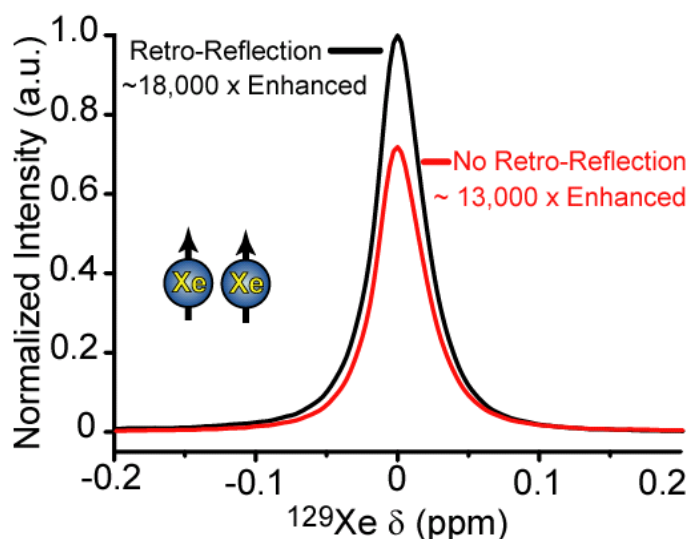


Fig. 9.3 NMR signal at 9.4 T from ~300 torr HP Xe (1 scan, $\alpha \approx 7.2^\circ$) with (black) and without (red) retro-reflection (Comet laser, $T_{\text{cell}} \sim 80^\circ\text{C}$, no cryo-collection).¹⁴

9.3 DEPENDENCE OF OPTIMAL CELL TEMPERATURE ON XE DENSITY^{14,205}

The low-field set-up was used to monitor HP ^{129}Xe signal *in situ* as a function of xenon density, nitrogen density, and OP cell temperature with the goal of elucidating more information about the anomalous P_{Xe} -vs.- $[\text{Xe}]_{\text{cell}}$ trend reported in Chapter 8.⁵⁹ The temperature at which the peak LF ^{129}Xe NMR signal was achieved was found to depend very sensitively on $[\text{Xe}]_{\text{cell}}$ (the experiments were conducted with a constant total cell pressure—2000 torr; backfilled with N_2). It was observed that high $[\text{Xe}]_{\text{cell}}$ achieved maximum P_{Xe} at lower T_{cell} , while decreased $[\text{Xe}]_{\text{cell}}$ favored higher temperatures (Fig. 9.4).

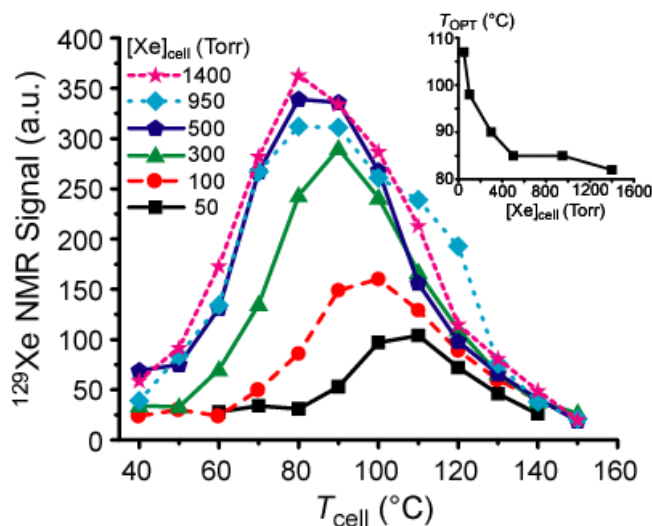


Fig. 9.4 *In situ* low-field (~ 32 G) NMR signal from HP ^{129}Xe gas as a function of the cell exhaust temperature (T_{cell}) for various $[\text{Xe}]_{\text{cell}}$. For all experiments, the OP cell was back-filled with N_2 to give a constant total pressure of ~ 2000 torr; OP time was fixed at 5 min. *Inset:* Dependence of T_{OPT} on $[\text{Xe}]_{\text{cell}}$, as estimated from the data in the main figure.²⁰⁵ There is a clear benefit to running at lower T_{cell} for higher $[\text{Xe}]_{\text{cell}}$ values; also, there is higher peak LF signal for higher $[\text{Xe}]_{\text{cell}}$ values, a result that runs counter to the previously expected steady-state signal-to-concentration ratio.⁶³

To our knowledge, this T_{OPT} dependence on $[\text{Xe}]_{\text{cell}}$ has not been previously reported in the literature. Indeed, the large dynamic range of cell temperatures and xenon densities in which we are interested, combined with the ability to quickly study SEOP via LF ^{129}Xe NMR, has allowed us to observe this unexpected dependence. At first glance, the $[\text{Xe}]_{\text{cell}}/T_{\text{OPT}}$ interdependence is counter to what would be expected: naively, higher $[\text{Xe}]_{\text{cell}}$ values should require higher Rb vapor densities (i.e., ‘more Rb needed to polarize more Xe’), and thus higher cell temperatures. The fact that the highest $[\text{Xe}]_{\text{cell}}$ values require lower T_{cell} (by up to 30 °C) for optimal P_{Xe} is quite surprising, as are the actual T_{OPT} values themselves—as the majority of OP set-ups run at higher T_{cell} values (typically ≥ 120 °C). On the other hand, higher T_{cell} is preferred for lower $[\text{Xe}]_{\text{cell}}$, so those particular set-ups that polarize only a few torr of xenon at a time are probably optimized for their own experimental conditions (assuming that, when polarizing larger $[\text{Xe}]_{\text{cell}}$ quantities, they do not lower T_{cell} —resulting in low P_{Xe} values at high $[\text{Xe}]_{\text{cell}}$).

Indeed, it would seem that this $[\text{Xe}]_{\text{cell}}/T_{\text{OPT}}$ interdependence is able to at least partially explain the xenon density anomaly previously observed at high field (from Chapter 8); all variable $[\text{Xe}]_{\text{cell}}$ experiments were conducted at one T_{cell} value (~ 80 °C; which was optimized for 300 torr Xe—hence the P_{Xe} maximum at 300 torr Xe). By using each $[\text{Xe}]_{\text{cell}}$'s particular T_{OPT} , it was also noticed that an increase in NMR signal was still achieved at increasing xenon densities (even at 1400 torr Xe), thus defying the conventionally expected⁶³ steady-state ^{129}Xe NMR signal with higher $[\text{Xe}]_{\text{cell}}$ (Fig. 9.4). By dividing the acquired low-field ^{129}Xe

NMR signal by $[\text{Xe}]_{\text{cell}}$ (to obtain a relative estimate of ^{129}Xe polarization), it was observed that P_{Xe} is higher at lower $[\text{Xe}]_{\text{cell}}$ --but only near T_{OPT} , and not to the degree that would maintain a constant SCR upon increased $[\text{Xe}]_{\text{cell}}$ (Fig. 9.5).¹⁴

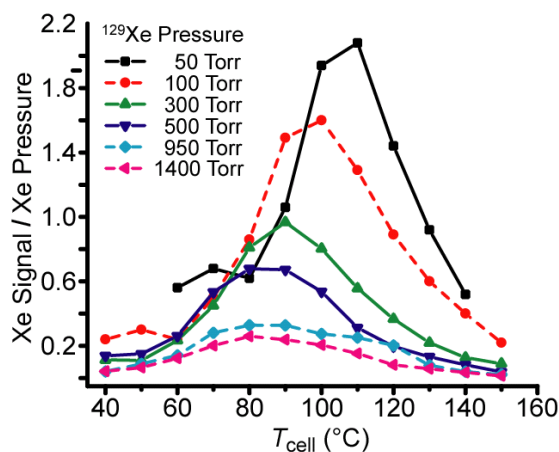


Fig. 9.5 Same as Fig. 9.4, only the LF HP ^{129}Xe signal is divided by the xenon partial pressure (torr) for each run, resulting in a relative estimate of P_{Xe} . By plotting the data this way, the generally expected trend of higher P_{Xe} at lower $[\text{Xe}]_{\text{cell}}$ is observed (but only at higher temperatures).¹⁴

9.4 DEPENDENCE OF T_{OPT} ON BUFFER GAS COMPOSITION/DENSITY¹⁴

A separate set of experiments was conducted (with a constant $[\text{Xe}]_{\text{cell}}$ of 300 torr) to determine the effects of $[\text{N}_2]_{\text{cell}}$, overall cell pressure, and the $[\text{N}_2]_{\text{cell}}/[\text{Xe}]_{\text{cell}}$ ratio on the LF ^{129}Xe signal. A slight increase in ^{129}Xe NMR signal was observed with higher overall cell pressures (likely due to additional collision-broadening; transmitted laser spectra showed evidence of additional light absorption at these higher cell pressures), but there was little discernable difference in the values for T_{OPT} (Fig. 9.6) upon increased $[\text{N}_2]_{\text{cell}}$. Later (similar) experiments using a tertiary gas mixture (Xe, N_2 , and He) also showed little

variation in optimal cell temperatures, signaling that this optimal temperature effect is most likely due to $[\text{Xe}]_{\text{cell}}$ itself and not other gas species composition, density, or pressure ratio.

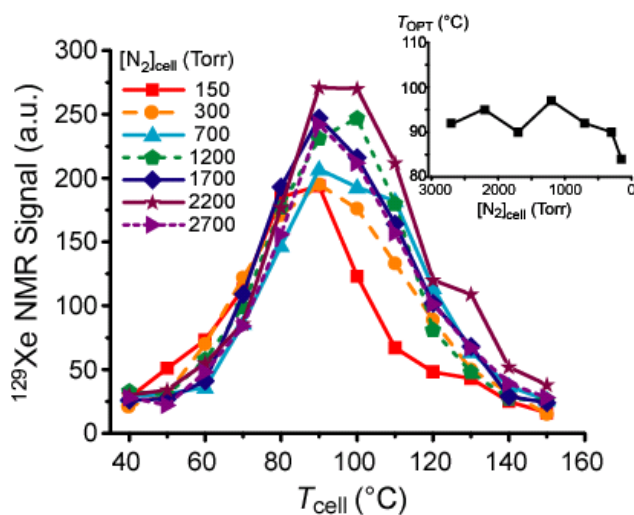


Fig. 9.6 Same as Fig. 9.4, but for various $[\text{N}_2]_{\text{cell}}$ (for these runs, $[\text{Xe}]_{\text{cell}}$ was held constant at 300 torr). Note the slight increase in P_{Xe} for higher cell pressure runs (likely due to increased pressure-broadening). There was no evidence of depolarizing violet emission at even the lowest $[\text{N}_2]_{\text{cell}}$. *Inset:* Dependence of T_{OPT} on $[\text{N}_2]_{\text{cell}}$ for corresponding OP runs, showing little discernable dependence on either $[\text{N}_2]_{\text{cell}}$ or overall cell pressure, signaling that the primary influence on T_{OPT} is likely $[\text{Xe}]_{\text{cell}}$ itself.²⁰⁵

9.5 XENON NUCLEAR SPIN POLARIZATION DYNAMICS^{14,136,205}

While at least partially explaining the previously reported results⁵⁹ regarding the uncharacteristically high P_{Xe} values at high $[\text{Xe}]_{\text{cell}}$ (as well as low P_{Xe} at low $[\text{Xe}]_{\text{cell}}$ —those data were taken at a low constant $T_{\text{cell}} = 80^{\circ}\text{C}$, favoring higher $[\text{Xe}]_{\text{cell}}$ values), the fundamental origin of the interplay between T_{OPT} and $[\text{Xe}]_{\text{cell}}$ was not immediately evident. To better study the origins of *this* effect, additional

LF studies were conducted to monitor the P_{Xe} buildup dynamics as they occurred in real time.

For each set of runs (typically, variable $[Xe]_{cell}$ or variable T_{cell}), the experiment progressed as follows: the OP set-up is brought to operational conditions (OP gas mixture loaded, cell heated to particular T_{cell} , laser set to optimal parameters). Then, the laser is blocked (with two beam-blocks in front of the CP box), and the P_{Xe} in the cell is 'reset' by the series of crusher pulses. After these pulses (when it is assumed that $P_{Xe} = 0$), the laser is unblocked, and the experiment begins. Over a pre-determined time duration (~20 minutes), a single (small tipping-angle) pulse (~0.625 ms; $\alpha \approx 26^\circ$) is regularly applied to detect the HP ^{129}Xe signal at a constant interval (say, once every minute). The cumulative effect of these pulses was experimentally determined to be equivalent to an additional relaxation contribution to the apparent time constant governing SEOP (i.e., Γ ; see Eq. 2.9) of $\sim 3.9 \times 10^{-4} \text{ s}^{-1}$ (typical range of Γ values measured from $\sim 2.7 \times 10^{-3}$ to $1.6 \times 10^{-2} \text{ s}^{-1}$); all Γ values were thus corrected for the effect of the rf pulses by subtracting this number from the results of all raw fits of the experimental data. The entire experiment is repeated four times, and the final dataset is obtained by averaging the 4 identical runs and subtracting the noise plateau; each dataset is then shifted in time so that the polarization growth begins at $t=0$ s. Because of the intrinsic difficulty in using Eq. 2.6 to fit $P_{Xe}(t)$, the build-up curves were fit to a similarly-formed generic equation:

$$S(t) = a \cdot (1 - \exp(-\Gamma t)) , \quad (9.1)$$

where S is the LF ^{129}Xe NMR signal at time (t), a is the steady-state ^{129}Xe signal, and Γ is the time constant of the curve. At short time intervals, $S(t)$ is given as:

$$S(t) = \xi \cdot [\text{Xe}]_{\text{cell}} \cdot P_{\text{Rb}} \cdot \gamma_{\text{SE}} \cdot t, \quad (9.2)$$

where ξ represents the ‘instrument function’ that is inherent to the low-field spectrometer/detection coil combination. Each P_{Xe} build-up curve can be evaluated by the two values, “ a ” (the steady-state polarized gas NMR signal) and “ Γ ” (the build-up rate time constant, corrected for losses due to the tipping angle of detection pulses). By multiplying ($a \cdot \Gamma$), and correcting for $[\text{Xe}]_{\text{cell}}$ (with the factor: 760 torr/Xe partial pressure), one is left with a figure of merit describing the efficiency of the optical pumping process under those experimental conditions (see below).

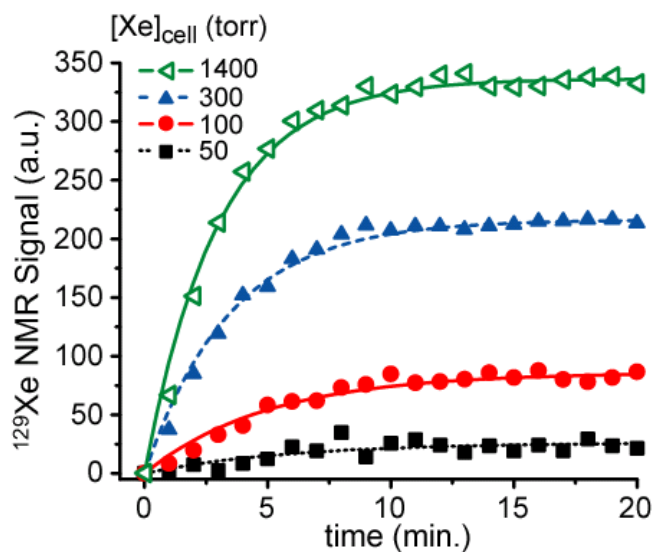


Fig. 9.7 Selected curves showing the time dependence of the *in situ* low-field HP ^{129}Xe NMR signal during SEOP, shown for various $[\text{Xe}]_{\text{cell}}$ (reported here as Xe partial pressures, in torr, at the time of cell loading; overall cell pressure = 2000 torr; $T_{\text{cell}} = 90\text{ }^\circ\text{C}$). Each dataset was obtained by averaging 4 identical runs; solid lines are exponential fits according to Eq. 9.1.²⁰⁵

The P_{Xe} build-up rate was observed to have a complex dependence on both T_{cell} and $[Xe]_{cell}$; P_{Xe} buildup curves also continued to demonstrate the increased (steady-state) ^{129}Xe signal at higher $[Xe]_{cell}$ (selected buildup curves at varying $[Xe]_{cell}$ shown in Fig. 9.7). Contrary to expectations (Eq. 2.7), higher $[Xe]_{cell}$ loadings seem to have increased P_{Xe} build-up rates at constant (relatively low) T_{cell} (higher $[Xe]_{cell}$ is expected to both decrease the spin-exchange rate and increase the Rb spin-destruction rate).

In situ LF P_{Xe} studies were also performed under constant $[Xe]_{cell}$, while varying the OP cell temperature. It is generally expected that, as T_{cell} increases, the P_{Xe} build-up rate will rise as well (due to rising $[Rb]_{cell}$ —Eq. 2.7). This trend was effectively reproduced in Fig. 9.8 (with $[Xe]_{cell}$ fixed at 500 torr Xe), where the fastest build-up time occurred at the highest OP cell temperature ($T_{cell} = 110$ °C). However, this set of curves also demonstrates the utility of optical pumping at T_{OPT} , as the highest steady-state ^{129}Xe signals were achieved at the optimal

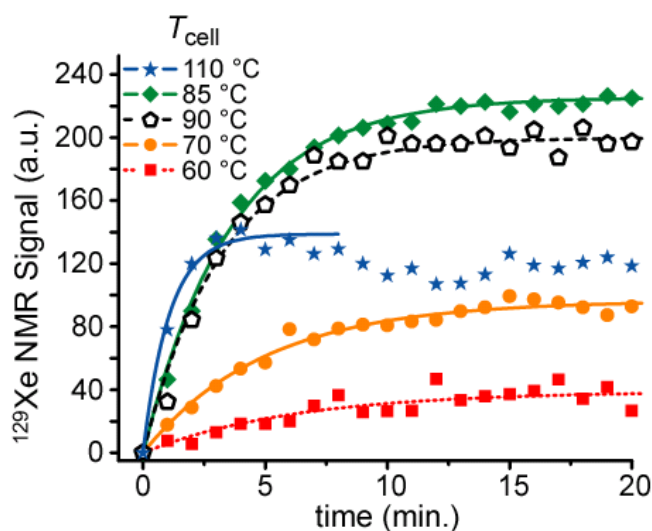


Fig. 9.8 Same as Fig. 9.7, but with variable T_{cell} and fixed $[Xe]_{cell}$ (i.e., Xe partial pressure = 500 torr).²⁰⁵ Curve fits were truncated at the highest T_{cell} values (e.g. 110 °C), due to instabilities likely caused by so-called ‘rubidium runaway’ effects.⁶⁵

cell temperature of 85 °C. Furthermore, evidence of ‘Rb runaway’⁶⁵ can be seen at the 110 °C run, as the P_{Xe} signal becomes progressively weaker with time (due to increasing levels of ‘dark’ Rb; this trend is evident for most P_{Xe} build-up curves at high T_{cell}). So, even if higher T_{cell} allows one to reach steady-state faster, the actual P_{Xe} level attainable may very well be quite lower than the one obtained at T_{OPT} .

Using the ‘a’ and ‘Γ’ values extracted from the plotted P_{Xe} build-up curves and Eqs. 9.1 & 9.2, a figure of merit for the optical pumping efficiency can be estimated (as a function of $\xi \cdot P_{Rb} \cdot \gamma_{SE} \cdot [Xe]_{cell}^{-1}$; Fig. 9.9). This OP efficiency is

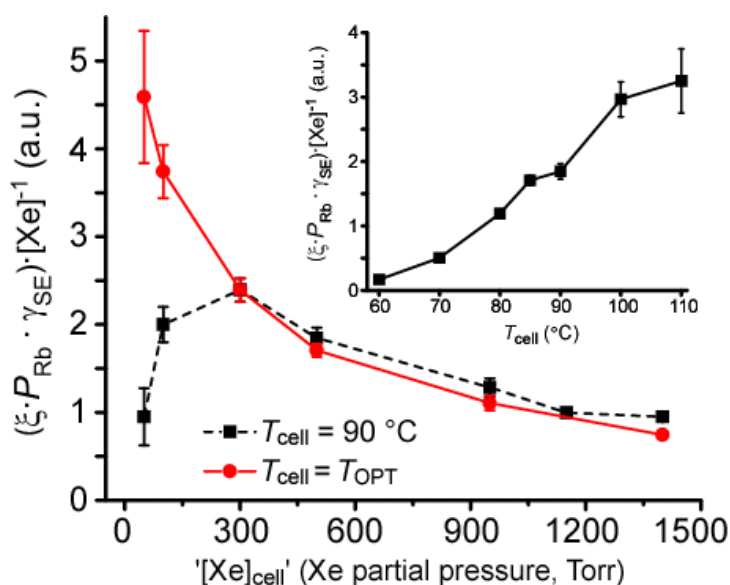


Fig. 9.9 Plots of the time constant for P_{Xe} build-up (Γ) multiplied by the steady-state value of the LF NMR signal (a), giving: $\xi \cdot \langle P_{Rb} \rangle \cdot \gamma_{SE}$, where ξ is an instrument function. Note that this factor is free of contributions from the ^{129}Xe nuclear spin relaxation rate (Γ_{Xe}). Data points are plotted as functions of $[Xe]_{cell}$; each point has been normalized by the Xe partial pressure at loading to adjust for the dependence of the NMR signal strength on the ^{129}Xe spin density. Black squares/dotted line: $T_{cell} = 90\text{ }^\circ\text{C}$; Red circles / solid line: $T_{cell} = T_{OPT}$. Inset: Same as main figure, except plotted versus T_{cell} for fixed $[Xe]_{cell}$ (500 torr Xe partial pressure). Error bars are fit uncertainties. Overall cell pressure was 2000 torr (N_2 balance) for all runs.²⁰⁵

free of contributions from the ^{129}Xe nuclear spin relaxation rate (Γ_{Xe}); plotting the data in this manner allows one to determine if the observed effects arise from $[\text{Xe}]_{\text{cell}}$ -dependent changes to Γ_{Xe} . When performing SEOP at a constant T_{cell} (90 °C), the ‘OP efficiency’ initially rises with increasing $[\text{Xe}]_{\text{cell}}$, peaks, and then slowly falls off at high Xe densities (Fig 9.9—black dashed line); this trend qualitatively follows the previously reported⁵⁹, unexpected dependence of P_{Xe} on $[\text{Xe}]_{\text{cell}}$ at high Xe densities. However, when SEOP is performed at each $[\text{Xe}]_{\text{cell}}$ ’s T_{OPT} (red solid curve), very high OP efficiency is observed at low $[\text{Xe}]_{\text{cell}}$, dropping off smoothly and dramatically with increased xenon density (i.e. the traditionally expected dependence).

At fixed gas density/composition, the P_{Xe} build-up rate increases as a function of T_{cell} (as the SE rate depends on $[\text{Rb}]_{\text{cell}}$ —see Eq. 2.7). Despite increases to the SE rate at higher T_{cell} (as $[\text{Rb}]_{\text{cell}}$ increases), global P_{Rb} and P_{Xe} may suffer due to inferior cell illumination (Fig. 9.9 *inset* higher T_{cell} runs), as more of the light is absorbed in the front of the cell (possibly leading to a ‘Rb runaway effect’)⁶⁵, leaving the rear of the cell optically opaque.⁶⁶ This high- T_{cell} effect may also explain fall-offs to the steady-state P_{Xe} values at increased time intervals (such as the 110 °C run in Fig. 9.8), as the cell becomes more opaque over time. Spin-exchange is also dependent on the OP gas composition/density due to different SE pathways on the molecular level (2-body vs. 3-body—see Eq. 2.9), affecting $[\text{Xe}]_{\text{cell}}$ ’s effect on the spin-exchange efficiency. These preliminary results demonstrate that the interdependence of $[\text{Xe}]_{\text{cell}}$ and T_{cell} that determines P_{Xe} is due to some facet of the SEOP process itself (and not, say, to

temperature- or density-dependent changes to ^{129}Xe spin relaxation, as the $a \cdot \Gamma$ factor is void of Γ_{Xe} contributions). The origin of this unexpected dependence of P_{Rb} or γ_{SE} (or both) on $[\text{Xe}]_{\text{cell}}$ that is compensated by T_{OPT} is not yet understood; to our knowledge it is not well explained by current models (i.e. Eqs. 2.6 & 2.7).

In principle, the P_{Xe} build-up curves can be further analyzed to determine the effects of T_{cell} and $[\text{Xe}]_{\text{cell}}$ on the 2-body and 3-body contributions to $\text{Rb}/^{129}\text{Xe}$ spin-exchange (2-body collisional cross-section and 3-body spin-exchange rate), intrinsic P_{Xe} relaxation characteristics, and estimates of the volume-averaged, in-cell P_{Rb} . By plotting the P_{Xe} build-up curve rate constant (Γ) as a function of $[\text{Rb}]_{\text{cell}}$ (as estimated from vapor pressure curves)⁷⁷, one should obtain a straight line whose slope is equal to γ' (sum of 2-body and 3-body contributions to the spin-exchange rate), with the y-intercept equal to Γ_{Xe} (the in-cell HP ^{129}Xe relaxation rate; see Eq. 2.9 & Fig 9.10). Indeed, this approach appears to work

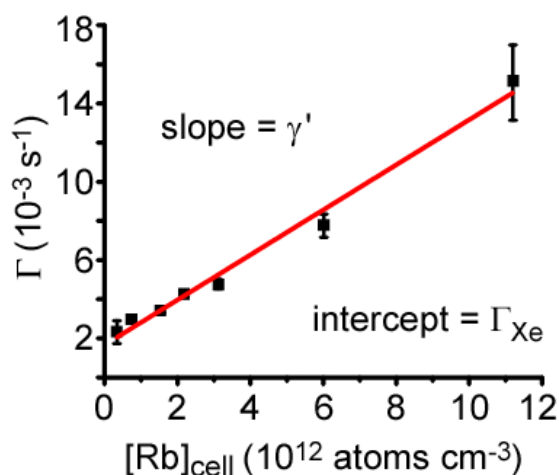


Fig. 9.10 Plot of the time constant (Γ) for P_{Xe} build-up (measured at $[\text{Xe}]_{\text{cell}} = 500$ torr) versus $[\text{Rb}]_{\text{cell}}$ (estimated from vapor pressure curves)⁷⁷. Following Ref.⁵³, a fit to the data (red line) should give a slope and intercept that respectively correspond to the total spin-exchange cross-section, γ' ($\sim 1.15 \times 10^{-15} \text{ cm}^3 \text{ s}^{-1}$) and the in-cell HP ^{129}Xe relaxation rate, Γ_{Xe} (0.00166 s^{-1} ; $^{129}\text{Xe } T_1 \sim 10$ min).

well, providing a good linear fit and a value of γ' (for $[\text{Xe}]_{\text{cell}} = 500$ torr) of $\sim 1.15 \times 10^{-15} \text{ cm}^3 \text{ s}^{-1}$; this seems to be a fairly reasonable estimate (most values of γ' range from $\sim 9 \times 10^{-15}$ to $\sim 8 \times 10^{-17}$, depending on gas mixture and detection technique).²⁰⁶ The in-cell HP ^{129}Xe nuclear spin relaxation rate (Γ_{Xe}) was found to be $\sim 0.00166 \text{ s}^{-1}$, corresponding to an in-cell ^{129}Xe T_1 of ~ 10 minutes (also perfectly reasonable, depending on OP gas mixture and cell preparation).

In principle, repeating this process (of determining γ') for multiple $[\text{Xe}]_{\text{cell}}$ values, one should be able to disentangle the 2-body and 3-body contributions to the spin-exchange rate. Plotting γ' as a function of $1/P_a$ (as described in Eqs. 2.10 & 2.11) is expected⁵³ to result in a straight line with a slightly increasing

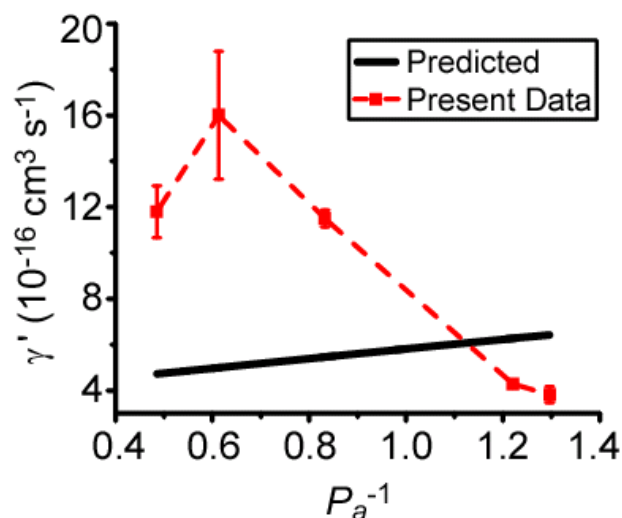


Fig. 9.11 Plot of γ' versus $1/P_a$ (see Eq. 2.10) determined for different values of $[\text{Xe}]_{\text{cell}}$ (red dotted line); the point at $P_a^{-1} \sim 0.83$ (corresponding to 500 torr Xe) was taken from the fit of Γ values obtained at multiple T_{cell} 's shown in Fig. 9.9; all other points were obtained by fitting Γ values obtained at two T_{cell} 's and using the Γ_{Xe} from Fig. 9.10 as the intercept (i.e., assuming no dependence of Γ_{Xe} on $[\text{Xe}]_{\text{cell}}$).¹³⁶ The solid line (black) is the predicted trend. In principle, fitting such data to a line should provide the 3-body contribution to the SE rate (slope) and the binary SE cross-section (intercept), previously measured to be $\sim 2.92 \times 10^4 \text{ s}^{-1}$ and $\sim 3.7 \times 10^{-16} \text{ cm}^3 \text{ s}^{-1}$, respectively; however, the experimental data does not show qualitative agreement with the expected trend.⁵³

slope; one can extract values for the 2-body (y -intercept) and 3-body (slope) contributions from the fit of this line. While this method is expected to work (and can be easily modeled using our $[\text{Xe}]_{\text{cell}}$ values to calculate a binary SE cross-section of $\sim 3.7 \times 10^{-16} \text{ cm}^3 \text{ s}^{-1}$, along with a three-body SE rate of $\sim 2.92 \times 10^4 \text{ s}^{-1}$)⁵³, our preliminary attempts at fitting experimental data to this form resulted in an unexpected trend (Fig. 9.11). Indeed, it appears that although the data are limited (see caption), we appear to achieve higher γ' values at higher $[\text{Xe}]_{\text{cell}}$'s (as $1/P_a$ is inversely proportional to $[\text{Xe}]_{\text{cell}}$; see Eq. 2.11), counter to expectation. The reason for this unexpected trend is unclear, but it does appear to reflect our overall findings of relatively high P_{Xe} values at high xenon densities.

9.6 ULTRA HIGH P_{Xe} VALUES AT HIGH XENON DENSITIES ^{116,205,207}

Following the low-field HP ^{129}Xe NMR studies shown above (as well as numerous experiments that are not shown), we turned our attention back to high field runs (i.e., to determine if we could obtain substantially higher P_{Xe} values for use in MR applications, such as polarization transfer to cryptophane-A and zinc-myoglobin).¹⁵⁴ By exploiting the new-found $[\text{Xe}]_{\text{cell}}/T_{\text{OPT}}$ interdependence (along with the further optimization of the SEOP apparatus and experimental parameters), we were able to achieve very high P_{Xe} values over a wide range of Xe partial pressures (50-2000 torr) using only $\sim 29 \text{ W}$ of frequency-narrowed laser power (provided by the Comet). Even after collection of the OP gas mixture and transfer to high field (9.4 T), we measured average P_{Xe} values of $\sim 52\%$, $\sim 32\%$, $\sim 23\%$, and $\sim 11\%$ at 50, 300, 500, and 2000 torr Xe, respectively

(averaged values shown in Fig. 9.12). To our knowledge, these are the highest P_{Xe} values ever reported at such high $[Xe]_{cell}$ (~ 0.06 to ~ 2.6 amagat) for Rb/ ^{129}Xe batch-mode SEOP, and correspond to substantial NMR signal enhancements of 4-5 orders of magnitude.²⁰⁷

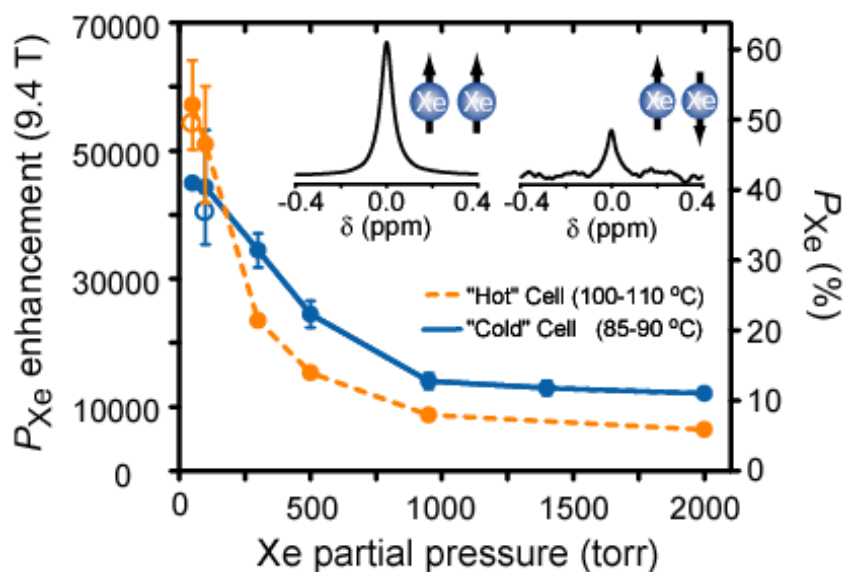


Fig. 9.12 High field (9.4 T) measurements of P_{Xe} (right axis) for a variety of $[Xe]_{cell}$ (polarization enhancement on left axis). Data grouped into two T_{cell} ranges: 'Hot Cell' (orange dotted line; $T_{cell} = 100-110$ °C); & 'Cold Cell' (blue solid line; $T_{cell} = 85-90$ °C) (lines are meant to guide the eye). Values and error bars correspond to averages and standard deviations obtained for multiple SEOP runs. Total cell pressure = 2000 torr, N_2 balance (exception: runs with 2000 torr Xe also contained 600 torr N_2). Inset: High-field (9.4 T) NMR spectra of HP (left) and thermal (right) ^{129}Xe for $[Xe]_{cell} = 300$ torr (left: single 6° pulse; right: averaged from 1,100 acquisitions with 90° pulses; calculated enhancement: $\sim 42,900$; $P_{Xe} = \sim 38.4\%$).²⁰⁵

These data shows our ability to hyperpolarize relatively small amounts of xenon to a very large extent (one of the 50 torr gas loading OP runs correspond to $P_{Xe} \sim 55\%$), as well as quite large $[Xe]_{cell}$ values to relatively high P_{Xe} levels (2000 torr Xe; $\sim 11\%$). Also, contrary to expectations, P_{Xe} was observed to level

off at increased $[\text{Xe}]_{\text{cell}}$ instead of significantly dropping; as such, we continued to achieve increased NMR signal intensity at high field upon increased $[\text{Xe}]_{\text{cell}}$ (relevant for MR applications that require large amounts of NMR signal). Finally, the data at high field follows the trends reported in Figs. 9.4 & 9.8 (at least qualitatively), with higher P_{Xe} values achieved at lower T_{cell} for increased $[\text{Xe}]_{\text{cell}}$ and vice-versa. Indeed, there is an appreciable difference in optical pumping at optimal versus non-optimal cell temperatures (in combination with improved cell preparation/experimental techniques).

A similar set of experiments were also conducted using the Integra as the laser source (~ 55 W; ~ 0.49 nm FWHM), with the idea being that the Integra should be able to further improve P_{Xe} levels (due to the previous Comet/Integra comparison in Chapter 8). While the resulting data curve (*not shown*) was similar in shape to that of Fig. 9.11, the overall P_{Xe} values were a bit lower (~ 10 - 20% less, varying run-to-run). This would seem to indicate that, under OP conditions that correspond to high P_{Xe} levels, the increased spectral-narrowing of the Comet may be more beneficial to SEOP than the increased laser power of the Integra (along with its correspondingly broader spectral lineshape); this would be especially true under low T_{cell} conditions, where a high percentage of the incident light is not absorbed.

9.7 CONCLUSIONS

The results presented in this chapter demonstrate the usefulness of *in situ* low-field NMR to examine P_{Xe} dynamics as they occur, thus facilitating quicker

optimization of experimental parameters and allowing fundamental SEOP studies that are not otherwise possible. Using this low-field detection capability, a sensitive xenon density-mediated dependence of the optimal cell temperature was discovered that (at least partially) explains the previously reported xenon density anomaly (i.e., Fig. 8.8). This $[\text{Xe}]_{\text{cell}}/T_{\text{OPT}}$ interdependence was further utilized to improve batch-mode Rb/ ^{129}Xe SEOP, and can be (at least partially) explained in terms of changes to the efficiency of the optical pumping process at different T_{cell} and $[\text{Xe}]_{\text{cell}}$ values. Preliminary studies attempted to extract fundamental SEOP parameters from P_{Xe} buildup curves (such as binary SE cross-sections and 3-body SE rates); however, the experimental data did not fit the expected trends (but do seem to indicate better-than-expected OP efficiency at higher $[\text{Xe}]_{\text{cell}}$ under our experimental conditions). By taking advantage of the effects of OP at each xenon density's optimal cell temperature, we were able to attain impressive P_{Xe} values at 50 torr Xe (~55%), as well as surprisingly high P_{Xe} values at significantly elevated $[\text{Xe}]_{\text{cell}}$ (~11% at 2000 torr Xe)—encompassing some of the highest—if not the highest— P_{Xe} values ever reported at such high in-cell xenon densities.

While relative estimates of the spin-exchange efficiency establish a window into the unexpected temperature/xenon density interdependence, it is unlikely to explain the entire phenomenon. Furthermore, while the T_{cell} values are reported as the measured OP cell oven exhaust temperature, they do not appropriately reflect the true temperature of the gas mixture inside the cell, as much of the laser energy absorbed by the Rb is transferred to the rovibrational manifold of

the N₂ buffer gas. This effect was demonstrated (via Raman scattering measurements of N₂ by Happer, *et al.*)¹¹² to approach 900 °C with only ~15 W of broadband laser light and significantly lower [N₂]_{cell} (the current set of experiments were conducted with considerably higher resonant laser flux and [N₂]_{cell}). This effect, coupled with [Xe]_{cell}-dependent changes to the Rb D₁ absorption lineshape and spectral offset¹¹⁴, may provide greater insight into the fundamental processes that give rise to the observed effects.

CHAPTER 10

VARIABLE EXCITATION WAVELENGTH STUDIES OF RB/¹²⁹XE SEOP

10.1 INTRODUCTION

The increased light absorption efficiency that is achieved by using frequency-narrowed VHG-LDAs has led to massive enhancements in P_{Xe} (as demonstrated in the last two chapters). However, the first-generation VHG-LDAs (such as the Comet and Integra) suffer from a common drawback—a thorough lack of spectral tunability. Furthermore, what little spectral tunability that is available comes at the cost of significant changes to the laser power and spectral linewidth (often resulting in ‘unlocked’, spurious output some distance in wavelength from the primary emission line; see Fig. 4.2). This problem prevents a true ‘apples-to-apples’ comparison of SEOP at different excitation wavelengths when using these first-generation, fixed-frequency lasers.

It is well-documented that the spectral shift, broadening, and lineshape of the alkali-metal absorption lines^{86,114} are dependent on gas density and composition—and are especially sensitive to the effects of xenon (and, to a lesser extent, nitrogen and helium). Changes to the line shift and broadening are due to differences between ground-state and excited-state interatomic potentials; these differences give rise to energies for the D-line transitions that depend on the interatomic separation of the colliding atoms. As higher-pressure gas loadings are introduced to the OP cell (i.e., the atoms are ‘packed in’ more closely), the resulting energetic ranges in which these transitions are possible

cover a wider spectral window (hence, ‘pressure broadening’ of the atomic absorption transitions). The polarizability of the colliding atoms also plays a part, as there is an interatomic attractive dependence on the van der Waals potential, hence the larger contribution to lineshape changes due to increased xenon density. This van der Waals potential is also responsible for changes to the spectral line shift; because the ground state potential is usually less attractive than the excited state potential, a lower-energy (i.e., longer wavelength) shift is expected for colliding atoms of high polarizability (such as xenon). However, the line shift will tend to higher energy (shorter wavelength) shifts when the colliding species is helium (due to its low polarizability).⁸⁶

Precise knowledge of the position, linewidth, and lineshape of the alkali absorption lines is quite important for SEOP when using frequency-narrowed laser sources—especially when the light source is not tunable (as one can miss the absorption line entirely).¹³⁷ Furthermore, variable excitation-wavelength studies of SEOP at different $[\text{Xe}]_{\text{cell}}$ values should provide insight into the optimal spectral offset/cell temperature for a variety of OP gas loading mixtures (especially useful under conditions of high $[\text{Xe}]_{\text{cell}}$). While the dependences of spectral shift and lineshape on temperature have been estimated for helium as the buffer gas¹¹⁴, any lineshape dependencies on T_{cell} for xenon or nitrogen gases have not been sufficiently characterized. Indeed, knowledge of changes to the Rb/Cs D-line spectral properties upon varied $[\text{Xe}]_{\text{cell}}$, buffer gas density (or composition, and T_{cell} may provide an avenue to further increase P_{Xe} values for

SEOP under conditions of high xenon density (by helping to determine the optimal excitation wavelength for the given set of OP conditions).

The remainder of this chapter details the use of high power, next-generation ‘on-chip’ VHG-LDAs (as introduced in Section 4.4.3) that are capable of spectral tuning without significant changes to the laser output power. This new technology allows for the systematic characterization of T_{cell} , $[\text{Xe}]_{\text{cell}}$, laser flux, and laser spectral offset, and allows the multidimensional set of experimental parameters to be further expanded and explored. A definite P_{Xe} dependence on excitation wavelength is explored for higher $[\text{Xe}]_{\text{cell}}$ values, using improved low-field detection capabilities and compared to the percent transmittance of the laser beam through the cell. The evaluation of P_{Xe} build-up curves shows an unexpected dependence of the P_{Xe} buildup rate on the excitation wavelength at a variety of $[\text{Xe}]_{\text{cell}}$ values. Finally, a summary and outlook on the future of Rb/ ^{129}Xe SEOP will detail some of the potential upcoming studies in the Goodson laboratory, as well as in the field of SEOP in general.

10.2 ‘ON-CHIP’ VHG-LDAS^{116,133,134}

To circumvent the current limitations of fixed-frequency VHG-LDAs (as well as other methods of spectrally tuning the laser modules, such as mechanically or through a TEC-mounted VHG), a laser module was developed (through QPC; see Section 4.4.3) that contains the VHG as an integral component of the laser itself (instead of as a grating optic mounted in front of the diode). As such, the VHG-spacing is exquisitely sensitive to the LDA temperature, thus providing a

simple and effective method of tuning the laser. Furthermore, because the grating is 'grown' into the laser itself (and is not a separate optic), multiple diodes can be placed into a single laser module, and focused into a single optical fiber. This can boost the output power of a typical module from only ~40 W to well over ~150+ W.

The first on-chip VHG-LDA introduced to the Goodson laboratory possessed an output power of ~80 W as measured directly from the fiber (providing ~68 W incident on the cell due to ~15% loss from CP box). The laser module sits atop a water-cooled chiller plate (cooled by a ThermoCube recirculating water chiller), is driven with a 6-volt power supply unit (Xantrex), and fiber-couples (via a 1 m fiber) into the same CP box as the fixed-frequency VHG-LDAs. Spectral tuning is achieved simply by varying the temperature of the module, which tunes the internal grating at the rate of ~0.069 nm/°C. The module was capable of tuning over a range in excess of 1.3 nm and allowed ample tuning to either side of the Rb absorption line over a wide range of power settings (15-40 amps) and operational temperatures (10 - 35 °C).

Figure 10.1 shows the tuning curves for this prototype laser module as a function of diode temperature (fixed current—Fig. 10.1a) and laser drive current (fixed temperature—Fig. 10.1b). The locked output spectra was observed to be less than 0.30 nm FWHM over the entire range of operational currents and temperatures with minimal variations in lineshape (nominal linewidth ~0.26 nm). Some parasitic unlocked output was noticed (ca. ~800 nm) at the highest power and temperature ($T > 30^{\circ}\text{C}$) settings; under normal conditions the output showed

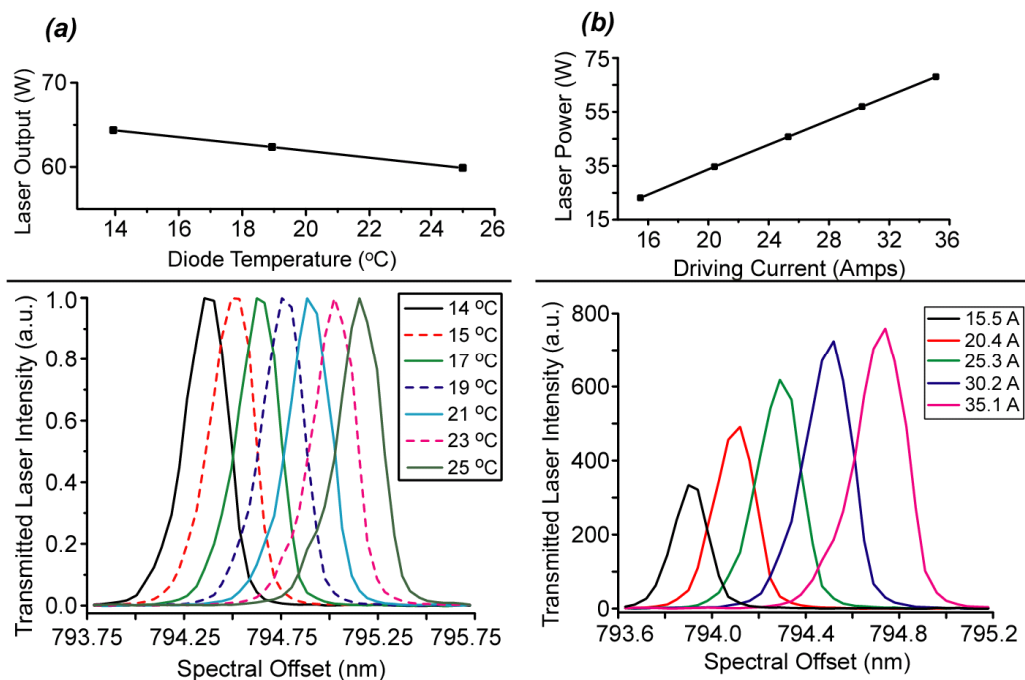


Fig. 10.1 (a) Normalized spectral output of tunable, ‘on-chip’ VHGLDA. Output is spectrally tunable (almost) independently of laser power by changing the diode temperature. *Top*: Slight power loss with increased diode temperature ($\sim 0.4 \text{ W}/^\circ\text{C}$). **(b)** Tunability of ‘on-chip’ VHGLDA at constant diode temperature (18°C) by varying the driving current ($\sim 0.041 \text{ nm}/\text{amp}$). *Top*: Linear increase in laser power as a function of driving current ($\sim 2.26 \text{ W}/\text{amp}$).¹³⁴

minimal or unobservable spurious output (also, no unlocked output was noticed under any conditions after upgraded diodes were placed in the module). There is a slight drop in output power with increases in diode temperature ($\sim 0.4 \text{ W}/^\circ\text{C}$ at 35.1 A driving current)—this drop is seen in Figure 10.1a—*top*. At fixed laser diode temperatures, the output can be tuned by changing the driving current by a factor of $\sim 0.041 \text{ nm}/\text{amp}$ (with a corresponding laser power increase of $\sim 2.26 \text{ W}/\text{amp}$; Fig. 10.1b—*top*).

10.3 IMPROVED LOW-FIELD DETECTION CAPABILITIES^{116,133}

In addition to the next-generation laser technology, improvements to the low-field detection capabilities were also implemented. Because there is no rf/af shielding used in the low-field set-up, a significant noise plateau necessitates the use of large tipping-angle pulses ($\alpha \sim 52^\circ$) to adequately detect the HP ^{129}Xe NMR signal. These strong pulses destroy the xenon magnetization during P_{Xe} build-up curves, thus artificially increasing the time-constant of the curves (and thus requiring the use of a tipping-angle correction factor). The large noise plateau also prevents the observation of small P_{Xe} signals that lie below the noise platform (i.e., P_{Xe} signals in the first minute of P_{Xe} buildup curves at low T_{cell} and/or low $[\text{Xe}]_{\text{cell}}$).

To combat these experimental obstacles, a new LF detection coil was designed that implemented a 'bucking' coil (Fig. 10.2). This new coil is very

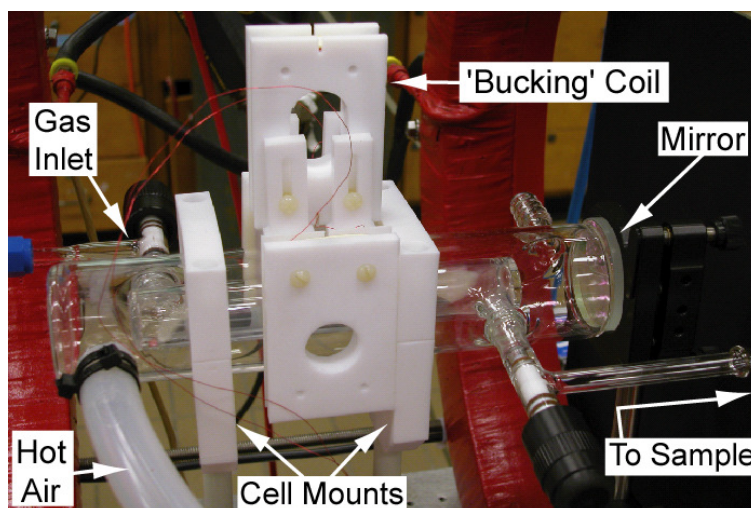


Fig. 10.2 New 'bucking' coil sitting atop OP cell (cell is resting in custom cell mounts). The bucking coil effectively lowers the noise baseline, thus increasing LF detection sensitivity. Retro-reflecting mirror is still used for increased cell illumination.¹¹⁶

similar to the first LF detection coil, with one main difference: an additional coil, with twice as many wraps counterwound (as compared to the other two coils) that sits atop the regular LF detection coil set. The new 'bucking' coil works in the following way: the regular LF coil set detects both P_{Xe} signal and random noise. Because the bucking coil has the same total number of wraps as the regular coil set, is wound in the opposite direction, and only samples the environmental noise (as it sits atop the OP cell, not around it), the random noise signals detected by the 'bucking' coil are of similar magnitude but opposite phase to those of the regular coil, and are effectively cancelled out (thus greatly reducing the noise baseline). Indeed, upon switching to the bucking coil, a ~ 2 orders-of-magnitude increase in detection sensitivity was observed due to the very clean baseline (Fig. 10.3). The bucking coil mount is also machined from PTFE, and is spatially adjustable in all three dimensions for optimal noise cancellation. The

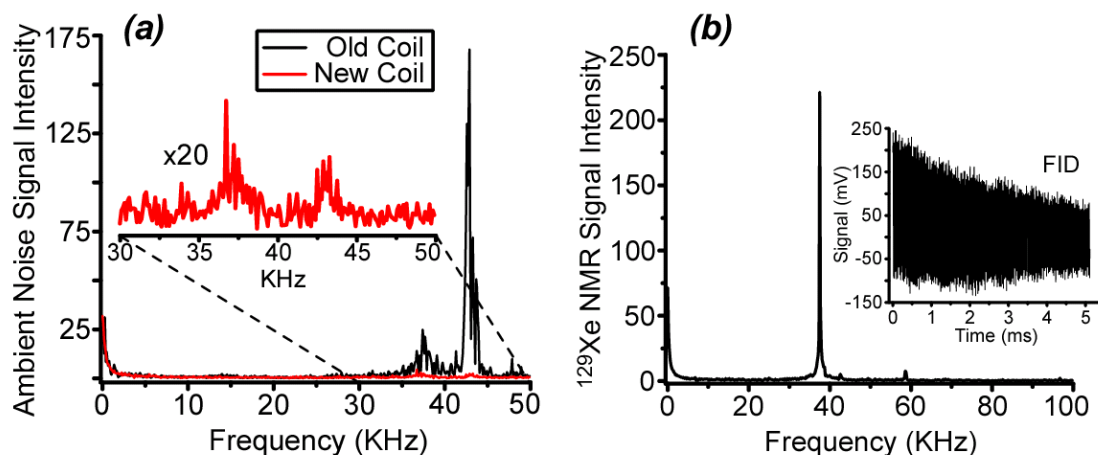


Fig. 10.3 (a) Noise baseline comparison of the two LF detection coils. New 'bucking' coil (red) increases detection sensitivity by ~ 2 orders of magnitude by decreasing ambient noise compared to regular detection coil (black). (b) Example HP ^{129}Xe LF NMR acquisition at 37.5 kHz with 'clean' baseline (using 'bucking' coil). *Inset*: free-induction decay signal of HP ^{129}Xe .¹¹⁶

total HP ^{129}Xe low-field signal is slightly less than that typically produced via the traditional low-field coil (possibly due to different Q factors), but the detection sensitivity is more than compensated for by the decreased noise baseline.

10.4 P_{Xe} DEPENDENCIES ON T_{CELL} , $[\text{Xe}]_{\text{CELL}}$, SPECTRAL OFFSET, & LASER FLUX^{116,133,134}

The on-chip VHG-LDA has allowed (for the first time) the simultaneous mapping of P_{Xe} dependencies on a variety of pertinent experimental parameters. While each variable can be now singled out and individually varied, many of the experimental parameters are highly interdependent, such as laser flux and T_{cell} , or spectral offset and $[\text{Xe}]_{\text{cell}}$. Thus, the following subsections will detail a variety of systematic studies aimed at determining the optimal optical pumping conditions at various xenon densities.

10.4.1 Dependence of P_{Xe} on Laser Flux and T_{cell}

Despite the unprecedented levels of resonant laser flux made available by the first-generation, fixed-frequency VHG-LDAs, they still did not ‘saturate’ the cell with laser power (i.e., P_{Xe} still increases linearly with laser flux—see Fig. 8.8 *inset*). The on-chip VHG-LDA allowed for the study of P_{Xe} saturation curves at much higher laser powers (due to the ability to place multiple diodes into a single module), without changing the output wavelength or linewidth. The SEOP studies were conducted at a variety of laser offsets, laser fluxes, and OP cell temperatures. A sensitive interdependence between laser flux and T_{cell} was

observed, where higher T_{cell} was favored at lower laser fluxes. However, increases in laser flux resulted in decreases to T_{OPT} and overall gains in P_{Xe} (Fig. 10.4). For example, at $[\text{Xe}]_{\text{cell}} = 2000$ torr (plus 600 torr N_2) and the laser emission line set to 794.76 nm (Rb D_1), T_{OPT} decreases from 95 °C to only 75 °C when increasing laser flux from ~20 W up to ~60 W. Indeed, at higher T_{cell} values, P_{Xe} plateaus with increasing laser power, and then begins to fall off, possibly due to Rb runaway.⁶⁵ Furthermore, the usefulness of additional laser power is demonstrated, as P_{Xe} does not ‘saturate’ even at ~68 W of resonant light at low cell temperatures ($T_{\text{cell}} = 75$ °C).

This dependence of T_{OPT} on laser flux is counterintuitive to what is typically expected: that increases to laser flux should increase T_{OPT} , as the additional Rb

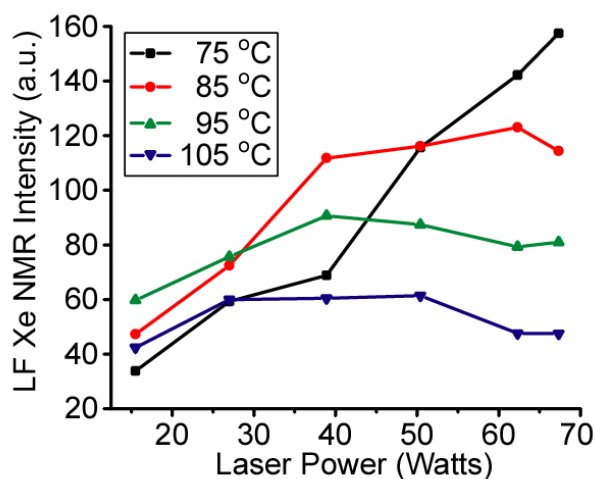


Fig. 10.4 Plots of HP ^{129}Xe signal intensity (at low-field) vs laser flux (‘on resonance’) for a variety of T_{cell} (at 2000 torr Xe, 600 torr N_2). While higher T_{cell} is preferred at low laser powers, the optimal cell temperature lowers upon increased laser flux. The highest P_{Xe} signals were attained at high laser flux and low T_{cell} ; additional laser flux may still be useful, as P_{Xe} does not ‘saturate’ at low T_{cell} .¹¹⁶

vapor density should be more than compensated for by the increased number of available photons. The fact that the opposite trend is observed reinforces the notion that optimal cell illumination is key to achieving high P_{Xe} (at least, at high $[Xe]_{cell}$) as opposed to increasing the spin-exchange rate (via increases to T_{cell}). It also emphasizes that all experimental variables must be optimized in concert, as one particular set of OP parameters may not translate well across various gas loadings. Furthermore, the effect is not due to a simple laser heating effect (i.e., increases in laser flux that bring about higher $[Rb]_{cell}$ through ‘internal’ heating), as there remains a benefit to optical pumping slightly off-resonance for a variety of $[Xe]_{cell}$ values.

10.4.2 Dependence of P_{Xe} on Laser Flux and Spectral Offset

Of course, the other major benefit of the ‘on-chip’ VHG-LDA is the ability to spectrally tune through the Rb D_1 absorption line without changes to the laser power or lineshape. This effect was utilized to study the effects of spectral offset on laser power for $[Xe]_{cell}$ loadings of 300 & 2000 torr Xe (at each $[Xe]_{cell}$ ’s T_{OPT}). For both $[Xe]_{cell}$ loadings, increases to laser flux resulted in increased LF ^{129}Xe NMR signal, with significantly more signal from the 2000 torr Xe run (Fig. 10.5a). The spectral range for peak P_{Xe} also broadens with increased laser flux for reasons that are not immediately clear—but are possibly due to increases in $[Rb]_{cell}$. Both $[Xe]_{cell}$ values enjoyed the benefits of OP with a slight (red-shifted) spectral offset, with the higher power 2000 torr run benefiting the most (likely helped by a red-shifted Rb absorption line).¹¹⁴ Indeed, while there is minimal P_{Xe}

signal at only ~ 0.25 nm blue-shifted from the Rb D_1 for both $[\text{Xe}]_{\text{cell}}$ loadings, the HP ^{129}Xe signal at ~ 0.25 nm red-shifted is still significant at both xenon densities and all three laser flux values.

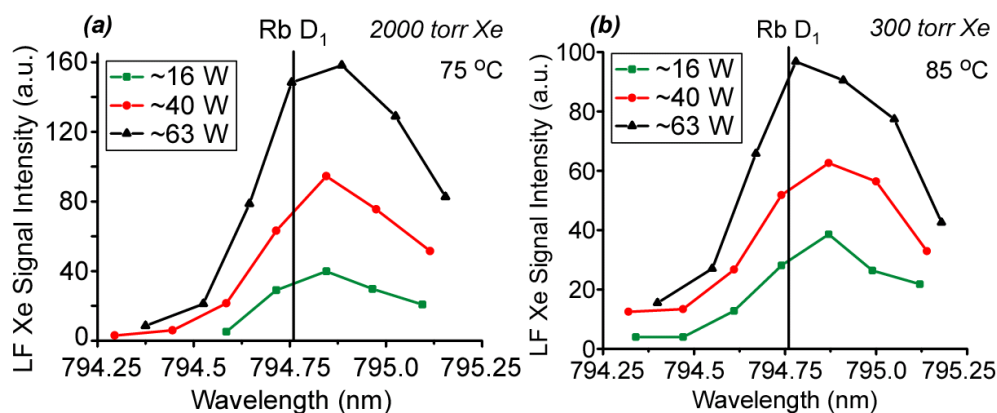


Fig. 10.5 Plots of low-field HP ^{129}Xe NMR signal intensity as a function of laser offset for three driving currents: 15.5 A (~ 16 W; green); 25.3 A (~ 40 W; red); and 35.1 A (~ 63 W; black). OP conditions: **(a)** 2000 torr Xe, 600 torr N_2 ; T_{cell} : 75 °C and **(b)** 300 torr Xe, 1700 torr N_2 , T_{cell} : 85 °C. Increases to laser flux bring about increased P_{Xe} and broader spectral range of peak P_{Xe} values; both $[\text{Xe}]_{\text{cell}}$ loadings benefit from slight spectral red-shift.^{116,134}

10.4.3 Dependence of P_{Xe} on Laser Flux at Different T_{cell} 's & Spectral Offset

Additional studies included examining the effects of varying the laser power and cell temperature at different spectral offsets for 300 and 2000 torr Xe. Three separate spectral offsets were chosen: 'on resonance' (~ 794.76 nm), 'blue side' (~ 794.61 nm), and 'red side' (~ 794.87 nm); laser power 'saturation' curves were determined at different T_{cell} values. Fig. 10.6 shows the results for the 300 torr Xe run; both the 'red side' and 'on resonance' offsets provided the highest P_{Xe} values (at $T_{\text{OPT}} = 85$ °C), while the 'blue side' offset was generally lower, but arrived at the same LF ^{129}Xe signal at the highest laser power (~ 68 W).

Furthermore, while the data sets for the ‘red side’ and ‘on resonance’ offsets appear to be nearing plateaus at the highest laser powers, the ‘blue side’ offset keeps steadily increasing, serving as further affirmation of the importance of optical pumping under conditions of high cell illumination, as laser saturation may be indicative of Rb runaway. Indeed, when T_{cell} is increased by only 20 °C (from 85 °C to 105 °C), all three offsets saturate and then dramatically decrease (in P_{Xe} values) when laser power exceeds ~40 W (likely due to Rb runaway). Additionally, when comparing the first 40 W of the 85 °C run to that at 105 °C, the ‘on resonance’ lines are quite similar, while the ‘red side’ decreases significantly and the ‘blue side’ increases (further evidence that effects from T_{cell} , laser power, and laser flux are all intricately interwoven—and highly dependent on cell illumination).

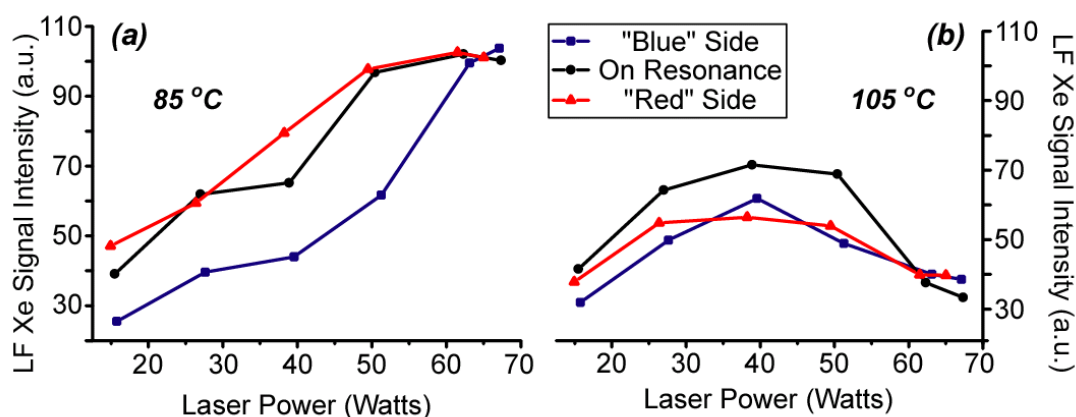


Fig. 10.6 Plots of LF HP ^{129}Xe signal intensity vs laser flux at three separate spectral offsets: ‘blue side’ (~794.61 nm); ‘on resonance’ (~794.76 nm); and ‘red side’ (~794.87 nm) for two separate T_{cell} 's: **(a)** 85 °C and **(b)** 105 °C. OP loading: 300 torr Xe, 1700 torr N_2 . **(a)** While ‘red side’ and ‘on resonance’ begin to saturate at increased laser flux, ‘blue side’ keeps increasing. **(b)** At increased T_{cell} , all three spectral offsets show evidence of Rb runaway⁶⁵ upon increases laser flux.¹¹⁶

While similar results were observed when the same experiment was conducted at 2000 torr Xe (Fig. 10.7), there were a few key differences. For example, the ‘blue side’ offset never approached P_{Xe} values attained by the other two offsets at $T_{OPT} = 75\text{ }^{\circ}\text{C}$, even at the highest incident laser powers. However, upon increased T_{cell} (85-105 $^{\circ}\text{C}$), the ‘blue side’ resonance provided the highest LF ^{129}Xe signal; furthermore, while overall P_{Xe} decreased upon increased T_{cell} , it did not plummet as dramatically as for the 300 torr Xe runs (*data not shown*).

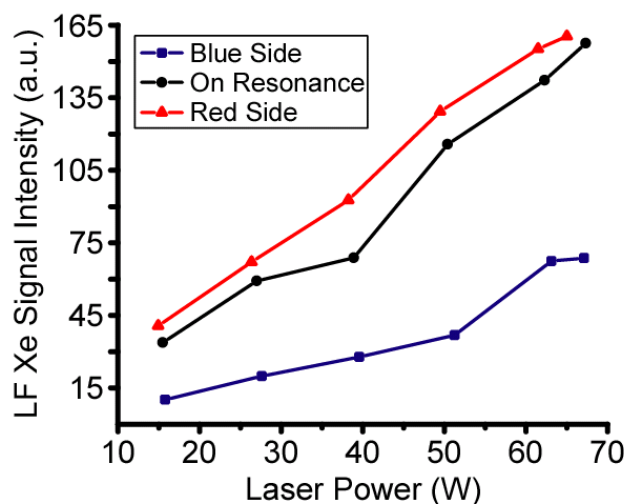


Fig. 10.7 Same as Fig. 10.6, but with a 2000 torr Xe (600 torr N_2) gas loading and $T_{cell}=75\text{ }^{\circ}\text{C}$. The ‘red side’ and ‘on resonance’ offsets do not appear to saturate at any point, and are clearly superior to the ‘blue side’ offset for all laser powers (at T_{OPT}).¹³⁴ Increases to T_{cell} resulted in lowered P_{Xe} signal and an emerging superiority of the ‘blue side’ offset (*data not shown*).

10.4.4 Dependence of P_{Xe} on T_{cell} and Spectral Offset

The narrowed spectral output ($\sim 0.26\text{ nm}$ FWHM) and ability to tune over a wide range of relevant wavelengths ($> 1.3\text{ nm}$) without changing output power has allowed the ‘on-chip’ VHGLDA to be used to map out the optimal spectral

offset as a function of T_{cell} for a variety of $[\text{Xe}]_{\text{cell}}$ loadings (e.g., the 2000 torr Xe cell loading shown in Fig. 10.8). The highest P_{Xe} values were achieved at a low T_{cell} value ($T_{\text{OPT}} = 75\text{ }^{\circ}\text{C}$) while the output was red-shifted from the Rb D_1 . Indeed, upon increasing T_{cell} , the HP ^{129}Xe low-field signal decreased, and the optimal spectral range for peak P_{Xe} broadened asymmetrically (on the ‘red’ side) as well as bifurcated (so that the highest P_{Xe} values are achieved at wavelengths that are increasingly distant from the Rb D_1 transition—on both sides). This bifurcation of optimal spectral offsets observed for increasing T_{cell} emphasizes the importance of OP at a slight spectral offset; even as the Rb absorption line broadens, it is important to compensate by being even further off resonance (to a point). This bifurcation may also help explain why we (previously) noticed improved P_{Xe} values with a blue-shifted offset while using the Comet laser (i.e., those runs were likely at T_{cell} 's higher than T_{OPT}). The optimal ranges for peak P_{Xe} at each T_{cell} match up quite well with the percent transmittance of laser light for each run (Fig. 10.8 bottom); at T_{OPT} , the wavelength for peak P_{Xe} also corresponds to the wavelength of highest light absorption. As the cell temperature increases, the peak absorption deepens, broadens, and red-shifts as well—and the highest T_{cell} values result in most of the laser light being absorbed even $\sim 0.75\text{ nm}$ on the ‘red’ side of the Rb D_1 . This data demonstrates the clear benefit to optical pumping at each $[\text{Xe}]_{\text{cell}}$'s T_{OPT} , especially using lower cell temperatures for higher xenon densities. It also indicates that the Rb absorption line may indeed asymmetrically-broaden and red-shift upon increases

to T_{cell} —an effect that could help further explain the $T_{\text{OPT}}/[\text{Xe}]_{\text{cell}}$ interdependence that was described earlier.

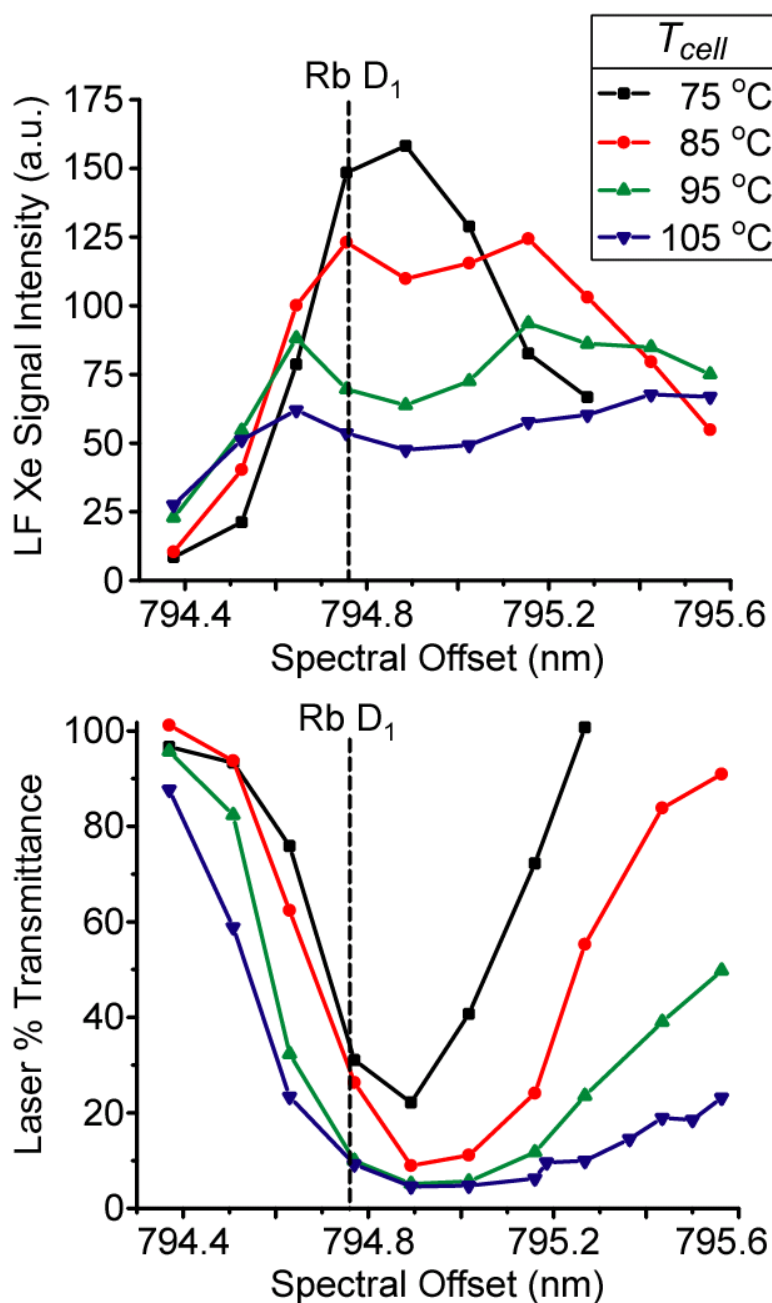


Fig. 10.8 *Top:* Low-field ^{129}Xe NMR signal as a function of laser spectral offset for a variety of T_{cell} . *Bottom:* Percent transmittance of polarizing laser beam as a function of T_{cell} . With increases in T_{cell} , optimal spectral offset range broadens, while P_{Xe} decreases (as does % transmittance). OP conditions: 2000 torr Xe, 600 torr N_2 ; driving current: 35.1 A (~ 63 W resonant laser power).¹¹⁶

10.4.5 Dependence of P_{Xe} on $[Xe]_{cell}$ and Spectral Offset

Changes to the Rb D_1 spectral shift and lineshape that are caused by the various in-cell xenon densities may affect the optimal spectral offset at which maximum P_{Xe} is achieved. Indeed, the absorbance of light by Rb is clearly

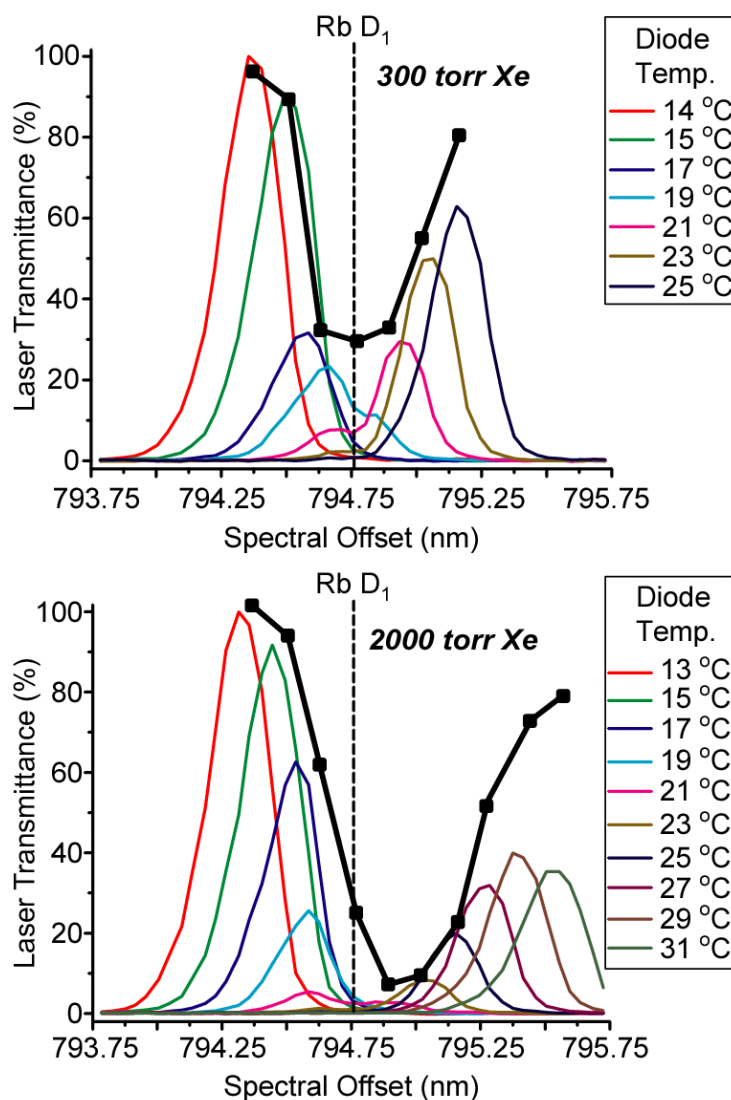


Fig. 10.9 *Top:* Transmitted laser spectra (35.1 Å; ~63 W) at various spectral offsets (i.e., LDA temps) plotted against the percent transmittance (black) of the laser light exiting the OP cell (300 torr Xe, 1700 torr N₂). *Bottom:* Same, but for 2000 torr Xe, 600 torr N₂ (T_{cell} : 85 °C for both data sets). Rb absorbance profile deepens, broadens, and red-shifts with increases in $[Xe]_{cell}$.¹¹⁶

dependent on $[\text{Xe}]_{\text{cell}}$, as changing from 300 to 2000 torr of xenon brings about broadening, red-shifting, and increased light absorption (Fig. 10.9).

While some amounts of increased broadening (due to increased overall cell pressure—2600 torr vs 2000 torr) and red-shifting are expected, the apparent $[\text{Xe}]_{\text{cell}}$ -dependent shift is significantly greater (~ 0.2 nm for 2000 torr Xe) than what is predicted (~ 0.04 nm)¹¹⁴. Also, the laser seems to be absorbed in a highly

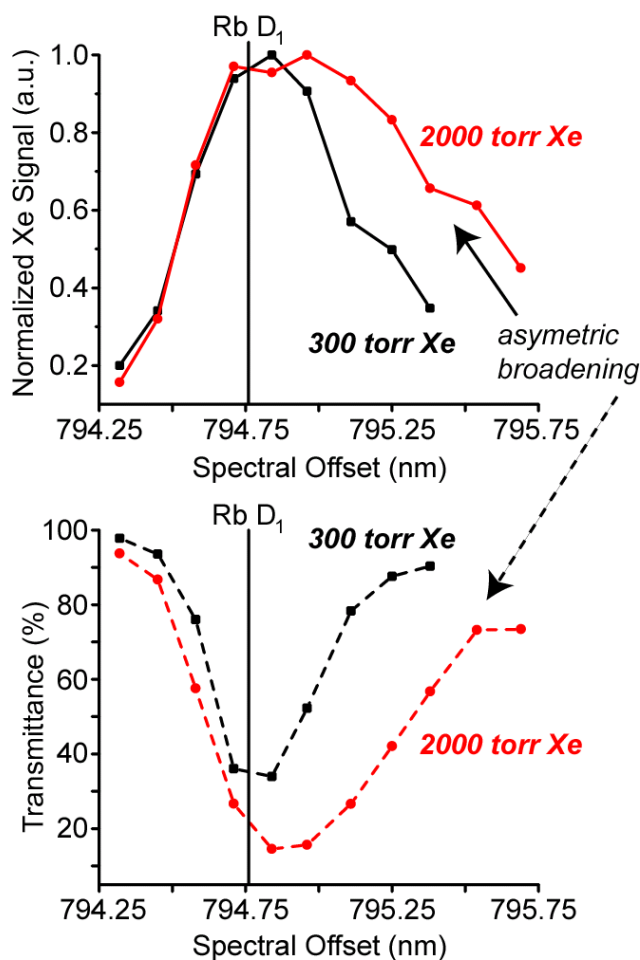


Fig. 10.10 *Top:* Normalized LF ^{129}Xe NMR signal as a function of spectral offset for two $[\text{Xe}]_{\text{cell}}$ loadings (300 torr-black; 2000 torr-red). *Bottom:* Percent transmittance of laser light passing through OP cell at different $[\text{Xe}]_{\text{cell}}$, spectral offsets. Runs at $T_{\text{cell}} = 85$ °C; ~ 63 watts laser power. Increased asymmetric broadening at higher wavelengths is noticed for both P_{Xe} and percent transmittance studies¹³⁶, due to changes to the Rb absorption lineshape at increased $[\text{Xe}]_{\text{cell}}$.¹¹⁴

asymmetric fashion, favored more heavily on the longer wavelength side. This effect is further demonstrated in Fig. 10.10, which includes both LF HP ^{129}Xe measurements and percent transmittance for 300 & 2000 torr Xe cell loadings.

10.5 P_{Xe} COMPARISON OF NARROWED VERSUS BROADBAND LDAS AT INCREASED LASER FLUX¹³⁴

When the Comet was first introduced, it was shown capable of providing a ~3-fold watt-for-watt increase in P_{Xe} (as measured at high field) when compared to a conventional broadband laser (Fig. 8.3). However, this was for a single laser power (of ~30 W) at various cell temperatures. Acquisition of a second, higher power broadband LDA (up to ~100 W; linewidth ~2.3 nm FWHM, relatively

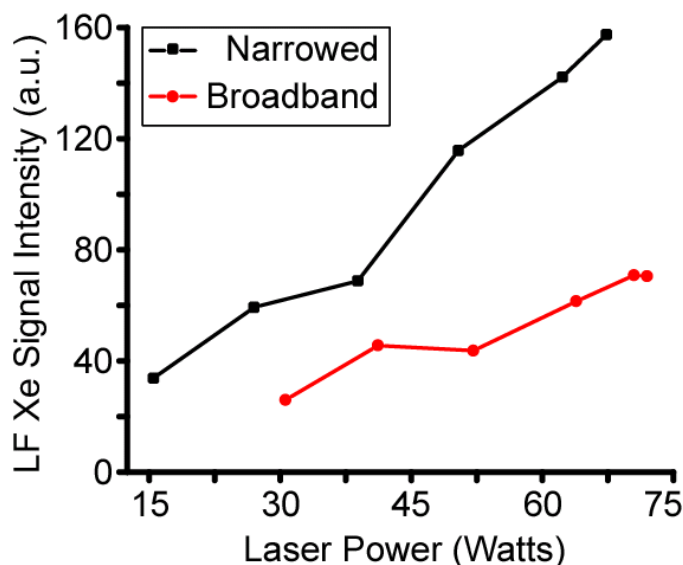


Fig. 10.11 LF ^{129}Xe NMR signal intensity as a function of laser power for a VHG-narrowed LDA (~0.26 nm FWHM- black) and a broadband LDA (~2.3 nm FWHM- red). OP cell conditions: 2000 torr Xe, 600 torr N_2 , $T_{\text{cell}} \sim 75^\circ\text{C}$. VHG-narrowed laser provides ~2.5 fold increase in ^{129}Xe signal over entire range of laser powers.¹³⁴

'clean' lineshape) from QPC has allowed for a direct comparison of narrowed versus broadband laser sources over a full range of laser powers (from ~30 to 68 W) for $[\text{Xe}]_{\text{cell}} = 2000$ torr. Over this range, the 'on-chip' VHG-LDA showed an average ~2.5 fold increase in HP ^{129}Xe NMR signal (detected at low field; Fig. 10.11), with remarkable advantages at increased laser fluxes—thus further demonstrating the superiority of VHG-narrowed laser sources for SEOP.

10.6 P_{Xe} DYNAMICS AS A FUNCTION OF T_{CELL} , $[\text{Xe}]_{\text{CELL}}$, & SPECTRAL OFFSET¹³⁶

To further study the dependence of P_{Xe} on spectral offset at various $[\text{Xe}]_{\text{cell}}$ values, P_{Xe} build-up curves were analyzed with the hope of extracting fundamental SEOP parameters (by applying essentially the same analysis as was in Section 9.5). To the author's knowledge, the effects of varying the excitation wavelength have not been studied extensively in the past; also, there are not expected to be any dependencies of the spin-exchange rate on the excitation wavelength. However, as certain $[\text{Xe}]_{\text{cell}}$ values seem to 'prefer' different spectral offsets, any resulting changes to the spin-exchange efficiency could shed additional light onto the origins of this preference. Thus, P_{Xe} buildup curves were acquired using an even higher powered (~140 W, measured directly from the fiber) 'on-chip' VHG-LDA at a variety of spectral offsets to determine how the OP efficiency depends on the excitation wavelength.

10.6.1 Higher Power, 'On-Chip' VHG-LDAs

Because the VHG grating is an integral component of the laser itself (as opposed to an optic placed in front of the diode) for the 'on-chip' design, many laser diodes can be placed inside a single laser module. This advantage was fully exploited, as we were recently able to obtain an 'on-chip' VHG LDA (from QPC) that is comprised of six laser diodes and capable of producing laser powers exceeding 140 W of frequency-narrowed light—thereby providing an unprecedented amount of resonant laser power.

This 'on-chip' laser works quite similarly to the previously characterized ~80 W narrowed laser; it is tuned by changing the temperature of the laser diode ($\sim 0.07 \text{ nm}/^\circ\text{C}$) and has a tuning range exceeding 1 nm (it can also be tuned by varying the driving current). While tuning, there is a slight drop in power with increased temperature ($\sim 0.5 \text{ W}/^\circ\text{C}$), but this can be compensated for by adjusting the driving current; also, the lineshape of the narrowed output ($\sim 0.30 \text{ nm FWHM}$) changes minimally with temperature. The laboratory footprint of this ~140 W narrowed laser is larger than that of the lower power models (Fig. 10.12 *left*), but is still relatively small (similar area as a common shoebox).

The new higher power on-chip VHG-LDA is water cooled (with the same water chiller mentioned earlier) and is driven with the same 6-volt power supply unit. Under conditions of very high power ($\sim 120 \text{ W}$) and blue-shifted spectral offset (requiring that the laser be extensively cooled), the water chiller was not able to sufficiently cool the laser, and an ice water bath had to be added in series to achieve the desired LDA temperatures.

For this laser set-up, we took advantage of newer, shorter fiber optics that are highly polarization-preserving (~ 30 cm in length; $800\ \mu\text{m}$ core size). This allowed the binocular CP box to be replaced with a new single-axis polarizer of a monacle design; this monacle simply consists of a collimator, corner cube, heat sink, and quarterwave plate. Because $\sim 90\%$ of the light emitted from the fiber is of a particular linear polarization (due to the efficiency of the 'on-chip' design), it transmits through the corner cube and quarterwave plate, and is directed at the OP cell. The 10% of light that is linearly polarized in a different direction reflects

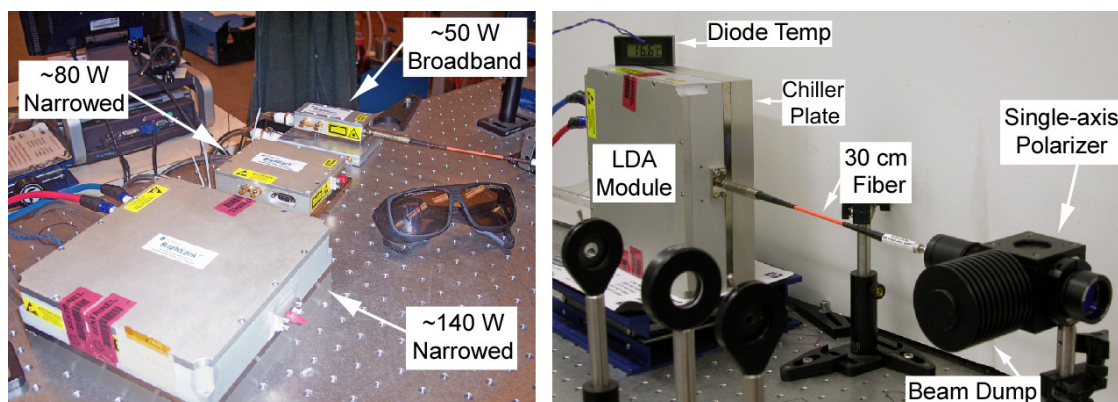


Fig. 10.12 *Left:* Size comparison of the high power, 'on-chip' VHGLDA (front) used in the following studies, vs. a similar model (middle) that is lower in power (~ 80 W) and a ~ 50 W, conventional broadband-type LDA (back) attached to short fiber optic (30 cm). All lasers were purchased from QPC. *Right:* High power, 'on-chip' VHGLDA coupled to single-axis polarizer via a short (30 cm) polarization-preserving fiber. Polarizing 'monacle' consists of collimator, corner cube, beam dump, and quarter-wave optics. Single-beam design removes the traditional 'skew' pump beam (which may be detrimental to SEOP) and makes laser/cell alignment much simpler (with minimal losses in laser flux).¹³⁶

off the corner cube and is dumped to the heat sink. While some of the overall laser power is lost, it is only $\sim 10\%$ (and not a significant amount when one has ~ 140 W of total available laser power). The benefits of this design are simplicity,

ease of laser/OP cell alignment, and removal of the skew beam (which is not as efficient at OP anyway).

Fig. 10.12 *right* shows the new, higher power VHG-LDA connected to the new single-axis polarizer via the short fiber; the laser is placed on its side to match the linear polarization of the emitted light with that which is allowed to transmit straight through the corner cube. Furthermore, the new monochrome polarizer is equipped with optics that can be used at 795 nm as well as 852 nm and 894 nm, to allow for use in Cs/¹²⁹Xe SEOP studies (to be detailed in Chapter 11) without a loss in optical efficiency.

While this high-powered laser is capable of outputs of ~140 W as measured directly from the fiber optic (Fig. 10.13; ~120 W incident on OP cell), the

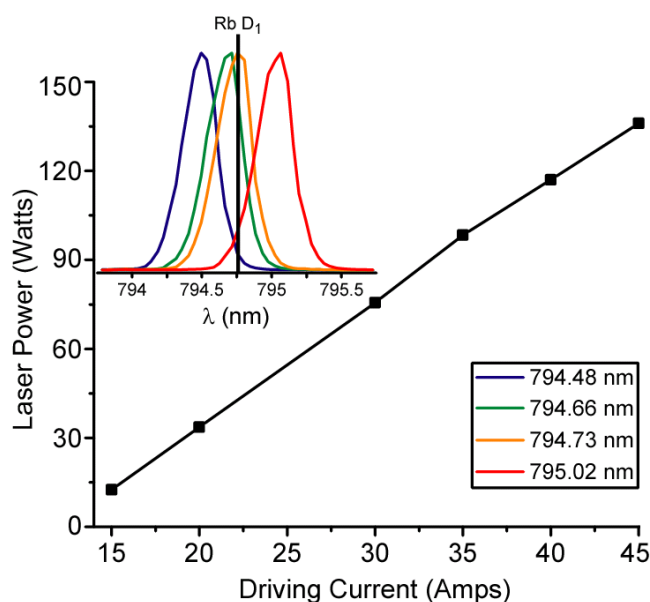


Fig. 10.13 Laser output power as a function of driving current for the high-power 'on-chip' VHG-narrowed LDA (from QPC). Power monitored after exiting fiber optic (LDA temp: ~21 °C). *Inset:* normalized transmitted laser spectra for the four λ -offsets used in the P_{Xe} buildup curve experiments (~80 W laser power; ~0.30 nm linewidth). Offset varied by changing driving current & diode temperature.¹³⁶

following P_{Xe} dynamics studies were conducted at ~ 80 W in order to remove the threats of both laser saturation (so that P_{Xe} vs laser flux is still in linear regime) and Rb runaway and to increase the comparability to previous variable offset experiments. The laser was tuned to four distinct excitation wavelengths (794.48 nm, 794.66 nm, 794.73 nm, and 795.02 nm) that cover a significant range of spectral offsets on both sides of the Rb D_1 absorption line (Fig. 10.13 *inset*).

10.6.2 P_{Xe} Build-Up Dynamics as a Function of Spectral Offset and $[Xe]_{cell}$

P_{Xe} build-up curves were measured for a variety of $[Xe]_{cell}$, T_{cell} , and spectral offsets (Fig. 10.14). The curves were attained in a slightly different fashion than

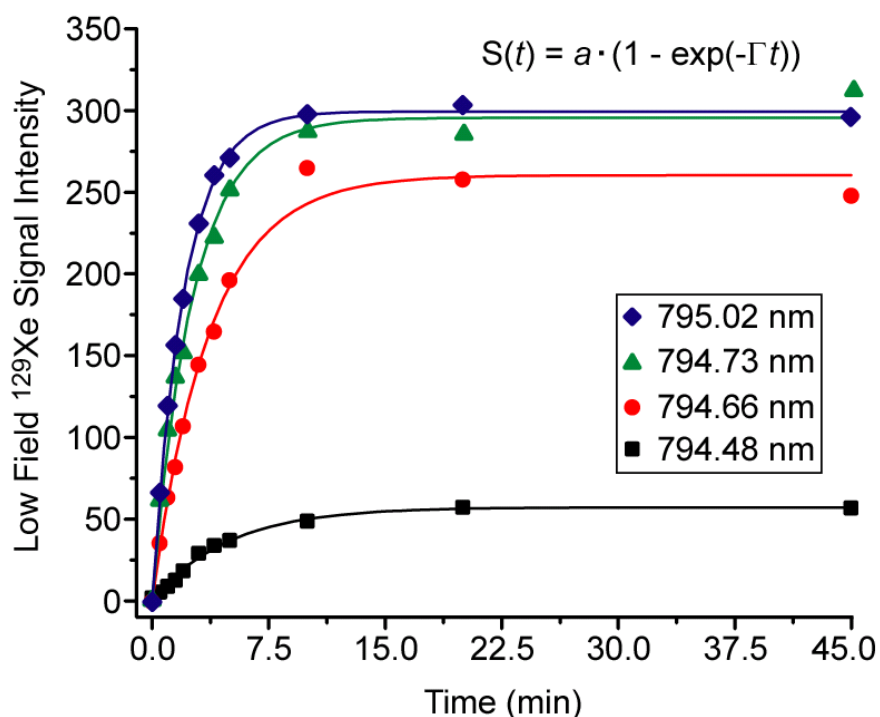


Fig. 10.14 Selected P_{Xe} buildup curves (collected at low-field) as a function of laser spectral offset. Cell conditions: 2000 torr Xe, 600 torr N_2 , $T_{cell} = 60$ °C, ~ 80 W resonant laser power. P_{Xe} buildup rate and overall signal intensity increase with higher wavelength light, signaling that the spin-exchange rate may have a dependence on the excitation wavelength.¹³⁶

those of Chapter 9: instead of continually sampling P_{Xe} at regular intervals during the polarization build-up, a more 'saturation recovery'-type approach was used, where the P_{Xe} was depleted (by crusher pulses), allowed to build for a set amount of time, and then detected. This process was repeated for each desired time point. While initially taking longer than the previously described method, the data is much smoother, and allows the final P_{Xe} curves to be generated from a single experiment instead of an average of four runs (thus rendering the two detection methods roughly equal in regards to time spent). Also, there is no need for a correction factor that takes into account the P_{Xe} magnetization loss from each pulse (as each acquisition is treated as its own separate experiment). Data points are weighted more heavily in the early time regime (one acquisition every 30 sec or 1 min for first 5 min), then a single point is acquired every several minutes for the longer time-interval runs. The curves are fit to Eq. 9.1, and the steady-state HP ^{129}Xe NMR signal (a) and build-up curve time constant (Γ) are extracted from each line fitting and used for additional data analysis. It appears that the excitation wavelength has great influence over the optimal OP conditions, as the initial slopes of the build-up curves rise more steeply for longer-wavelength spectral offsets, as well as attain the highest steady-state P_{Xe} signals (Fig. 10.14 demonstrates this for a 2000 torr Xe cell loading).

By plotting the values of Γ versus the rubidium number density (as calculated from vapor pressure curves)⁷⁷, one is left with a straight line whose slope is equal to γ' and y -intercept provides the in-cell ^{129}Xe spin-relaxation rate ($1/T_1$; see Eq. 2.9); indeed, Fig. 10.15 demonstrates this type of data plot for a

2000 torr Xe cell loading with an excitation wavelength of 794.73 nm (closest offset to Rb D₁ in this set of experiments). Typical values of γ' that were observed for these experiments ranged from 3-9 $\times 10^{-15}$ cm³ s⁻¹; while these values are approximately an order of magnitude higher than what is predicted⁵³ for these [Xe]_{cell} loadings, they still fall within an acceptable range of commonly reported γ' values for Rb/¹²⁹Xe SEOP.²⁰⁶ For the different excitation wavelengths, γ' typically increased with longer wavelength illumination. Also, the in-cell ¹²⁹Xe T₁ was quite short (only ~3.37 min); this could possibly be caused by contaminations due to OP cell impurities (exacerbated by the high spin-destruction rate commonly expected with high [Xe]_{cell} loadings).

By plotting the γ' values (as determined from the Γ vs [Rb]_{cell} plots) as a

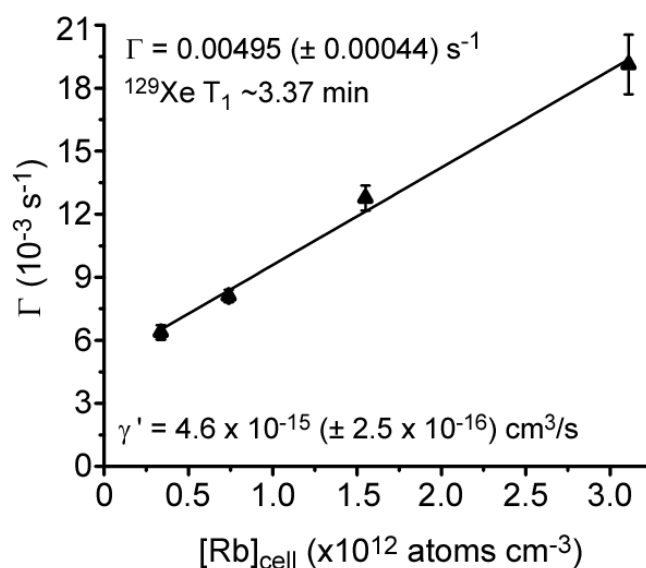


Fig. 10.15 P_{Xe} growth curve time constant (Γ) vs. estimated Rb number density for 2000 torr Xe cell loading (plus 600 torr N₂); 794.73 nm excitation wavelength. Slope of line provides γ' ; intercept gives Γ_{Xe} .¹³⁶ γ' values typically increase with excitation wavelength at a given [Xe]_{cell}.

function of $1/P_a$, the spin-exchange contributions from binary collisions (y -intercept) and three-body interactions (slope) can in principle be determined⁵³ (Eq. 2.10). It is generally expected that the resulting plot should resemble a straight line with a gently increasing slope (see Fig. 9.10, '*predicted*'). However, while the runs for 100 & 2000 torr Xe gas loadings appear to fit this type of general trend for the three shortest wavelength offsets, the runs at 500 torr, along with all runs at $\lambda = 795.02$ nm, do not fit the expected trend (Fig. 10.16). Furthermore, if the plots could be trusted as being accurate (omitting the 500 torr Xe & 795.02 nm runs for the time being), then the values for γ_{RbXe} and σ_V would also be about an order of magnitude higher than expected.⁵³

In an attempt to shed more light on the anomalous points at 500 torr Xe (and possibly determine if it is completely due to $[\text{Xe}]_{\text{cell}}$), the data was also

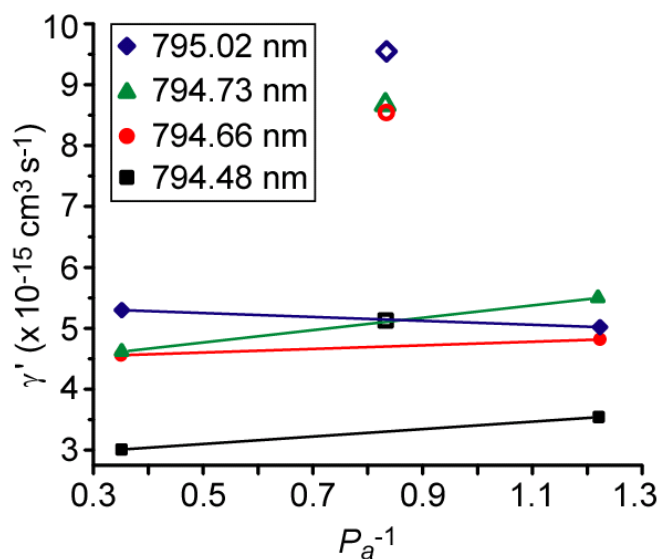


Fig. 10.16 γ' values (i.e., as determined in Fig 10.15) plotted as a function of OP gas composition/density (P_a^{-1}) for the four laser offsets. Open symbols denote runs at 500 torr Xe; these runs do not fit the expected trend.¹³⁶

analyzed in another fashion: instead of plotting γ' as a function of $1/P_a$ (which takes into account both xenon and nitrogen densities), γ' was simply plotted against $[\text{Xe}]_{\text{cell}}$ (Fig. 10.17). In this type of graph, γ' is expected to fall off upon increases to the xenon density, as the 3-body contribution to γ' should decrease with increases to $[\text{Xe}]_{\text{cell}}$. However (and similarly to Fig. 10.16), only the three shortest wavelength runs for 100 and 2000 torr Xe fit this general type of trend; additionally, γ' is expected to decrease significantly more than it does in Fig. 10.17, and should be relatively flat by $[\text{Xe}]_{\text{cell}} \sim 350$ torr Xe.⁵³

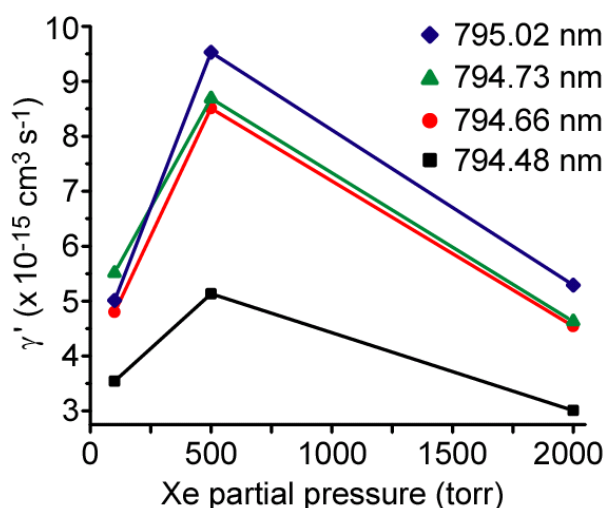


Fig. 10.17 γ' values plotted as a function of $[\text{Xe}]_{\text{cell}}$ for the four laser offsets. γ' is expected to decrease with increased xenon density.¹³⁶

It is unclear why the 500 torr Xe (and all 795.02 nm) experiments do not fit these expected trends, or why, if the 500 torr runs were to be omitted, the γ' dependence on $[\text{Xe}]_{\text{cell}}$ would still not be as steep as what would be expected. Of course, as there is not expected to be a dependence of γ' on the excitation wavelength, the above results are puzzling. The reasons behind this apparent λ -

dependence are not well understood (but could be due to changes in $[Rb]_{\text{cell}}$ due to differential laser heating at different wavelengths) and will be the subject of future studies.

10.6.3 P_{Xe} Build-Up Rates and Steady-State Values as a Function of T_{cell} at Different $[Xe]_{\text{cell}}$, Spectral Offsets

Additional studies attempted to determine the optimal SEOP parameters needed to achieve maximal P_{Xe} values by studying the LF HP ^{129}Xe NMR signal, P_{Xe} build-up curve time constants, and percent transmittance of the laser light at a variety of $[Xe]_{\text{cell}}$, T_{cell} , and spectral offsets (Fig. 10.18). Plots of the steady-state P_{Xe} NMR signal intensity as a function of T_{cell} demonstrate the optimal cell temperature for each spectral offset (Fig. 10.18 *left*). As expected, the 100 torr Xe runs have a higher T_{OPT} than the runs at 2000 torr Xe (90 °C vs 70 °C). However, while the runs at 500 torr Xe are expected to peak at around 75 °C (794.48 nm data most consistent), the highest steady-state P_{Xe} signals were actually found at 60 °C (after 45 min of OP) for the three longest wavelength offsets. Furthermore, the LF ^{129}Xe signal found at 60 & 70 °C for the three longest wavelength offsets is much higher than expected (and even higher than those found during the 2000 torr Xe run). This dramatically increased signal for the 500 torr Xe experiment is the most likely reason for the anomalously high γ' value at that $[Xe]_{\text{cell}}$, and the cause of our inability to fit the data set to a relevant SEOP equation. However, it is unclear why such large ^{129}Xe signal intensities were found for this particular gas loading.

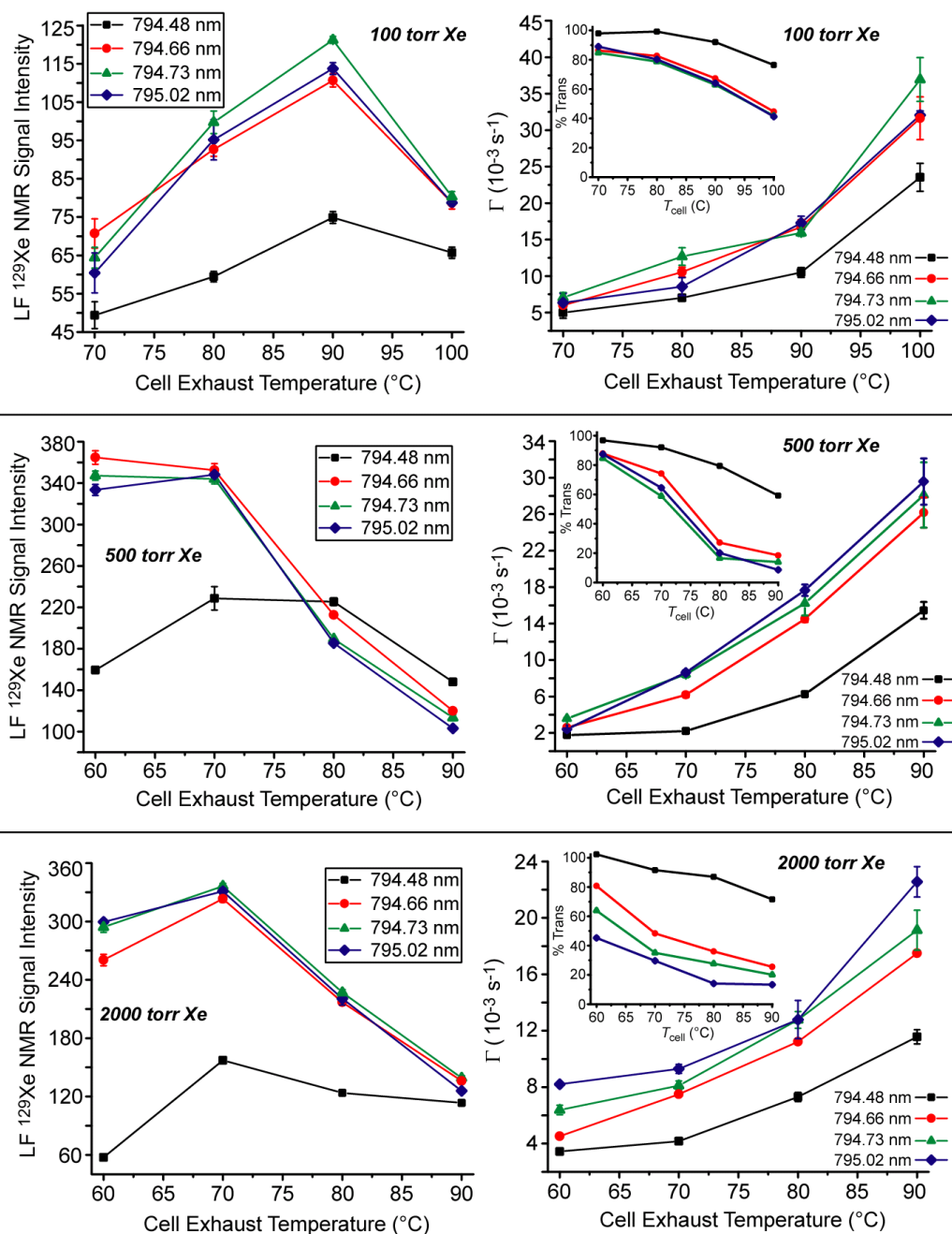


Fig. 10.18 *Left:* Steady-state P_{Xe} NMR signal intensities (collected at low field) as a function of T_{cell} at different laser excitation wavelengths for three $[\text{Xe}]_{\text{cell}}$ -loadings (100 torr Xe-top; 500 torr Xe-middle; 2000 torr Xe-bottom). *Right:* P_{Xe} growth-curve rate constant (Γ) as a function of T_{cell} at different spectral offsets, $[\text{Xe}]_{\text{cell}}$'s. *Insets:* percent transmittances of the laser light exiting the rear of the OP cell for the corresponding laser offsets at each $[\text{Xe}]_{\text{cell}}$.

In an attempt to ‘step back’ from the efforts to extract fundamental SEOP parameters, and instead try to attain a more intuitive feel of how the build-up rate varies as a function of cell temperature and laser spectral offset, the P_{Xe} build-up curve rate constant (Γ) was plotted as a function of T_{cell} (as opposed to $[Rb]_{cell}$) at each offset (Fig. 10.18 *right*). For all runs, the shortest wavelength of excitation (794.48 nm) consistently provided the lowest Γ values as a function of temperature; additionally, the separation in Γ between this particular spectral offset and the others grew increasingly with $[Xe]_{cell}$. Correspondingly, the 794.48 nm runs all exhibited the highest percent transmittance of laser light through the cell; indeed, even at the highest T_{cell} values, never more than half of the laser light at 794.48 nm was absorbed by the Rb vapor. The remaining three excitation wavelengths remained more clustered together throughout the different T_{cell} 's and $[Xe]_{cell}$'s, although they did become increasingly separated at higher xenon cell densities; increased $[Xe]_{cell}$ loadings also demonstrated a clear preference for the longer wavelength offsets (this trend both holds for Γ values and percent transmittances). As expected, the excitation wavelength that is the most highly absorbed by the Rb vapor (typically the red-shifted offsets) usually corresponds to the fastest P_{Xe} build-up times.

10.7 CONCLUSIONS

The addition of VHG-LDAs with integrated ‘on-chip’ gratings have allowed for a number of SEOP experimental parameters to be mapped out individually, including the dependencies of P_{Xe} on $[Xe]_{cell}$, T_{cell} , spectral offset, and laser flux.

Because the laser output is spectrally tunable independent of laser flux and with minimal changes to the emission lineshape, true ‘apples-to-apples’ comparisons can be made at the different experimental conditions. Combined with an improved low-field detection capability (i.e., the ‘bucking’ coil), an unexpected interdependence of T_{cell} and laser flux was observed, where T_{OPT} was lowered upon increases to laser power (counter to general expectations). Indeed, at high T_{cell} and high laser flux, Rb runaway can be observed at a variety of $[\text{Xe}]_{\text{cell}}$ and spectral offsets. It was also noticed that the optimal spectral offset varies with both $[\text{Xe}]_{\text{cell}}$ and T_{cell} ; the Rb absorption line itself appears to asymmetrically broaden and red-shift upon increases to $[\text{Xe}]_{\text{cell}}$, while the spectral offset for peak P_{Xe} will broaden, red-shift, and bifurcate upon increased cell temperatures. Corresponding percent transmittance measurements of the laser beam show similar dependencies of $[\text{Xe}]_{\text{cell}}$ and T_{cell} on the spectral offset. Also, the previously reported ~ 3 -fold watt-for-watt increase in P_{Xe} upon switching from a broadband laser to a VHG-LDA was reaffirmed over a wider range of laser powers.

An even more powerful ‘on-chip’ VHG-LDA (capable of emitting ~ 140 W from the end of the fiber optic), in addition to a new single-axis polarizer, were used to study P_{Xe} build-up dynamics as a function of laser spectral offset. While the spin-exchange contributions from 2-body and 3-body interactions could not be measured separately, it does appear that the spin-exchange rate may have an unexplained dependence on the excitation wavelength. The currently leading theory is that the wavelengths that experience increased light absorption provide

heat to the system, thus increasing $[\text{Rb}]_{\text{cell}}$ at a rate that is not reflected in the T_{cell} measurements (therefore skewing the Γ vs estimated $[\text{Rb}]_{\text{cell}}$ plots that determine γ'). This hypothesis is supported by the decreased light transmission for the longer excitation wavelengths—especially prevalent at high $[\text{Xe}]_{\text{cell}}$ (Fig. 10.18). Indeed, in order to truly get to the bottom of these (thus far) failed attempts at extracting fundamental SEOP parameters from P_{Xe} build-up curves, *in-situ* measurements of $[\text{Rb}]_{\text{cell}}$ and P_{Rb} will likely be necessary.

10.7 SUMMARY AND OUTLOOK ON $\text{Rb}/^{129}\text{Xe}$ SEOP

While it has been used for many years to produce hyperpolarized xenon for a variety of NMR/MRI applications, and despite the in-depth characterization of the underlying physics of the system (throughout the years), $\text{Rb}/^{129}\text{Xe}$ SEOP remains a robust and ever-changing area of active research. Indeed, while the work that is presented in this dissertation has mostly focused on increasing P_{Xe} values of high $[\text{Xe}]_{\text{cell}}$ batch-mode SEOP, many of the results can be applied to both stop-flow and continuous-flow apparatuses. Furthermore, many of the findings presented in this work detail results that are not commonly expected (or predicted, using the equations in Chapter 2), especially at high $[\text{Xe}]_{\text{cell}}$ loadings.

There are several results that occurred throughout the course of this work that warrant further highlighting; one can think of them as a general guidelines for high xenon density $\text{Rb}/^{129}\text{Xe}$ SEOP: The increases in light absorption efficiency afforded by frequency-narrowed laser sources can increase xenon polarization levels by at least a factor of three. By taking advantage of low-field

HP ^{129}Xe NMR polarimetry, *in situ* studies have demonstrated that there is a sensitive dependence of the optimal cell temperature for P_{Xe} on the in-cell xenon density; by utilizing this temperature dependence, very high P_{Xe} values can be achieved, including high P_{Xe} values at high $[\text{Xe}]_{\text{cell}}$'s. Changes to the Rb absorption lineshape and offset can be used to optimize the excitation wavelength and laser power at increased $[\text{Xe}]_{\text{cell}}$. Indeed, it seems most important (as it has been shown many times throughout this work) to optimize the amount of light transmitting through the OP cell. Many OP groups spend great amounts of time and energy trying to increase the spin-exchange rate (typically by increasing T_{cell} and lowering $[\text{Xe}]_{\text{cell}}$); one could argue, based on the results in this work, that optimal OP cell illumination (working in tandem with minimal spin-destructive processes) could prove key to achieving the highest P_{Xe} values throughout a wide range of $[\text{Xe}]_{\text{cell}}$ values.

Given the results shown in this dissertation as a starting point, there are a number of directions to expand on the Rb/ ^{129}Xe SEOP studies initiated in the Goodson laboratory. First and foremost would be a method to optically detect both the rubidium number density (as it is likely much different than that estimated from vapor pressure curves) and the rubidium electron spin polarization.^{56,208} The ability to measure these two parameters would greatly increase our understanding of the spin-exchange physics, and figuring out how to maximize P_{Rb} is truly the first step to maximizing P_{Xe} . Optical electron spin resonance methodologies can be used to map P_{Rb} across the cell, and study

SEOP under conditions of varying cell geometries and degrees of cell illumination (i.e., looking at effects of 'dark' Rb).

A number of surprising temperature dependencies (i.e., $[\text{Xe}]_{\text{cell}}$, laser flux, spectral offset) have been discussed in this work. However, our best ability to measure T_{cell} has simply been to monitor the temperature of the air blowing across the outer surface of the inner OP cell. While this information is useful in a practical, qualitative way (i.e., how hot the cell has to be in order to attain a specific level of P_{Xe}), it is not sufficiently indicative of the temperature of the actual gas mixture during OP. Previous work¹¹² has shown, through *in situ* Raman spectroscopy, that the rovibrational temperature of the nitrogen buffer gas can easily exceed 900 °C with only 15 W of broadband laser irradiation, T_{cell} (*surface*) ~100 °C, and only enough N₂ to quench Rb emissions (a few hundred torr). Under the OP conditions described in this dissertation (high power, frequency narrowed lasers and several hundreds of torr of N₂ with no helium buffer gas), it is expected that the N₂ temperature could be even higher. This excessive gas heating may affect the nature of energy transport across the cell, both on the macroscopic and local/molecular levels; for instance, this could lead to longitudinal currents that prolong the HP ¹²⁹Xe's contact time with the cell walls, leading to increased depolarization. Furthermore, if the Rb D₁ absorption lineshift and broadening effects are dependent on the gas temperature (especially for xenon and nitrogen), then the massive amounts of heat in the cell could play a significant role in the T_{cell} dependencies on spectral offset that were observed. As VHG-LDAs become even more powerful (hundreds of watts) and

spectrally narrower (approaching the Rb absorption linewidth), the issue of energy transport within the OP cell will become increasingly more important.

In addition to further fundamental studies of SEOP, the results presented in this work could also introduce a new protocol for producing HP ^{129}Xe for human lung imaging. Presently, continuous flow set-ups are used to polarize a small amount of gas at an instant, and collect the product over time (typically via freezing). A cheaper and simpler solution could be to use high $[\text{Xe}]_{\text{cell}}$ batch-mode SEOP to polarize the same total amount of gas (to the same P_{Xe} levels) in a single batch. In order to achieve this, a 'scaled-up' version would be required to produce the needed amount of polarized gas in a relevant time frame (approximately one atmospheric liter per hour). This would require a much larger OP cell, as well as novel laser excitation designs (such as even higher-power frequency-narrowed lasers, or possibly simultaneous laser illumination at each end of the OP cell). Further characterization of cell volumes and geometries (such as minimizing the surface-to-volume ratio) should also be an area of extensive research interest. Furthermore, a way to bypass the cryogenic collection step would also be a highly valuable advancement, as the acts of freezing and sublimating lowers P_{Xe} values and adds experimental complexity that is not desired in a clinical setting. There has been recent progress⁷⁰ in long-term storage of gaseous HP ^{129}Xe (~4-6 hrs); when combined with a 'xenon-rich' OP mixture, a gaseous collection system (as opposed to a cryogenic freeze-out) could be a simpler, cheaper, and more efficient innovation. Despite these issues (along with numerous others) that will need to be addressed, a batch-mode

SEOP apparatus could very well be used in the future for human lung imaging with HP ^{129}Xe .

CHAPTER 11

PRELIMINARY STUDIES OF Cs/¹²⁹Xe SEOP

11.1 INTRODUCTION

Rubidium has long served as the ‘workhorse’ alkali metal for the SEOP community⁵⁴, mostly due to its large spin-exchange cross sections⁷⁵, low vaporization temperature⁷⁶, and the abundance of inexpensive, high-powered light sources (i.e. laser diode arrays) that can readily reach its absorption wavelengths.⁷⁸ Despite these benefits, there may be even greater advantages to using *cesium* for SEOP: namely, the Cs/¹²⁹Xe spin-exchange cross section is estimated⁷⁸ to be ~1.9 times greater than that of Rb/¹²⁹Xe, while the Cs/¹²⁹Xe collisional spin-destruction cross section⁸² may be half that of Rb/¹²⁹Xe.⁸³ Additionally, cesium has an even lower vaporization temperature (~28.5 °C), more photons per Watt of light (due to lower energy absorption lines)⁸⁴, and greater energy spacing between the D-lines (as Rb/¹²⁹Xe SEOP may be disadvantageously affected by simultaneous pumping of the (red-side) wing of the Rb D₂ line^{85,86}).

Although the above factors would indicate improved generation of HP ¹²⁹Xe through cesium optical pumping, there has yet to be any clear advancement to HP ¹²⁹Xe production using this method; in fact, Cs/¹²⁹Xe SEOP is still not widely practiced, and reported P_{Xe} values (to-date) significantly lag behind those for Rb/¹²⁹Xe OP. Arguably, the most likely reason for the hindered progression of Cs/¹²⁹Xe SEOP is the lack of available high power, resonant light sources that

are able to reach the Cs D-line wavelengths (i.e. equivalent to current lasers that exist for the Rb D-lines). This technological deficiency places limits on the achievable P_{Xe} values via Cs/ ^{129}Xe SEOP, and prevents the proper ‘mapping out’ of the experimental ‘parameter space’ for the system—a process that has been shown critical to achieving very high P_{Xe} values via Rb/ ^{129}Xe SEOP at high in-cell xenon densities.²⁰⁹

The remainder of Chapter 11 reports our preliminary studies of Cs/ ^{129}Xe SEOP using two broadband LDAs, one tuned to each Cs absorbance line ($D_1 \sim 894.3$ nm; $D_2 \sim 852.1$ nm); the findings are also compared to those attained via Rb/ ^{129}Xe SEOP using the Rb D_1 absorbance (794.76 nm). This access to high power (~ 50 W) light sources for both Cs absorbance lines has resulted in the first ever equal comparison of Cs/ ^{129}Xe SEOP using both D-lines; the results of which have determined which absorption line is more favorable for producing highly polarized ^{129}Xe at a variety of experimental parameters (laser flux, $[\text{Xe}]_{\text{cell}}$, overall cell pressure, T_{cell} , etc.). These findings (utilizing *in situ* low-field NMR polarimetry and high-field P_{Xe} measurements) are then compared to results from Rb/ ^{129}Xe SEOP under identical experimental conditions ($[\text{Xe}]_{\text{cell}}$, laser flux, OP cell geometry, etc.) to evaluate the (previously) expected benefits of Cs vs. Rb optical pumping (especially at high xenon partial pressures). Preliminary P_{Xe} dynamics studies are also conducted to ascertain where the benefits of Cs/ ^{129}Xe SEOP originate (i.e., increased spin-exchange rate, decreased spin-destruction rate, higher steady-state P_{Cs} as compared to P_{Rb} , etc.). Lastly, a brief summary

of these initial results and an outlook on what the future may hold for Cs/¹²⁹Xe SEOP will be discussed.

11.2 EXPERIMENTAL CONSIDERATIONS⁸⁷

Although many of the experimental protocols for Rb optical pumping directly transfer over to the field of Cs/¹²⁹Xe SEOP, there are several important adjustments of note. Because of the very low melting temperature of Cs (it will generally melt in one's hand), the alkali-metal loading procedure may require significantly less heating in order to pipette the liquid metal into the OP cell. While rubidium appears as variations of a silver and/or 'gunsmoke' color after sufficient distribution within the OP cell, cesium retains a gold-colored appearance (whereas gold-colored Rb is generally indicative of severe contamination). The optimal cell temperatures for Cs OP were a bit lower (~10-20 °C) than those for the corresponding Rb experiments. Also, the OP cell must be cooled to a lower temperature (<26 °C) before HP ¹²⁹Xe gas collection (as the Cs is likely to still be in the vapor phase, and will subsequently exit the cell if the valve is opened to vacuum before the cesium is allowed to condense).

While the adjustments listed above serve as a general guideline for Cs/¹²⁹Xe SEOP, the following specific changes were made to our particular experimental arrangement. The Cs was loaded into a nearly identical OP cell as the Rb studies; unfortunately, the new outer cell was approximately 0.5 inches wider than our regular OP cell. As such, new cell mounts had to be machined, as well as PTFE extenders that were added to the LF detection coil. The inner cell

was not optimally positioned within the outer cell, as it gently sloped downward in the back, and a little to one side (this made laser/cell alignment particularly challenging). The cell was not able to properly mate with the rest of the vacuum manifold, and some integral glass components of the vacuum rack had to be replaced with Teflon tubing (connected by brass connectors with PTFE ferrules). Furthermore, in addition to changing lasers, the water chiller plates, optical fiber, laser power supply unit, IR spectrometer (with accompanying software), and laser safety goggles all needed to be appropriately switched (and then switched back for intermittent Rb/¹²⁹Xe SEOP studies).

11.3 IMPROVING LASER TECHNOLOGY FOR CESIUM OPTICAL PUMPING⁸⁷

As a result of our extended collaboration with QPC, we were able to obtain two (~50 W) broadband LDAs, each one capable of exciting either the Cs D₁ (894.3 nm) or Cs D₂ (852.1 nm) wavelengths. This allowed, for the first time, a direct comparison of Cs D₁ vs D₂ optical pumping; by including the (previously described—Sec. 10.5) ~100 W broadband LDA for pumping the Rb D₁ line (794.76 nm), we were then able to directly compare HP ¹²⁹Xe production via the Cs D₁, D₂, and Rb D₁ wavelengths (Fig 11.1a). Furthermore, the ~45 W of laser light incident on the OP cell at the Cs D-lines constitutes some of the highest laser fluxes ever used for Cs/¹²⁹Xe SEOP.

Both Cs D-line lasers have similar characteristics (see Fig. 4.8), and can be evaluated on nearly equal footing; the Cs D₁ laser is capable of ~46.3 W of light, with a ~2.16 nm linewidth, while the Cs D₂ laser can emit up to ~48.1 W at only

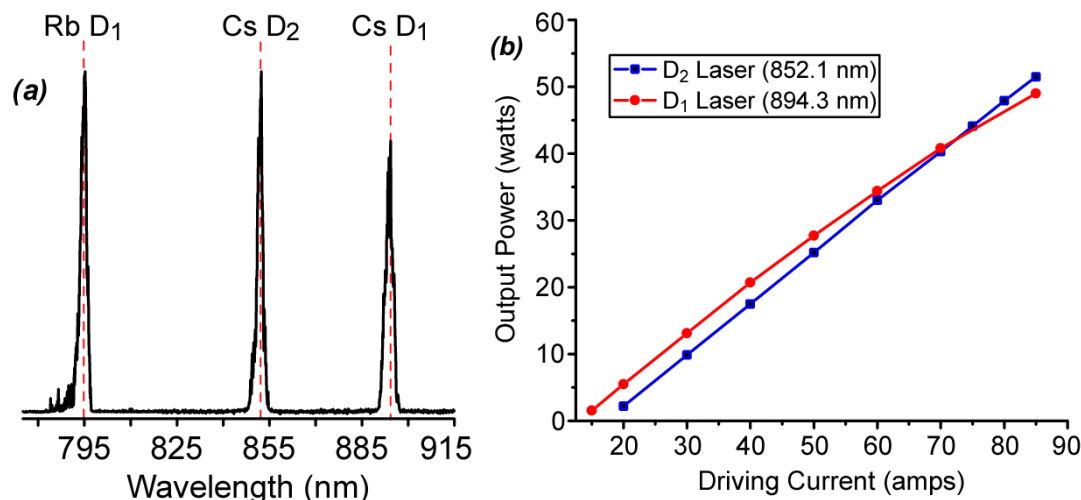


Fig. 11.1 (a) Transmitted laser spectra of three broadband laser sources capable of exciting the Rb D₁ and Cs D₁ & D₂ absorption lines. Laser characteristics (from left to right): $\lambda \sim 794.76$ nm, ~ 100 W, FWHM ~ 2.3 nm; $\lambda \sim 852.1$ nm, ~ 48 W, FWHM ~ 1.9 nm; $\lambda \sim 894.3$ nm, ~ 46 W, FWHM ~ 2.2 nm (*Rb D₁ output not drawn to vertical scale*). (b) Output power vs driving current for the two featured Cs-excitation lasers. Diode temp: ~ 26.5 °C. Laser output increases linearly with driving current.⁸⁷

~ 1.9 nm FWHM (Fig. 11.1b). For an equal comparison to Rb/¹²⁹Xe SEOP, the ~ 100 W (power is adjustable for equal comparisons with the Cs lasers) Rb broadband laser (~ 2.3 nm FWHM) was used for OP experiments at similar laser powers, T_{cell} 's and $[\text{Xe}]_{\text{cell}}$'s. The Cs lasers were powered by a 12-V power supply unit (Xantrex), while the Rb laser used the traditional 6-V PSU (also Xantrex); all three lasers mounted to water chiller plates that were cooled by the same ThermoCube recirculating water chiller. All three lasers fiber-couple (via 30 cm fibers; 852.1 & 894.3 nm lasers used the same fiber; 794.76 nm laser required a separate fiber) into the same single-axis polarizer (Fig. 11.2); the central wavelength of the quarterwave plate was chosen to be halfway between the Rb

D_1 and Cs D_1 so that the single quarterwave optic could efficiently function with all three lasers.

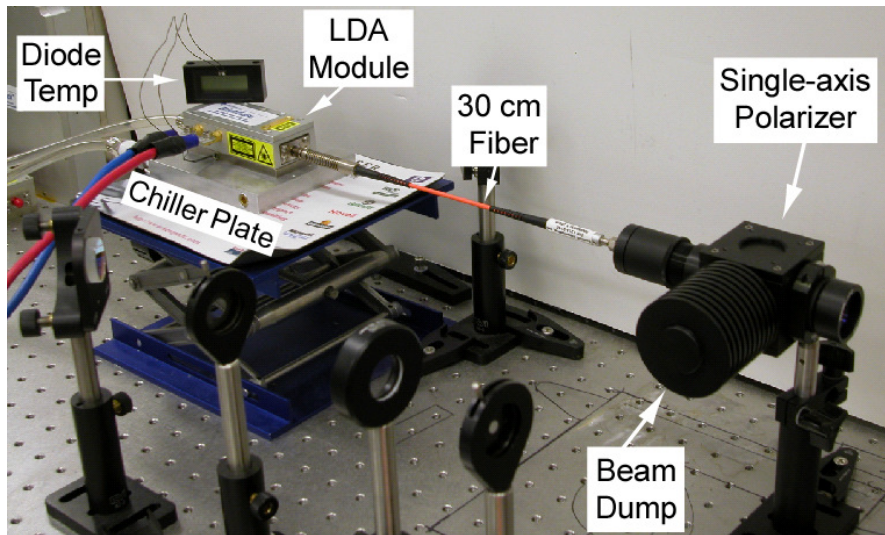


Fig. 11.2 Cesium D-line broadband laser fiber coupled to single-axis polarizer via short (30 cm) polarization-preserving fiber. Components of monochromator described in Fig. 10.12.⁸⁷

This recent progress has enabled rudimentary studies of the proficiency of the laser technology, with the (presently-demonstrated) application to fundamental SEOP studies, and the future hope to increase sensitivity enhancements for a variety of MR applications using Cs/¹²⁹Xe SEOP. Future laser developments should include the fabrication of a high-power 'on-chip' VHG-LDA at one of the cesium D-lines for HP ¹²⁹Xe production; the ability to use frequency-narrowed light sources for Cs/¹²⁹Xe SEOP should greatly increase the optical pumping efficiency, and lead to even higher P_{Xe} values.

11.4 P_{Xe} DYNAMICS STUDIES AT THE CS D₁, D₂, AND RB D₁ ABSORPTION LINES⁸⁷

The differences in optical pumping efficiency were studied via low-field NMR at the Cs D₁, D₂, and Rb D₁ wavelengths, using the (quite familiar) method of analyzing P_{Xe} build-up curve dynamics. Experiments were conducted at a variety of $[Xe]_{cell}$ (100, 300, 500, 1400, & 2000 torr Xe) and T_{cell} 's (~40-110 °C), with laser fluxes typically between ~40-53 W (lower laser power experiments also conducted with ~30 W laser flux—*not shown*). Figure 11.3 demonstrates an example set of P_{Xe} build-up curves for the three excitation wavelengths for a $[Xe]_{cell}$ = 2000 torr Xe (600 torr N₂) cell loading at each run's T_{OPT} . Laser excitation at the Cs D₁ line produced the most HP ¹²⁹Xe signal, followed by Rb

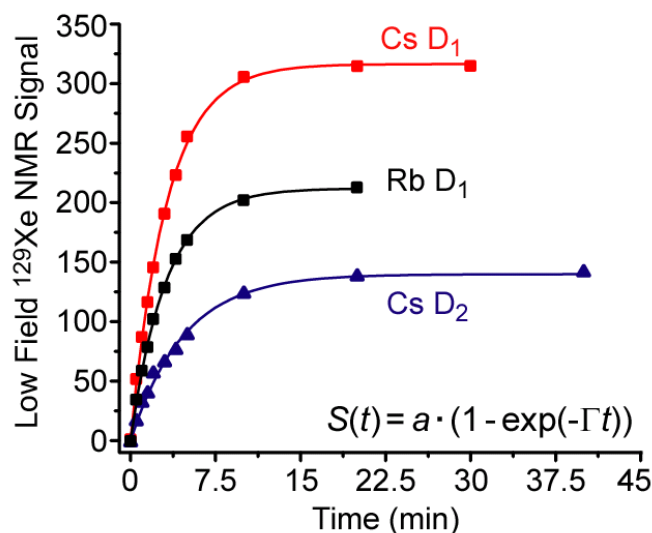


Fig. 11.3 P_{Xe} build-up curves (collected at low-field) as a function of alkali metal absorption line. Cell conditions: 2000 torr Xe, 600 torr N₂; optimal T_{cell} & laser power for each set of runs: 70 °C & ~46 W for Cs D₁; 60 °C & ~40 W for Cs D₂; and 80 °C & ~53 W for Rb D₁ excitation. Cs D₁ excitation produced the most HP ¹²⁹Xe low-field signal, more than 1.5 times that of Rb and over twice as much as from Cs D₂ excitation.⁸⁷

D₁ (~0.67 compared to Cs D₁) and Cs D₂ (a little less than half that of Cs D₁) SEOP. Rubidium runs possessed the highest T_{OPT} values, which are typically ~10 °C above those for Cs D₁ excitation and ~20 °C warmer than what is needed to attain maximum P_{Xe} via the Cs D₂ line; however, the low vapor pressure of Cs provides increased alkali metal number densities at lower temperatures than what is found with rubidium.

By plotting the P_{Xe} growth-rate time constant (Γ) as a function of alkali-metal number density (calculated using vapor pressure curves⁷⁷), one is left with a straight line whose slope is equal to γ' , and the intercept provides the ^{129}Xe in-cell T_1 relaxation rate⁵³ (Fig. 11.4). The calculated γ' values for the Cs D₁ & D₂ wavelengths are very similar (to within error); indeed, the numbers should be the same since it should not matter how the Cs atoms become polarized. Both Cs

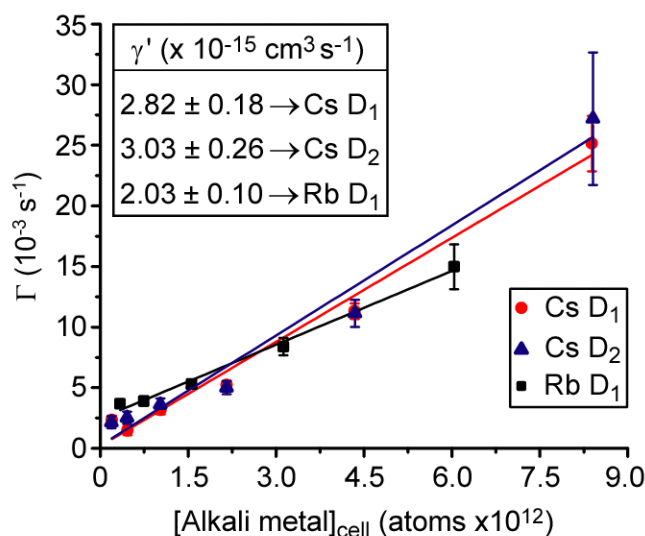


Fig. 11.4 P_{Xe} build-up growth curve time constant (Γ) vs. estimated alkali-metal number density for 2000 torr Xe (600 torr N₂) cell loading using a Cs D₁ (45.5 W), Cs D₂ (39.8 W), & Rb D₁ (53.5 W) broadband LDAs; slope gives γ' (*inset*), intercept supplies Γ_{Xe} . Both Cs excitation methods provide higher γ' values than those attained with Rb.⁸⁷

excitation methods are significantly higher than that for the Rb D_1 (Fig. 11.4 *inset*). These increased γ' values indicate the potential utility of Cs as a superior alkali metal for ^{129}Xe SEOP. Also, the in-cell ^{129}Xe relaxation time is significantly longer in the Cs cells (on the order of ~ 80 minutes) compared to the Rb cells (on the order of ~ 8 minutes)—leading to much longer-lasting P_{Xe} . It is not yet clear if the ability to increase the in-cell HP ^{129}Xe T_1 is an inherent property of Cs itself, or if it could possibly be a manifestation of an improved OP cell preparation and a general lack of impurities in the Cs cell (for that particular loading). This longer-lasting P_{Xe} will prove most beneficial for high-field runs, as a significant portion of available P_{Xe} is often depleted through relaxation while waiting for the OP cell to cool down. Although the Cs cells generally take longer to cool down (as they have to reach a lower temperature before xenon collection), a larger fraction of the polarized gas may survive the cool-down period, thus increasing the total amount of available ^{129}Xe magnetization at high field.

In principle, plotting γ' as a function on OP gas loading density/composition ($1/P_a$; see Eq. 2.11) should provide a measurement of the binary spin-exchange cross section (y -intercept) and contribution to the spin-exchange rate from the formation of van der Waals molecules (slope); however, similarly to our previous attempts, we were unable to fit the data to the predicted linear dependence, and thus could not extract the fundamental SEOP parameters. γ' is expected to steadily (and linearly) increase as a function of P_a^{-1} (which is inversely proportional to $[\text{Xe}]_{\text{cell}}$).⁵³ However, the γ' vs P_a^{-1} plots had the opposite trends, where γ' falls off dramatically for increased P_a^{-1} values; the two cesium plots had

a more pronounced fall-off than the rubidium experiment (Fig. 11.5*b*). Similarly, γ' should be expected to decrease upon increases to $[\text{Xe}]_{\text{cell}}$, as higher in-cell xenon densities hinder the formation of three-body complexes that contribute to Cs- ^{129}Xe spin-exchange. The two Cs plots of γ' vs $[\text{Xe}]_{\text{cell}}$ showed an opposite trend, with low γ' for low $[\text{Xe}]_{\text{cell}}$'s, increasing with xenon density, peaking (at ~ 500 torr Xe), and remaining relatively constant at even higher $[\text{Xe}]_{\text{cell}}$ (with some fluctuations); compared to the Cs curves, the Rb trend is relatively flat throughout most of the $[\text{Xe}]_{\text{cell}}$ range (Fig. 11.5*a*). The origins of these affects are unclear, and prevent our adequate fitting of the experimental data to extract reasonable values for the binary spin-exchange cross section and the spin-exchange rate due to three-body complex formations. However, the increased γ' values found at elevated $[\text{Xe}]_{\text{cell}}$ indicates that Cs could be a good choice for high xenon density optical pumping.

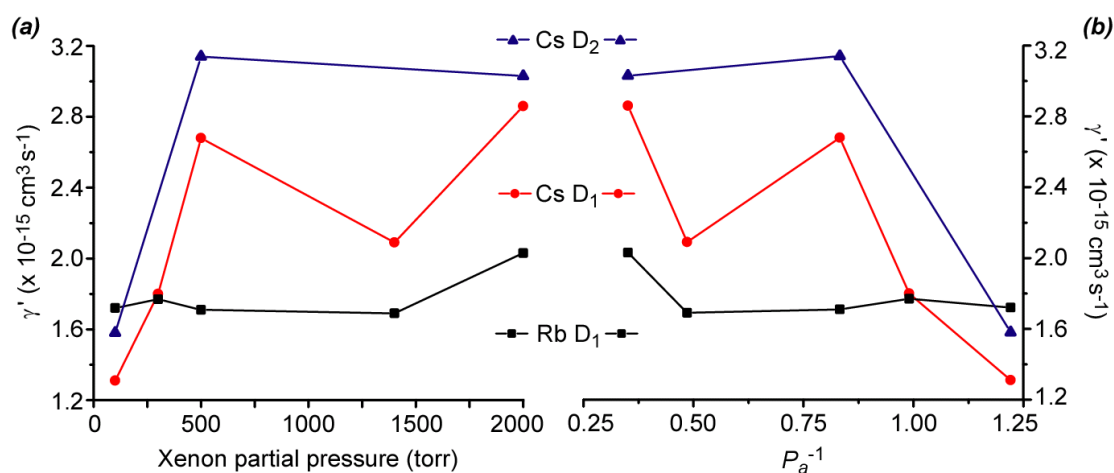


Fig. 11.5 (a) γ' as a function of $[\text{Xe}]_{\text{cell}}$ for the three excitation wavelengths. γ' is typically expected to decrease upon increased $[\text{Xe}]_{\text{cell}}$, due to losses in 3-body complexes that facilitate spin-exchange. **(b)** Same data as **(a)**, but with γ' plotted as a function of $1/P_a$ for the three excitation methods. γ' is typically expected to increase linearly with P_a^{-1} ; the resulting curves *should* fit to Eq. 2.10 so that the binary SE cross-section and 3-body SE rate can be extracted. It is unclear why the data does not fit the predicted trends.⁸⁷

Previous studies (i.e., Fig. 9.4) have shown a significant temperature dependence of optimal P_{Xe} values for Rb/ ^{129}Xe SEOP using frequency-narrowed laser sources, one in which lower xenon densities achieve their highest P_{Xe} values at high T_{cell} , whereas increased $[\text{Xe}]_{\text{cell}}$ values are polarized better at lower cell temperatures. The P_{Xe} growth curve time constants (Γ) generally scale with $[\text{Rb}]_{\text{cell}}$ (as T_{cell} increases). By plotting the values of Γ taken from each gas density's T_{OPT} (Fig. 11.6), it appears that the Rb D_1 data behaves as would be expected: high P_{Xe} build-up rates at low $[\text{Xe}]_{\text{cell}}$ (higher T_{OPT}), falling off with increased $[\text{Xe}]_{\text{cell}}$ (lower T_{OPT}). However, the Cs data appears to have an opposite trend, with small build-up rates at low xenon density, increasing with $[\text{Xe}]_{\text{cell}}$ (up to ~ 500 torr Xe) before reaching steady-state. Importantly when using the broadband lasers the optimal cell temperature range did not appear to

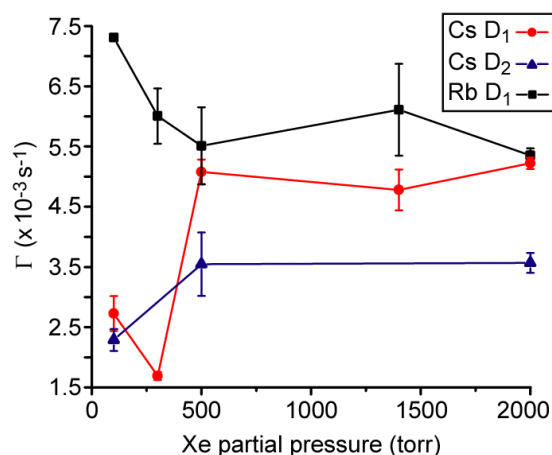


Fig. 11.6 Γ values taken from the T_{OPT} of each OP gas loading plotted as a function of $[\text{Xe}]_{\text{cell}}$ for the three excitation methods. Cs & Rb exhibit different trends regarding the build-up rate constant at optimal OP conditions for each $[\text{Xe}]_{\text{cell}}$: Rb behaves as expected (high Γ for low $[\text{Xe}]_{\text{cell}}$, decreasing upon higher $[\text{Xe}]_{\text{cell}}$). Cs has an opposite trend, where Γ is small for low $[\text{Xe}]_{\text{cell}}$, then increases with $[\text{Xe}]_{\text{cell}}$ and reaches steady-state. It is unclear why the two alkali metals behave differently in this regard.⁸⁷

change dramatically with variations in $[\text{Xe}]_{\text{cell}}$ (at least, not to the extent of Fig. 9.4); therefore, changes to $[\text{Xe}]_{\text{cell}}$ itself (and not changes to T_{cell}) should be the dominant factor in the observed Γ dependency. This preliminary result may further indicate the usefulness of Cs for high xenon density optical pumping (as the OP efficiency appears to improve with $[\text{Xe}]_{\text{cell}}$).

11.5 OPTICAL PUMPING AT THE CS D₁ VS D₂ WAVELENGTHS⁸⁷

It is generally accepted that, all things being equal, D₁ optical pumping (of any alkali metal) should be superior to D₂ pumping; indeed, it has even been stated that D₂ pumping should be virtually impossible.²¹⁰ While SEOP using D₂ excitation is not impossible (and in fact, has been well-documented by the Wuhan Goup²¹¹⁻²¹³), D₂ optical pumping is in fact inferior to D₁ OP; however, the reasons for this are not commonly documented in the literature (thus allowing ample opportunities for confusion). The ability to compare SEOP results at the Cs D₁ and D₂ wavelengths has given us the ability to demonstrate the differences in optical pumping between the two excitation wavelengths. Moreover, if the only available Cs-excitation light source is at the D₂ resonance, it should provide some amount of optical polarization (i.e., it is better than having no light source at all).

Illumination of the D₁ line (we'll use cesium in this case, but the following should apply to all alkali metals) with a circularly-polarized laser beam selectively induces excitation from one particular m_j sublevel (say, $m_j = -1/2$) in the ground-state to the $m_j = +1/2$ excited state level (following the quantum selection rule

$\Delta m_j = \pm 1$). After collisional mixing between excited states, the electron has a 50% chance of relaxing into the $m_j = +1/2$ ground state; because the $m_j = -1/2$ is being constantly depleted, and a significant portion of the electrons accumulate in the $m_j = +1/2$ state, the net electron spin polarization (P_{Cs}) quickly approaches unity (upon $m_j = +1/2$ 'saturation'; Fig. 11.7a).

Optical pumping at the Cs D_2 line is not as straightforward, as there are additional m_j levels to consider (Fig. 11.7b). Remembering the $\Delta m_j = \pm 1$ selection rule, electrons can be driven from the ground state $m_j = -1/2$ to excited states $m_j = -3/2$ or $+1/2$; also, electrons can be driven from the ground state $m_j = +1/2$ to the excited states $m_j = -1/2$ or $+3/2$, depending on the helicity of the light. Because electrons are constantly pumped from both ground-state m_j sublevels, and subsequently relax back into both ground state sublevels, P_{Cs} can never reach unity. Indeed, the highest P_{Cs} values achievable rely on the Clebsch-Gordan coefficients for the transitions (roughly a 3 to 1 ratio, also depending on the helicity of the light), resulting in the highest attainable P_{Cs} value being 50% (see Eq. 2.1).

Also, the same helicity of light will optically pump out of the opposite ground-state m_j sublevels for D_1 and D_2 (i.e., if $\sigma+$ light pumps every electron out of $m_j = -1/2$ for D_1 , it will pump ~25% out of the $m_j = -1/2$ and ~75% out of the $m_j = +1/2$ sublevels for D_2); this leads to oppositely-phased ^{129}Xe NMR spectra for D_1 vs D_2 SEOP with the same light helicity. Therefore, if one was to simultaneously pump both D-lines during SEOP (using the same light helicity), the resulting P_{Xe} levels would decrease, as a significant portion of the P_{Cs}

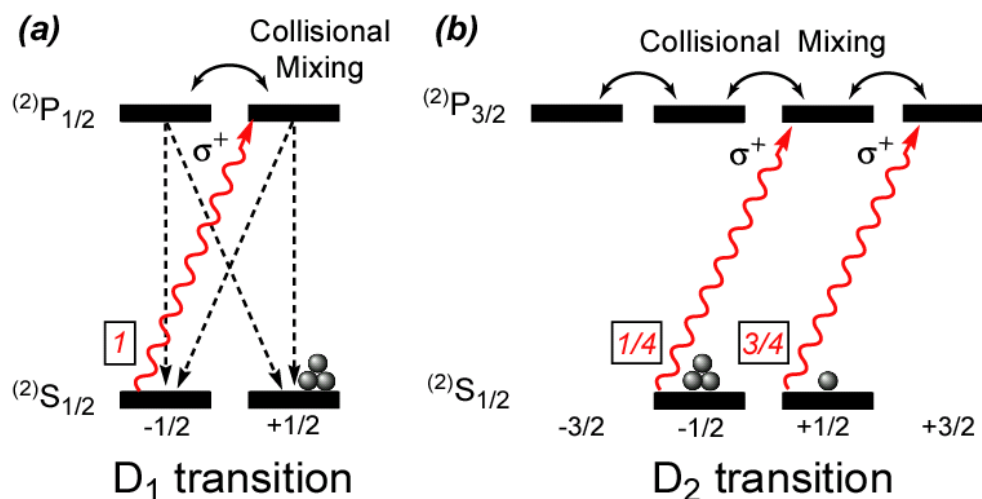


Fig. 11.7 (a) Depletion pumping of the D₁ transition: σ^+ light selectively depletes electrons from $m_j = -1/2$ sublevel, accumulating electrons in the ground-state $m_j = +1/2$ level. Highest P_{Cs} attainable $\sim 100\%$ (b) Optical pumping of the D₂ transition: σ^+ light depopulates from both ground-state magnetic sublevels, in a roughly 3:1 ratio. Highest P_{Cs} attainable $\sim 50\%$ (relaxation pathways and the effects of nuclear sublevels not illustrated for clarity). Using the same helicity of light, D₁ & D₂ pumping will accumulate electrons in opposite m_j sublevels.

cancels itself; this unintentional, simultaneous D-line pumping is a greater worry in Rb/¹²⁹Xe SEOP, as the Rb D-lines are only separated by <15 nm. This process may play a larger role under conditions of high $[Xe]_{cell}$, as both the D₁ and D₂ lines are shifted and asymmetrically broadened towards longer wavelengths.^{114,86} Simultaneous D-line pumping has also been postulated to be a possible cause to the (so-called) 'X-factor' in ³He SEOP^{85,86}, where steady-state P_{He} levels never reach close to 100%, despite operating under conditions of extremely inhibited spin-destruction processes. An additional consequence of simultaneous electron pumping from both m_j sublevels (i.e., D₂ pumping) is the

increased amount of light absorbed (due to the Cs D₂ transition having roughly twice the oscillator strength⁷⁷ than the D₁). Indeed, a significant increase in light absorption was observed for Cs D₂ optical pumping as compared to Cs D₁ OP; additionally, because of the increased light absorption, the Cs D₂ runs exhibited a lower T_{OPT} for all $[\text{Xe}]_{\text{cell}}$.

To further demonstrate the differences in Cs D₂ pumping, two high field HP ¹²⁹Xe NMR experiments were conducted (Fig 11.8). All experimental parameters were kept constant (including $[\text{Xe}]_{\text{cell}}$ and T_{OPT}), aside from the excitation wavelength. As predicted the resulting high field ¹²⁹Xe NMR signals were of

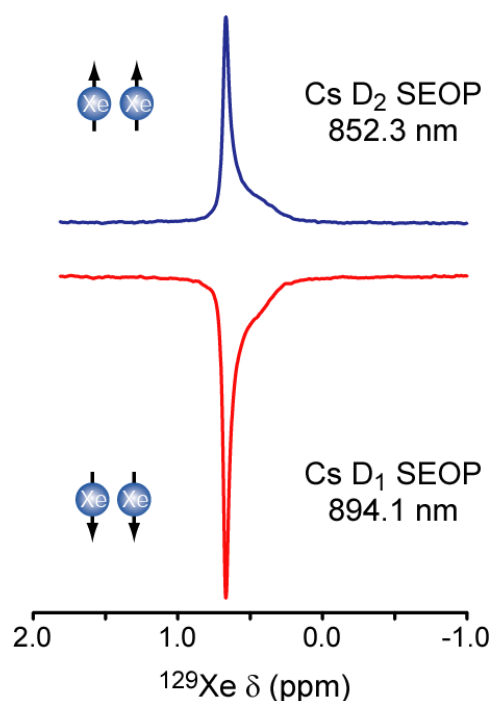


Fig. 11.8 High field (9.4 T) HP ¹²⁹Xe NMR signals using Cs/¹²⁹Xe SEOP at the Cs D₂ (*top*) and Cs D₁ (*bottom*) excitation wavelengths. Cs D₁ SEOP provides $\sim 1.5\times P_{\text{Xe}}$ than Cs D₂ OP ($\sim 7\%$ vs. $\sim 4.5\%$, respectively), and the two excitation methods result in opposite nuclear spin polarizations (as expected); Cs D₁ OP is also polarized opposite to that of thermally polarized ¹²⁹Xe (*not shown*). Both runs conducted under optimal conditions, with similar laser characteristics (power and linewidth).

opposite phase, and the Cs D₁ run produced approximately 1.5 times the P_{Xe} levels attained by the Cs D₂ run. Furthermore, the amount of light absorbed for the Cs D₂ run was much greater than for the Cs D₁ run (despite being ~10 °C lower T_{cell}).

These results affirm what is theoretically expected, and demonstrate the utility of D₂ optical pumping. While Cs D₂ pumping is not advantageous compared to Cs D₁ OP, it can be somewhat comparable to OP at the Rb D₁. Cs D₂ SEOP can partially compensate for its low P_{Cs} levels by its increased spin-exchange efficiency (as compared to Rb D₁ SEOP); in the end, Cs D₂ OP may not be ideal, but it could be useful if no other alternatives existed (such as an absence of D₁ excitation sources).

11.6 COMPARISON OF STEADY-STATE HP ¹²⁹XE PRODUCTION VIA RB/¹²⁹XE VERSUS CS/¹²⁹XE SEOP⁸⁷

In order to further compare HP ¹²⁹Xe production at high $[Xe]_{cell}$ values via Cs vs. Rb SEOP, a direct comparison was made of low-field ¹²⁹Xe signal versus in-cell xenon density at the three excitation wavelengths (Fig. 11.9). While all three experiments exhibited increased LF signal as a function of $[Xe]_{cell}$ (thus besting the typically-expected flat signal-to-concentration ratio⁶³), the Cs D₂ line seemed to provide the poorest results (as expected), with ¹²⁹Xe signal slightly increasing over the ~1900 torr range of $[Xe]_{cell}$'s. The Rb D₁ excitation method produced steeply-climbing ¹²⁹Xe signals up to ~500 torr Xe, then began to flatten out a bit while continuing to gently rise with $[Xe]_{cell}$. Finally, the Cs D₁ data had

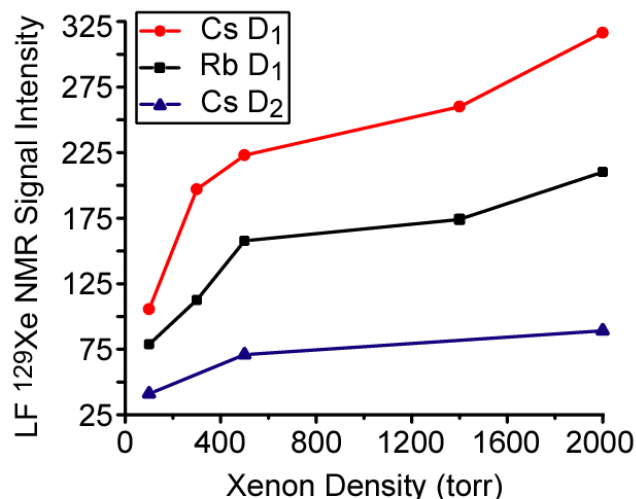


Fig. 11.9 Steady-state P_{Xe} signal intensities (collected at low-field) as a function of $[Xe]_{cell}$ for a variety of alkali metal absorption lines. Each run at that OP cell loading's T_{OPT} ; laser power for each set of runs: ~ 46 W for Cs D₁, ~ 40 W for Cs D₂, and ~ 53 W for Rb D₁ excitation. Cs D₁ runs show the highest steady-state HP ^{129}Xe signals, with increasing xenon signal even at the highest $[Xe]_{cell}$'s.⁸⁷

the most dramatic increase in ^{129}Xe signal with xenon density, continuing to steadily rise even at the highest $[Xe]_{cell}$ values. While the Cs D₁ runs provided the best signal at low field, the extent was larger at high field ($\sim 1.5x$ vs $\sim 2x$; see *below*); this increase is likely due to the extended in-cell ^{129}Xe relaxation times for Cs—the origins of which remain unclear (but likely due to a decreased Cs-Xe spin-destruction cross-section). Also, despite the increased ^{129}Xe signals at high $[Xe]_{cell}$, the difference between Cs D₁ and Rb D₁ at low $[Xe]_{cell}$ (~ 100 torr Xe) is not nearly as great, consistent with differentially improved SEOP using Cs at higher $[Xe]_{cell}$ values (as compared to lower xenon densities). Indeed, this propensity for increased ^{129}Xe signal at increased xenon densities indicates that

Cs/ ^{129}Xe SEOP may be the superior method for producing highly polarized xenon at high $[\text{Xe}]_{\text{cell}}$ values.

Following our preliminary characterization of Cs/ ^{129}Xe SEOP at low field, we turned to high-field NMR for an ‘apples-to-apples’ comparison of absolute P_{Xe} values generated via SEOP using either rubidium or cesium as the alkali metal. Each experiment was conducted at its own optimal conditions (i.e., T_{OPT} , laser flux, spectral offset, etc.), the results of which are shown in Fig. 11.10. It is immediately apparent that the Cs OP runs resulted in higher P_{Xe} values, especially at the higher $[\text{Xe}]_{\text{cell}}$ loadings. In fact, cesium optical pumping produced roughly twice the P_{Xe} levels compared to rubidium OP for all of the runs except for the 100 torr Xe cell loading (qualitatively following the low field *in*

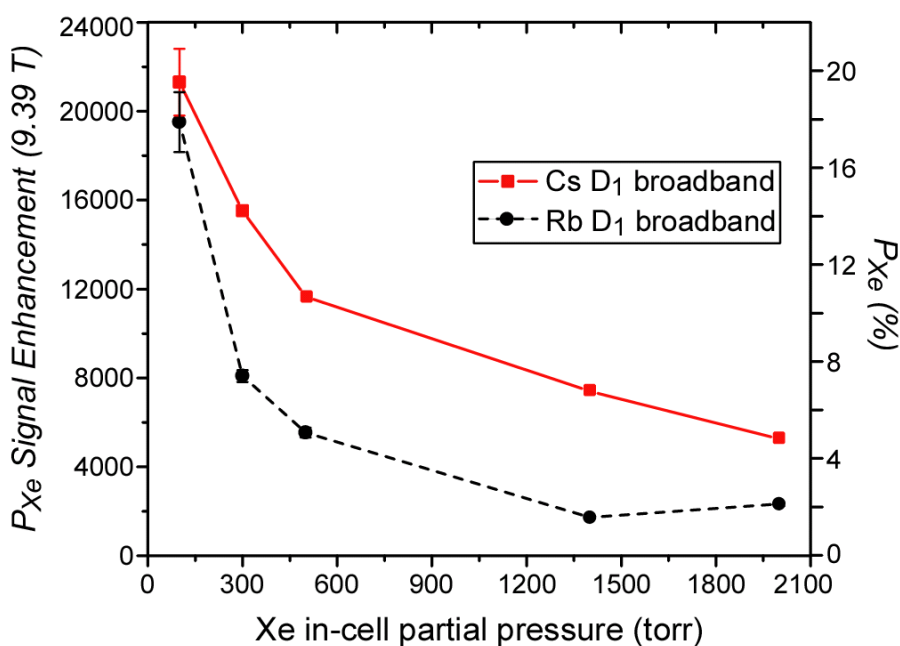


Fig. 11.10 P_{Xe} , NMR enhancements as a function of $[\text{Xe}]_{\text{cell}}$ with batch-mode SEOP performed with two alkali metals: cesium (*red squares*, ~48 W) & rubidium (*black circles*, ~52 W). $[\text{Xe}]_{\text{cell}}$ values of 100, 300, 500, 1400, & 2000 torr Xe (backfilled with N_2 to 2000 torr total; 2000 torr Xe run has 600 torr N_2); each run conducted at that $[\text{Xe}]_{\text{cell}}$'s optimal OP conditions.⁸⁷

situ results. Moreover the cesium runs may have benefited from longer in-cell ^{129}Xe T_1 's, allowing more of the xenon magnetization to be observed at high field; in contrast, a larger fraction of HP ^{129}Xe produced by Rb OP likely became depolarized during the cell cool-down period (probably the reason why there is a larger difference between Rb and Cs OP results at high field as compared to low-field).

These results comprise the first true 'apples-to-apples' comparison of Rb and Cs SEOP for the production of hyperpolarized xenon using high laser fluxes (~50 W), as many previous studies only used fractions of a watt up to a few watts.^{78,84,137} This also marks the first time that Cs/ ^{129}Xe SEOP has successfully been demonstrated to improve P_{Xe} production, as compared to Rb/ ^{129}Xe SEOP. It is not yet completely evident where the benefits of Cs/ ^{129}Xe SEOP lie; due to our inability extract (and decouple) the binary spin-exchange cross section and three-body spin-exchange rate contributions, it cannot yet be established if one of those two parameters is the determining factor. However, it does appear that γ' (the sum of those two contributions) is higher for Cs than for Rb by a factor of ~1.5 (Fig. 11.4), indicating that the spin-exchange rate is higher for Cs- ^{129}Xe (this ~1.5x increase in γ' is mirrored by the ~1.5x increase in low-field ^{129}Xe NMR signal). Furthermore, the extended in-cell HP ^{129}Xe T_1 's for Cs OP are roughly an order of magnitude longer than for rubidium optical pumping, signaling that the Cs- ^{129}Xe spin-destruction rate is significantly lower than for Rb- ^{129}Xe . Not to be discounted, the actual P_{Xe} levels attained in this preliminary study of Cs/ ^{129}Xe

SEOP are somewhat remarkable; P_{Xe} values of $\sim 19\%$ and $\sim 5\%$ for $[Xe]_{\text{cell}} = 100$ & 2000 torr Xe are quite high, especially for using broadband laser sources.

While we do not currently have a method in place for measuring absolute alkali-metal electron spin polarizations *in situ* (although an optical ESR set-up is in the works), Eq. 2.12 may be used to estimate P_{AM} ('alkali-metal' electronic spin polarization) throughout the OP cell. If the absolute P_{Xe} values are known (here, the high-field results—which are a bit lower than the actual in-cell P_{Xe} values—are used), along with Γ_{Xe} ($1/T_1$, as measured at low field) and γ_{SE} (basically γ'), estimated values for P_{AM} can be extracted. While it is not an absolute measure of the alkali-metal polarization (the main sources of error being the differences of P_{Xe} at high field vs. in-cell and $[Rb]_{\text{cell}}$ estimates using vapor pressure curves), it should provide a reasonable indication of how closely P_{Xe} and P_{AM} track each other.

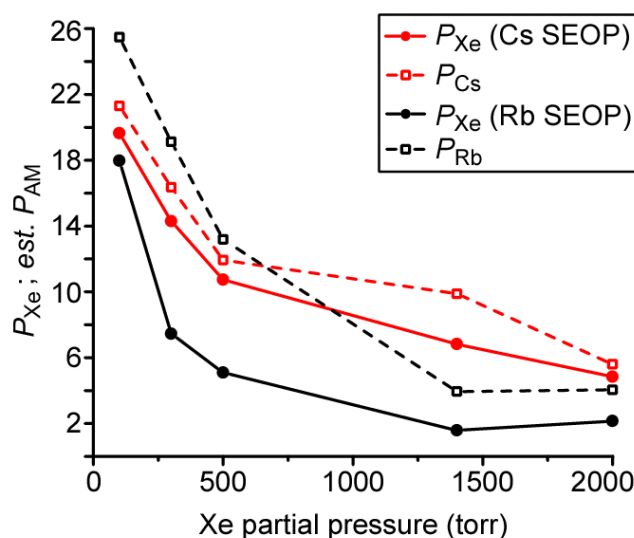


Fig. 11.11 P_{Xe} values (measured at 9.4 T) as a function of $[Xe]_{\text{cell}}$ for Cs (red-solid) & Rb (black-solid) SEOP, with corresponding estimated alkali-metal electron spin polarization (P_{AM}) values for Cs (red-dashed) and Rb (black-dashed), as calculated from Eq. 2.12. P_{Xe} tracks P_{Cs} more closely than P_{Rb} , likely due to increased SE (as well as decreased SD) efficiencies.⁸⁷

Figure 11.11 shows a comparison of P_{Xe} (as measured at high field) and estimated P_{AM} values for both Rb and Cs SEOP. The estimated P_{Rb} values are higher than those of P_{Cs} for the lower $[Xe]_{cell}$ values; at increased cell density, P_{Cs} is favored. Despite the increased P_{Rb} at low $[Xe]_{cell}$, the highest P_{Xe} values achieved throughout the curve were from Cs OP. Indeed, the most valuable piece of information from this graph is how closely P_{Xe} and P_{AM} track each other; there is a very small separation between P_{Xe} and P_{Cs} throughout the range, as opposed to the larger gap between P_{Xe} and P_{Rb} . This indicates that the spin-exchange itself is more efficient for Cs- ^{129}Xe , as there are minimal losses between P_{Cs} and P_{Xe} . Generally, the gap between P_{Rb} and P_{Xe} is much greater, likely due to less efficient spin-exchange (and more efficient ^{129}Xe spin-destruction). If methods can be enacted that boost P_{Cs} even higher, it follows that P_{Xe} should continue to closely track the alkali-metal polarization, resulting in even higher P_{Xe} values.

11.7 SUMMARY AND OUTLOOK ON CS/ ^{129}Xe SEOP

The results presented in this chapter represent the first true ‘apples-to-apples’ comparison of Rb and Cs SEOP at high laser fluxes for a variety of $[Xe]_{cell}$ values. By using high power (~50 W) broadband LDAs, we were able to show that SEOP using cesium as the alkali metal provides higher P_{Xe} values as compared to Rb/ ^{129}Xe SEOP. The origins of the increased P_{Xe} are not independently confirmed; however, it is not likely to be the alkali-metal electron spin polarization, but is more likely due to higher spin-exchange efficiencies,

along with a lower ^{129}Xe spin-destruction rate. Importantly, cesium seems to provide better results than rubidium—particularly at higher $[\text{Xe}]_{\text{cell}}$ loadings; thus, cesium may prove to be differentially beneficial, depending on the particular OP cell gas-loading.

This chapter's results are merely the 'tip of the iceberg' for Cs/ ^{129}Xe SEOP. Indeed, now that the potential superiority of Cs OP has been adequately demonstrated, the next step is to develop high power, tunable, frequency-narrowed lasers—much like the ones that already exist (and have been extensively characterized in this dissertation) for Rb optical pumping. This advancement will allow the multidimensional mapping of the various OP experimental parameters, such as T_{cell} , buffer gas density/composition, laser flux, spectral offset, laser linewidth, etc. Upon completion of these studies, a second Rb vs. Cs comparison (all parameters being equal) using high-power, frequency-narrowed lasers should further establish which alkali metal is best used for large-scale HP ^{129}Xe production. Increased interest in Cs OP will boost demand, speed the development of the technology, and eventually lower prices for diodes that lase at the Cs D_1 wavelength (as of now, they have to be special-ordered, and can be rather expensive).

In addition to directly comparing Rb and Cs optical pumping, a more intriguing experiment would be to combine them, essentially as a Rb-Cs hybrid approach (see Sec. 3.2.3; similar to the K-Rb hybrid used to optically pump $^3\text{He}^{85}$). If the transfer efficiency of electronic spin polarization between Rb and Cs is higher than spin-exchange between Rb and ^{129}Xe , then this method, where Rb

polarizes Cs, which subsequently polarizes ^{129}Xe with high efficiency, may show some advantages. Indeed, Fig. 11.10 indicates that spin-exchange between Cs- ^{129}Xe is more efficient than between Rb- ^{129}Xe ; additionally, this method would not require updated laser techniques, as only the Rb D_1 absorption line would be illuminated. Or, if high-power VHG-LDAs are developed at the Cs D_1 wavelength, the cell could be illuminated with both 794.76 nm & 894.3 nm light, with the hopes to further boost P_{Cs} (& P_{Xe}).

The advancement of high-power, tunable VHG-LDAs at the Cs D_1 line would also facilitate the *in situ* study of P_{Cs} throughout the cell under different experimental conditions, as well as the measurement of the rovibrational temperature of N_2 during Cs/ ^{129}Xe SEOP—allowing the comparison to the results obtained with rubidium optical pumping. One intriguing possibility would be to characterize the production of HP ^{83}Kr via Cs optical pumping; this type of arrangement has never been attempted (to the author's knowledge), and could possibly improve HP ^{83}Kr production (and it would be interesting to see if the long-lasting HP ^{129}Xe in-cell T_1 's could directly translate to increased HP ^{83}Kr relaxation times). Also, if the Rb/Cs hybrid approach is proven viable for HP ^{129}Xe production, it could be worth attempting for ^{83}Kr (as well as ^{131}Xe).

If cesium can be further demonstrated to be superior to Rb for ^{129}Xe SEOP, it may be worthwhile for many current Rb OP groups to switch to Cs (especially if a factor of ~ 1.5 to 2 in P_{Xe} enhancements can be gained). Indeed, the transition should be fairly seamless, with the only major purchase being new laser equipment (and possibly a new IR spectrometer). Cs/ ^{129}Xe SEOP may have

further benefits for continuous-flow setups; the higher spin-exchange rate may allow for faster gas flow-through, resulting in increased amounts of P_{Xe} collected in a shorter amount of time. The added P_{Xe} values would be valuable for clinical polarizers, which produce HP ^{129}Xe for human lung imaging—as well as for materials studies, which use large quantities of the highly polarized gas.

REFERENCES

1. Levitt, M. H. (2002). *Spin Dynamics: Basics of Nuclear Magnetic Resonance*, John Wiley & Sons, Ltd.
2. Callaghan, P. T., Eccles, C. D., Haskell, T. G., Langhorne, P. J. & Seymour, J. D. (1998). *J. Magn. Reson.* **133**, 148-154.
3. Harel, E., Schroder, L. & Xu, S. (2008). *Annu. Rev. Anal. Chem.* **1**, 133-163.
4. Bax, A., Freeman, R. & Frenkie, T. A. (1981). *J. Am. Chem. Soc.* **103**, 2102-2104.
5. Jeener, J., Meier, B. H., Bachmann, P. & Ernst, R. R. (1979). *J. Chem. Phys.* **71**.
6. Bax, A. & Grzesiek, S. (1993). *Acct. of Chem. Res.* **26**, 131-138.
7. Mittermaier, A. & Kay, L. E. (2006). *Science* **312**, 224-228.
8. Hore, P. J., Zuiderweg, E. R. P., Kaptein, R. & Dijkstra, K. (1981). *Chem. Phys. Lett.* **83**, 376-383.
9. Lauterbur, P. (1973). *Nature* **242**, 190-191.
10. Levine, I. N. (2000). *Quantum Chemistry*, Prentice Hall.
11. Atkins, P. & De Paula, J. (2002). *Physical Chemistry*, W.H. Freeman and company.
12. Sanders, J. K. M. & Hunter, B. K. (1993). *Modern NMR Spectroscopy*, Oxford University Press.

13. Abragam, A. (1961). *Principles of Nuclear Magnetism*, Oxford Science Publications.
14. Whiting, N., Nikolaou, P., Eschmann, N., Barlow, M. J. & Goodson, B. M. (2008). *49th Exptl. Nucl. Magn. Reson. Conf.*, Asilomar, CA.
15. Bax, A., Szevernyi, N. M. & Maciel, G. E. (1983). *J. Magn. Reson* **55**, 494-497.
16. Gasparro, F. P. & Kolodny, N. H. (1977). *J. Chem. Ed.* **54**, 258-267.
17. Guntert, P., Mumenthaler, C. & Wuthrich, K. (1997). *J. Mol. Biol.* **273**, 283-298.
18. Chandler, D. (1987). *Introduction to Modern Statistical Mechanics*, Oxford Press.
19. Goodson, B. M. (2002). *J. Magn. Reson.* **155**, 157-216.
20. Abragam, A. & Goldman, M. (1978). *Rep. Prog. Phys.* **41**, 395-467.
21. Barker, W. (1962). *Rev. Mod. Phys.* **34**, 173-185.
22. Bajaj, V. S. et al. (2003). *J. Magn. Reson* **160**, 85-90.
23. Kaptein, R. & Oosterhoff, J. L. (1969). *Chem. Phys. Lett.* **4**, 195-197.
24. Hore, P. J., Winder, S. L., Roberts, C. H. & Dobson, C. M. (1997). *J. Am. Chem. Soc.* **119**, 5049-5050.
25. Kuprov, I., Goetz, M., Abbot, P. A. & Hore, P. J. (2005). *Rev. Sci. Instrum.* **76**.
26. Bouchard, L.-S., Kovtunov, K.V., Burt, S.R., Anwar, M.S., Koptuyug, I.V., Sagdeev, R.Z., Pines, A. (2007). *Angewandte Chemie International Edition* **46**.

27. Duckett, S. B. & Blazina, D. (2003). *Eur. J. Inorg. Chem.*, 2901-2912.
28. Bouchard, L.-S. et al. (2008). *Science* **319**, 442-445.
29. Golman, K. et al. (2001). *Magn. Reson. in Med.* **46**, 1-5.
30. Blazina, D., Duckett, S. B., Dunne, J. P. & Godard, C. (2004). *Dalton Trans.*, 2601-2609.
31. Brossel, J. & Kastler, A. (1949). *Compt. Rend. Acad. Sci. (Paris)* **229**, 1213-1215.
32. Kastler, A. (1950). *J. Phys. Radium* **11**, 255-265.
33. Kastler, A. (1955). *J. Phys. Radium* **11**, 255.
34. Kastler, A. J. (1957). *Opt. Soc. Am.* **47**, 460-465.
35. Cagnac, B. & Brossel, (1958). *J. Compt. Rend. Acad. Sci. (Paris)* **246**, 1827.
36. Cagnac, B. (1961). *Ann. Phys. (Paris)* **6**, 467.
37. Lehmann, J. C. (1964). *J. Phys. (Paris)* **25**, 809.
38. Bouchiat, M. R., Carver, T. R. & Varnum, C. M. (1960). *Phys. Rev. Lett.* **5**, 373-375.
39. Colegrove, F. D., Schearer, L. D. & Walters, G. K. (1963). *Phys. Rev.* **132**, 2561-2572.
40. Grover, B. C. (1978). *Phys. Rev. Lett.* **40**, 391.
41. Maier, G., Haeberlen, U., Wolf, H. C. & Hausser, K. H. (1967). *Optische Kernspin-Polarisation in Anthracen - Kristallen. Phys. Lett. A* **25**, 384-385.
42. Jeffries, C. D. (1967). *Phys. Rev. Lett.* **19**, 1221-1224.

43. Mollenauer, L. F., Grant, W. B. & Jeffries, C. D. (1968). *Phys. Rev. Lett.* **20**, 488-490.
44. Lampel, G. (1968). *Phys. Rev. Lett.* **20**, 491.
45. Ekimov, A. L. & Safarov, V. I. (1972). *Proc. Int. Conf. Phys. Semicond.* **11th**, 1351.
46. Kaptein, R., Dijkstra, K. & Nikolay, K. (1978). *Nature* **274**, 233-294.
47. Eckert, G., Heil, W., Meyerhoff, M., Otten, E.W., Surkau, R., Werner, M., Leduc, M., Nacher, P.J., Scheerer, L.D. (1992). *Nucl. Instrum. Methods. Phys. Res. A* **320**, 53-65.
48. Becker, J., Bermuth, J., Ebert, M., Grossmann, T., Heil, W., Hofmann, D., Humblot, H., Lecud, M., Otten, E.W., Rohe, D., Surkau, R. (1998). *Nucl. Instrum. Methods. Phys. Res. A* **402**, 327-336.
49. Leduc, M., Laloe, F. & Brossel (1970). *J. C.R. Acad. Sci.* **271**, 342.
50. Happer, W. (1972). *Rev. Mod. Phys.* **44**, 169-249.
51. Happer, W., Miron, E., Schaefer, S., Schreiber, D., van Wijngaarden, W.A., Zeng, X. (1984). *Phys. Rev. A* **29**, 3092-3110.
52. Zeng, X., Wu, Z., Call, T., Miron, E., Schreiber, D., Happer, W. (1985). *Phys. Rev. A* **31**, 260-278.
53. Cates, G. D., Fitzgerald, R.J., Barton, A.S., Bogorad, P., Gatzke, M., Newbury, N.R., Saam, B. (1992). *Phys. Rev. A* **45**, 4631-4639.
54. Walker, T. & Happer, W. (1997). *Rev. Mod. Phys.* **69**, 629-642.
55. Appelt, S., Ben-Amar Baranga, A., Erickson, C.J., Romalis, M.V., Young, A.R., Happer, W. (1998). *Phys. Rev. A* **58**, 1412-1439.

56. Chann, B., Babcock, E., Anderson, L. W. & Walker, T. G. (2002). *Phys. Rev. A* **66**.
57. Driehuys, B., Cates, G.D., Miron, E., Sauer, K., Walter, D.K., Happer, W. (1996). *Appl. Phys. Lett.* **69**, 1668-1670.
58. Rosen, M. S., Chupp, T. E., Coulter, K. P., Welsh, R. C. & Swanson, S. D. (1999). *Rev. Sci. Instrum.* **70**, 1546-1552.
59. Nikolaou, P., Whiting, N., Eschmann, N.A., Chaffee, K.E., Barlow, M.J., Goodson, B.M. (2009). *J. Magn. Reson* **197**, 249-254.
60. Brunner, E. (1999). *Concepts Magn. Reson.* **11**, 313-335.
61. Chann, B., Nelson, I. A., Anderson, L. W., Driehuys, B. & Walker, T. G. (2002). *Phys. Rev. Lett.* **88**.
62. Berry-Pusey, B. N., Anger, B. C., Laicher, G. & Saam, B. (2006). *Phys. Rev. A* **74**.
63. Mortuza, M. G., Anala, S., Pavlovskaya, G. E., Dieken, T. J. & Meersmann, T. (2003). *J. Chem. Phys.* **118**, 1581-1584.
64. Saha, I., Nikolaou, P., Whiting, N. & Goodson, B. M. (2006). *Chem. Phys. Lett.* **428**, 268-276.
65. Zook, A. L., Adhyaru, B. B. & Bowers, C. R. (2002). *J. Magn. Reson.* **159**, 175-182.
66. Fink, A., Baumer, D. & Brunner, E. (2005). *Phys. Rev. A* **72**, 053411.
67. Shah, N. J., Unlu, T., Wegener, H.P., Halling, H., Ziles, K., Appelt, S. (2000). *NMR Biomed.* **13**, 214-219.

68. Baranga, A. B.-A., Appelt, S., Erickson, C., Young, A. R. & Happer, W. (1998). *Phys. Rev. A* **58**, 2282-2294.
69. Kadlecek, S., Anderson, S. W. & Walker, T. G. (1998). *Phys. Rev. Lett.* **80**, 5512-5515.
70. Anger, B. C., Schrank, G., Schoeck, A., Butler, K.A., Solum, M.S., Pugmire, R.J., Saam, B. (2008). *Phys. Rev. A* **78**.
71. Breeze, S. R., Lang, S., Moudrakosvski, I., Ratcliffe, C.I., Ripmeester, J.A., Santyr, G., Simard, B., Zuger, I. (2000). *J. Appl. Phys* **87**, 8013-8017.
72. Breeze, S. R. Lang, S., Moudrakosvski, I., Ratcliffe, C.I., Ripmeester, J.A., Simard, B., Santyr, G. (1999). *Journal of Applied Physics* **86**, 4040-4042.
73. Magnus, F., Boatwright, A. L., Flodin, A. & Shiell, R. C. (2005). *J. Opt. B.* **7**, 109-118.
74. Hau, L. V., Harris, S. E., Dutton, Z. & Behroozi, C. H. (1999). *Nature* **397**, 594-598.
75. Bhaskar, N. D., Happer, W. & McClelland, T. (1982). *Phys. Rev. Lett.* **49**, 25.
76. Franzen, W. (1959). *Phys. Rev.* **115**, 850-856.
77. Steck, D. A. (2008). *Rb 85 & 87; Cs D-line Data*.
78. Jau, Y.-Y., Kuzma, N. N. & Happer, W. (2004). *Phys. Rev. A* **69**.
79. Wu, Z., Kitano, M., Happer, W., Hou, M. & Daniels, J. (1986). *Appl. Opt.* **28**, 4483-4492.
80. Pavlovskaya, G. E., Cleveland, Z. I., Stupic, K. F., Basaraba, R. J. & Meersmann, T. (2005). *Proc. Natl. Acad. Sci. USA* **102**, 18275-18279.

81. Ruset, I. C., Ketel, S. & Hersman, F. W. (2006). *Phys. Rev. Lett.* **96**, 053002.
82. Walker, T. G. (1989). *Phys. Rev. A* **40**, 4959-4964.
83. Nelson, I. A. & Walker, T. G. (2001). *Phys. Rev. A* **65**.
84. Levron, D., Walter, D.K., Appelt, S., Fitzgerald, R.J., Kahn, D., Korbly, S.E., Sauer, K.L., Happer, W., Earles, T.L., Mawst, L.J., Botez, D., Harvey, M., DiMarco, L., Connolly, J.C., Moller, H.E., Chen, X.J., Cofer, G.P., Johnson, G.A. (1998). *Appl. Phys. Lett.* **73**, 2668-2668.
85. Babcock, E., Nelson, I., Kadlecsek, S., Driehuys, B., Anderson, L.W., Hersman, F.W., Walker, T.G. (2003). *Phys. Rev. Lett.* **91**, 123003.
86. Couture, A. H., Clegg, T. B. & Driehuys, B. (2008). *Journal of Applied Physics* **104**.
87. Whiting, N., Nikolaou, P., Eschmann, N., Barlow, M. & Goodson, B. M. (2010), *51st Exp. Nucl. Magn. Reson. Conf. (Daytona Beach, FL)*.
88. Baranga, A. B.-A., Appelt, S., Romalis, M.V., Erisckson, C., Young, A.R., Cates, G.D., Happer, W. (1998). *Phys. Rev. Lett.* **80**, 2801-2804.
89. Salerno, M., de Lange, E.E., Altes, T.A., Truwit, J.D., Brookeman, J.R., Mugler III, J.P. (2002). *Radiology* **222**, 252-260.
90. Goodson, B. M. (2006). *Phys. World* **19**, 28-33.
91. Bifone, A. & Cherubini, A. (2003). *Prog. Nucl. Magn. Reson. Spectrosc.* **42**, 1-30.

92. Schmiedeskamp, J., Elmer, H.J., Heil, W., Otten, E.W., Sobolev, Y., Kilian, W., Rinneberg, H., Sander-Thommes, T., Seifert, F., Zimmer, J. (2006). *Eur. Phys. J. D* **38**, 445-454.
93. Babcock, E., Chann, B., Walker, T., Chen, W. C. & Gentile, T. R. (2006). *Phys. Rev. Lett.* **96**.
94. Driehuys, B., Pollaro, J. & Cofer, G. P. (2008). *Magn. Reson. Imaging* **60**, 14-20.
95. de Lange, E., Altes, T.A., Patrie, J.T., Parmar, J., Brookeman, J.R., Mugler III, J.P., Platts-Mills, T.A.E. (2007). *J. Allergy and Clinical Immunology* **119**, 1072-1078.
96. Woodhouse, N., Wild, J.M., Palesy, M.N.J., Fichele, S., Said, Z., Swift, A.J., van Beek, E.J.R. (2005). *J. Magn. Reson. Image.* **21**, 365-369.
97. Friar, J. L., Gibson, B. F., Payne, G. L., Bernstein, A. M. & Chupp, T. E. (1990). *Phys. Rev. C* **42**, 2310 - 2314.
98. Stoner, R. E., Rosneberry, M.A., Wright, J.T., Chupp, T., Oteiza, E.R., Walsworth, R.L. (1996). *Phys. Rev. Lett.* **77**, 3971-3974.
99. Mugler III, J. (2006). *ISMRM* (Seattle, WA).
100. Barlow, M. J., Li, C.H., Mair, R.W., Rosen, M.S., Walsworth, R.L., Whiting, N., Nikolaou, P., Chaffee, K.E., Saha, I., Goodson, B.M., Stupic, K.F., Cleveland, Z.I., Pavlovskaya, G.E., Meersmann, T. (2007). *48th Experimental Nucl. Magn. Reson. Conference* (Daytona, FL).
101. Cleveland, Z. I., Pavlovskaya, G. E., Stupic, K. F., LeNoir, C. F. & Meersmann, T. (2006). *J. Chem. Phys.* **124**, 044312.

102. Stupic, K. F., Cleveland, Z. I., Pavlovskaya, G. E. & Meersmann, T. (2006). *Solid State Nucl. Magn. Reson.* **29**, 79-84.
103. Cleveland, Z. I. & Meersmann, T. (2008). *ChemPhysChem* **9**, 1375-1379.
104. Cleveland, Z. I. & Meersmann, T. (2007). *Magn. Reson. in Chem.* **45**, 12-23.
105. Luhmer, M., Goodson, B.M., Song, Y.Q., Laws, D.D., Kaiser, L., Cyrier, M.C., Pines, A. (1999). *J. Am. Chem. Soc.* **121**, 3502-3512.
106. Ruth, U., Hof, T., Schmidt, J., Fick, D. & Jansch, H. J. (1999). *Appl. Phys. B* **68**, 93.
107. Desvaux, H., Gautier, T., Le Goff, G., Petro, M. & Berthault, P. (2000). *European Physical Journal D* **12**, 289-296.
108. Fukutomi, J., Suzuki, E., Shimizu, T., Kimura, A. & Fujiwara, H. (2003). *J. Magn. Reson.* **160**, 26-32.
109. Hersman, F. W., Ruset, I.C., Ketel, S., Muradian, I., Covrig, S.D., Distelbrink, J., Porter, W., Watt, D., Ketel, J., Brackett, J., Hope, A., Patz, S. (2008). *Acad. Radiol.* **15**, 683-692.
110. Rosenberry, M. A., Reyes, J. P., Tupa, D. & Gay, T.J. (2007). *Phys. Rev. A* **75**.
111. Nikolaou, P., Whiting, N., Chaffee, K.E., Saha, I., Barlow, M.J., Goodson, B.M. (2007). *48th Exptl. Nucl. Magn. Reson. Conf.* (Daytona, FL).
112. Walter, D. K., Griffith, W. M. & Happer, W. (2001). *Phys. Rev. Lett.* **86**, 3264-3267.

113. Knagge, K., Prange, J. & Raftery, D. (2004). *Chem. Phys. Lett.* **397**, 11-16.
114. Romalis, M. V., Miron, E. & Cates, G. D. (1997). *Phys. Rev. A* **56**, 4569-4578.
115. Fink, A. & Brunner, E. (2007). *Appl. Phys. B* **89**, 65-71.
116. Whiting, N., Nikolaou, P., Eschmann, N., Barlow, M. & Goodson, B. M. (2009). *50th Exptl. Nucl. Magn. Reson. Conf.* (Pacific Grove, CA).
117. Franz, F. A. & Sooriamoorthi, C. E. (1974). *Phys. Rev. A*. **10**, 126-140.
118. Wagshul, M. E. & Chupp, T. E. (1989). *Phys. Rev. A* **40**, 4447 - 4454.
119. Cummings, W. J., Hausser, O. & Lorenzon, W. (1995). *Phys. Rev. A* **51**, 4842-4851.
120. Nelson, I. A., Chann, B. & Walker, T. G. (2000). *Appl. Phys. Lett.* **76**, 1356.
121. Nakamura, S. (1998). *Annu. Rev. Mater. Sci.* **28**, 125-152.
122. Nakamura, S., Senoh, M., Nagahama, S., Iwasa, N., Yamada, T., Kiyoku, H., Matsushita, T., Sugimoto, Y., Kozaki, T., Umemoto, H., Sano, M., Chocho, K. (1998). *Appl. Phys. Lett.* **72**, 2014-2016.
123. Saleathe, R. P. (1979). *Appl. Phys. A*. **20**, 1-18.
124. Yoshida, H., Kuwabar, M., Yamashita, Y., Takagi, Y., Uchiyama, K., Kan, H. (2009). *New. J. Phys.* **11**, 1-14.
125. Newport. (2010). *Product Notes*.
126. Lammert, R. M., Oh, S.W., Osowski, M.L., Panja, C., Rudy, P.T., Stakelon, T., Ungar, J.E. (2006). *White Paper*, 1-12.

127. Zhu, H., Ruset, I. C. & Hersman, F. W. (2005). *Opt. Lett.* **30**, 1342-1344.
128. Babcock, E., Chann, B., Nelson, I. A. & Walker, T. (2005). *Appl. Opt.* **44**, 3098-3104.
129. Barlow, M. J. (2006). *47th Exptl. Nucl. Magn. Reson. Conf.* (Pacific Grove, CA).
130. Gourevitch, A., Venus, G., Smirnov, V., Hostutler, D. A. & Glebov, L. (2008). *Opt. Lett.* **33**, 702-704.
131. Moser, C. & Steckman, G. (2005). *Photonics Spectra* **82**.
132. Volodin, B. L., Dolgy, S.V., Melnik, E.D., Downs, E., Shaw, J., Ban, V.S. (2004). *Opt. Lett.* **29**, 1891-1893.
133. Whiting, N., Nikolaou, P., Eschmann, N., Barlow, M.J. & Goodson, B. M. (2010). *Manuscript in preparation for submission to Optics Express*.
134. Barlow, M.J., Eschmann, N., Whiting, N., Nikolaou, P. & Goodson, B. M. (2009). *50th Exptl. Nucl. Magn. Reson. Conf.* (Pacific Grove, CA).
135. Barlow, M. J., Nikolaou, P., Whiting, N., Eschmann, N.A., Goodson, B.M. (2008). *49th Experimental Nucl. Magn. Reson. Conference* (Asilomar, CA).
136. Barlow, M.J., Eschmann, N., Whiting, N., Nikolaou, P. & Goodson, B. M. (2010). *51st Exp. Nucl. Magn. Reson. Conf* (Daytona Beach, FL).
137. Driehuys, B. (2009). *American Physics Society: Division of Molecular, Atomic, and Optical Physics* (Charlottesville, VA).
138. Poliakoff, M., Howdle, S. M. & Kazarian, S. G. (1995). *Angew. Chem. Int. Ed. Engl.* **24**, 1275-1295.

139. Tilton Jr., R. F., Kuntz Jr., I. D. & Petsko, G. A. *Biochemistry* **23**, 2849-2857 (1984).
140. Miller, K. W., Reo, N.V., Uiterkamp, A.J.M., Stengle, D.P., Stengle, T.R., Williamson, K.L. (1981). *Proc. Natl. Acad. Sci. USA* **78**, 4946-4949.
141. Rubin, S. M., Spence, M. M., Goodson, B. M., Wemmer, D. & Pines, A. (2000). *Proc. Natl. Acad. Sci. USA* **97**, 9472-9475.
142. Albert, M. S. & Balamore, D. (1998). *Nucl. Instr. and Meth. in Phys. Res.* **402**, 441-453.
143. Gatzke, M., Gates, G.D., Driehuys, B., Fox, D., Happer, W., Saam, B. (1993). *Phys. Rev. Lett.* **70**, 690-693.
144. Cates, G. D., Benton, D.R., Gatzke, M., Happer, W., Hasson, K.C., Newbury, N.R. (1990). *Phys. Rev. Lett.* **65**, 2591-2594.
145. Hunt, E. R. & Carr, H. Y. (1963). *Phys. Rev.* **130**, 2302-2305.
146. Haake, M., Pines, A., Reimer, J. A. & Seydoux, R. (1997). *J. Am. Chem. Soc.* **119**, 11711-11712.
147. Seydoux, R., Haake, M., Pines, A. & Reimer, J. A. (1999). *J. Phys. Chem. B.* **103**, 4629-4637.
148. Bowers, C. R., Long, H. W., Pietrass, T., Gaede, H. C. & Pines, A. (1993). *Chem. Phys. Lett.* **205**, 168-170.
149. Driehuys, B., Cates, G.D., Happer, W., Mabuchi, H., Saam, B., Albert, M.S., Wishnia, A. (1993). *Phys. Lett. A* **184**, 88-92.
150. Lisitza, N., Muradian, I., Frederick, E., Patz, S., Hatabu, H., Chekmenev, E.Y. (2009). *J. Chem. Phys.* **131**.

151. Carver, T. R. & Slichter, C. P. (1953). *Phys. Rev.* **92**, 212-213.
152. Navon, G., Song, Y.Q., Room, T., Appelt, S., Taylor, R.E., Pines, A. (1996). *SCIENCE* **271**, 1848-1851.
153. Cherubini, A., Payne, G., Leach, M. O. & Bifone, A. (2003). *Chem. Phys. Lett.* **371**, 640-644.
154. He, P., Walkup, L.L., Whiting, N., Nikolaou, P., Chaffee, K., Li, X., Goodson, B.M. (2010). *51st Exp. Nucl. Magn. Reson. Conf.* (Daytona Beach, FL).
155. Rubin, S. M., Spence, M. M., Pines, A. & Wemmer, D. (2001). *J. Magn. Reson* **152**, 79-86.
156. Lowery, T., Rubin, S.M., Ruiz, E.J., Spence, M.M., Winssinger, N., Schultz, P.G., Pines, A., Wemmer, D.E. (2003). *Magn. Reson. Imaging* **21**, 1235-1239.
157. Schoenborn, B. P., Watson, H. C. & Kendrew, J. C. (1965). *Nature* **207**, 28-30.
158. Tilton Jr., R. F. & Kuntz Jr., I. D. (1982). *Biochemistry* **21**, 6850-6857.
159. Locci, E., Dehouch, Y., Casu, M., Saba, G., Lai, A., Luhmer, M., Reisse, J., Bartik, K.J. (2001). *J. Magn. Reson* **150**, 167-174.
160. Tilton Jr., R. F., Singh, U. C., Kuntz Jr., I. D. & Kollman, P. A. (1988). *J. Mol. Biol.* **199**, 195-211.
161. Stryer, L. (1975). *Biochemistry* (W.H. Freeman and Co., San Fransisco).
162. Wang, Y., Baskin, J. S., Xia, T. & Zewail, A. H. (2004). *Proc. Natl. Acad. Sci. USA* **101**, 18000-18005.

163. Li, X. (2007). *Dept. of Chemistry & Biochemistry* (Southern Illinois University, Carbondale).
164. Hill, P. A., Wei, Q., Eckenhoff, G. & Dmochowski, I. J. (2007). *J. Am. Chem. Soc.* **129**, 9262-9263.
165. Fogarty, H. A., Berthault, P., Brotin, T., Huber, G., Desvaux, H., Dutasta, J.P. (2007). *J. Am. Chem. Soc.* **129**, 10332-10333.
166. Song, Y.-Q., Goodson, B.M., Taylor, R.E., Laws, D.D., Navon, G., Pines, A. (1997). *Angew. Chem. Int. Ed. Engl.* **36**, 2368-2370.
167. Collet, A. (1987). *Tetrahedron* **24**, 5725-5759.
168. Collet, A., Dutasta, J.-P., Lozach, B. & Canceill, J. (1993). *Topics in Current Chemistry (Supramolecular Chemistry I)* **165**, 103-129.
169. Bartik, K. J., Luhmer, M., Dutasta, J.-P., Collet, A. & Reisse, J. (1998). *J. Am. Chem. Soc.* **120**, 784-791.
170. Kirchhoff, P. D., Bass, M.B., Hanks, B.A., Briggs, J.M., Collet, A., McCammon, J.A. (1996). *J. Am. Chem. Soc.* **118**, 3237-3246.
171. Mynar, J. L., Lowery, T., Wemmer, D., Pines, A. & Frechet, J. M. (2006). *J. Am. Chem. Soc.* **128**, 6334-6335.
172. Spence, M. M., Rubin, S.M., Dimitrov, I.E., Ruiz, E.J., Wemmer, D.E., Pines, A., Qin-Yao, S., Tian, F., Schultz, P.G. (2001). *Proc. Natl. Acad. Sci. USA* **98**, 10654-10657.
173. Raftery, D., Long, H. W., Reven, L., Tang, P. & Pines, A. (1992). *Chem. Phys. Lett.* **191**, 385-390.

174. Moudrakovski, I., Lang, S., Ratcliffe, C.I., Simard, B., Santyr, G., Ripmeester, J.A. (2000). *J. Magn. Reson* **144**, 372-377.
175. Kaiser, L., Meersmann, T., Logan, J. W. & Pines, A. (2000). *Proc. Natl. Acad. Sci. USA* **97**, 2414-2418.
176. Kneller, J. M., Soto, R.J., Surber, S.E., Colomer, J.F., Fonseca, A., Nagy, J.B., Van Tendeloo, G., PietraB, T. (2000). *J. Am. Chem. Soc.* **122**, 10591-10597.
177. Room, T., Appelt, S., Seydoux, R., Hahn, E. L. & Pines, A. (1997). *Phys. Rev. B.* **55**, 11604-11610.
178. Bowers, C. R., Storhaug, V., Webster, C.E., Bharatam, J., Cottone III, A., Gianna, R., Betsey, K., Gaffnewy, B.J. (1999). *J. Am. Chem. Soc.* **13**, 9370-9377.
179. Raftery, D. (2006). *Proc. Natl. Acad. Sci. USA* **103**, 12657-12658.
180. Savukov, I. M., Seltzer, S. J. & Romalis, M. V. (2005). *Phys. Rev. Lett.* **95**.
181. Blumich, B., Casanova, F. & Appelt, S. (2009). *Chem. Phys. Lett.* **477**, 231-240.
182. Moule, A. J., Spence, M.M., Han, S.I., Seeley, J.A., Pierce, K.L., Saxena, S., Pines, A. (2003). *Proc. Natl. Acad. Sci. USA* **100**, 9122-9127.
183. Granwehr, J., Harel, E., Han, S.-I., Garcia, S. & Pines, A. (2005). *Phys. Rev. Lett.* **95**.
184. Seeley, J. A., Han, S.-I. & Pines, A. (2004). *J. Magn. Reson* **167**, 282-290.
185. McDonnell, E. E., Han, S.-I., Hilty, C., Pierce, K. L. & Pines, A. (2005). *Anal. Chem.* **77**, 8109-8114.

186. Hilty, C., McDonnell, E.E., Granwehr, J., Pierce, K.L., Han, S.I., Pines, A. (2005). *Proc. Natl. Acad. Sci. USA* **102**, 14960-14963.
187. Harel, E., Granwehr, J., Seeley, J. A. & Pines, A. (2006). *Nature Mat.* **5**, 321-327.
188. Patz, S., Hersman, F.W., Muradian, I., Hrovat, M.I., Ruset, I.C., Ketel, I.C., Jacobson, F., Topulos, G.P., Hatabu, H., Butler, J.P. (2007). *Eur. J. Radiol* **64**, 335-344.
189. Driehuys, B., Cofer, G.P., Pollaro, J., Mackel, J.B., Hedlund, L.W., Johnson, G.A. (2006). *Proc. Natl. Acad. Sci. USA* **103**, 18278-18283.
190. Albert, M. S., Tseng, C.H., Williamson, D., Oteiza, E.R., Walsworth, R.L., Kraft, B., Kacher, D., Holman, B.L., Jolesz, F.A. (1996). *J. Magn. Reson. B.* **111**, 204-207.
191. Rizi, R. R., Dimitrov, I.E., Thompson, A., Jones, G., Gentile, T.R., Ishii, M., Reddy, R., Schnall, M.D., Leigh, J.S. (1998) *Magn. Reson. Med.* **39**, 865-868.
192. Phillips, C. D., Goldstein, J. H., Brookeman, J., Mugler III, J. & Maier, T. (1999). *Rev. Neuroradiol.* **12**, 183-185.
193. Goodson, B. M. (1999). *Concepts in Magnetic Resonance* **11**, 203-222.
194. Albert, M. S., Schepkin, V. D. & Budinger, T. F. (1995). *J. Comput. Assisted Tomogr.* **19**, 975-978.
195. Sakai, K., Bilek, A.M., Oteiza, E.R., Walsworth, R.L., Balamore, D., Jolesz, F.A., Albert, M.S. (1996). *J. Magn. Reson. B.* **111**, 300-304.

196. Wolber, J., Cherubini, A., Leach, M. O. & Bifone, A. (2000). *Magn. Reson. Med.* **43**, 491-496.
197. Li, X., Newberry, C., Saha, I., Nikolaou, P., Whiting, N., Goodson, B.M. (2006). *Chem. Phys. Lett.* **419**, 233-239.
198. Li, X., Whiting, N., Vasudevan, S. Rubin, S.M., Musick, B., Nikolaou, P., Goodson, B.M. (2006). *47th Experimental Nucl. Magn. Reson. Conference* (Asilomar, CA).
199. Li, X., Musick, B., Whiting, N., Rubin, S. M. & Goodson, B. M. (2010). *manuscript in preparation for submission to J. Phys. Chem. B.*
200. Kuzma, N. N., Patton, B., Raman, K. & Happer, W. (2002). *Phys. Rev. Lett.* **88**, 147602.
201. Augustine, M. P. & Zilm, K. W. (1996). *J. Chem. Phys.* **105**, 2998-3011.
202. Gibbs, H. (1965). *Phys. Rev.* **139**, 1374-1391.
203. Gibbs, H. M. & Hull, R. J. (1967). *Phys. Rev.* **153**, 132-151.
204. Tupa, D. & Anderson, L. W. (1986). *Phys. Rev. A* **33**, 1045-1051.
205. Whiting, N., Nikolaou, P., Eschmann, N., Barlow, M. & Goodson, B. M. (2010). *manuscript in preparation for submission to J. Magn. Reson.*
206. Rice, C. V. & Raftery, D. (2002). *J. Phys. Chem.* **117**, 5632-5641.
207. Barlow, M. J., Whiting, N., Nikolaou, P., Eschmann, N.A., Mair, R., Goodson, B.M. (2009). *Diffusion Fundamentals (Special Issue, Proc. Magn. Reson. Porous Media)* **10**, 116.
208. Young, A. R., Appelt, S., Baranga, A. B.-A., Erickson, C. & Happer, W. (1997). *Appl. Phys. Lett.* **70**, 3081-3083.

209. Whiting, N., Nikolaou, P., Eschmann, N.A., Barlow, M.J., & Goodson, B.M. (2010). *manuscript in preparation*.
210. NSF Reviewer Comment. (2010).
211. Luo, J., Mao, X., Chen, J., Wang, S., Zhao, M., Fu, L., Zeng, X. (1999). *Appl. Magn. Reson.* **17**, 587-595.
212. Zhou, X., Luo, J., Sun, X-P., Zeng, X-Z., Zhan, M-S., Ding, S-W., Liu, M-L. (2003). *Cond. Mat.* **1**.
213. Zhou, X. Luo, J., Sun, X-P., Zeng, X-Z., Ding, S-W., Liu, M-L. Zhan, M-S. (2004). *Cond. Mat.* **1**.

VITA

Graduate School
Southern Illinois University

Nicholas Whiting

Date of Birth: April 26, 1983

217 S. Giant City Rd. Lot 16, Carbondale, Illinois 62902

1185 Telephone Rd, Galatia, Illinois 62935

whiting_nick@hotmail.com (email address after graduation)

Southeastern Illinois College
Associate of Science, May 2003

Southern Illinois University Carbondale
Bachelor of Science, Chemistry, May 2005

Special Honors and Awards:

NSF International Research Fellowship (2010-2012)
38th SEMRC Student Travel Stipend Award (2009)
SIU Dissertation Research Award (2009-2010)
Gower Summer Research Fellowship (2009)
49th & 51st ENC Student Travel Stipend Award (2008 & 2010)
Participant: 57th Meeting of Nobel Laureates and Student Researchers,
Lindau, Germany (2007)
Schulbach Teaching Assistant Award (2007)
College of Science Dean's List (2005)
Summer Research Fellowship (2004)
Jim and Jean Neckers Chemistry Scholarship (2004)
Scholastic Honors Award (2004)
Phi Theta Kappa Honor Society Academic Scholarship (2003-2004)
Sam Porter Sophomore Chemistry Award (2003)
Jr. College Academic Scholarship (2001-2003)

Dissertation Title:

USING HIGH-POWERED, FREQUENCY-NARROWED LASERS FOR
RB/¹²⁹XE AND CS/¹²⁹XE SPIN-EXCHANGE OPTICAL PUMPING TO ACHIEVE
IMPROVED PRODUCTION OF HIGHLY SPIN-POLARIZED XENON FOR USE
IN MAGNETIC RESONANCE APPLICATIONS

Major Professor: Boyd M. Goodson

Publications:

"Rb/Xe Spin Exchange Optical Pumping with Tunable, High-Power LDAs Narrowed with On-Chip Volume Holographic Gratings." N. Whiting, P. Nikolaou, N. Eschmann, M.J. Barlow, and B.M. Goodson, (manuscript in preparation for submission to *Optics Express*).

"Cesium/Xenon Spin Exchange Optical Pumping at the Cs D₁ and D₂ Wavelengths using High-Power Broadband Laser Diode Arrays". N. Whiting, P. Nikolaou, N. Eschmann, M.J. Barlow, and B.M. Goodson, (manuscript in preparation).

"Site-Specific Interactions Between Xenon and a Diamagnetic, Structurally Intact Myoglobin in Solution." X. Li, B. Musick, N. Whiting, S.M. Rubin, and B.M. Goodson, (manuscript in preparation for submission to *Journal of Physical Chemistry B*).

"Interdependence of In-Cell Xenon Density and Temperature during Rb/¹²⁹Xe Spin- Exchange Optical Pumping." N. Whiting, P. Nikolaou, N. Eschmann, M.J. Barlow, and B.M. Goodson, (manuscript in preparation for submission to *Journal of Magnetic Resonance*).

"A New Spin Exchange Optical Pumping (SEOP) Modality for Hyperpolarized ¹²⁹Xe Production and Use in Porous Media." M. J. Barlow, N. Whiting, P. Nikolaou, N. Eschmann, R. Mair, and B. M. Goodson. *Diffusion Fundamentals*, **10**, 116 (2009).

"Generation of Laser-Polarized Xenon Using Fiber-Coupled Laser Diode Arrays Narrowed with Integrated Volume Holographic Gratings." P. Nikolaou, N. Whiting, N. Eschmann, K.E. Chaffee, M.J. Barlow, and B.M. Goodson. *Journal of Magnetic Resonance*, **197**, 249-254 (2009).

"Characterization of Violet Emission from Rb Optical Pumping Cells Used in Laser-Polarized Xe NMR Experiments." I. Saha, P. Nikolaou, N. Whiting, and B.M. Goodson, *Chemical Physics Letters*, **428**, 268-276 (2006).

"Interactions Between Xenon and Phospholipid Bicelles Studied by ²H / ¹²⁹Xe / ¹³¹Xe NMR and Optical Pumping of Nuclear Spins." X. Li, C. Newberry, I. Saha, P. Nikolaou, N. Whiting, B.M. Goodson, *Chemical Physics Letters*, **419**, 233-239 (2006).

Conference Presentations:

“Cesium/Xenon Spin-Exchange Optical Pumping using High-Power Laser Diode Arrays at the Cs D_1 & D_2 Wavelengths.” (Poster). N. Whiting, P. Nikolaou, N. Eschmann, M.J. Barlow, B.M. Goodson. *51th Experimental Nuclear Magnetic Resonance Conference (ENC)*: Daytona Beach, FL April 18-23, 2010.

“Using High-Power Tunable ‘On-Chip’ Grating-Narrowed Laser Diode Arrays to Study the Interplay of Wavelength, Offset, Temperature, and Xe Density During Xe SEOP.” (Poster). M. J. Barlow, N. Eschmann, N. Whiting, P. Nikolaou, B. M. Goodson. *51th Experimental Nuclear Magnetic Resonance Conference (ENC)*: Daytona Beach, FL April 18-23, 2010.

“Studies of ^{129}Xe to ^1H Spin Polarization Transfer in Aqueous Xenon-Binding Systems.” (Poster) P. He, L. Walkup, N. Whiting, P. Nikolaou, K. E. Chaffee, X. Li, B. M. Goodson. *51th Experimental Nuclear Magnetic Resonance Conference (ENC)*: Daytona Beach, FL April 18-23, 2010.

“Improved Production of Large Quantities of Highly Spin-Polarized Xenon for Use in Magnetic Resonance Applications.” (Talk). N. Whiting, P. Nikolaou, N. Eschmann, M. J. Barlow, B. M. Goodson. *38th Southeastern Magnetic Resonance Conference (SEMRC)*. Vanderbilt University, Nashville, TN Nov. 6-8, 2009.

“Preparation of Laser-Polarized Xenon at High Xe Densities and High Resonant Laser Powers Provided by Volume Holographic Grating-Narrowed LDAs.” (Talk). B.M. Goodson, N. Whiting, P. Nikolaou, N. Eschmann, M.J. Barlow. *40th Division of Atomic, Molecular, and Optical Physics (DAMOP) of the American Physical Society*: University of Virginia, Charlottesville, VA May 19-23, 2009.

“Interplay of Cell Temperature and Xenon Density Resulting in Anomalously High Xe Polarization during Optical Pumping at High Xe Densities.” (Poster). N. Whiting, P. Nikolaou, N. Eschmann, M.J. Barlow, B.M. Goodson. *50th Experimental Nuclear Magnetic Resonance Conference (ENC)*: Pacific Grove, CA March 29- April 3, 2009.

“Investigation of Xenon Nuclear Polarization as a Function of Laser Wavelength and Optical Power Using Narrowed Laser Sources.” (Poster). M.J. Barlow, N. Eschmann, N. Whiting, P. Nikolaou, B.M. Goodson. *50th Experimental Nuclear Magnetic Resonance Conference (ENC)*: Pacific Grove, CA March 29- April 3, 2009.

“Anomalously High Xenon Polarization at High Xenon Densities Achieved via Optical Pumping with Volume Holographic Grating (VHG)-Narrowed Laser Diode Arrays.” (Talk) N. Whiting, P. Nikolaou, N. Eschmann, M. J. Barlow, B. M.

Goodson. *Chicago Area Nuclear Magnetic Resonance Discussion Group (CANMRDG)*. Washington University, St. Louis, MO. Nov. 8, 2008.

"A New Spin Exchange Optical Pumping (SEOP) Modality for Hyperpolarized ^{129}Xe Production and Use in Porous Media." (Poster) M. J. Barlow, N. Whiting, P. Nikolaou, N. Eschmann, R. Mair, B. M. Goodson. *9th Magnetic Resonance in Porous Media Conference (MRPM9)*. Cambridge, MA. July 13-17, 2008.

"Anomalous High Xenon Polarization at High Xenon Partial Pressures with Tunable Volume Holographic Grating (VHG) Frequency Narrowed Lasers." (Poster) M. J. Barlow, P. Nikolaou, N. Whiting, N. Eschmann, B. M. Goodson. *EUROMAR*. St. Petersburg, Russia. July 6-11, 2008.

"Effects of Power, Linewidth, and Component Gas Densities on Xenon Polarization with Fixed-Frequency Volume Holographic Grating (VHG)-Narrowed Laser Diode Arrays." (Poster) N. Whiting, P. Nikolaou, N. Eschmann, M.J. Barlow, B.M. Goodson. *49th Experimental Nuclear Magnetic Resonance Conference (ENC)*: Pacific Grove, CA. March 9-14, 2008.

"A Next-Generation Xenon-Polarization Laser source with Adjustable Wavelength, Spectral Width, and Flux for Biomedical and Materials Spectroscopy and Imaging." (Poster) M. J. Barlow, P. Nikolaou, N. Whiting, N. Eschmann, B.M. Goodson, C.H. Li, R.W. Mair, M.S. Rosen, R.L. Walsworth. *49th ENC*: Pacific Grove, CA. March 9-14, 2008.

"Improved generation of laser-polarized xenon using a fiber-coupled laser diode array narrowed with an integrated volume holographic grating." (Poster) P. Nikolaou, N. Whiting, K.E. Chaffee, I. Saha, M.J. Barlow, B.M. Goodson. *48th ENC*: Daytona Beach, FL April 22-27, 2007.

"Volume holographic grating frequency narrowed laser for improved ^3He and ^{129}Xe Polarization for use with in materials, porous media, and lung MRI studies." (Poster) M.J. Barlow, C.H. Li, R.W. Mair, M.S. Rosen, R.L. Walsworth, N. Whiting, P. Nikolaou, K. Chaffee, I. Saha, B.M. Goodson. *48th ENC*: Daytona Beach, FL April 22-27, 2007.

"Site-specific interactions between xenon and a diamagnetic, structurally intact myoglobin in solution" (Poster) X. Li, B. Musick, N. Whiting, B. M. Goodson. *47th ENC*: Pacific Grove, CA April 23-28, 2006.

“An inexpensive, modular optical pumping apparatus for use in laser-polarized ^{129}Xe NMR experiments.” (Poster) I. Saha, P. Nikolaou, N. Whiting, X. Li, B.M. Goodson. 46th ENC: Providence, RI April 10-15, 2005.

“Enhancing the NMR signatures of weak intermolecular interactions using laser-polarized xenon and liquid crystalline matrices.” (Invited Talk) B.M. Goodson, X. Li, K. Chaffee, I. Saha, C. Newberry, P. Nikolaou, N. Whiting, M. Marjanska. 229th ACS National Meeting: San Diego, CA March 13-17, 2005.